

Lappeenrannan teknillinen yliopisto
Lappeenranta University of Technology

Antti Tarkiainen

**POWER QUALITY IMPROVING WITH VIRTUAL FLUX-
BASED VOLTAGE SOURCE LINE CONVERTER**

*Thesis for the degree of Doctor of Science
(Technology) to be presented with due per-
mission for public examination and criti-
cism in the Auditorium 1383 at Lappeen-
ranta University of Technology, Lappeen-
ranta, Finland on the 11th of March, 2005,
at noon.*

Acta Universitatis
Lappeenrantaensis
206

Supervisor Professor Juha Pyrhönen
Department of Electrical Engineering
Lappeenranta University of Technology
Lappeenranta, Finland

Reviewers Dr. Volker Staudt
Institute for Electrical Power Engineering and Power Electronics
Ruhr-Universität Bochum
Bochum, Germany

Dr. Jouko Niiranen
ABB Oy
Helsinki, Finland

Opponent Professor Marian P. Kazmierkowski
Warsaw University of Technology
Institute of Control and Industrial Engineering
Warsaw, Poland

ISBN 952-214-011-2
ISBN 952-214-012-0 (PDF)
ISSN 1456-4491

Lappeenrannan teknillinen yliopisto
Digipaino

Abstract

Antti Tarkkainen

Power quality improving with virtual flux-based voltage source line converter

Lappeenranta 2005

140 p.

Acta Universitatis Lappeenrantaensis 206

Diss. Lappeenranta University of Technology

ISBN 952-214-011-2, ISBN 952-214-012-0 (PDF), ISSN 1456-4491

Line converters have become an attractive AC/DC power conversion solution in industrial applications. Line converters are based on controllable semiconductor switches, typically insulated gate bipolar transistors. Compared to the traditional diode bridge-based power converters line converters have many advantageous characteristics, including bidirectional power flow, controllable dc-link voltage and power factor and sinusoidal line current.

This thesis considers the control of the line converter and its application to power quality improving. The line converter control system studied is based on the virtual flux linkage orientation and the direct torque control (DTC) principle. A new DTC-based current control scheme is introduced and analyzed. The overmodulation characteristics of the DTC converter are considered and an analytical equation for the maximum modulation index is derived.

The integration of the active filtering features to the line converter is considered. Three different active filtering methods are implemented. A frequency-domain method, which is based on selective harmonic sequence elimination, and a time-domain method, which is effective in a wider frequency band, are used in harmonic current compensation. Also, a voltage feedback active filtering method, which mitigates harmonic sequences of the grid voltage, is implemented. The frequency-domain and the voltage feedback active filtering control systems are analyzed and controllers are designed. The designs are verified with practical measurements. The performance and the characteristics of the implemented active filtering methods are compared and the effect of the L- and the LCL-type line filter is discussed. The importance of the correct grid impedance estimate in the voltage feedback active filter control system is discussed and a new measurement-based method to obtain it is proposed. Also, a power conditioning system (PCS) application of the line converter is considered. A new method for correcting the voltage unbalance of the PCS-fed island network is proposed and experimentally validated.

Keywords: Line converter, PWM rectifier, voltage source converter, current control, active power filter

UDC 621.314.63 : 681.537 : 621.316.7

Acknowledgments

This research work was carried out at Lappeenranta University of Technology (LUT) during the years 2000–2004 as a part of the “ISU-project.” The preparation of this manuscript took a good part of the year 2004. These five years I have been a member of the Finnish Graduate School of Electrical Engineering and worked in Carelian Drives and Motor Centre (CDMC) in the Department of Electrical Engineering in LUT. CDMC is a research center jointly organized by ABB Oy and LUT. I appreciate the enthusiastic spirit and devoted professional personnel of the Department of Electrical Engineering—it has been a pleasure and a privilege to work with you.

I thank my supervisor, Professor Juha Pyrhönen, for his valuable comments and guidance and for always being encouraging and supporting. The excellent research environment and lively research tradition established in the Department of Electrical Engineering owes much to his enthusiasm and dedication. I wish to express my gratitude to Dr. Markku Niemelä, the leader of CDMC research activities, for discussions, comments and highly appreciated support during the project. And, not forgetting, organizing the project meetings.

I wish to thank my colleague Dr. Riku Pöllänen for the numerous technical discussions, which, from the very beginning of this project, proved to be very valuable to me. Also the collaboration during the years is greatly appreciated.

Many thanks are due to Mrs. Julia Vauterin for carefully reviewing the language of this manuscript.

I thank the reviewers, Dr. Volker Staudt and Dr. Jouko Niiranen, for thoroughly examining the manuscript and for many valuable comments and corrections.

This research work was financed by Finnish Graduate School of Electrical Engineering, ABB Oy and Lappeenranta University of Technology. Also, the financial support by Walter Ahlström Foundation (Walter Ahlströmin säätiö), The Finnish Cultural Foundation North-Savo Regional Fund (Suomen Kulttuurirahaston Pohjois-Savon rahasto), The Finnish Cultural Foundation (Suomen Kulttuurirahasto), The Foundation of Technology (Tekniikan edistämissäätiö), Ulla Tuominen Foundation (Ulla Tuomisen säätiö), Lahja and Lauri Hotinen Fund (Lahja ja Lauri Hotisen rahasto) and Association of Electrical Engineers in Finland (Sähköinsinööriiliiton Säätiö) is gratefully acknowledged.

Helsinki, January 2005

Antti Tarkiainen

List of Publications

- I A. Tarkiainen, R. Pöllänen, M. Niemelä, and J. Pyrhönen, Current Controlled Line Converter Using Direct Torque Control Method, *European Transactions on Electrical Power*, vol. 14, no. 5., Sept./Oct. 2004, pp. 277–291.
- II A. Tarkiainen, R. Pöllänen, M. Niemelä, J. Pyrhönen, and M. Vertanen, Compensating the Island Network Voltage Unsymmetry with DTC-Modulation-Based Power Conditioning System, *IEEE Transactions on Industry Applications*, vol. 40, no. 5, Sept./Oct. 2004, pp. 1398–1405.
- III A. Tarkiainen, R. Pöllänen, M. Niemelä, and J. Pyrhönen, DC-Link Voltage Effects on Properties of a Shunt Active Filter, *IEEE Power Electronics Specialists Conference*, Aachen Germany, 2004, pp. 3169–3175.
- IV A. Tarkiainen, R. Pöllänen, M. Niemelä, and J. Pyrhönen, Mitigating Grid Voltage Harmonics Using a Line Converter with Active Filtering Feature, *Electrical Engineering*, in press.
- V A. Tarkiainen, R. Pöllänen, M. Niemelä, and J. Pyrhönen, Identification of Grid Impedance for Purposes of Voltage Feedback Active Filtering, *IEEE Power Electronics Letters*, vol. 2, no. 1, March 2004, pp. 6–10.

Contents

| | |
|---|------------|
| Abstract | iii |
| Acknowledgments | v |
| List of Publications | vi |
| Nomenclature | xi |
| 1 Introduction | 1 |
| 1.1 From electric light to controlled drives | 1 |
| 1.2 Line converter | 2 |
| 1.3 Some mathematical concepts used in electrical engineering | 5 |
| 1.3.1 Space-vectors | 5 |
| 1.3.2 Per unit values | 8 |
| 1.3.3 Fourier series | 9 |
| 1.4 The outline of the thesis | 11 |
| 1.5 Scientific contributions | 13 |
| 2 Power quality | 15 |
| 2.1 What is power quality? | 15 |
| 2.2 Harmonics and harmonic sequences | 16 |
| 2.3 Power quality indices | 24 |
| 2.3.1 General harmonic indices | 24 |
| 2.3.2 Unbalance | 27 |
| 2.4 Summary | 27 |

| | | |
|----------|--|-----------|
| 3 | Power components | 29 |
| 3.1 | Averaged power components | 29 |
| 3.1.1 | Single-phase system | 29 |
| 3.1.2 | Three-phase system | 31 |
| 3.2 | Instantaneous power components | 32 |
| 3.2.1 | The Fryze-Buchholz-Depenbrock method | 32 |
| 3.2.2 | The instantaneous reactive power theory | 34 |
| 3.3 | Numerical example | 37 |
| 3.4 | Summary | 43 |
| 4 | Modeling and control of line converter | 45 |
| 4.1 | Dynamic model of line converter | 45 |
| 4.1.1 | Ideal converter bridge | 46 |
| 4.1.2 | Direct current and dc-link model | 49 |
| 4.1.3 | Model of a line filter | 49 |
| 4.2 | Line converter control principles | 50 |
| 4.2.1 | Power angle control | 50 |
| 4.2.2 | Current vector control | 51 |
| 4.2.3 | Direct torque control | 52 |
| 4.3 | Current control with DTC line converter | 58 |
| 4.3.1 | Converter virtual flux linkage orientation | 58 |
| 4.3.2 | Modeling the DTC current control | 61 |
| 4.4 | Overmodulation characteristics of a DTC converter | 72 |
| 4.4.1 | Carrier-based and space-vector modulation | 72 |
| 4.4.2 | Fundamental voltage of DTC converter | 74 |
| 4.5 | Summary | 81 |
| 5 | Power Quality Improving | 83 |
| 5.1 | Power conditioning system | 83 |
| 5.2 | Active filters | 85 |
| 5.3 | Active filtering feature of a line converter | 87 |
| 5.4 | The test setup | 88 |
| 5.5 | Frequency-domain active filtering with DTC controlled line converter | 90 |
| 5.5.1 | The method of harmonic synchronous reference frames | 90 |

| | | |
|----------|---|------------|
| 5.5.2 | Analysis | 93 |
| 5.5.3 | Practical verification | 101 |
| 5.6 | Voltage feedback active filtering | 104 |
| 5.6.1 | Operation principle of voltage feedback active filter | 104 |
| 5.6.2 | Control system analysis | 106 |
| 5.7 | Time-domain active filtering | 109 |
| 5.7.1 | Implementation of the control system | 109 |
| 5.7.2 | Hysteresis current control | 110 |
| 5.8 | Experimental results of the active filtering | 112 |
| 5.8.1 | Steady-state measurements | 112 |
| 5.8.2 | Dynamic performance | 119 |
| 5.8.3 | Measurements with a 490 kVA line converter with voltage feedback active filtering function | 119 |
| 5.8.4 | Discussion on the active filtering results | 119 |
| 6 | Conclusions | 127 |
| | References | 129 |
| | Appendix 1 | 139 |

Nomenclature

Uppercase roman letters

| | |
|-----------------|--|
| A | Magnitude |
| C | Capacitance |
| D | Distortion power, disturbance |
| G | Conductance, transfer function, gain |
| \underline{G} | Transfer function matrix, static matrix |
| I | Current (RMS value) |
| \underline{I} | Unit matrix |
| K | Controller gain |
| L | Inductance |
| M_p | Peak response |
| N | Number of samples in period |
| P | Power |
| Q | Reactive power |
| R | Resistance |
| S | Apparent power |
| T | Time |
| U | Voltage (RMS value) |
| X | RMS value of a general quantity, reactance |
| Z | Impedance |

Lowercase roman letters

| | |
|-----|---|
| a | Fourier series coefficient, theoretical ratio between active voltage vectors increasing the flux linkage modulus and all active vectors, parameter of a discrete filter |
| b | Fourier series coefficient, theoretical ratio between active voltage vectors decreasing the flux linkage modulus and all active vectors |
| c | Scaling constant of a space-vector, Fourier series coefficient |
| e | Error |
| f | Frequency |
| h | Harmonic |
| i | Current |
| j | Imaginary unit |
| k | Frequency index of DFT, controller gain |

| | |
|------------|---|
| m | Modulation index |
| n | Time index, integer |
| n_c | Number of cascaded filter stages |
| p | Instantaneous power, transfer function pole |
| q | Instantaneous reactive power |
| s | Apparent power, Laplace-transform variable, unit vector corresponding to harmonic synchronous reference frame |
| sw | Switching function |
| t | Time, torque |
| Δt | Time difference |
| u | Voltage, unbalance |
| x | General quantity |
| z | z-transform variable, transfer function zero |
| z_v | Theoretical ratio between zero vectors and all voltage vectors |

Greek letters

| | |
|----------------|--|
| α | Angle of the reference voltage space-vector |
| γ | Angle of the converter virtual flux linkage vector measured from the sector border, phase shift |
| δ | Power angle |
| ζ | Damping ratio |
| κ | Sector index |
| λ | Power factor |
| τ | Time constant, logical output of the torque or the power comparator |
| ϕ | Rotation angle of a space-vector, phase angle, logical output of the flux linkage modulus comparator |
| $\Delta\phi$ | Rotation angle difference |
| χ | Angle between converter and line virtual flux linkage vectors |
| ψ | Flux linkage |
| ω | Angular frequency |
| $\Delta\omega$ | Slip angular frequency |

Subscripts

| | |
|----|--|
| + | Positive dc-link potential |
| - | Negative dc-link potential |
| 0 | Zero-vector, dc-component, subcycle |
| 1 | Converter side quantity of the LCL-filter, fundamental wave related quantity, case 1 |
| 2 | Line side quantity of the LCL-filter, case 2 |
| AF | Active filter |
| B | Budeanu's definition |
| D | Derivative |
| F | Fryze's definition |
| L | Load |

| | |
|-------------------|--|
| PI | Proportional integral control |
| S | Supply |
| Z_{grid} | Grid impedance |
| a | Active quantity |
| a | Phase a, voltage vector adjacent to reference voltage space-vector, amplitude modulation ratio |
| ac | Alternating current |
| ave | Average |
| b | Phase b, voltage vector adjacent to reference voltage space-vector |
| base | Base value |
| c | Phase c |
| cl | Closed-loop |
| comp | Compensator |
| d | Direct axis quantity |
| dc | Direct current quantity |
| dpf | Displacement power factor |
| e | Electromechanical |
| end | End of interval under study |
| eq | Equivalent |
| err | Error |
| est | Estimated |
| f | Line filter |
| fund | Fundamental wave quantity |
| grid | Power grid |
| h | Harmonic |
| href | Harmonic reference |
| i | Integral |
| id | Ideal |
| init | Initial value |
| k | Index representing phases of three-phase system, frequency index of DFT |
| limit | Limiting value |
| loop | Control loop |
| lpf | Low-pass filter |
| max | Maximum value |
| min | Minimum value |
| n | Time index, general index |
| n | Nominal, natural |
| na | Nonactive quantity |
| neg. seq. | Negative sequence |
| orig | Original |
| p | Power, converter pulse number |
| p | Proportional |
| phys | Physical |
| pos. seq. | Positive sequence |
| ppb | Per phase basis calculated quantity |
| proc | Process |
| pu | Per unit |
| q | Quadrature axis quantity |

| | |
|---------------------|---|
| q + d+ | Synchronous frame voltage vector, which is increasing converter flux linkage modulus |
| q + d− | Synchronous frame voltage vector, which is decreasing converter flux linkage modulus |
| ref | Reference |
| ref0 | Reference value assumed to be constant |
| rms | Root mean square |
| s | Supply grid, stator, switching, sample |
| \underline{s}^ν | Quantity related to unit vector corresponding to the ν^{th} harmonic synchronous frame |
| sc | Short circuit |
| six step | Six-step mode |
| st | Standard form |
| tot | Total |
| trafo | Transformer |
| v | Variation quantity |
| v1, v2, ... | Voltage vector 1, voltage vector 2, ... |
| x | Related to general quantity |
| z | Zero-power quantity |
| Σ | Collective quantity |
| α | Real axis component of the stationary reference frame |
| β | Imaginary axis component of the stationary reference frame |
| ζ | Zero sequence of three-phase quantity |
| ψ_1 | Converter virtual flux linkage related value |

Superscripts

| | |
|---------------------|--|
| + | Positive harmonic sequence |
| − | Negative harmonic sequence |
| 1, 2, 3, ... | Fundamental wave, second harmonic, third harmonic, ... |
| dq | Space-vector expressed in synchronous reference frame |
| (dq ¹⁺) | Space-vector expressed in fundamental wave positive sequence reference frame |
| $\alpha\beta$ | Space-vector expressed in stationary reference frame |
| ζ | Zero harmonic sequence |
| ν | General harmonic sequence |

Other notations

| | |
|-------------------|-----------------------------------|
| LPF(...) | Low-pass filtering |
| \underline{x} | Space-vector |
| \underline{x}^* | Complex conjugate of space vector |
| \bar{x} | Mean value |
| \underline{X} | Matrix |

Acronyms

| | |
|-------|---|
| AC | Alternating Current |
| CBEMA | Computer and Business Equipment Manufacturers Association |
| CFO | Converter Flux Orientation |
| DC | Direct Current |
| DFT | Discrete Fourier Transform |
| DIN | Distortion Index |
| DPC | Direct Power Control |
| DSC | Direct Self-Control |
| DTC | Direct Torque Control |
| EMF | Electromotive Force |
| FBD | Fryze-Buchholz-Depenbrock |
| FW | Fundamental Wave |
| IEC | International Electrotechnical Commission |
| IEEE | The Institute of Electrical and Electronics Engineers, Inc. |
| IGBT | Insulated Gate Bipolar |
| IMC | Internal Model Control |
| ITI | Information Technology Industry Council |
| LFO | Line Flux Orientation |
| LPF | Low-Pass Filter |
| LUT | Lappeenranta University of Technology |
| NEMA | National Equipment Manufacturers Association |
| PCC | Point of Common Coupling |
| PCS | Power Conditioning System |
| PI | Proportional Integral |
| PLL | Phase Locked Loop |
| PWM | Pulse Width Modulation |
| RMS | Root Mean Square |
| SCR | Short Circuit Ratio |
| SVPWM | Space-Vector Pulse Width Modulation |
| TDD | Total Demand Distortion |
| THD | Total Harmonic Distortion |
| UPS | Uninterruptible Power Supply |

Chapter 1

Introduction

1.1 From electric light to controlled drives

The history of the commercial utilization of electrical energy dates back to the 19th century. The first electrical utility was founded in 1882 by Thomas Alva Edison to light the lower Manhattan. A couple of years earlier, the first steps of electrification of the Finnish industry was taken in Varkaus by Gottfrid Strömberg, who, at the age of 18, constructed a dynamo, which was used to provide lighting to a local sawmill. Ever since the importance of electrical energy has increased steadily. In the early days the lighting was the most important electrical application. The following decades saw the industrial use of the electricity extending to varieties of industrial processes. First, electrical motors replaced steam engines in driving the main shafts. Craftsmen and designers skilled in trade and the characteristics of the motors and apparatuses improved and the costs reduced. Individual electric motors were started to be installed directly into applications, which made the main shafts obsolete.

Two trends were emerging. First, the industry became dependent on the electrical power. At the time electricity was mainly used in lighting short interruptions were commonplace and even a longer outage mainly slowed the work down. Later, when the electrical energy became a key part of the industrial processes themselves, the interruptions and outages had more serious economical consequences. The importance of, what we now call power quality, was realized.

The other trend, resulting from the tight integration of the electrical motors and the industrial processes, was an increased need to control the motors. Even though the alternating current (AC) system was the dominating power system in the latter half of the 20th century, the direct current (DC) motors were used in industrial applications where speed control was needed. At first, Ward-Leonard drives, comprising an ac-motor, a dc-generator and a dc-motor, were typically used in controlled drive systems. These were rather complex installations requiring lots of maintenance. In the 60's thyristor-based dc-drives replaced the Ward-Leonard systems and only one dc-motor was needed to construct a speed controlled drive. The advantages of the ac-motors were still apparent—they were rugged and reliable and almost maintenance-free—but the impossibility of controlling the speed limited their applicability in the industry. Something that was described as an “AC Ward-Leonard” was needed. According to Jahns and Owen (2001), the first mature thyristor-based ac-drives were introduced in the 1960's. In the

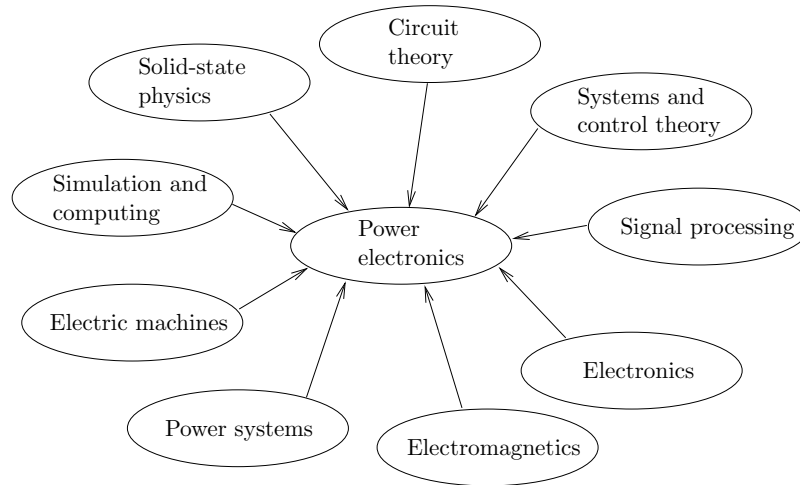


Figure 1.1: Interdisciplinary nature of power electronics. (Mohan et al., 1995)

beginning, there were several alternative ac-drive technologies from which the voltage source pulse width modulated (PWM) inverter eventually became the technological mainstream. In the 70's, significant breakthroughs were achieved in the theory of the AC motor control, which improved the dynamical performance of the drives. Now, the favorable properties of the AC machines were combined with a good controllability—a combination that was to replace the DC motors in the industrial use.

Power electronics have been a key enabling technology that has led to a widespread use of controlled drive systems and great improvements both in productivity and energy savings. The word “power” in power electronics signifies the ability to process substantial amounts of electrical energy. This is a very important difference compared to signal electronics, where the electricity is typically used only to indicate and transfer logical states. Wilson (2000) gives a definition of the power electronics as

“Power Electronics is the technology associated with the efficient conversion, control and conditioning of electric power by static means from its available input form into the desired electrical output form.”

The goal of power electronics is, again according to Wilson (2000), to control the flow of energy from an electrical source to an electrical load with high efficiency, high availability, high reliability, small size, light weight, and low cost. The power electronics is a very broad and interdisciplinary field of engineering. Power electronic systems encompass many elements, as shown in Fig. 1.1. This broad diversity makes the power electronics a challenging as well as interesting field of engineering.

1.2 Line converter

This thesis considers the three-phase voltage source line converter. In order to introduce this device we first have to look at the “AC Ward-Leonard”, or frequency converter, as we

nowadays are accustomed to call it. Fig. 1.2(a) shows the most typical frequency converter topology—a two-level three-phase voltage source inverter with diode bridge rectifier. The motor converter consists of a full-bridge of insulated gate bipolar (IGB) transistors and anti-parallel connected freewheeling diodes. This frequency converter topology is the work horse of the industry and the heart of the vast majority of the world's speed controlled drives. The term “voltage source” alludes to the dc-link configuration, meaning that there is a voltage source—typically a capacitor—in the dc-link. There exist also the current source inverter, having an inductor in the dc-link, and direct converters, such as the cycloconverter and matrix converter, which do not have a dc-link at all. The direct converters produce AC/AC conversion at once rather than having separate AC/DC and DC/AC conversion stages.

The development efforts have been focused on improving the motor converter and its characteristics. The diode bridge has served as a rectifier supplying the power from the grid to the intermediate dc-circuit. The diode bridge rectifier is naturally commutated, meaning that it does not need an external control to perform its rectification function. This, obviously, is a very favorable characteristic reducing the complexity and the cost of the frequency converter. However, the diode bridge rectifier has also some shortcomings, the most important of which is the unidirectional power flow—the diode bridge can not transfer power from the dc-link to the grid. The motor converter can transfer power in both directions, but, as the amount of the energy stored in the dc-link capacitors is very limited, it is of no use to transfer energy from the motor to the dc-link unless it is somehow consumed there. Braking resistors can be arranged to connect to the dc-link and consume the excess power when the dc-voltage rises high enough. Braking resistors, however, lead to increased losses and cooling problems especially with high braking energies.

The other drawback of the diode bridge rectifier is the line current waveform, which is not sinusoidal. The line current harmonics cause extra losses in the cables and transformers and may weaken the quality of the supply voltage. Sufficient voltage quality is an important element for the electrical equipment to function properly. As reported by Grady and Santoso (2001), deteriorated voltage may cause nuisance tripping of sensitive electronic loads or even prevent manufacturing equipment from operating.

Fig. 1.2(b) shows a frequency converter equipped with a line converter. The line converter is a full-bridge IGB transistor-based converter similar to the motor converter. Physically the line converter and the motor converter may be identical the only difference being the control software. Sometimes, the line converters are also called active rectifiers, PWM rectifiers or active front-ends. The line converter is usually controlled independently from the motor converter and it has a separate control system. This is a drawback and increases the complexity and the cost of the frequency converter, but in many cases the benefits offered by the line converter offset the drawbacks. Another disadvantage of the line converter is, compared to the diode bridge, the increased losses which degrades the system efficiency.

The most important advantage is the bidirectional power flow. The line converter can operate in rectifying or inverting mode, that is, transfer energy to or from the dc-link. These modes of operation are sometimes called motoring and generating mode, respectively. With a line converter the braking energy does not have to be consumed in a dc-link, but it can be transferred to the grid for other loads. This feature, which is called regenerative braking, is very useful if efficient braking is needed regularly. If the frequency converter is feeding a generator instead of the motor, the line converter is indispensable because generating is the primary mode of operation.

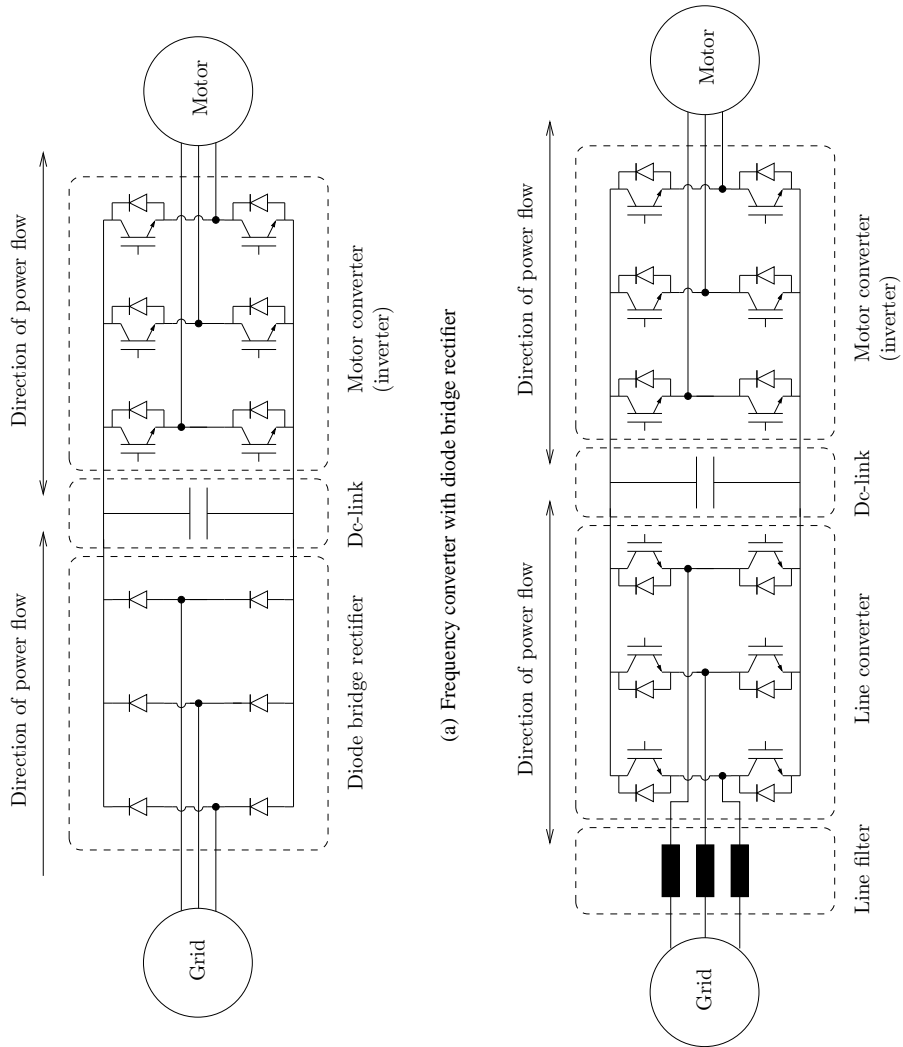


Figure 1.2: Frequency converters with different line side bridges

The other strength of the line converter is the high quality of the line current. The line current of the line converter can be controlled to be very sinusoidal and, hence, very propitious to the quality of power. However, as the measurements in this dissertation demonstrate, the ripple resulting from the converter switching action needs to be filtered, especially in weak grids. The fundamental wave power factor of the line converter is also controllable. Typically, unity power factor operation is desired, but the line converters may operate with a leading or lagging power factor, if that is necessary. The dc-link voltage of the line converter can be regulated to a higher level than what is available in the diode bridge converter. In motor drive applications the higher dc-link voltage allows to increase the field weakening point and provides more torque in the field weakening region.

A typical application of the line converter is the integrated line side bridge of the frequency converter. Line converters are also manufactured as independent units, which can be used in larger systems. One line converter can, e.g., be used to provide dc-voltage to several motor drive units, or several line converters may be paralleled to reach higher power levels or improved reliability. Figs. 1.3 and 1.4 show pictures of a frequency converter integrated line converter and an independent line converter unit. The components are identified by the author. Currently, one large manufacturer offers low-voltage line converters in power levels ranging from 11 kVA to 5.4 MVA, where in the low power end the line converters are integrated to frequency converters and at the highest power levels twelve individual units are paralleled. The line converters are typically used in winding machines, cranes, elevators, centrifuges and processing lines. Distributed power generation is a new application area of line converters. Fuel cells, which produce dc-voltage, and microturbines, which produce high-frequency ac-voltage, require a power electronic interface device, such as the line converter, to connect to the power grid. In windmill applications the line converter may be used to achieve a variable speed turbine, which has a better overall efficiency compared to fixed speed turbine. Also, in miniature hydro power applications, particularly with low fall heights, it may be advantageous to use a power electronic interface that allows the generator to operate with lower electrical frequency than the line frequency. New or emerging line converter applications include energy storage systems, such as battery, flywheel, supercapacitor and superconducting magnetic storage based systems, static reactive power compensators and power conditioning systems that improve the end user power quality.

1.3 Some mathematical concepts used in electrical engineering

1.3.1 Space-vectors

Originally, space-vectors have been used to characterize spatial flux distribution and to study transients in ac-machines. The concept of space-vectors was formally introduced by Kovács and Rácz (1959). However, transforming the three-phase quantities to orthogonal two-phase system and a zero-sequence system was known considerably earlier, see e.g. (Park, 1929). Park (1929) modeled a synchronous machine in a rotor oriented co-ordinate system and presented transforms and inverse transforms from the three-phase quantities to the rotor oriented two-phase system and the zero-sequence system. The transforms are nowadays known as the Park-transforms.

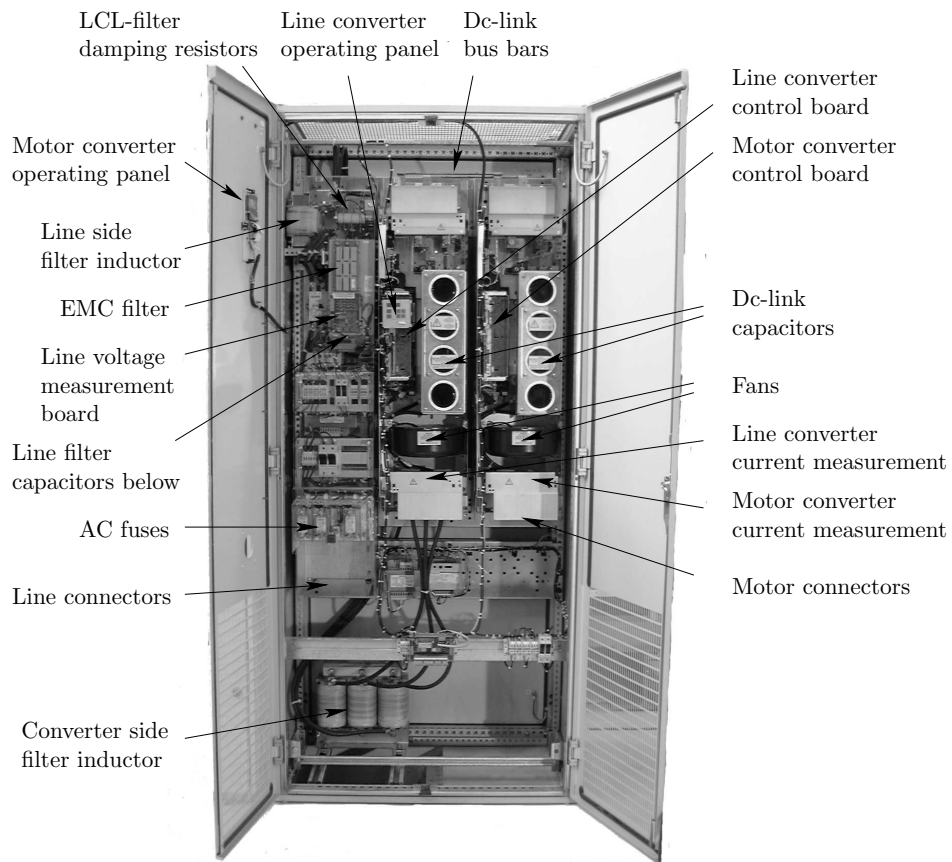
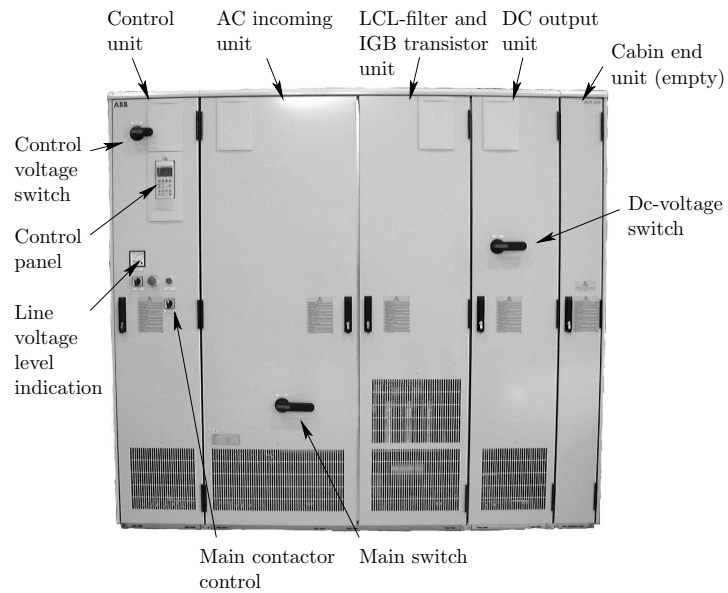
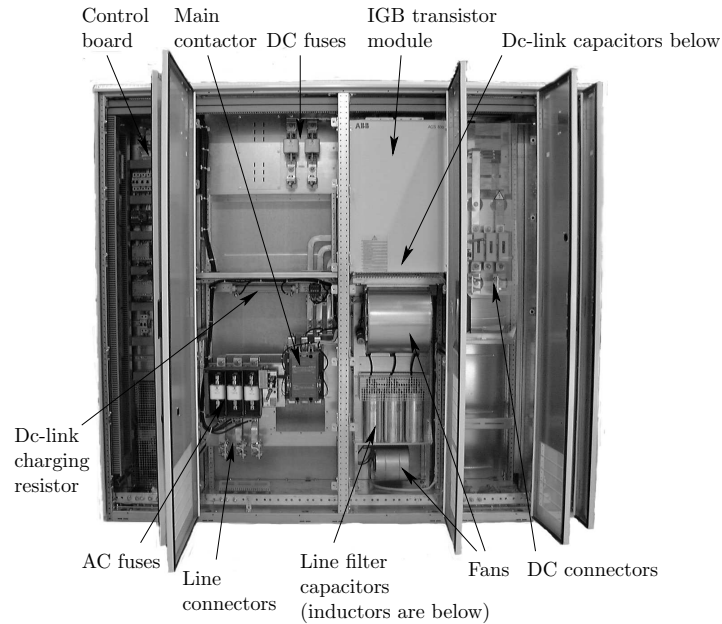


Figure 1.3: A frequency converter with a line converter (Siemens Simovert). Nominal input values $U_n = 400$ V, $I_n = 92$ A. Output: $U = 0-480$ V, $f = 0-600$ Hz. Nominal output power $P_n = 45$ kW.



(a) Cabin doors closed



(b) Cabin doors open

Figure 1.4: A line converter unit (ABB ACS 600). Nominal input values: $U_n = 690 \text{ V}$, $I_n = 410 \text{ A}$, $S_n = 490 \text{ kVA}$.

The concept of the space-vector is very useful in modeling three-phase systems. A three-phase quantity is characterized by the values of the phase quantities. Space-vectors are used to express a three-phase quantity as a complex vector. A comprehensive introduction may be found in Vas (1992). A space-vector of a general three-phase quantity is defined as

$$\underline{x} = c \left(x_a + x_b e^{j\frac{2\pi}{3}} + x_c e^{j\frac{4\pi}{3}} \right) \quad (1.1)$$

$$= x_\alpha + jx_\beta \quad (1.2)$$

$$= x e^{j\phi_x} . \quad (1.3)$$

where c is a constant. The subscripts a, b and c refer to the phases of the three-phase system, α and β refer to the phases of the equivalent two-phase system and ϕ_x is the rotation angle of the space-vector. The constant c may be selected freely, but it is common to choose $c = 2/3$, which is a non-power invariant scaling, or $c = \sqrt{2/3}$, which is a power invariant form. In this thesis the non-power invariant form is used. This form is also known as peak-value scaling, because the length of the space-vector defined in this way equals the peak-value of the corresponding phase quantity in symmetrical sinusoidal conditions without a zero sequence. Kovács and Rácz (1959) and Park (1929) used the peak-value scaling in their equations.

The space-vector (1.1) does not include the zero-sequence component. The zero-sequence component is defined as

$$x_\zeta = c_2 (x_a + x_b + x_c) , \quad (1.4)$$

where the constant $c_2 = 1/3$ for the peak-value scaling and $c_2 = 1/\sqrt{3}$ for the power invariant scaling. If the system is a three-phase three-wire system without neutral conductor the zero-sequence current does not have a path to flow and the zero-sequence components may be neglected. The transformation from three-phase quantities to space-vector and zero-sequence quantities may be considered to be the transformation from abc-axis to $\alpha\beta\zeta$ -axis, and is presented as a matrix equation using peak-value scaling as

$$\begin{bmatrix} x_\alpha \\ x_\beta \\ x_\zeta \end{bmatrix} = \frac{2}{3} \begin{bmatrix} 1 & -\frac{1}{2} & -\frac{1}{2} \\ 0 & \frac{\sqrt{3}}{2} & -\frac{\sqrt{3}}{2} \\ \frac{1}{2} & \frac{1}{2} & \frac{1}{2} \end{bmatrix} \begin{bmatrix} x_a \\ x_b \\ x_c \end{bmatrix} . \quad (1.5)$$

The back transformation from the $\alpha\beta\zeta$ -axis to the abc-axis is

$$\begin{bmatrix} x_a \\ x_b \\ x_c \end{bmatrix} = \begin{bmatrix} 1 & 0 & 1 \\ -\frac{1}{2} & \frac{\sqrt{3}}{2} & 1 \\ -\frac{1}{2} & -\frac{\sqrt{3}}{2} & 1 \end{bmatrix} \begin{bmatrix} x_\alpha \\ x_\beta \\ x_\zeta \end{bmatrix} . \quad (1.6)$$

In electrical drives, these transformations are typically applied to quantities such as voltage, current and flux linkage.

1.3.2 Per unit values

In electrical drives engineering it is often convenient to use scaled per unit (p.u.) values instead of absolute physical values like Volts, Amperes or Henrys. Per unit values are scaled in relation to the base values, which are related to the nominal values of the application or

apparatus. By using per unit values, apparatuses with different power levels can be meaningfully compared. The per unit value x_{pu} of the general absolute physical quantity x_{phys} is calculated as

$$x_{\text{pu}} = \frac{x_{\text{phys}}}{x_{\text{base}}}, \quad (1.7)$$

where x_{base} is the corresponding base value. In electrical drives engineering following fundamental base values are typically used:

Voltage: $u_{\text{base}} = \sqrt{2/3} U_n$ (peak-value of the nominal phase voltage)

Current: $i_{\text{base}} = \sqrt{2} I_n$ (peak-value of the nominal phase current)

Angular frequency: $\omega_{\text{base}} = 2\pi f_s$ (nominal power system angular frequency)

where U_n is the nominal line-to-line RMS voltage, I_n is the nominal RMS phase current and f_s is the nominal power system frequency. The other base values can be derived using the fundamental base values as follows:

Impedance: $Z_{\text{base}} = \frac{u_{\text{base}}}{i_{\text{base}}}$

Inductance: $L_{\text{base}} = \frac{u_{\text{base}}}{\omega_{\text{base}} i_{\text{base}}}$

Capacitance: $C_{\text{base}} = \frac{i_{\text{base}}}{\omega_{\text{base}} u_{\text{base}}}$

Flux: $\psi_{\text{base}} = \frac{u_{\text{base}}}{\omega_{\text{base}}}$

Apparent power: $s_{\text{base}} = \frac{3}{2} u_{\text{base}} i_{\text{base}} = \sqrt{3} U_n I_n$

Time: $t_{\text{base}} = \frac{1}{\omega_{\text{base}}}$

It is important to note that also the physical time t has per unit scaling. Because we have $t_{\text{pu}} = \omega_{\text{base}} t$, it follows that, if the physical time is used in the per unit valued equations, it has to be multiplied with the base value of the angular frequency. In practical control systems this occurs frequently, because typically all quantities except the time are scaled to per unit values.

1.3.3 Fourier series

In engineering and physics it is frequently very convenient to express a periodic signal or a function in terms of simple periodic functions like sines and cosines or complex exponentials. According to the theory of the Fourier series, any periodic continuous function repetitive in an interval T can be represented by the summation of a fundamental sinusoidal component and a series of higher order harmonic components at frequencies which are integer multiples of the fundamental frequency (Arrillaga and Watson, 2003). Originally, the theory was introduced in (Fourier, 1822). According to (Arrillaga and Watson, 2003) and (Kreyszig, 1993) the Fourier series of a periodic function $x(t)$ has the expression

$$x(t) = a_0 + \sum_{h=1}^{\infty} \left(a_h \cos\left(\frac{2\pi ht}{T}\right) + b_h \sin\left(\frac{2\pi ht}{T}\right) \right), \quad (1.8)$$

where a_0 , a_h and b_h , are the coefficients of the series and h is denoting the harmonic. Simplifying the formulas by introducing an angular frequency $\omega = \frac{2\pi}{T}$, the analysis equations are given as

$$a_0 = \frac{1}{T} \int_0^T x(t) dt \quad (1.9)$$

$$a_h = \frac{2}{T} \int_0^T x(t) \cos(h\omega t) dt \quad (1.10)$$

$$b_h = \frac{2}{T} \int_0^T x(t) \sin(h\omega t) dt. \quad (1.11)$$

The magnitude of a component h is given by

$$A_h = \sqrt{a_h^2 + b_h^2}, \quad (1.12)$$

and the phase angle as

$$\phi_h = \arctan\left(\frac{b_h}{a_h}\right). \quad (1.13)$$

The complex Fourier series can be used to present periodic signals with complex exponentials as (Kreyszig, 1993; Proakis and Manolakis, 1996)

$$x(t) = \sum_{h=-\infty}^{\infty} c_h e^{jh\omega t}, \quad (1.14)$$

and the analysis equation is written as

$$c_h = \frac{1}{T} \int_0^T x(t) e^{-jh\omega t} dt. \quad (1.15)$$

If the periodic signal is real valued the coefficients c_h and c_{-h} are complex conjugates $c_h = c_{-h}^*$. In the analysis of the real valued signal this symmetry property is utilized and only the coefficients with $h \geq 0$ are needed in determining the signal in the frequency domain. However, when the analyzed function is complex valued the complex form expression is very convenient. The c_h coefficients and a_0 , a_h , b_h coefficients are related as $a_0 = c_0$, $a_h = c_h + c_{-h}$ and $b_h = j(c_h - c_{-h})$ (Råde and Westergren, 1993).

The generalization of the Fourier series to continuous aperiodic signals is the Fourier transform (Arrillaga and Watson, 2003; Kreyszig, 1993; Proakis and Manolakis, 1996). From the practical electrical engineering viewpoint the discrete Fourier transform (DFT) is probably the most important transform. Proakis and Manolakis (1996) give a transform pair for the discrete periodic signal as

$$x_n = \frac{1}{N} \sum_{k=0}^{N-1} c_k e^{j2\pi kn/N}, \quad n = 0, 1, 2, \dots, N-1 \quad (1.16)$$

$$c_k = \sum_{n=0}^{N-1} x_n e^{-j2\pi kn/N}, \quad k = 0, 1, 2, \dots, N-1, \quad (1.17)$$

where N is the number of samples in a period, n is the time index and k is the frequency index.

1.4 The outline of the thesis

The goal of this work is to research and develop new control methods for line converters employing the converter virtual flux linkage orientation and direct torque control (DTC) principle. The main emphasis is on methods, which extend the application area of line converters to the field of power quality improving. This work is part of a larger project, focusing on enhancing the properties of virtual flux linkage based line converters. The main topics of the project were

- Methods to improve the control performance of virtual flux linkage based line converters
- Parallel operation of independent line converter units
- Power conditioning system application and an island operation
- Active filtering application

This work contributes to the first, third and fourth topic. Pöllänen (2003) reported results from the first two topics. This dissertation is composed of the summarizing part and the appended original publications. The contents of the summarizing part are divided into six chapters.

Chapter 1 introduces the line converter to the reader and gives the background to the work.

Chapter 2 discusses on power quality and its meaning. Power quality indices and harmonics and harmonic sequences are introduced.

Chapter 3 introduces various power components and other quantities used in the electrical engineering profession. A numerical example is worked out to clarify the formulae presented.

Chapter 4 is devoted to the modeling and control of the line converter. First, a basic time-domain-based dynamic model of a line converter is presented and different control strategies are discussed. A DTC current control, originally proposed in Appended Publication I, is presented. A model of the DTC current control is derived and compared with simulation results and experimental results. Practical aspects of the current controller tuning are discussed. Overmodulation properties of the DTC converter are studied and an analytical equation for the maximum modulation index of a DTC converter is derived.

Chapter 5 considers the line converter in power quality improving. Power conditioning system application of the line converter is introduced. Appended Publication II introduces a voltage unsymmetry compensating method for an island grid, which is fed by a power conditioning system. The active filtering application of a line converter is introduced. The frequency-domain method for shunt active filtering is studied, modeled and implemented. Controllers are tuned according to the model and tuning is validated

with practical measurements. The dc-link voltage requirement in active filtering is discussed. Appended Publication III considers this subject in the case of L-type line filter. Voltage feedback active filtering is discussed, analyzed and implemented. The controller design is presented. This application is considered in Appended Publication IV. The effect of grid impedance and a method to its identification are presented in Appended Publication V. A time-domain shunt-active filtering method is implemented. The steady-state active filtering performance of the frequency-domain method, the voltage feedback method and the time-domain method is measured. The dynamical performance of the frequency-domain and the time-domain method is measured. The results obtained are discussed.

Chapter 6 is the final chapter, which presents the conclusions and suggests future research work.

In following, the contents of the appended publications are summarized and the author's and co-author's contribution to them is reported.

Publication I introduces the line converter current vector control, which employs the DTC method and converter virtual flux linkage orientation. The author developed and implemented the DTC-based current control method. The reactive power estimation and control methods are contributions of co-author Pöllänen. The manuscript was written and the measurements were performed by the author and co-author Pöllänen.

Publication II considers the power conditioning system (PCS) application of the line converter. The paper introduces an island network unbalance compensation method. The paper is entirely written and the experiments are performed by the author. Co-author Vertanen delivered the implementation of the DTC modulation-based scalar control. The inclusion of negative sequence components to the flux reference was also suggested by co-author Vertanen. The island grid unbalance detection method and the procedure of calculating the negative sequence flux reference are developed and implemented by the author.

Publication III studies the effect of the dc-link voltage to the compensation characteristics of a shunt active filter. The 5th negative sequence and 7th positive sequence harmonics are considered. The scientific contents of the article are produced and written by the author.

Publication IV considers the voltage feedback active filter. The control system is described and experimental results are given to validate the concept. The scientific contents of the article are produced and written by the author.

Publication V introduces a grid impedance identification method for the voltage feedback active filter. The method uses the control system of the active filter to measure the grid impedance at selected frequencies. The scientific contents of the article are produced and written by the author.

The co-authors not listed above have participated in the research group operations and project co-ordination. They have also contributed to the preparation of the articles by revision comments and suggestions.

1.5 Scientific contributions

The scientific contributions of this dissertation are:

- Modeling and implementation of converter virtual flux linkage oriented current vector control (Chapter 4 and Appended Publication I)
- Derivation of the maximum modulation index of a DTC line converter (Chapter 4)
- New island network voltage unbalance compensation method (Appended Publication II)
- New grid impedance identification method for a voltage feedback active filter (Appended Publication V)

Other results that may not be scientific, but are believed to be important advances or to have a significant practical value, are listed as:

- Application of a DTC line converter to active filtering
- Analysis of harmonic current control loops of a frequency-domain active filter
- Analysis of harmonic voltage control loops of a voltage feedback active filter
- Validation of the voltage feedback active filter concept by extensive measurements with two line converters in different power levels (19 kVA and 490 kVA)

In total, four patents have been granted on the basis of the line converter research project conducted at Lappeenranta University of Technology (LUT).

Chapter 2

Power quality

This chapter introduces the concept of power quality. The power system harmonics and harmonic sequences are discussed and power quality indices are introduced.

2.1 What is power quality?

This thesis and the technology on which it is grounded is largely motivated by the power quality issues. The term power quality is a rather general concept. Broadly, it may be defined as a provision of voltages and system design so that the user of electric power can utilize electric energy from the distribution system successfully, without interference or interruption (Heydt, 1998). Utilities may want to define power quality as a reliability. Equipment manufacturers, in turn, may define it as a power that enables the equipment to work properly. Dugan et al. (2002), similarly to Heydt (1998), prefer the customer's point of view and define the power quality problem as

“Any power problem manifested in voltage, current or frequency deviations that results in failure or misoperation of customer equipment.”

The issue of electric power quality is gaining importance because of several reasons.

1. The society is becoming increasingly dependent on the electrical supply. A small power outage has a great economical impact on the industrial consumers. A longer interruption harms practically all operations of a modern society.
2. New equipment are more sensitive to power quality variations.
3. The advent of new power electronic equipment, such as variable speed drives and switched mode power supplies, has brought new disturbances into the supply system.
4. Deregulation is resulting in structural changes in the utility industry (see e.g. (McGranaghan et al., 1998)). Traditionally, the generation, transmission, distribution and retail services have been bundled into one regulated company the task of which, among the others, was to be responsible for the quality of power. In a deregulated environment, it is worthwhile to ask, who will be responsible for the power quality?

5. The deregulated environment may reduce the maintenance of and investments into the power system and, hence, reduce the margins in the system. Deregulation has already led to a big increase in the inter-regional power transport (Arrillaga et al., 2000).
6. Emerging of distributed generation (known also as embedded and dispersed generation) as a side effect of the deregulation. Distributed generation changes the way how the utility grid is operated and introduces new power quality challenges (e.g. (Jenkins et al., 2000)).
7. The end users' awareness in power quality issues has increased.

The nature of electricity as a product is special, as discussed in (EN 50160, 1999). Similar to the conventional products its characteristics affect its usefulness to the customer. Different from the conventional products the application of it is one of the main factors that has an influence on its characteristics. The current that the customer's appliance draws from the supply network flows through the impedances of the supply system and causes a voltage drop, which affects the voltage that is delivered to the customer. Hence, both the voltage quality and the current quality are important. It is rather natural to split up the responsibilities so that the power distribution supplier is responsible for the voltage quality and the customer is accountable for the quality of current that he or she is taking from the utility.

Table 2.1 shows the categorization of power system electromagnetic phenomena that affect the power quality, as presented by Dugan et al. (2002). In following, some possible causes of the phenomena listed are given as explained by Dugan et al. (2002). Transients may be impulsive or oscillatory in nature. Impulsive transients are typically caused by lightnings and high oscillatory transients as a response of a local system to the impulsive transient. A low frequency oscillatory transient may be a result of a capacitor switching. Short duration variations are typically caused by faults or energization of large loads which require high starting currents. Long duration under- or overvoltages usually result in switching of large load or generation unit or a capacitor bank. An incorrect transformer tap setting may also be a cause of such a situation. Voltage unbalance may be caused by excess of poorly balanced single phase loads or blown fuses in one phase of a capacitor bank. Waveform distortions are caused by nonlinear loads in the power systems. A half-wave rectification may cause dc-offset. Harmonics are originating from many sources, in which typically power electronics are involved, but may also be produced by nonlinearly magnetizing inductances. Interharmonics are mainly caused by cycloconverters and arcing devices. Notching is a periodic voltage disturbance typically caused by commutations of power electronic device. Notching could be regarded as harmonics with high orders, but is typically considered as a special case. Voltage fluctuation may be caused by rapidly varying loads or generation. Certain voltage fluctuations are often called flicker, because of the visible effect to incandescent lamps. Power frequency variations may be caused by power system faults or disconnection or connection of large load or generation unit.

2.2 Harmonics and harmonic sequences

In power systems harmonics appear as a waveform distortion of the voltage or the current. The harmonics are generated by nonlinear loads. The sinusoidal voltage applied to the nonlinear load does not result in a sinusoidal current. Further, this nonsinusoidal current will produce

Table 2.1: Categories and characteristics of power system electromagnetic phenomena (Dugan et al., 2002).

| Categories | Typical spectral content | Typical duration | Typical voltage magnitude |
|-----------------------------------|------------------------------|------------------|---------------------------|
| Transients | | | |
| <i>Impulsive</i> | | | |
| Nanosecond | 5 ns rise time | < 50 ns | |
| Microsecond | 1 μ s rise time | 50 ns – 1 ms | |
| Millisecond | 0.1 ms rise time | > 1 ms | |
| <i>Oscillatory</i> | | | |
| Low frequency | < 5 kHz | 0.3–50 ms | 0–4 p.u. |
| Medium frequency | 5–500 kHz | 20 μ s | 0–8 p.u. |
| High frequency | 0.5–5 MHz | 5 μ s | 0–4 p.u. |
| Short duration variations | | | |
| <i>Instantaneous</i> | | | |
| Interruption | | 0.5–30 cycles | < 0.1 p.u. |
| Sag (dip) | | 0.5–30 cycles | 0.1–0.9 p.u. |
| Swell | | 0.5–30 cycles | 1.1–1.8 p.u. |
| <i>Momentary</i> | | | |
| Interruption | | 30 cycles – 3 s | < 0.1 p.u. |
| Sag (dip) | | 30 cycles – 3 s | 0.1–0.9 p.u. |
| Swell | | 30 cycles – 3 s | 1.1–1.4 p.u. |
| <i>Temporary</i> | | | |
| Interruption | | 3 s – 1 min | < 0.1 p.u. |
| Sag (dip) | | 3 s – 1 min | 0.1–0.9 p.u. |
| Swell | | 3 s – 1 min | 1.1–1.2 p.u. |
| Long duration variations | | | |
| Interruption, sustained | | > 1 min | 0.0 p.u. |
| Undervoltages | | > 1 min | 0.8–0.9 p.u. |
| Overvoltages | | > 1 min | 1.1–1.2 p.u. |
| Voltage unbalance | | | |
| | | Steady state | 0.5%–2% |
| Waveform distortion | | | |
| DC offset | | Steady state | 0%–0.1% |
| Harmonics | 0–100 th harmonic | Steady state | 0%–20% |
| Interharmonics | 0–6 kHz | Steady state | 0%–2% |
| Notching | | Steady state | |
| Noise | Broadband | Steady state | 0%–1% |
| Voltage fluctuations | | | |
| | < 25 Hz | Intermittent | 0.1%–7% |
| Power frequency variations | | | |
| | | < 10 s | |

a nonsinusoidal voltage drop while flowing through the finite source impedance, and, hence, cause harmonic voltages. Alongside with the harmonics, interharmonics and dc-component may distort the waveform. Gunther (2001) gives simple but effective definitions: The spectral component with frequency of f is

Harmonic if $f = nf_{\text{fund}}$, where n is an integer > 0

Dc-component if $f = 0$ ($f = nf_{\text{fund}}$, where $n = 0$)

Interharmonic if $f \neq nf_{\text{fund}}$, where n is an integer > 0

Subharmonic if $f > 0$ and $f < f_{\text{fund}}$,

where f_{fund} is the fundamental power system frequency. The interharmonics and subharmonics are also referenced in IEC Std 60050-551-20 (2001).

In power systems the harmonics have an interesting property called the sequence. The sequence indicates the phase sequence of the phase quantities. The fundamental component is of positive sequence, meaning that phase a is leading phase b, which is leading phase c. The phase order is then a–b–c. The phase order of a negative sequence component is a–c–b. With zero-sequence components all phase quantities are similar and the phase order can not be defined. If a space-vector is constructed from a harmonic sequence it is noticed that positive sequence components rotate into the positive direction and negative sequence components into the negative direction. The zero-sequence component does not contribute to the space-vector at all, as was pointed out in section 1.3.1.

Let us define a fundamental positive sequence component for a general quantity x as

$$x_a^{1+}(t) = x^{1+} \cos(\omega t) \quad (2.1)$$

$$x_b^{1+}(t) = x^{1+} \cos\left(\omega t - \frac{2\pi}{3}\right) \quad (2.2)$$

$$x_c^{1+}(t) = x^{1+} \cos\left(\omega t + \frac{2\pi}{3}\right), \quad (2.3)$$

and a fundamental negative sequence component as

$$x_a^{1-}(t) = x^{1-} \cos(\omega t) \quad (2.4)$$

$$x_b^{1-}(t) = x^{1-} \cos\left(\omega t + \frac{2\pi}{3}\right) \quad (2.5)$$

$$x_c^{1-}(t) = x^{1-} \cos\left(\omega t - \frac{2\pi}{3}\right), \quad (2.6)$$

and a fundamental zero-sequence component as

$$x_a^{1\zeta}(t) = x^{1\zeta} \cos(\omega t) \quad (2.7)$$

$$x_b^{1\zeta}(t) = x^{1\zeta} \cos(\omega t) \quad (2.8)$$

$$x_c^{1\zeta}(t) = x^{1\zeta} \cos(\omega t). \quad (2.9)$$

The sequence is indicated with a superscript, where the ordinal number indicates the order of the harmonic frequency and the symbol ‘+’, ‘–’ or ‘ ζ ’, indicates that the sequence is

Table 2.2: Natural sequences of characteristic current harmonics of converters. (Heydt, 1991)

| Order | Sequence | Order | Sequence | Order | Sequence |
|-------|----------|-------|----------|-------|----------|
| 1 | Positive | 6 | Zero | 11 | Negative |
| 2 | Negative | 7 | Positive | 12 | Zero |
| 3 | Zero | 8 | Negative | 13 | Positive |
| 4 | Positive | 9 | Zero | 14 | Negative |
| 5 | Negative | 10 | Positive | 15 | Zero |

positive, negative or zero, respectively. Hence ‘1+’ means the positive sequence of the fundamental frequency and ‘5 ζ ’ would mean the zero-sequence of the fifth harmonic frequency. The dc-component (zero harmonic frequency) can be of zero sequence or non-zero sequence but, naturally, does not have any associated rotation direction. The space-vector containing components (2.1)–(2.9) calculated with (1.1) using peak-value scaling yields

$$\underline{x} = x^{1+} e^{j\omega t} + x^{1-} e^{-j\omega t}, \quad (2.10)$$

having components rotating in both the positive and negative directions corresponding to positive and negative sequences, respectively. The zero-sequence component calculated with (1.4) gives

$$x_{\zeta} = x^{1\zeta} \cos(\omega t) . \quad (2.11)$$

The phase quantities, calculated e.g. for phase a as $x_a = x_a^{1+} + x_a^{1-} + x_a^{1\zeta}$, evidently contain only one frequency component even though all three sequences are present. Hence, it is seen that from a single phase quantity it is impossible to determine what sequences of the harmonics are present. The positive and the negative sequence components may be decomposed using the complex Fourier analysis. A periodic space-vector signal may be presented as (Ferrero and Superti-Furga, 1990, 1991)

$$\underline{x} = \sum_{h=-\infty}^{\infty} \underline{x}_h e^{jh\omega t} . \quad (2.12)$$

The Fourier series terms are space-vectors with constant amplitudes \underline{x}_h and rotating with angular speed $h\omega$. Each harmonic frequency $h\omega$ is described by two space-vectors, of which one is rotating into the positive direction and the other into the negative direction.

It is well known that AC/DC converters have characteristic current harmonics. In an ideal six-pulse bridge the characteristic current harmonics are of the order $6n \pm 1$, where $n = 1, 2, 3, \dots$ (i.e. 5th, 7th, 11th, 13th, etc.). The lower harmonics, i.e. $6n - 1$, are of negative sequence and the higher harmonics $6n + 1$ of positive sequence. Generally, for the p pulse converter the characteristic harmonics are of the order $pn \pm 1$. The sequences of the characteristic harmonics are shown in Tab. 2.2 as given in (Heydt, 1991).

Practicing drives engineers frequently consider the space-vector loci in the $\alpha\beta$ -frame while assessing the operation of the drive. The circular locus indicates a sinusoidal waveform and deviation from the circle indicates harmonics or unbalance. Let us present how the different harmonic sequences show up in the $\alpha\beta$ -frame space-vector locus. A general three-phase quantity is graphed in cases where a distorting 0.2 p.u. harmonic sequence component is

added to the fundamental positive sequence component (2.1)–(2.3). The harmonic sequence is either a positive sequence component

$$x_a^{h+}(t) = x^{h+} \cos(h\omega t) \quad (2.13)$$

$$x_b^{h+}(t) = x^{h+} \cos\left(h\omega t - \frac{2\pi}{3}\right) \quad (2.14)$$

$$x_c^{h+}(t) = x^{h+} \cos\left(h\omega t + \frac{2\pi}{3}\right), \quad (2.15)$$

or a negative sequence component

$$x_a^{h-}(t) = x^{h-} \cos(h\omega t) \quad (2.16)$$

$$x_b^{h-}(t) = x^{h-} \cos\left(h\omega t + \frac{2\pi}{3}\right) \quad (2.17)$$

$$x_c^{h-}(t) = x^{h-} \cos\left(h\omega t - \frac{2\pi}{3}\right). \quad (2.18)$$

Zero-sequence components are not considered. The cases are depicted in Fig. 2.1 in phase quantities, $\alpha\beta$ quantities and in $\alpha\beta$ -axis. The $\alpha\beta$ -axis presentation interestingly shows, that different sequences may cause deformations of the $\alpha\beta$ -axis locus having similar characteristics. The dc-component and the 2nd positive sequence move the center of the locus from the origin. Further, if the locus is observed to have an elongated shape, one can conclude that either a fundamental negative sequence or third positive sequence harmonic is present. The number of the apexes, i.e. the maxima of the vector length, of the $\alpha\beta$ -axis locus is $1 + h$ for the negative sequences and $1 - h$ for the positive sequences of harmonic h .

Considering the $\alpha\beta$ -axes in Fig. 2.1 it is quite easy to understand why only certain harmonic sequences tend to exist in three-phase systems. By considering the abc-axes in Fig. 2.1 it may be observed that, in the case of the even harmonics, the positive and the negative half cycles are not symmetrical. This means, that the electric device generating even harmonics treats the positive and the negative half cycle differently. As this generally does not happen, no even harmonics are produced. One notable exception is the half-wave rectification, which is a well-known source of even harmonics. The odd harmonics, except 5th negative sequence (5–) and 7th positive sequence (7+), are not symmetrical with respect to the different phases. A load producing such harmonics would have to have different electrical characteristics in each phase, which, generally, is a rare condition of a three-phase apparatus. In Fig. 2.1, only the sequences 5– and 7+ are symmetrical with respect to the positive and negative cycles and with respect to the different phases. This property makes them very common harmonic sequences in three-phase systems. However, if the source voltages are not balanced or the grid impedance is not equal in all phases, uncharacteristic harmonics may occur. A perfectly symmetrical three-phase apparatus may draw an unsymmetrical current in unbalanced supply. The unbalanced condition is a well-known cause of uncharacteristic harmonics, mentioned e.g. in (Arrillaga and Watson, 2003; Dugan et al., 2002; Heydt, 1991; IEEE Std 519–1992, 1993).

However, there are no reasons why an electronic device could not have a line current with uncommon harmonics even in a balanced supply. This is demonstrated in Figs. 2.2 and 2.3, which illustrate a case where the line current of an electrical device contains a nominal 27 A positive sequence fundamental component and a 0.2 p.u. of uncommon harmonic. The harmonic source measured is a frequency selective active filter unit, which, by using the feedback control, can very efficiently control the harmonic content of the supply current. The frequency selective active filter is discussed in greater details later in this work.

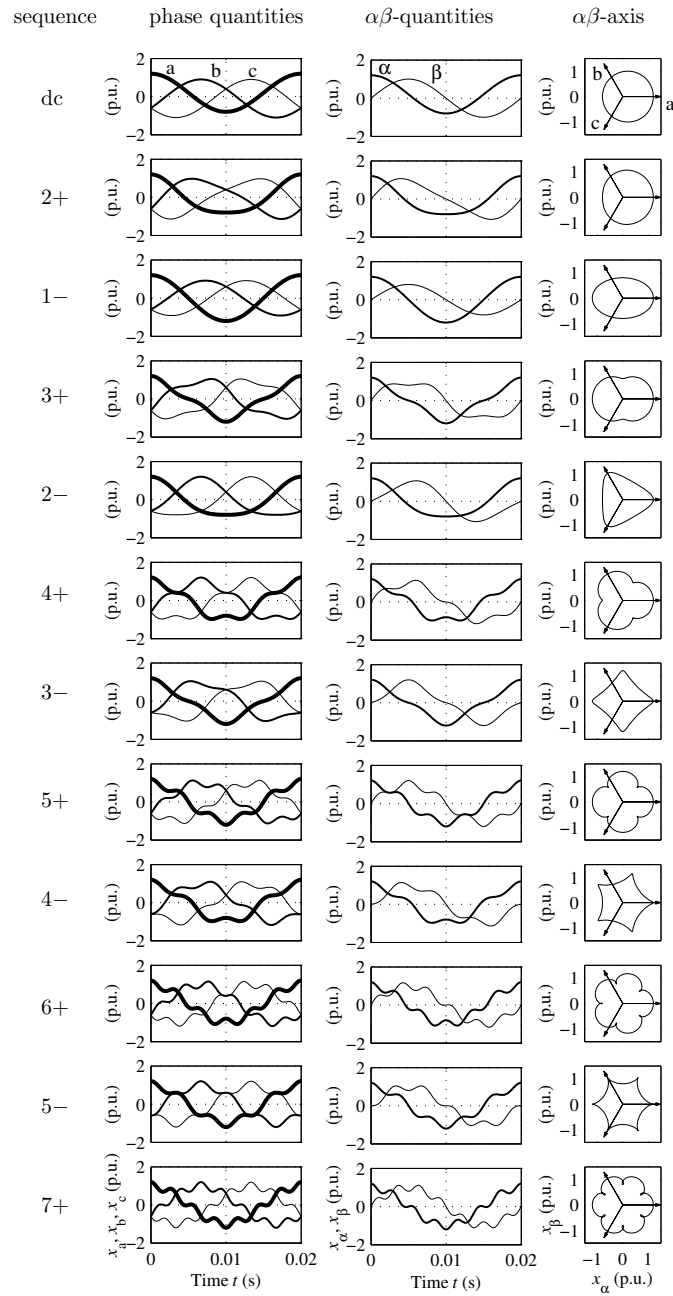
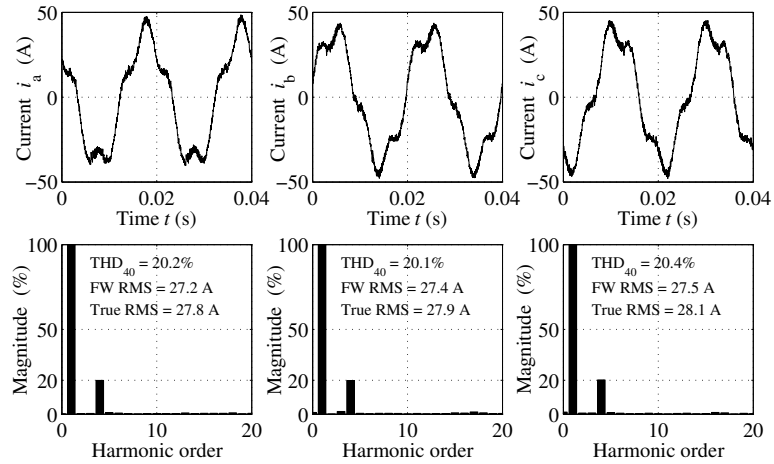
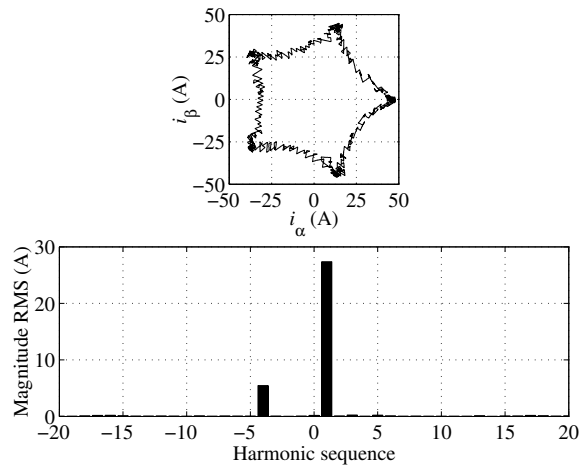


Figure 2.1: Nominal positive fundamental sequence and added 0.2 p.u. harmonic sequences. Presented with abc- and $\alpha\beta$ -components in time-domain and in $\alpha\beta$ -axis.

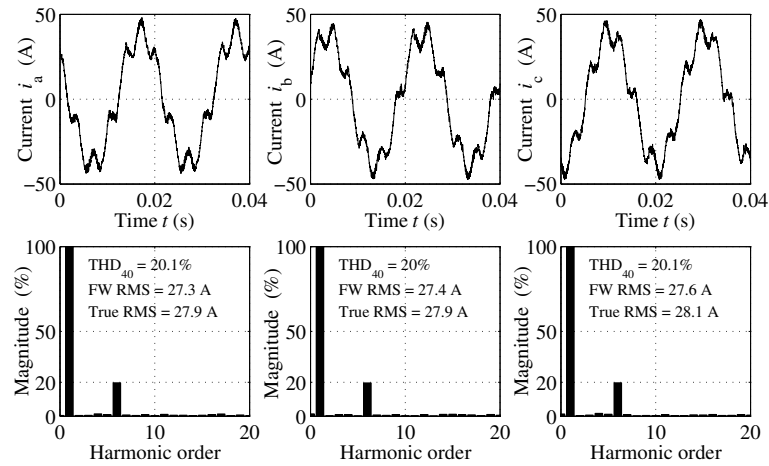


(a) Phase currents in the time domain and in the frequency domain. THD up to 40th harmonic, fundamental wave and true RMS values are calculated.

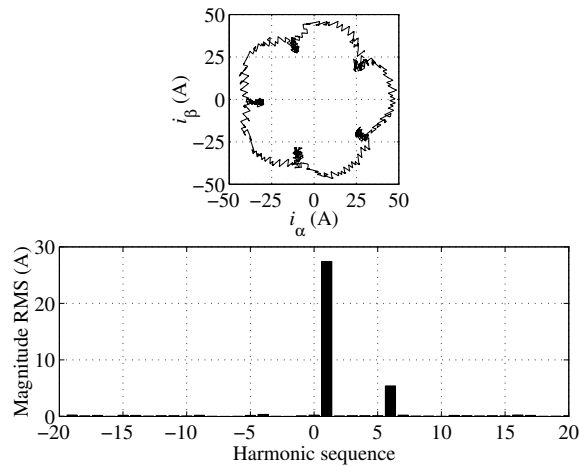


(b) Current space-vector locus in $\alpha\beta$ -axis and its harmonic sequences.

Figure 2.2: Measured line current of an electrical device with 27 A of the fundamental wave capacitive current (leading power factor) and 5.4 A of the 4th negative sequence harmonic current.



(a) Phase currents in the time domain and in the frequency domain. THD up to 40th harmonic, fundamental wave and true RMS values are calculated.



(b) Current space-vector locus in $\alpha\beta$ -axis and its harmonic sequences.

Figure 2.3: Measured line current of an electrical device with 27 A of the fundamental wave capacitive current (leading power factor) and 5.4 A of the 6th positive sequence harmonic current.

2.3 Power quality indices

2.3.1 General harmonic indices

A complete description of a given distortion is the spectrum, but it is not very practical for rough comparisons and assessments. Hence, several harmonic indices have been developed to measure and characterize harmonic distortions with a single figure. The most common harmonic index is the total harmonic distortion (THD) (Arrillaga and Watson, 2003; Dugan et al., 2002; IEEE Std 519–1992, 1993)

$$\text{THD} = \frac{\sqrt{\sum_{h=2}^{h_{\max}} X_h^2}}{X_1} . \quad (2.19)$$

X_1 is the fundamental wave RMS value and X_h is the RMS value of the harmonic component h . The THD is calculated up to the harmonic h_{\max} , which is typically 40 or 50, but in some cases, if it is known that harmonics higher than that exist, it is justified to calculate the THD, e.g., up to the 200th harmonic. It is advisable to report the number of harmonics taken into the calculation. The THD may be calculated with either the RMS values or the peak-values. There exists a connection between the THD and the waveform's true RMS value X_{rms} as

$$X_{\text{rms}} = X_1 \sqrt{1 + \text{THD}^2} , \quad (2.20)$$

provided that no harmonics exist above h_{\max} and the waveform is periodic with a fundamental wave period (Dugan et al., 2002; Holmes and Lipo, 2003). The THD is solved from (2.20) as

$$\text{THD} = \sqrt{\left(\frac{X_{\text{rms}}}{X_1}\right)^2 - 1} . \quad (2.21)$$

The THD may be calculated for the voltage or the current. It is a measure that quantifies “how close the waveform is to pure sine”. The smaller the THD the closer the wave-shape approximates sine. Typical rule-of-thumb values for acceptable waveforms are a 5% THD for the current and a 2% THD for the voltage in the customer's point of connection. There exists also an alternative definition of the THD, which is sometimes called distortion index (DIN)

$$\text{DIN} = \frac{\sqrt{\sum_{h=2}^{h_{\max}} X_h^2}}{\sqrt{\sum_{h=1}^{h_{\max}} X_h^2}} = \frac{\sqrt{\sum_{h=2}^{h_{\max}} X_h^2}}{X_{\text{rms}}} . \quad (2.22)$$

DIN is frequently used in the European literature but rarely in the United States (Heydt, 1991; Holmes and Lipo, 2003). The advantage of this formulation is that it is always between zero and one. The THD calculated according to (2.19) goes infinitely large as the distortion increases. For small distortions, however, both definitions give approximately the same result.

The THD is defined for signals, which are periodic with the fundamental wave period. However, in practical power engineering the signal may have subharmonics, interharmonics, or distortion above h_{\max} to which the harmonic analysis is extended. Usually, the THD is used as the measure of the power quality in case of interharmonics and subharmonics, even though it is, strictly speaking, not defined for these signals, if the power frequency is used as the fundamental frequency. This is understandable because the majority of the power analyzers

calculate it automatically and many standards refer to it. Also, very often the practical signal is well approximated by the power frequency fundamental wave periodic signal and the calculated THD is a meaningful quantity. Sometimes, however, the opposite is true. The THD denotes the ratio of the energy content of the harmonics to that of the fundamental component. Accordingly, Heydt (2000) has defined a THD-like index

$$\text{THD}' = \frac{\text{Total signal energy} - \text{Fundamental wave signal energy}}{\text{Fundamental wave signal energy}}, \quad (2.23)$$

where the fundamental frequency (and hence also the fundamental wave period) is defined by the power frequency. Heydt and Jewell (1998) calculate THD' as¹

$$\text{THD}' = \frac{\sqrt{X_{\text{rms}}^2 - X_1^2}}{X_1}, \quad (2.24)$$

which, in fact, is the same as (2.21). The difference is that the signal does not need to be periodic. In a periodic case, evidently, THD' = THD. In IEC Std 61800-4 (2002) THD' is called total distortion ratio, and it is noted that it may be approximated with THD if interharmonics are disregarded due to their low amplitude. Further, it is noted that assessment of THD and THD' lead typically to the same result in case of a voltage, but there may be significant differences in case of a current.

The RMS value of an aperiodic signal $x(t)$ may be calculated as

$$X_{\text{rms}} = \sqrt{\frac{1}{T_{\text{end}}} \int_0^{T_{\text{end}}} x(t)^2 dt}, \quad (2.25)$$

where T_{end} is the time horizon under study (Heydt and Jewell, 1998). In practical power engineering, T_{end} should be chosen as an integer multiple of the power frequency cycle time because the amplitudes of the interharmonic and subharmonic components are typically far lower than the power frequency component.

The THD is not always a very good measure of the detrimental effect of the current. Especially in variable speed drives, the THD of the line current may be very high in light loads but within the acceptable limits in full load. Despite the high THD value under light load condition the absolute magnitudes of the harmonics are low and do not harm the power system. With a line converter the THD may approach infinity when the fundamental current approach to zero while some harmonics are present because of the switching action of the converter bridge. This misleading property may be avoided by relating the harmonics to the nominal or the maximum current instead of the fundamental wave of the present current waveform. This is known as the total demand distortion (TDD) (Arrillaga and Watson, 2003; Dugan et al., 2002; IEEE Std 519–1992, 1993)

$$\text{TDD} = \frac{\sqrt{\sum_{h=2}^{h_{\text{max}}} I_h^2}}{I_n}, \quad (2.26)$$

where I_n is the nominal or maximum current, depending on what is appropriate. When assessing the THD of a variable speed drive, the measurement should be always performed under nominal load conditions.

¹Actually, Heydt and Jewell (1998) give equation in incorrect form—without the square root and squares in the nominator. However, the corresponding equation for the DIN is given correctly as $\text{DIN}' = \frac{1}{X_{\text{rms}}} \sqrt{X_{\text{rms}}^2 - X_1^2}$.

Table 2.3: Current distortion limits for general distribution systems (120 V through 69 000 V) according to IEEE Std 519–1992 (1993). The values should be used as design values for the worst case for normal operation, conditions lasting longer than one hour. For shorter periods the limits may be exceeded by 50%.

| Maximum harmonic current distortion in percent of I_L | | | | | | |
|---|------|------------------|------------------|------------------|-------------|------|
| Individual harmonic order (odd harmonics) | | | | | | |
| I_{sc}/I_L | < 11 | $11 \leq h < 17$ | $17 \leq h < 23$ | $23 \leq h < 35$ | $35 \leq h$ | TDD |
| < 20* | 4.0 | 2.0 | 1.5 | 0.6 | 0.3 | 5.0 |
| 20 < 50 | 7.0 | 3.5 | 2.5 | 1.0 | 0.5 | 8.0 |
| 50 < 100 | 10.0 | 4.5 | 4.0 | 1.5 | 0.7 | 12.0 |
| 100 < 1000 | 12.0 | 5.5 | 5.0 | 2.0 | 1.0 | 15.0 |
| > 1000 | 15.0 | 7.0 | 6.0 | 2.5 | 1.4 | 20.0 |

Even harmonics are limited to 25% of the odd harmonics limits above.

Current distortions that result in a dc offset, e.g., a half-wave converters, are not allowed.

*All power generation equipment is limited to these values of current distortion, regardless of actual I_{sc}/I_L .

where

$I_{sc} \triangleq$ maximum short-circuit current at PCC.

$I_L \triangleq$ maximum demand load current (fundamental frequency component) at PCC.

Arrillaga et al. (2000) note that the THD does not distinguish between the “injected” and “absorbed” currents, i.e. whether the harmonic current is causing a voltage distortion or remedying it. Arrillaga et al. (2000) conclude that the THD is not a suitable index to allocate the financial responsibilities in the deregulated environment to guarantee agreed levels of power quality. In this thesis, the voltage feedback active filter application demonstrates this weakness of the THD in practice.

In IEEE Std 519–1992 (1993) the current distortion limits for general distribution systems are given as in Tab. 2.3. The current harmonic limit is dependent on the short circuit ratio (SCR) I_{sc}/I_L , which is the ratio of the short-circuit current available at the point of common coupling (PCC) to the customer’s maximum fundamental load current. Hence, the limit for the large customer (low SCR) is more stringent than for the small customer because the large customer represent a larger portion of the total system load. The purpose of the limits is to limit the maximum individual harmonic voltage to 3% and the voltage THD to 5% for systems without major parallel resonances at harmonic frequencies. The current limits assume that there will be some diversity between the harmonic currents injected by the different customers. The current limits are developed so that the maximum individual harmonic voltage caused by a single customer will not exceed the limits listed in Tab 2.4 for systems that can be characterized by a short-circuit impedance. Also, it is noted in IEEE Std 519–1992 (1993) that if there is not sufficient diversity between the customers, it may be that the current limits are met but the voltage distortion levels are higher than listed in Tab 2.4.

Table 2.4: Basis for harmonic current limits in (IEEE Std 519–1992, 1993). Maximum individual harmonic voltage caused by a single customer should not exceed the values in the table.

| SCR at PCC | Maximum individual harmonic voltage | Related assumption |
|------------|-------------------------------------|----------------------------------|
| 10 | 2.5%–3.0% | Dedicated system |
| 20 | 2.0%–2.5% | 1–2 large customers |
| 50 | 1.0%–1.5% | A few relatively large customers |
| 100 | 0.5%–1.0% | 5–20 medium size customers |
| 1000 | 0.05%–0.10% | Many small customers |

2.3.2 Unbalance

In a symmetrical sinusoidal three-phase system the phase voltages are equal in magnitudes and the phase angles are 120 degrees apart. If either the magnitudes are not equal or the phase angles deviate from the symmetrical case the system is unbalanced. The unbalance is defined with the symmetrical components as the ratio between the negative sequence and positive sequence components (Bollen, 2002; EN 50160, 1999; Pillay and Manyage, 2001). With space-vectors corresponding to harmonic sequences this may be expressed as

$$u = \frac{|x^{1-}|}{|x^{1+}|} . \quad (2.27)$$

Commonly, the unbalance of voltages is monitored but the current unbalance may be calculated as well. A typical limiting value of the voltage unbalance is 2%. Other definitions of voltage unbalance have been presented, see e.g. (Bollen, 2002; Pillay and Manyage, 2001), which avoid the complex algebra involved in calculation of the symmetrical components. Pillay and Manyage (2001) and Bollen (2002) have shown that the NEMA (National Equipment Manufacturer's Association) definition of unbalance

$$u_{\text{NEMA}} = \frac{\text{maximum voltage deviation from the average line-to-line voltage}}{\text{average line-to-line voltage}} \quad (2.28)$$

is a good approximation of the true unbalance in small, below 5%, unbalances.

2.4 Summary

This chapter introduced the concept of the power quality. Power system harmonics, harmonic sequences and harmonic indices were introduced. The appearances of waveforms with different harmonic sequences were shown. Demonstrating measurements were performed in two cases. It was shown that the sequences of the different harmonics can not be determined by measuring only one phase of the three-phase quantity. The sequences may be found out by considering the space-vector and the zero-sequence component of the three-phase quantity and by using the complex Fourier analysis.

Chapter 3

Power components

In this chapter, various power components are introduced. Average value-based as well as instantaneous value-based definitions are considered. A numerical example is calculated to clarify the formulae presented.

3.1 Averaged power components

3.1.1 Single-phase system

Let us, at first, consider a general single phase ac-system with instantaneous voltage and current as $u(t)$ and $i(t)$. Let us assume that the waveforms are periodic with a fundamental period T . Such a waveform can be decomposed into the harmonic components and is presented in the frequency domain by its Fourier series. The apparent power S is defined as

$$S = U_{\text{rms}} I_{\text{rms}} , \quad (3.1)$$

where U_{rms} and I_{rms} are the RMS values of the voltage and the current. The RMS values (or the so called true RMS values) are calculated as shown in the case of the voltage

$$U_{\text{rms}} = \sqrt{\frac{1}{T} \int_0^T u(t)^2 dt} . \quad (3.2)$$

The RMS value can be expressed with the RMS values of individual harmonic components as

$$U_{\text{rms}} = \sqrt{\sum_h U_h^2} , \quad (3.3)$$

where U_h is the RMS value of the harmonic component of the order h , ($h = 0, 1, 2, \dots$). The active power is calculated as

$$P = \frac{1}{T} \int_0^T u(t)i(t) dt . \quad (3.4)$$

In a sinusoidal case, where only the fundamental components of the voltage and the current, U_1 and I_1 , are present the apparent power may be split up into the active and the reactive parts as

$$P_1 = S_1 \cos(\phi_1) = U_1 I_1 \cos(\phi_1) \quad (3.5)$$

$$Q_1 = S_1 \sin(\phi_1) = U_1 I_1 \sin(\phi_1) , \quad (3.6)$$

where ϕ_1 is the phase shift between the fundamental voltage and the fundamental current components. Further, it holds that

$$S_1^2 = P_1^2 + Q_1^2 . \quad (3.7)$$

The power factor is generally accepted as the measure of the power transfer efficiency and is defined as

$$\lambda = \frac{P}{S} . \quad (3.8)$$

For the fundamental wave quantities we have

$$\lambda_{\text{dpf}} = \frac{P_1}{S_1} = \frac{U_1 I_1 \cos(\phi_1)}{U_1 I_1} = \cos(\phi_1) , \quad (3.9)$$

which is known as the displacement power factor. In a nonsinusoidal case, the definition for P is not altered, obviously, because it has a clear physical interpretation as the rate of change of the energy. Further, the definition of the apparent power in nonsinusoidal case may be written as

$$S^2 = P^2 + Q_F^2 , \quad (3.10)$$

where Q_F is Fryze's reactive power. This quantity, introduced by Fryze (1932), is defined as

$$Q_F = \sqrt{S^2 - P^2} . \quad (3.11)$$

There is, however, different definitions for the reactive power in nonsinusoidal case. Another formulation, called Budeanu's reactive power, is defined by summing the reactive power contributions of each individual harmonic components

$$Q_B = \sum_h U_h I_h \sin(\phi_h) , \quad (3.12)$$

where ϕ_h is a phase shift between the h^{th} harmonic voltage and current. Further, to decompose the apparent power a new quantity D is introduced, which may be called distortion power. The apparent power is now divided as

$$S^2 = P^2 + Q_B^2 + D^2 . \quad (3.13)$$

The definition of Q_B in (3.12) seems well justified by recognizing that the active power may be expressed as

$$P = \sum_h U_h I_h \cos(\phi_h) . \quad (3.14)$$

Budeanu's reactive power has also been adopted by the IEEE in IEEE Std 100–1984 (1984). However, Czarnecki (1987) has shown that the Budeanu's reactive power Q_B and the distortion power D do not possess attributes, which can be related to the power phenomena

in circuits with nonsinusoidal waveforms. Moreover, Czarnecki (1987) notes that the distortion power does not provide information related to waveform distortion. The Budeanu's concept has also been criticized by Filipinski et al. (1994) and by Emanuel (1990) for being misleading and having no physical meaning in nonsinusoidal situations. In (Pretorius et al., 2000) Budeanu's definition was found to be impractical and concluded to yield erroneous results in some cases. As pointed out by Czarnecki (1987), Pretorius et al. (2000) and also noted by Filipinski et al. (1994), the reactive powers in different harmonic frequencies may have opposite signs because of the sine term in (3.12) and hence be canceled out. As a result, Budeanu's reactive power may yield a zero value when there is reactive power in some harmonic frequencies (calculated as $Q_h = U_h I_h \sin(\phi_h)$). Even though each term Q_h has a physical meaning, their sum Q_B has not. Further, Budeanu's reactive power is defined in the frequency domain, which is not very practical. The conclusion is that the Budeanu's reactive power is not sensible in nonsinusoidal cases and it should not be used.

Also, (3.10) and (3.13) are not the only decompositions of the apparent power S presented. Arrillaga and Watson (2003) give also a decomposition proposed by Shepherd and Zakikhani and a decomposition by Kusters and Moore.

3.1.2 Three-phase system

Several definitions of apparent power in three-phase systems using Budeanu's definition and Fryze's definition of reactive power have been proposed (Arrillaga and Watson, 2003). Probably the most practical ones are the definitions not involving Budeanu's reactive power. The apparent power calculated per phase basis is

$$S_{\text{ppb}} = \sum_k U_{k, \text{rms}} I_{k, \text{rms}} = \sum_k \sqrt{P_k^2 + Q_{\text{F}, k}^2}, \quad (3.15)$$

where k denotes a phase. The system apparent power that considers a three-phase network as unit is calculated as

$$S_{\Sigma} = \sqrt{\sum_k U_{k, \text{rms}}^2} \sqrt{\sum_k I_{k, \text{rms}}^2} = U_{\Sigma} I_{\Sigma} = \sqrt{P_{\Sigma}^2 + Q_{\text{F}}^2}, \quad (3.16)$$

where P_{Σ} is the average three-phase power in the fundamental cycle. Eq. (3.16) is equivalent to the total apparent power used in the Fryze-Buchholz-Depenbrock (FBD) method described in (Depenbrock, 1993). Further, it corresponds to the IEEE Working Group approach (IEEE Working Group on Nonsinusoidal situations, 1996), to which, however, Depenbrock and Staudt (1996) suggested some enhancements for the three-phase four-wire case. In (Pretorius et al., 2000) some methods of power resolution were compared considering their practicability and the use of the IEEE Working Group approach was recommended. Generally

$$S_{\Sigma} \geq S_{\text{ppb}}, \quad (3.17)$$

and further, the corresponding power factors relate as $\lambda_{\Sigma} \leq \lambda_{\text{ppb}}$ (Arrillaga and Watson, 2003). The active power in a three-phase system is, obviously, the sum of the active powers of the individual phases. The three-phase reactive power may be defined as a sum of Fryze's reactive powers of individual phases, as in (3.15) or as the total Fryze's reactive power of the three-phase system as in (3.16). Also the sum of Budeanu's reactive powers of individual phases may be used, although not recommended.

3.2 Instantaneous power components

The above presented power definitions are based on an average value concept. Some loads, e.g. an arc furnace or power electronic loads, may be dynamically changing so that the information of how the load is behaving during the cycle in average is not enough, but the information on the instantaneous quantities is needed. Typically, the instantaneous values are needed in the compensation of the unwanted components of the load current. Such actively controlled compensator is known as the active filter, see e.g. (Akagi, 1996; Mattavelli, 2001; Sonnenschein and Weinhold, 1999). Further, the control systems of modern line converters, even without any harmonic compensation capabilities, process instantaneous active power and reactive power quantities, see e.g. (Malinowski et al., 2001; Noguchi et al., 1998; Pöllänen et al., 2003). Let us summarize two theories of the instantaneous power components to help us understand what these quantities are. The first theory is the Fryze-Buchholz-Depenbrock method, which is a generally applicable method to analyze the relations connecting currents, voltages, instantaneous-, active-, nonactive-, and apparent power quantities in nonsinusoidal, unbalanced polyphase systems (Depenbrock, 1993). The second method is the theory of instantaneous reactive power in three-phase circuits introduced by Akagi et al. (1983, 1984).

3.2.1 The Fryze-Buchholz-Depenbrock method

The Fryze-Buchholz-Depenbrock method has its roots in the single-phase system study of Fryze (1932). According to Depenbrock and Staudt (1998), the work of Fryze was extended to polyphase systems by Buchholz in 1950. In 1962 Depenbrock published his dissertation, which presented extensions to the theory. The FBD-method was summed up in (Depenbrock, 1971). In English, the FBD-method was published in (Depenbrock, 1993). The FBD-method uses the sets of collective quantities, called collective magnitudes, denoted with a subscript ‘ Σ ’. The instantaneous collective values of voltage and current are calculated from the instantaneous phase quantities as

$$u_{\Sigma} = \sqrt{\sum_k u_k^2} \quad (3.18)$$

$$i_{\Sigma} = \sqrt{\sum_k i_k^2}, \quad (3.19)$$

where the voltages are between the phase and a virtual star point so that always $\sum_k u_k = 0$. Also, the currents must add up to zero, satisfying $\sum_k i_k = 0$. The theory assumes n-terminal circuit, which means that the neutral conductor, if it exists, is treated similarly to the phase conductors. The collective RMS values U_{Σ} and I_{Σ} may be calculated analogously

$$U_{\Sigma} = \sqrt{\sum_k U_{k, \text{rms}}^2} \quad (3.20)$$

$$I_{\Sigma} = \sqrt{\sum_k I_{k, \text{rms}}^2}. \quad (3.21)$$

The total collective apparent power S_Σ is defined as in (3.16). The instantaneous power $p_\Sigma(t)$ is calculated as

$$p_\Sigma(t) = \sum_k u_k i_k . \quad (3.22)$$

The phase currents are split up into the so called power currents $i_{k,p}$ and zero-power, or “powerless”, currents $i_{k,z}$ so that $i_k = i_{k,p} + i_{k,z}$. The power currents produce, with the corresponding voltages, the same instantaneous collective power $p_\Sigma(t)$ as the complete currents and have the smallest possible collective magnitude. Hence, $p_\Sigma(t) = \sum_k u_k i_{k,p}$ and $\sum_k u_k i_{k,z} = 0$. The power currents are determined in phases as

$$i_{k,p} = G_p(t) u_k \quad (3.23)$$

and as a collective quantity as

$$i_{\Sigma,p} = G_p(t) u_\Sigma , \quad (3.24)$$

where $G_p(t)$ is the equivalent time dependent conductance calculated as

$$G_p(t) = \frac{p_\Sigma(t)}{u_\Sigma^2} . \quad (3.25)$$

The zero-power current in phases is given as

$$i_{k,z} = i_k - i_{k,p} , \quad (3.26)$$

and in a collective quantity as

$$i_{\Sigma,z} = i_\Sigma - i_{\Sigma,p} . \quad (3.27)$$

The power currents can further be divided into the active currents $i_{k,a}$ and the variation currents $i_{k,v}$. The currents delivering a given mean value of collective instantaneous power $\overline{p_\Sigma(t)}$ with the smallest possible collective RMS value $I_{\Sigma,a}$ are called the active currents $i_{k,a}$. The mean value of the collective instantaneous power is the active power, or power, P_Σ . The following equations are given

$$i_{k,a} = G u_k \quad (3.28)$$

$$I_{k,\text{rms},a} = G U_{k,\text{rms}} \quad (3.29)$$

$$p_{k,a}(t) = G u_k^2 \quad (3.30)$$

$$i_{\Sigma,a} = G u_{\Sigma,a} \quad (3.31)$$

$$I_{\Sigma,a} = G U_\Sigma \quad (3.32)$$

$$p_{\Sigma,a}(t) = G u_\Sigma^2 , \quad (3.33)$$

where $p_{k,a}(t)$ and $p_{\Sigma,a}(t)$ are the phase and collective instantaneous active powers, respectively. Instantaneous collective power $p_\Sigma(t)$ may be split up into the active component $p_{\Sigma,a}(t)$ and the variation component $p_{\Sigma,v}(t)$ as

$$p_\Sigma(t) = p_{\Sigma,a}(t) + p_{\Sigma,v}(t) . \quad (3.34)$$

The phase instantaneous power may be split up analogously. The equivalent active conductance G in (3.28)–(3.33) is given as

$$G = \frac{\overline{p_\Sigma(t)}}{u_\Sigma^2} = \frac{P_\Sigma}{U_\Sigma^2} , \quad (3.35)$$

where $\overline{u_\Sigma^2}$ is the mean value of the squared collective instantaneous voltage. It should be noted that G can not be determined instantaneously because it involves the averaged values P_Σ and U_Σ^2 , which generally can not be calculated for a shorter period than one fundamental cycle. Therefore, the instantaneous active currents $i_{k,a}$ can be correctly estimated only in the steady-state conditions. The FBD-method decomposes the phase currents to the following components

$$i_k = \underbrace{i_{k,a}}_{\substack{\text{active} \\ \text{power current, } i_{k,p}}} + \underbrace{i_{k,v}}_{\text{variation}} + \underbrace{i_{k,z}}_{\text{zero power}} . \quad (3.36)$$

Also, the phase currents may be decomposed to the active and the nonactive components as

$$i_k = \underbrace{i_{k,a}}_{\text{active}} + \underbrace{i_{k,v} + i_{k,z}}_{\substack{\text{variation} \\ \text{zero power} \\ \text{nonactive current, } i_{k,na}}} . \quad (3.37)$$

The collective quantities may be decomposed similarly.

3.2.2 The instantaneous reactive power theory

The instantaneous reactive power theory, or the p - q -theory, was introduced in the early 80's by Akagi et al. (1983, 1984). The theory introduced an interesting concept of instantaneous reactive power, or instantaneous imaginary power as this quantity was named by the authors. However, some conceptual limitations of this theory were pointed out by Willems (1992), particularly if zero-sequence currents or voltages are present. A modified theory was proposed by Nabae et al. in 1993. The modified theory is also presented in (Nabae et al., 1995) and summarized in (Akagi et al., 1999). However, as analyzed by Depenbrock et al. (2003), both theories yield incorrect results in a four-wire case compared to the generally valid FBD-method. However, if the zero-sequence components are absent the results of both instantaneous power theories correspond to the results of the FBD-method. This is a typically valid assumption in three-phase three-wire systems.

Let us summarize the original theory of instantaneous power in three-phase three-wire systems without zero-sequence components. The instantaneous power may be calculated with instantaneous phase currents and voltages as

$$p = u_a i_a + u_b i_b + u_c i_c . \quad (3.38)$$

If the zero-sequence components are absent, the instantaneous power may be expressed by using the peak-value scaled space-vector representation as

$$p = \frac{3}{2}(u_\alpha i_\alpha + u_\beta i_\beta) . \quad (3.39)$$

Akagi et al. (1983, 1984) name this quantity the instantaneous real power. In order to define the instantaneous reactive power Akagi et al. (1983, 1984) introduced the instantaneous imaginary power space-vector, the magnitude of which is the instantaneous imaginary power¹

$$q = \frac{3}{2}(u_\beta i_\alpha - u_\alpha i_\beta) . \quad (3.40)$$

¹Akagi et al. (1983, 1984) originally defined instantaneous imaginary power as negation of (3.40).

Expressing with phase quantities by applying $\alpha\beta\zeta$ -to-abc transform yields

$$q = -\frac{1}{\sqrt{3}}(u_a(i_b - i_c) + u_b(i_c - i_a) + u_c(i_a - i_b)) . \quad (3.41)$$

By using a space-vector notation $\underline{u} = u_\alpha + ju_\beta$ and $\underline{i} = i_\alpha + ji_\beta$ Eqs. (3.39) and (3.40) are conveniently written as

$$p = \operatorname{Re}\{\underline{u}\underline{i}^*\} \quad (3.42)$$

$$q = \operatorname{Im}\{\underline{u}\underline{i}^*\} . \quad (3.43)$$

As clearly pointed out by Akagi et al. (1983, 1984) the instantaneous imaginary power is not a conventional electrical quantity, because the terms $u_\beta i_\alpha$ and $u_\alpha i_\beta$ are products of the instantaneous current in one axis and the instantaneous voltage in another axis. Therefore, Akagi et al. (1983, 1984) suggested that a new dimension should be introduced for q . The authors proposed “imaginary watt”. The instantaneous powers are conveniently written as

$$\begin{bmatrix} p \\ q \end{bmatrix} = \frac{3}{2} \begin{bmatrix} u_\alpha & u_\beta \\ u_\beta & -u_\alpha \end{bmatrix} \begin{bmatrix} i_\alpha \\ i_\beta \end{bmatrix} . \quad (3.44)$$

The inverse is calculated as

$$\begin{bmatrix} i_\alpha \\ i_\beta \end{bmatrix} = \frac{2}{3(u_\alpha^2 + u_\beta^2)} \begin{bmatrix} u_\alpha & u_\beta \\ u_\beta & -u_\alpha \end{bmatrix} \begin{bmatrix} p \\ q \end{bmatrix} . \quad (3.45)$$

The instantaneous currents may be written as

$$i_\alpha = \frac{2}{3} \frac{u_\alpha}{u_\alpha^2 + u_\beta^2} p + \frac{2}{3} \frac{u_\beta}{u_\alpha^2 + u_\beta^2} q \quad (3.46)$$

$$= i_{\alpha p} + i_{\alpha q} \quad (3.47)$$

$$i_\beta = \frac{2}{3} \frac{u_\beta}{u_\alpha^2 + u_\beta^2} p + \frac{2}{3} \frac{-u_\alpha}{u_\alpha^2 + u_\beta^2} q \quad (3.48)$$

$$= i_{\beta p} + i_{\beta q} , \quad (3.49)$$

where

$i_{\alpha p}$ is the α -axis instantaneous active current

$i_{\beta p}$ is the β -axis instantaneous active current

$i_{\alpha q}$ is the α -axis instantaneous reactive current

$i_{\beta q}$ is the β -axis instantaneous reactive current.

It should be noted that the instantaneous active current here is different from the instantaneous active current in the FBD-method. Further, the instantaneous powers in the α - and the β -axis, p_α and p_β , respectively, may be expressed as

$$p_\alpha = \frac{3}{2} u_\alpha i_\alpha = \frac{3}{2} u_\alpha i_{\alpha p} + \frac{3}{2} u_\alpha i_{\alpha q} \quad (3.50)$$

$$p_\beta = \frac{3}{2} u_\beta i_\beta = \frac{3}{2} u_\beta i_{\beta p} + \frac{3}{2} u_\beta i_{\beta q} \quad (3.51)$$

Using (3.46)–(3.51) the power in the three-phase three-wire circuit may be expressed as

$$p = p_\alpha + p_\beta \quad (3.52)$$

$$= \underbrace{\frac{u_\alpha^2}{u_\alpha^2 + u_\beta^2} p}_{p_{\alpha p}} + \underbrace{\frac{u_\beta^2}{u_\alpha^2 + u_\beta^2} p}_{p_{\beta p}} + \underbrace{\frac{u_\alpha u_\beta}{u_\alpha^2 + u_\beta^2} q}_{p_{\alpha q}} + \underbrace{\frac{-u_\alpha u_\beta}{u_\alpha^2 + u_\beta^2} q}_{p_{\beta q}}, \quad (3.53)$$

where

$p_{\alpha p}$ is the α -axis instantaneous active power

$p_{\beta p}$ is the β -axis instantaneous active power

$p_{\alpha q}$ is the α -axis instantaneous reactive power

$p_{\beta q}$ is the β -axis instantaneous reactive power.

Also, in here it is noted that the concept of the instantaneous active power is different from the instantaneous active power of the FBD-method. From (3.53) it is noticed that always $p_{\alpha q} + p_{\beta q} = 0$. Hence

$$p = u_\alpha i_{\alpha p} + u_\beta i_{\beta p} = p_{\alpha p} + p_{\beta p} \quad (3.54)$$

$$0 = u_\alpha i_{\alpha q} + u_\beta i_{\beta q} = p_{\alpha q} + p_{\beta q}. \quad (3.55)$$

It is interesting to remark that in (3.55) the $p_{\alpha q}$ and $p_{\beta q}$ are calculated as a product of the voltage and the current in the same axis, and that their dimension is Watt. Akagi et al. (1999) explained that $p_{\alpha q}$ contributes to the energy transfer within the α -circuit only and similarly $p_{\beta q}$ contributes to the energy transfer within the β -circuit only. If the $\alpha\beta$ -circuit is considered as a whole these energy transfers add up to zero meaning that $p_{\alpha q}$ and $p_{\beta q}$ do not contribute to the energy transfer to or from the $\alpha\beta$ -circuit but only to the circulating energy flow inside the $\alpha\beta$ -circuit. At the same time, they increase the current magnitudes in both axes leading to increased line losses. This is quite an intriguing view on the essence of reactive power.

Akagi et al. (1984) stated that in a balanced sinusoidal case the instantaneous reactive power is numerically equal to three times the conventional reactive power per one phase. Later, Ferrero and Superti-Furga (1991) developed the Akagi's instantaneous power concept further and derived interesting properties.² By utilizing complex Fourier series representation of the space-vector Ferrero and Superti-Furga (1991) stated that in a steady state the average value of instantaneous power is

$$\bar{p} = \frac{3}{2} \operatorname{Re} \left\{ \sum_{h=-\infty}^{\infty} \underline{u}_h \underline{i}_h^* \right\}, \quad (3.56)$$

where \underline{u}_h and \underline{i}_h are the coefficients of the complex Fourier series as shown in (2.12). Further, the average value of the instantaneous reactive power is

$$\bar{q} = \frac{3}{2} \operatorname{Im} \left\{ \sum_{h=-\infty}^{\infty} \underline{u}_h \underline{i}_h^* \right\}. \quad (3.57)$$

²Ferrero and Superti-Furga (1991) used the name Park-powers.

The expressions may be decomposed to reveal the contributions from different harmonic sequences as

$$\bar{p} = \underbrace{\frac{3}{2} \operatorname{Re} \left\{ \sum_{h=1}^{\infty} \underline{u}_h \underline{i}_h^* \right\}}_{\bar{p}_{\text{pos. seq.}}} + \underbrace{\frac{3}{2} \operatorname{Re} \left\{ \sum_{h=-\infty}^{-1} \underline{u}_h \underline{i}_h^* \right\}}_{\bar{p}_{\text{neg. seq.}}} + \underbrace{\frac{3}{2} \operatorname{Re} \{ \underline{u}_0 \underline{i}_0^* \}}_{\bar{p}_{\text{dc}}} \quad (3.58)$$

$$\bar{q} = \underbrace{\frac{3}{2} \operatorname{Im} \left\{ \sum_{h=1}^{\infty} \underline{u}_h \underline{i}_h^* \right\}}_{\bar{q}_{\text{pos. seq.}}} + \underbrace{\frac{3}{2} \operatorname{Im} \left\{ \sum_{h=-\infty}^{-1} \underline{u}_h \underline{i}_h^* \right\}}_{-\bar{q}_{\text{neg. seq.}}} + \underbrace{\frac{3}{2} \operatorname{Im} \{ \underline{u}_0 \underline{i}_0^* \}}_{\bar{q}_{\text{dc}}}, \quad (3.59)$$

where $\bar{p}_{\text{pos. seq.}}$ is the contribution of the positive sequence components, $\bar{p}_{\text{neg. seq.}}$ is the contribution of the negative sequence components and \bar{p}_{dc} is resulting from the dc-components of the voltage and the current space-vectors, denoted with the subscript 0. For the reactive power the same notations are used. It should be noted, however, that in the definition of the reactive power originating from the negative sequence components in (3.59) the sign is different than with the positive sequence reactive power. This is because the change of the rotational direction also changes the sign of the reactive power. Ferrero and Superti-Furga (1991) further showed that Budeanu's reactive power may be expressed as

$$Q_B = \bar{q}_{\text{pos. seq.}} + \bar{q}_{\text{neg. seq.}} \quad (3.60)$$

An important contribution of Ferrero and Superti-Furga (1991) was that they showed how the over-the-cycle averaged instantaneous reactive power relates with the other definitions of reactive power. In practical power electronic devices \bar{q} is, as a time-domain quantity, easily calculated and, hence, frequently used.

3.3 Numerical example

To clarify the power definitions given above a numerical example analyzing a line current of common nonlinear load is worked out. The nonlinear load used is a six-pulse diode bridge with ac-reactors, shown in Fig. 3.1. The phase currents are shown in Fig. 3.2 together with the calculated corresponding harmonics. The phase voltages of the grid have about 1.5% of the 5th harmonic and about 0.5% of the 7th harmonic. Numerical information of the phase voltages is given in Tab 3.1.

In Fig. 3.3(a) the current space vector is presented in the $\alpha\beta$ -axis. The harmonic sequences obtained with the complex Fourier series are presented in Fig. 3.3(b). By using both the magnitude and the phase information of the complex Fourier series we may present individual harmonic space vectors. This is shown in Fig. 3.3(c), where the fundamental wave space-vector and the space-vectors of the largest harmonic sequences are presented. The phase currents in Fig. 3.2 are quite symmetrical but small differences are observed—in the phase a the first spike is higher than the second but in the phase c the second spike is higher. This implies that uncharacteristic harmonics are present. The sequence analysis in Fig. 3.3 reveals that a small amount of the 3rd positive sequence and the 1st negative sequence are present. However, their amount is so small that no clear asymmetry is observed from the $\alpha\beta$ -axis space-vector locus.

The current decomposition according to the FBD-method is shown in Fig. 3.4. First, in Fig. 3.4(a), the phase a current i_a is decomposed to power current $i_{a,p}$ and zero-power current $i_{a,z}$. Then, in Fig. 3.4(b) the power current is further decomposed to active current $i_{a,a}$ and variation current $i_{a,v}$. The active current, which, by the definition, conveys the power between the source and the load with the smallest possible RMS value, has the unity power factor. Hence, the wave shape of the active current is identical to the supply voltage. This is evident from (3.28). The variation current is responsible for the energy exchange between the source and the load that is not included in the active current. The zero-power current, in turn, does not contribute any energy exchange between the source and the load. In the three-phase case without the zero-sequence components the power currents correspond to the Akagi's instantaneous active currents $i_{\alpha p}$ and $i_{\beta p}$ and the zero-power currents correspond to the Akagi's instantaneous reactive currents $i_{\alpha q}$ and $i_{\beta q}$ in Eqs. (3.47) and (3.49). Similar to Akagi's instantaneous reactive current, the zero-power current is responsible for the energy exchange between the phases of the load.

From the energy transfer point of view, only the active current of the FBD-method is important and the rest produces line losses. The optimal compensator current canceling the unwanted current components is then the inverse of the load nonactive current

$$-i_{a,na} = -(i_{a,v} + i_{a,z}) . \quad (3.61)$$

This is shown in Fig. 3.4(c). Such a compensator was proposed by Depenbrock and Staudt (1998). The zero-power current may be compensated without any energy storage in the compensator. In order to compensate the variation current an energy storage is needed to absorb and dissipate the power associated with the variation current.

If the FBD-decomposition is carried out on a per phase basis, i.e. treating each phase as an individual single phase system, instead of the three-phase approach the resulting current components are different. The active current is obviously the same, but the zero-power current is always zero. In the individual single-phase consideration the zero-power current of the three-phase case is included in the variation current. The optimal compensator current is, hence, the same in both cases. Clearly, in the single phase case there can not be any power exchange between the phases since there is not any other phase to change with. Therefore, all the phase current has to be power current. Graphs of Akagi's instantaneous power and instantaneous reactive power are shown in Fig. 3.5. Several numerical values corresponding to different formulations and definitions were calculated. The results are gathered in Tabs. 3.1 and 3.2.

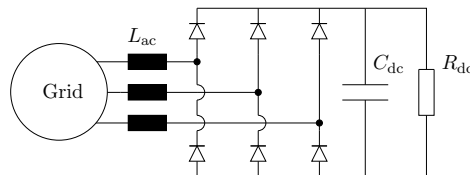


Figure 3.1: Configuration of the example case. $L_{ac} = 1180 \mu\text{H}$, $C_{dc} = 2.35 \text{ mF}$ and $R_{dc} = 23.5 \Omega$. The nominal voltage of the supply grid is 400 V and the nominal frequency is 50 Hz. The positive direction of currents is from the grid to the dc-link and the positive direction of voltages is from the phase to the virtual star point.

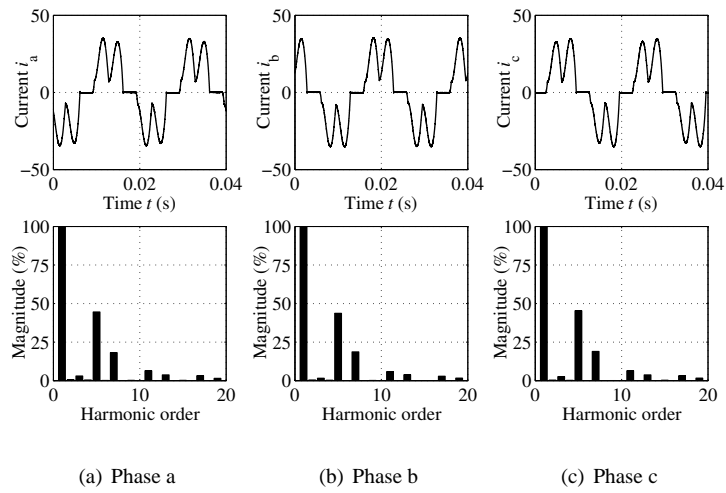


Figure 3.2: Phase currents in time domain and in frequency domain.

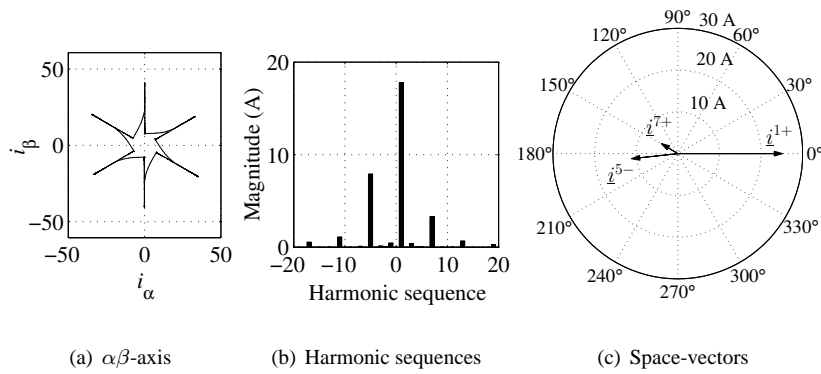


Figure 3.3: Current space-vector locus in $\alpha\beta$ -axis, harmonic sequences in frequency domain and space-vectors of positive fundamental sequence and negative 5th and positive 7th harmonic sequences.

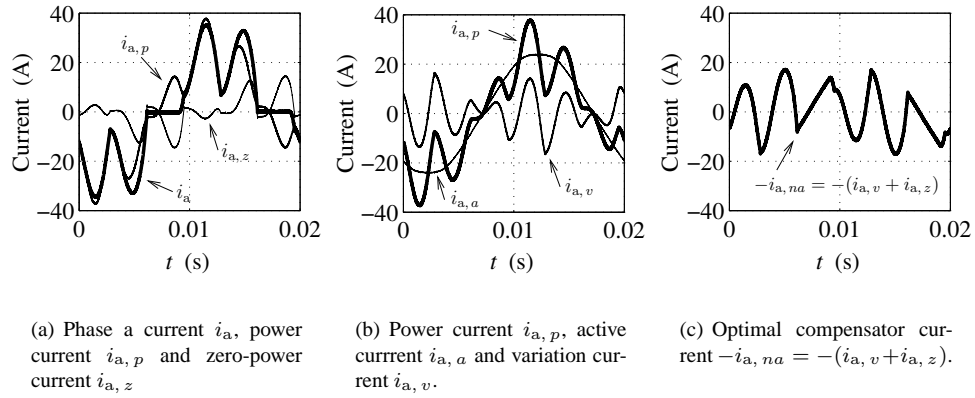


Figure 3.4: Current decomposition according to FBD-method.

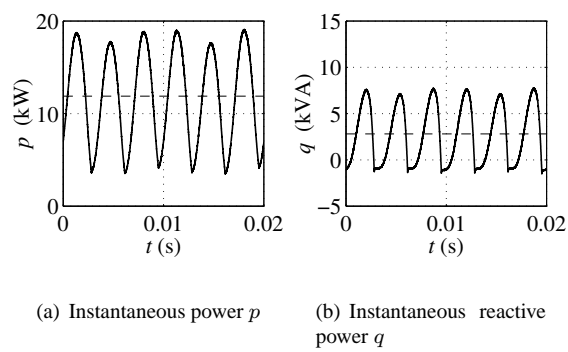
Figure 3.5: Instantaneous power components. Mean values \bar{p} and \bar{q} are shown with dashed line.

Table 3.1: Numerical values calculated in an example case. Single-phase system related quantities.

| Quantity | Phase a | Phase b | Phase c | Unit | Comment |
|---|---------|---------|---------|------|---|
| $U_{\text{rms}} = \sqrt{\frac{1}{T} \int_0^T u(t)^2 dt}$ | 229.3 | 229.3 | 228.6 | V | True RMS |
| $I_{\text{rms}} = \sqrt{\frac{1}{T} \int_0^T i(t)^2 dt}$ | 19.61 | 20.30 | 19.57 | A | True RMS |
| $S = U_{\text{rms}} I_{\text{rms}}$ | 4495 | 4655 | 4473 | VA | Apparent power |
| $P = \frac{1}{T} \int_0^T u(t)i(t) dt$ | 3946 | 4075 | 3866 | W | Average active power |
| $Q_{\text{F}} = \sqrt{S^2 - P^2}$ | 2155 | 2251 | 2249 | VA | Fryze's reactive power |
| U_1 | 229.2 | 229.3 | 228.6 | V | Fundamental wave RMS |
| I_1 | 17.60 | 18.28 | 17.50 | A | Fundamental wave RMS |
| S_1 | 4035 | 4191 | 3999 | VA | Fundamental apparent power |
| P_1 | 3942 | 4074 | 3866 | W | Fundamental active power |
| Q_1 | 863.7 | 986.1 | 1024 | VA | Fundamental reactive power |
| $Q_{\text{B}} = \sum_h U_h I_h \sin(\phi_h)$ | 891.6 | 1020 | 1054 | VA | Budeanu's reactive power |
| $D = \sqrt{S^2 - P^2 - Q_{\text{B}}^2}$ | 1961 | 2006 | 1987 | VA | Budeanu's distortion power |
| $\lambda = \frac{P}{S}$ | 0.878 | 0.875 | 0.864 | – | Power factor |
| $\lambda_{\text{dpf}} = \frac{P_1}{S_1}$ | 0.977 | 0.972 | 0.967 | – | Displacement power factor |
| $\text{THD}_{40} = \frac{\sqrt{\sum_{h=2}^{40} U_h^2}}{U_1}$ | 1.6 | 1.8 | 1.6 | % | Voltage THD up to 40 th harmonic |
| $\text{THD}_{40} = \frac{\sqrt{\sum_{h=2}^{40} I_h^2}}{I_1}$ | 49.05 | 48.29 | 50.05 | % | Current THD up to 40 th harmonic |
| $\text{DIN}_{40} = \frac{\sqrt{\sum_{h=2}^{40} U_h^2}}{U_{\text{rms}}}$ | 1.6 | 1.8 | 1.6 | % | Voltage DIN up to 40 th harmonic |
| $\text{DIN}_{40} = \frac{\sqrt{\sum_{h=2}^{40} I_h^2}}{I_{\text{rms}}}$ | 44.03 | 43.49 | 44.76 | % | Current DIN up to 40 th harmonic |
| $\text{THD}' = \frac{\sqrt{U_{\text{rms}}^2 - U_1^2}}{U_1}$ | 1.6 | 1.9 | 1.6 | % | Ratio of voltage harmonic energy to fundamental wave energy |
| $\text{THD}' = \frac{\sqrt{I_{\text{rms}}^2 - I_1^2}}{I_1}$ | 49.06 | 48.31 | 50.06 | % | Ratio of current harmonic energy to fundamental wave energy |

Table 3.2: Numerical values calculated in an example case. Three-phase system related quantities.

| Quantity | Value | Unit | Comment |
|---|-------|------|--|
| $U_{\Sigma} = \sqrt{\sum_k U_{k, \text{rms}}^2}$ | 396.7 | V | Collective 3-phase voltage |
| $I_{\Sigma} = \sqrt{\sum_k I_{k, \text{rms}}^2}$ | 34.34 | A | Collective 3-phase current |
| $S_{\Sigma} = U_{\Sigma} I_{\Sigma}$ | 13625 | VA | Collective apparent power |
| $P_{\Sigma} = \overline{p_{\Sigma}(t)} = \frac{1}{T} \int_0^T \sum_k u_k i_k dt$ | 11887 | W | Average active power |
| $S_{\text{ppb}} = \sum_k S_k$ | 13624 | VA | Apparent power calculated per phase basis |
| $\lambda_{\Sigma} = \frac{P_{\Sigma}}{S_{\Sigma}}$ | 0.872 | – | Collective power factor |
| $\lambda_{\text{ppb}} = \frac{P_{\Sigma}}{S_{\text{ppb}}}$ | 0.873 | – | Per phase basis calculated power factor |
| $\sum_k Q_{B, k}$ | 2964 | VA | Sum Budeanu's reactive power |
| $\bar{p} = \frac{1}{T} \int_0^T \frac{3}{2} (u_{\alpha} i_{\alpha} + u_{\beta} i_{\beta}) dt$ | 11887 | W | Mean instantaneous power |
| $\bar{q} = \frac{1}{T} \int_0^T \frac{3}{2} (u_{\beta} i_{\alpha} - u_{\alpha} i_{\beta}) dt$ | 2811 | VA | Mean instantaneous reactive power |
| $\bar{p}_{\text{pos. seq.}} = \frac{3}{2} \text{Re} \left\{ \sum_{h=1}^{\infty} \underline{u}_h \underline{i}_h^* \right\}$ | 11872 | W | Positive sequence harmonics power |
| $\bar{p}_{\text{neg. seq.}} = \frac{3}{2} \text{Re} \left\{ \sum_{h=-\infty}^{-1} \underline{u}_h \underline{i}_h^* \right\}$ | 15 | W | Negative sequence harmonics power |
| $\bar{q}_{\text{pos. seq.}} = \frac{3}{2} \text{Im} \left\{ \sum_{h=1}^{\infty} \underline{u}_h \underline{i}_h^* \right\}$ | 2888 | VA | Positive sequence harmonics reactive power |
| $\bar{q}_{\text{neg. seq.}} = \frac{3}{2} \text{Im} \left\{ \sum_{h=-\infty}^{-1} \underline{u}_h \underline{i}_h^* \right\}$ | 77 | VA | Negative sequence harmonics reactive power |
| $\bar{q}_{\text{pos. seq.}} + \bar{q}_{\text{neg. seq.}} (= \sum_k Q_{B, k})$ | 2965 | VA | Alternative expression for sum Budeanu's reactive power |
| $\bar{q}_{\text{pos. seq.}} - \bar{q}_{\text{neg. seq.}} + \underbrace{\bar{q}_{\text{dc}}}_{\approx 0} (= \bar{q})$ | 2811 | VA | Alternative expression for mean instantaneous reactive power |
| $u = \frac{ z^1 - 1 }{ z^1 + 1 }$ | 2.7 | % | Current unbalance |

3.4 Summary

In this chapter, various power components used in electrical engineering were introduced. Two theories considering the instantaneous power quantities were summarized—the Fryze-Buchholz-Depenbrock method and the instantaneous reactive power theory. Finally, a practical numerical example was worked out to demonstrate the various formulations presented.

Chapter 4

Modeling and control of line converter

This chapter introduces a dynamical model of the line converter and reviews the line converter control methods presented in the literature. A new DTC-based current vector control method is introduced, analyzed and modeled. The issues of controller tuning are considered. Finally, the overmodulation characteristics of the DTC converter are discussed and a new analytical formula for the maximum modulation index is presented.

4.1 Dynamic model of line converter

This thesis considers line converters with both L- and LCL-line filters, shown in Fig. 4.1. The L-filter is practically a three-phase series inductor L_1 . The LCL-filter is obtained by adding a parallel capacitor C_f and another three-phase series inductor L_2 to the L-filter. One purpose of the line filter is to reduce the converter current distortion. Another purpose of the inductor L_1 is to provide energy storage for the step-up action. The step-up action, or voltage boost, is required to make the rectified current to flow to the dc-link potential, which is higher than the peak line-to-line voltage of the grid.

One inverter leg, comprising two IGB-transistors and anti-parallel freewheeling diodes, forms a switch, which can connect the phase to either a positive or negative dc-link potential. In practical converters there has to be a short period of time when neither of the transistors is in conducting state. This blanking time, or dead time, is required to prevent the shoot-through, which is a failure occurring when both transistors in a leg are conducting at the same time. During the blanking time the direction of the current determines which one of the diodes is conducting and whether the phase is clamped to the positive or the negative potential. Typically, blanking times are about 2 μ s. The effects of the blanking time are discussed, e.g., in (Holmes and Lipo, 2003).

The inverter phase voltage is determined by the transistor switchings, but the phase current can flow freely to both directions regardless of the transistor switching state. This means that there can be an arbitrary phase shift between the converter output voltage and the output

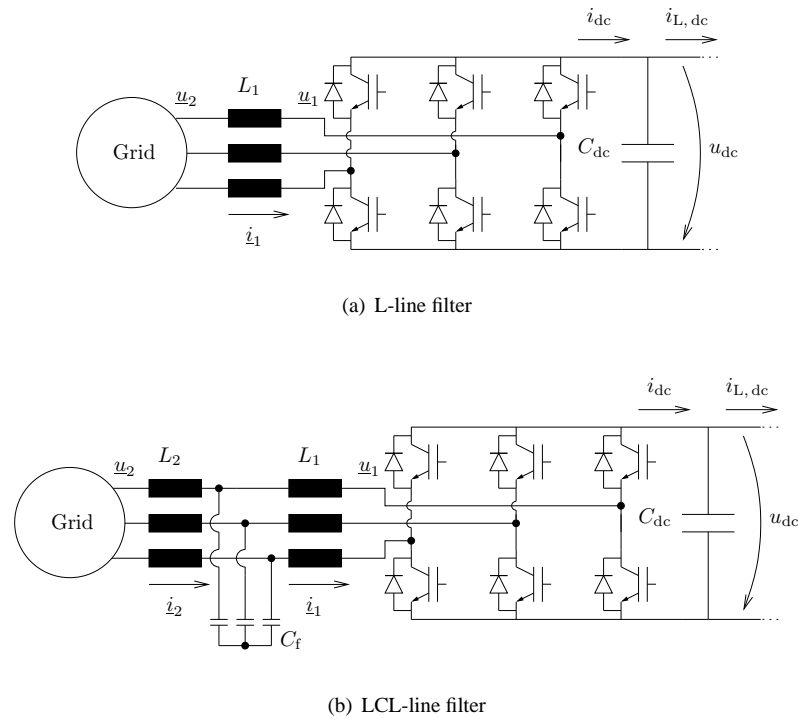


Figure 4.1: Line converter connected to a grid through different line filters.

current—a property that makes it possible to operate in motoring and generating mode and with leading or lagging power factor.

The dynamic model of a three-phase voltage source line converter consists of three parts: The model of the converter bridge, the model of the line filter and the model of the dc-link. The dynamic model is usually needed for studying the converter behavior in transient states, and understanding of the transient states is essential in designing the control system of the converter. Detailed models of the power switches are not usually needed for control system purposes and it is customary to use ideal switch models. An ideal switch changes between the conducting and non-conducting states instantaneously and its leakage current and conduction losses are zeros. Further, parasitic components and nonlinearities of passive components, such as inductors and capacitors, are typically neglected. For some other simulation purposes, such as efficiency calculation, more detailed switch models and component models are necessary.

4.1.1 Ideal converter bridge

The space-vector modeling of a voltage source converter is quite thoroughly considered in (Ollila, 1993). In the ideal converter each supply phase is connected either to the positive or to the negative dc-link voltage. The switching state of the converter is characterized with the

switching function space-vector \underline{sw} , which is defined as

$$\underline{sw} = \frac{2}{3} \left(sw_a + sw_b e^{j\frac{2\pi}{3}} + sw_c e^{j\frac{4\pi}{3}} \right) , \quad (4.1)$$

where sw_a , sw_b and sw_c are phase switching functions. The value of a phase switching function is $+\frac{1}{2}$, if a corresponding phase is connected to the positive dc-link potential and $-\frac{1}{2}$, if it is connected to the negative dc-link potential. The reference voltage is the middle point voltage of the dc-link. If the negative dc-link potential is used as a reference, the phase switching function can have the values 0 and 1. The switching function space-vector may be decomposed in components as

$$\underline{sw} = sw_\alpha + j sw_\beta . \quad (4.2)$$

The converter terminal voltage space-vector is calculated as

$$\underline{u}_1 = \underline{sw} u_{dc} . \quad (4.3)$$

The two-level converter switch combinations form 8 voltage vectors, of which 6 are active vectors and 2 are zero vectors. The active voltage vectors are shown in Fig. 4.2. Eqs. (4.1) and (4.3) constitute a model of a converter bridge with three change-over switches, shown in Fig. 4.3(a). The phase switching functions can be defined with the switching functions of individual switches as

$$sw_a = \frac{1}{2} (sw_{a+} - sw_{a-}) \quad (4.4)$$

$$sw_b = \frac{1}{2} (sw_{b+} - sw_{b-}) \quad (4.5)$$

$$sw_c = \frac{1}{2} (sw_{c+} - sw_{c-}) , \quad (4.6)$$

where sw_{a+} is the upper potential switch and sw_{a-} is the lower potential switch of the phase a. The other phases are analogous. The individual switch related switching functions have a value of 0, if the switch is not conducting and a value of 1, if the switch is conducting. An individual switch-based model is shown in Fig. 4.3(b).

The switching function vector (4.1) has also an associated zero-sequence component

$$sw_\zeta = \frac{1}{3} (sw_a + sw_b + sw_c) , \quad (4.7)$$

from which the zero-sequence component of the converter terminal voltage is calculated as

$$u_{1\zeta} = sw_\zeta u_{dc} . \quad (4.8)$$

The dc-link middle point voltage is regarded as a reference point. The phase switching functions and the zero sequences corresponding to different voltage vectors are shown in Tab. 4.1. The zero-sequence voltage is usually neglected because in three-wire systems the zero-sequence current path does not exist and therefore the zero-sequence voltage does not produce any current. However, if two line converters are directly coupled at the AC and DC sides a circulating zero-sequence current has a path to flow, see e.g. (Pöllänen, 2003; Wei et al., 2003; Ye et al., 2000). In this case, the zero-sequence voltage can not be neglected.

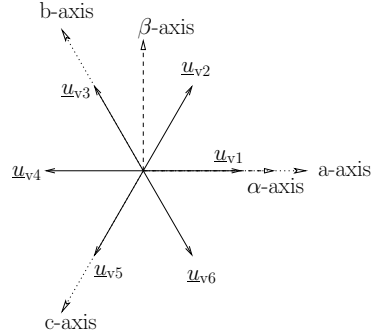


Figure 4.2: Active voltage vectors of a two-level converter. The $\alpha\beta$ -axes and abc-axes are also shown.

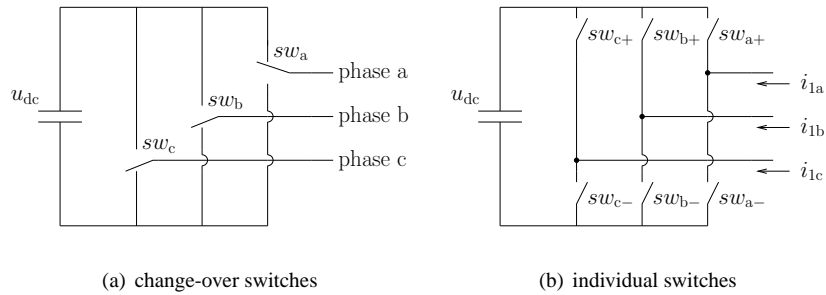


Figure 4.3: Switch models of a line converter. The phase related and switch related switching functions are shown.

Table 4.1: Components of phase switching functions and zero-sequence component corresponding to different voltage vectors. Voltage vectors \underline{u}_{v0} and \underline{u}_{v7} are zero vectors.

| Voltage vector | sw_a | sw_b | sw_c | sw_ζ |
|----------------------|----------------|----------------|----------------|----------------|
| \underline{u}_{v0} | $-\frac{1}{2}$ | $-\frac{1}{2}$ | $-\frac{1}{2}$ | $-\frac{1}{2}$ |
| \underline{u}_{v1} | $\frac{1}{2}$ | $-\frac{1}{2}$ | $-\frac{1}{2}$ | $-\frac{1}{6}$ |
| \underline{u}_{v2} | $\frac{1}{2}$ | $\frac{1}{2}$ | $-\frac{1}{2}$ | $\frac{1}{6}$ |
| \underline{u}_{v3} | $-\frac{1}{2}$ | $\frac{1}{2}$ | $-\frac{1}{2}$ | $-\frac{1}{6}$ |
| \underline{u}_{v4} | $-\frac{1}{2}$ | $\frac{1}{2}$ | $\frac{1}{2}$ | $\frac{1}{6}$ |
| \underline{u}_{v5} | $-\frac{1}{2}$ | $-\frac{1}{2}$ | $\frac{1}{2}$ | $-\frac{1}{6}$ |
| \underline{u}_{v6} | $\frac{1}{2}$ | $-\frac{1}{2}$ | $\frac{1}{2}$ | $\frac{1}{6}$ |
| \underline{u}_{v7} | $\frac{1}{2}$ | $\frac{1}{2}$ | $\frac{1}{2}$ | $\frac{1}{2}$ |

4.1.2 Direct current and dc-link model

The direct current of the line converter is found by considering the power balance on the AC and DC sides. Neglecting the losses we may write

$$p_{dc} = p_{ac} \quad (4.9)$$

$$u_{dc}i_{dc} = \frac{3}{2}\text{Re}\{\underline{u}_1\underline{i}_1^*\} + 3u_{1\zeta}i_{1\zeta} \quad (4.10)$$

$$u_{dc}i_{dc} = \frac{3}{2}\text{Re}\{s\underline{w}u_{dc}\underline{i}_1^*\} + 3s\underline{w}_\zeta u_{dc}i_{1\zeta} \quad (4.11)$$

$$u_{dc}i_{dc} = \frac{3}{2}u_{dc}(s\underline{w}_\alpha i_{1\alpha} + s\underline{w}_\beta i_{1\beta}) + 3s\underline{w}_\zeta u_{dc}i_{1\zeta} \quad (4.12)$$

and the dc-current is

$$i_{dc} = \frac{3}{2}(s\underline{w}_\alpha i_{1\alpha} + s\underline{w}_\beta i_{1\beta}) + 3s\underline{w}_\zeta i_{1\zeta} . \quad (4.13)$$

Typically, the zero-sequence current does not exist and the latter term may be left out. The dc-link voltage is calculated with the equation of an ideal capacitor

$$u_{dc} = \frac{1}{C_{dc}} \int (i_{dc} - i_{L,dc}) dt , \quad (4.14)$$

where C_{dc} is the capacitance of the dc-link capacitor and $i_{L,dc}$ is the load current drawn from the dc-link.

4.1.3 Model of a line filter

For the L-type line filter the following equations for the phase quantities may be written

$$L_1 \frac{di_{1a}}{dt} + R_1 i_{1a} = u_{2a} - u_{1a} \quad (4.15)$$

$$L_1 \frac{di_{1b}}{dt} + R_1 i_{1b} = u_{2b} - u_{1b} \quad (4.16)$$

$$L_1 \frac{di_{1c}}{dt} + R_1 i_{1c} = u_{2c} - u_{1c} , \quad (4.17)$$

where R_1 is the equivalent series resistance of the filter inductor. Using the space-vector notation and by assuming that the zero-sequence circuit does not exist, the L-filter model may be expressed as

$$L_1 \frac{d\underline{i}_1^{\alpha\beta}}{dt} + R_1 \underline{i}_1^{\alpha\beta} = \underline{u}_2^{\alpha\beta} - \underline{u}_1^{\alpha\beta} , \quad (4.18)$$

where superscript $\alpha\beta$ is used to explicitly indicate that the space-vector is expressed in the stationary co-ordinates. A stationary co-ordinate space vector, let us say $\underline{i}_1^{\alpha\beta}$, may be transformed to a synchronous dq-frame rotating with supply angular frequency ω_s as

$$\underline{i}_1^{dq} = \underline{i}_1^{\alpha\beta} e^{-j\omega_s t} . \quad (4.19)$$

Expressing (4.18) using the synchronous co-ordinate space-vectors, denoted with superscript dq, we have

$$L_1 \frac{d}{dt} \left(\underline{i}_1^{dq} e^{j\omega_s t} \right) + R_1 \underline{i}_1^{dq} e^{j\omega_s t} = \underline{u}_2^{dq} e^{j\omega_s t} - \underline{u}_1^{dq} e^{j\omega_s t} , \quad (4.20)$$

and further

$$L_1 \frac{d\underline{i}_1^{\text{dq}}}{dt} + (R_1 + j\omega_s L_1) \underline{i}_1^{\text{dq}} = \underline{u}_2^{\text{dq}} - \underline{u}_1^{\text{dq}} . \quad (4.21)$$

By separating the real and the imaginary parts (e.g. $\underline{i}_1^{\text{dq}} = i_{1d} + ji_{1q}$) and using a matrix notation we have

$$\begin{bmatrix} \frac{d}{dt} i_{1d} \\ \frac{d}{dt} i_{1q} \end{bmatrix} = \begin{bmatrix} -\frac{R_1}{L_1} & \omega_s \\ -\omega_s & -\frac{R_1}{L_1} \end{bmatrix} \begin{bmatrix} i_{1d} \\ i_{1q} \end{bmatrix} + \begin{bmatrix} \frac{1}{L_1} & 0 & -\frac{1}{L_1} & 0 \\ 0 & \frac{1}{L_1} & 0 & -\frac{1}{L_1} \end{bmatrix} \begin{bmatrix} u_{2d} \\ u_{2q} \\ u_{1d} \\ u_{1q} \end{bmatrix}, \quad (4.22)$$

which is of general state-space form. Eq. (4.22) is valid also in stationary co-ordinates, if $\omega_s = 0$ is substituted. For the LCL-filter a similar model is presented in Appended Publication I.

4.2 Line converter control principles

4.2.1 Power angle control

The simplest line converter control principles are based on the power angle control. The characterizing property of the power angle control is that the feedback from the converter currents is not needed. The power angle control methods are based on the steady-state fundamental wave equations

$$p = \frac{3}{2\omega_s L_1} u_1 u_2 \sin(\delta) \quad (4.23)$$

$$q = -\frac{3}{2\omega_s L_1} (u_1 u_2 \cos(\delta) - u_2^2), \quad (4.24)$$

where δ is the angle between the converter voltage vector \underline{u}_1 and the grid voltage vector \underline{u}_2 . The angle δ is called power angle or, analogously to the synchronous machines, load angle. The power angle control can be used without the concept of space-vector. In that case, δ is the phase angle difference between the converter and grid fundamental voltages.

The active power is controlled by adjusting the power angle and the reactive power is controlled with the fundamental wave amplitude of the converter voltage vector, both shown in Fig. 4.9 on page 60. Control systems employing the power angle control have been presented e.g. by Green et al. (1988) and by Ooi and Wang (1990). The control system may be implemented with fixed PWM amplitude modulation ratio, leaving the dc-link voltage controller the only controller in the system. Variants of this have been presented by J60s et al. (1991) and Weinhold (1991). The disadvantage is, however, that the dc-link voltage and the reactive power can not be controlled separately with the constant amplitude modulation ratio. Generally, the power angle control based methods suffer from poor dynamic performance, e.g. see analysis in (Ollila, 1993), and hence vector control or direct power control methods are favored today.

4.2.2 Current vector control

The most common control principle of the line converter is the line voltage oriented current vector control, shown in Fig. 4.4. The concepts of the vector control and field orientation were invented in Germany in the late 60's to enhance the control of induction motors. In 1972 Felix Blaschke published the famous paper (Blaschke, 1972) describing new "TRANSVEKTOR" control.

The underlying idea of the field orientation is the synchronously rotating reference frame, in which the fundamental wave AC quantities appear as DC quantities. Efficient current control is achieved by transforming and controlling the current vector in the synchronous co-ordinates. The synchronous frame is oriented so that the transformed current components have different characteristics. In the case of a motor, for example, one is proportional to the torque and the other to the magnetic flux of the motor. In the case of a line converter it is advantageous to select the synchronous frame such that the active power can be controlled with one current component and the reactive power with the other. Another favorable property of the field orientation is that the control of the synchronous frame current components can be effectively done with simple PI-controllers. The control references, which are DC signals in the synchronous frame, are easily tracked with the PI-controllers. Contrary to that, if the control would have been performed in the stationary co-ordinates the steady-state waveforms of the control references would be sinusoidal. The PI-controllers are known to perform badly in tracking the sinusoidal reference values, see e.g. (Harnefors, 1997; Rowan and Kerkman, 1986), and, hence, some other control algorithm than the PI-control would have to be used.

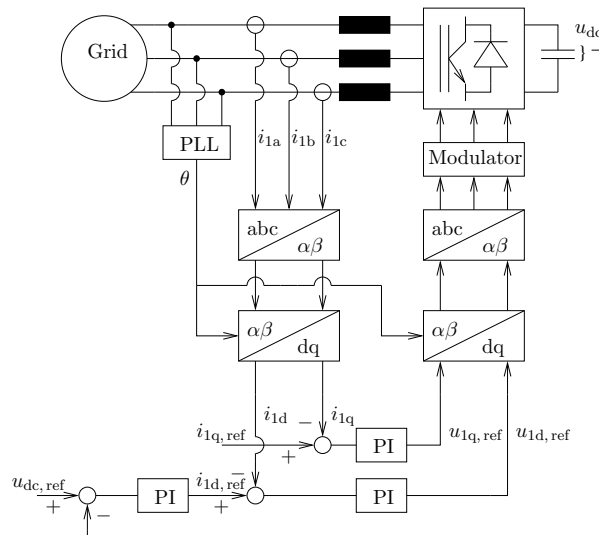


Figure 4.4: Schematic of the line voltage oriented current vector control system of a line converter. The d-axis of the synchronous frame is fixed to the line voltage vector. The angle of the line voltage vector is detected with a phase locked loop (PLL) to find out the rotation angle θ that is used in the co-ordinate transformations.

4.2.3 Direct torque control

DTC motor drive

The direct torque control was originally proposed for controlling an induction motor. The fundamental principles of the DTC were independently invented by Depenbrock (1985, 1988) and by Takahashi and Noguchi (1986). Depenbrock called his method direct self-control (DSC), but Takahashi and Noguchi originally did not name their method. They only called it “quick-response and high-efficiency control strategy,” and noted that it is quite different from the field-oriented control. Later, Takahashi’s and Noguchi’s method has become commonly known as the direct torque control. The DTC and DSC are based on the estimation of the stator flux linkage vector $\underline{\psi}_s$ of a motor with an integral

$$\underline{\psi}_s = \int (\underline{u}_s - R_s \underline{i}_s) dt , \quad (4.25)$$

where \underline{u}_s is the stator voltage vector, R_s is the stator resistance and \underline{i}_s is the stator current vector. The electromechanical torque of the motor is estimated as

$$t_e = \frac{3}{2} \text{Im}\{\underline{\psi}_s^* \underline{i}_s\} . \quad (4.26)$$

The DTC method uses two hysteresis control loops, one controlling the torque and the other controlling the magnetization of the motor with the modulus of the stator flux linkage vector. This is very advantageous, since both primary control variables of the motor are directly controlled with fast hysteresis control loops. The hysteresis control loops are implemented by comparing both the torque and the stator flux linkage amplitude with corresponding references and by selecting the inverter voltage vector according to the results of the comparisons. The method of Takahashi and Noguchi (1986) uses a switching table (the so called “optimum switching table”), from which the inverter voltage vectors are looked up according to the hysteresis comparisons and the location of the stator flux linkage vector in the complex plane. This implementation results in a circular stator flux linkage trajectory in the steady state. The DSC proposed by Depenbrock (1985, 1988) does not use a look-up table but three hysteresis comparators for the flux linkage and one for the torque. The resulting flux trajectory in the steady state is a hexagon. The DTC was commercialized in the 90’s by the ABB company (Tiitinen et al., 1995). The block diagram representation of a direct torque controlled AC motor is depicted in Fig. 4.5.

In the DTC method the complex plane is divided into six sectors so that each voltage vector is located in the middle of the sector. In each sector two active voltage vectors and two zero vectors are used in the modulation. The active vectors used in each sector are shown in Fig. 4.6 for a counter-clockwise direction of rotation. The switching logic assumes that either of the two active vectors increases the torque and that the zero vector decreases the torque. Hence, if the estimated torque is above the tolerance band a zero vector is applied to decrease it. Correspondingly, if the estimated torque is below the tolerance band an active vector is switched. Selection between the active vectors is made according to the flux linkage modulus comparison. One of the active vectors in each sector is oriented so that it increases the flux linkage modulus and the other is oriented to decrease it. In sector 1, e.g., the voltage vector \underline{u}_{v2} is increasing and \underline{u}_{v3} is decreasing the flux linkage modulus. The flux linkage modulus is controlled by always selecting the active vector which reduces the error.

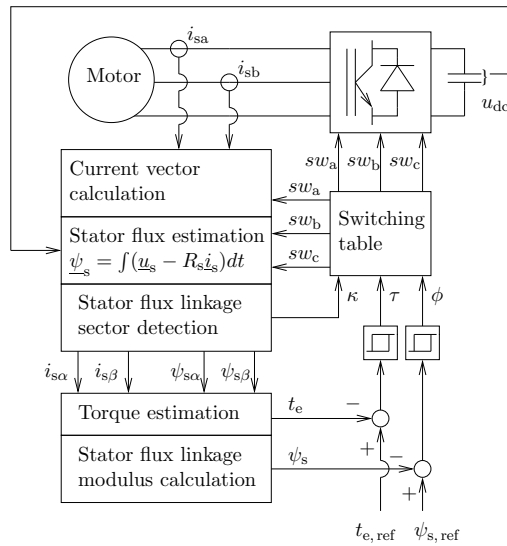


Figure 4.5: Direct torque controlled AC motor.

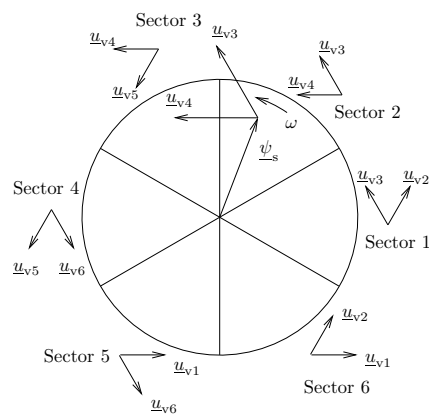


Figure 4.6: Sector division of the complex plane. Active voltage vectors used in each sector are shown.

Albeit the fundamentals of the DTC based motor controller are seemingly simple, additions are required to achieve good overall performance under all operation conditions. As pointed out by Kaukonen (1999), especially in the low rotation speeds the stator flux linkage estimation (4.25) becomes erroneous. This shows up as the drifting of the flux linkage estimate to non-origin centered. The following reasons for the estimation errors are given by Kaukonen (1999):

1. dc-link voltage measurement errors
2. stator current measuring error
3. power switch voltage loss and blanking time estimation error
4. stator resistance estimation error

One method to overcome the problems in the stator flux linkage estimation is to use an inductance-based current model as a supervising model, which is used to correct the flux linkage estimate (4.25). Overview of other methods proposed to reduce the problem of the drifting stator flux linkage estimate are presented by Niemelä (1999), together with two new methods. Later, Luukko (2000); Luukko et al. (2003) has proposed improvements to Niemelä's methods and, finally, Pöllänen (2003) has adapted one method to line converter application.

DTC in line converter control

Even though the DTC method is originally invented as a motor control method, also a line converter may be controlled by using it. Manninen (1995) has introduced basic principles of the DTC control method applied to the line converter. The block diagram of direct torque controlled line converter is shown in Fig. 4.7. The physical structure of the line converter may be exactly similar to the motor converter, the only exceptions being the connection to the grid instead of the motor and the introduction of the line filter. The software is modified to control the power factor and the dc-link voltage instead of the magnetization level and the torque of the electrical machine.

The use of the DTC in a line converter may be justified, as explained by Pöllänen (2003), by assuming the resistance and the inductance of the line filter as the stator resistance and the stator leakage inductance of a virtual electrical machine. The line voltage represents the back-EMF induced by the air-gap flux of the virtual machine. With these assumptions, there is no theoretical difference from the DTC viewpoint whether the controlled system is a line converter or an ac-machine. The concept of the virtual ac-machine is also used in (Malinowski et al., 2001) in conjunction of the line converter.

For the line converter use we redefine the voltage integral (4.25) as

$$\underline{\psi}_1 = \int (\underline{u}_1 + R_1 \underline{i}_1) dt + \underline{\psi}_{1, \text{init}} , \quad (4.27)$$

where $\underline{\psi}_1$ is the converter virtual flux linkage vector, \underline{u}_1 is the converter voltage vector, R_1 is the resistance of the line filter inductor, \underline{i}_1 is the converter current vector and $\underline{\psi}_{1, \text{init}}$ is the initial value of the converter virtual flux linkage vector. The converter virtual flux linkage is a quantity analogous to the motor stator flux linkage, but in the line converter it does not clearly

Assuming that no zero-sequence current flows (i.e. the phase currents add up to zero) the instantaneous power in the network terminals is calculated as

$$p = \frac{3}{2} \operatorname{Re} \{ \underline{u}_2 \dot{i}_1^* \} = \frac{3}{2} (u_{2\alpha} i_{1\alpha} + u_{2\beta} i_{1\beta}) . \quad (4.33)$$

Substituting the line voltage components from (4.31) gives

$$p = \frac{3}{2} \operatorname{Re} \left\{ \frac{d\psi_2}{dt} e^{j\omega_s t} \right\} i_{1\alpha} - \frac{3}{2} \omega_s \psi_{2\beta} i_{1\alpha} + \frac{3}{2} \operatorname{Im} \left\{ \frac{d\psi_2}{dt} e^{j\omega_s t} \right\} i_{1\beta} + \frac{3}{2} \omega_s \psi_{2\alpha} i_{1\beta} . \quad (4.34)$$

Now, if we assume that the modulus of the virtual line flux linkage vector is constant, i.e. $\frac{d\psi_2}{dt} = 0$, the power equation is simplified to

$$p = \frac{3}{2} \omega_s (\psi_{2\alpha} i_{1\beta} - \psi_{2\beta} i_{1\alpha}) = \frac{3}{2} \omega_s \operatorname{Im} \left\{ \underline{\psi}_2^* \dot{i}_1 \right\} . \quad (4.35)$$

Substituting $\underline{\psi}_2$ from (4.32) yields

$$p = \frac{3}{2} \omega_s (\psi_{1\alpha} i_{1\beta} - \psi_{1\beta} i_{1\alpha}) = \frac{3}{2} \omega_s \operatorname{Im} \left\{ \underline{\psi}_1^* \dot{i}_1 \right\} , \quad (4.36)$$

which is controlled by the hysteresis control loop. By comparing (4.36) and (4.26) it is noticed that the expression $\frac{3}{2} \operatorname{Im} \left\{ \underline{\psi}_1^* \dot{i}_1 \right\}$ is analogous to the torque of the electrical motor. This expression is sometimes referred to as the “torque” of the line converter. It is a calculatory quantity which, however, can be understood in the context of the virtual AC machine assumption.

The network angular frequency ω_s in (4.36) is assumed constant, and usually in per unit values $\omega_s = 1$ p.u. This means that the multiplication by ω_s is not necessary and from the control system point of view it is irrelevant whether the controlled quantity is the instantaneous power or the converter torque. Nevertheless, the instantaneous power is still a better and less confusing concept than the converter torque and it should be preferred.

Eq. (4.36) estimates the instantaneous power between the line filter inductors and the grid. This is different from the dc-side power because the line filter inductors store energy into the magnetic field. The instantaneous power calculated in the converter bridge terminals, which, if the lossless bridge is assumed, equals the dc-side power is

$$p = \frac{3}{2} \operatorname{Re} \{ \underline{u}_1 \dot{i}_1^* \} . \quad (4.37)$$

The instantaneous power (4.37) has more ripple compared to (4.33) because the converter voltage \underline{u}_1 is, due to the modulation, discontinuous in nature. The problems which this ripple component may introduce to the control system are avoided by estimating the network power (4.33) instead of the bridge power (4.37).

Noguchi et al. (1998) proposed a direct power control (DPC) in which the network power is estimated as

$$p = L \left(\frac{di_{1a}}{dt} i_{1a} + \frac{di_{1b}}{dt} i_{1b} + \frac{di_{1c}}{dt} i_{1c} \right) + u_{dc} (s w_a i_{1a} + s w_b i_{1b} + s w_c i_{1c}) . \quad (4.38)$$

The first term represents the power of the inductor and the second term the bridge power. This approach, however, requires rather high sampling frequency in order to estimate the power

successfully. In (Noguchi et al., 1998) the sample time of 111 kHz was used with 8 kHz switching frequency. The DPC method resembles the DTC method because both methods use switching table-based modulation and do not require line voltage sensors. Malinowski et al. (2001) proposed a virtual flux-based variant of DPC. In their system the power estimation is based on the virtual line flux linkage vector and the converter current vector, as shown in (4.35). The virtual line flux linkage vector is estimated without line voltage sensors using (4.32). Because the powers in (4.35) and (4.36) are equal when the inductor losses are negligible, the power estimation used by Malinowski et al. (2001) is equal to the power estimation of a DTC based line converter.

The instantaneous reactive power of a line converter with L-filter is calculated as

$$q = \frac{3}{2} \text{Im} \{ \underline{u}_2 \underline{i}_1^* \} = \frac{3}{2} (u_{2\beta} i_{1\alpha} - u_{2\alpha} i_{1\beta}) , \quad (4.39)$$

which, after substituting (4.31) in place of \underline{u}_2 , gives

$$q = \frac{3}{2} \text{Im} \left\{ \frac{d\psi_2}{dt} e^{j\omega_s t} \right\} i_{1\alpha} + \frac{3}{2} \omega_s \psi_{2\alpha} i_{1\alpha} - \frac{3}{2} \text{Re} \left\{ \frac{d\psi_2}{dt} e^{j\omega_s t} \right\} i_{1\beta} + \frac{3}{2} \omega_s \psi_{2\beta} i_{1\beta} . \quad (4.40)$$

Assuming again that $\frac{d\psi_2}{dt} = 0$, we have

$$q = \frac{3}{2} \omega_s (\psi_{2\alpha} i_{1\alpha} + \psi_{2\beta} i_{1\beta}) = \frac{3}{2} \omega_s \text{Re} \left\{ \underline{\psi}_2^* \underline{i}_1 \right\} . \quad (4.41)$$

Substituting (4.32) in place of $\underline{\psi}_2$ yields

$$q = \frac{3}{2} \omega_s \text{Re} \left\{ \left(\underline{\psi}_1 + L_1 \underline{i}_1 \right)^* \underline{i}_1 \right\} = \frac{3}{2} \omega_s (\psi_{1\alpha} i_{1\alpha} + \psi_{1\beta} i_{1\beta} + L_1 (i_{1\alpha}^2 + i_{1\beta}^2)) , \quad (4.42)$$

which can be further expressed as

$$q = \frac{3}{2} \omega_s \text{Re} \left\{ \underline{\psi}_1^* \underline{i}_1 \right\} + \frac{3}{2} \omega_s \text{Re} \left\{ (L_1 \underline{i}_1)^* \underline{i}_1 \right\} . \quad (4.43)$$

The first term may be interpreted as the reactive power calculated at the converter bridge terminals and the last as the reactive power of the line filter inductor. The sum of these reactive powers is the reactive power of the line converter at the grid terminals. By solving \underline{i}_1 from (4.32) and substituting in (4.41) and simplifying gives

$$q = -\frac{3\omega_s}{2L_1} (\psi_{2\alpha} \psi_{1\alpha} + \psi_{2\beta} \psi_{1\beta} - \psi_{2\alpha}^2 - \psi_{2\beta}^2) , \quad (4.44)$$

which further may be expressed using the dot product as

$$q = -\frac{3\omega_s}{2L_1} \left(\underline{\psi}_1 \cdot \underline{\psi}_2 - \underline{\psi}_2 \cdot \underline{\psi}_2 \right) \quad (4.45)$$

$$= -\frac{3\omega_s}{2L_1} (\psi_1 \psi_2 \cos(\chi) - \psi_2^2) , \quad (4.46)$$

where χ is the angle between the virtual line and converter flux linkages. In Fig. 4.9 χ is shown using fundamental wave quantities. From this form we may easily observe that the reactive power of the line converter may be controlled with the converter virtual flux linkage

modulus ψ_1 . This result together with (4.36) justifies the control of the active and reactive powers of a line converter with the DTC method.

With an L-filter the grid reactive power may be estimated using (4.42). With an LCL-filter the reactive power estimation is more complicated if the line voltage is not measured. In Appended Publication I the equations for estimating the reactive power of the line converter with LCL-filter are presented. This subject is investigated in greater detail in (Pöllänen et al., 2003) and in (Pöllänen, 2003).

The instantaneous power of a line converter may be also expressed without the current by solving i_1 from (4.32) and substituting in (4.36), giving

$$p = \frac{3\omega_s}{2L_1} (\psi_{2\beta}\psi_{1\alpha} - \psi_{2\alpha}\psi_{1\beta}) , \quad (4.47)$$

which may be expressed as

$$p = \frac{3\omega_s}{2L_1} \psi_1 \psi_2 \sin(\chi) . \quad (4.48)$$

Equations (4.46) and (4.48) are analogous to equations (4.23) and (4.24) involving the power angle.

4.3 Current control with DTC line converter

4.3.1 Converter virtual flux linkage orientation

If the DTC is applied to line converter control in the way described in the previous section, the converter currents are not actively controlled but indirectly determined according to the power and converter virtual flux linkage amplitude commands. The harmonic content of the line currents is frequently used to measure the line converter's conformity to the standards, see e.g. (EN 50160, 1999; IEEE Std 519–1992, 1993). This rises a need to actively control the line currents to be as sinusoidal as possible. Another reason for implementing a current control is that, if the line converter is desired to act also as an active filter, the current control is almost a necessity.

The current control may be introduced to a DTC line converter as shown in Fig. 4.8. The system implements a vector control, in which the measured current vector is transformed to a synchronously rotating dq-reference frame. The current vector is divided into components as

$$\underline{i}_1^{\text{dq}} = i_{1d} + j i_{1q} . \quad (4.49)$$

The synchronous dq-frame is depicted in a vector diagram shown in Fig. 4.9. The current vector decomposition to the $\alpha\beta$ - and the dq-components is also shown. Different from the conventional line voltage orientation the synchronous reference frame is fixed to the converter virtual flux linkage vector $\underline{\psi}_1$. This is called converter flux orientation (CFO). The co-ordinate transformation from the stationary $\alpha\beta$ -frame to the synchronous dq-frame may be calculated as

$$i_{1d} = \frac{\psi_{1\alpha} i_{1\alpha} + \psi_{1\beta} i_{1\beta}}{\psi_1} \quad (4.50)$$

$$i_{1q} = \frac{\psi_{1\alpha} i_{1\beta} - \psi_{1\beta} i_{1\alpha}}{\psi_1} . \quad (4.51)$$

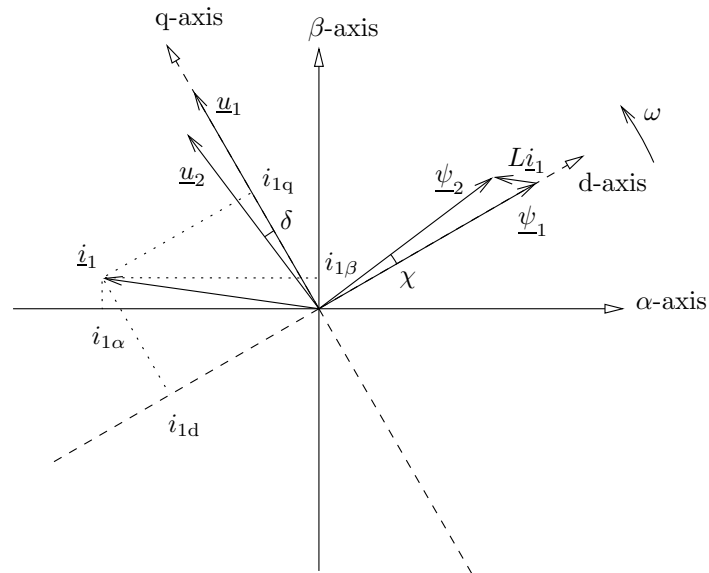


Figure 4.9: Vector diagram of the line converter with L-filter operating as a rectifier with leading power factor. The stationary $\alpha\beta$ - and synchronous dq -reference frames are shown. ω is the angular frequency of the converter virtual flux linkage vector. The diagram is drawn using the fundamental wave quantities and parameters $p = \frac{1}{\sqrt{2}}$ p.u., $q = -\frac{1}{\sqrt{2}}$ p.u., $L_1 = 0.2$ p.u., $u_2 = 1$ p.u., $u_1 = 1.15$ p.u. and $\delta = \chi = 7.06^\circ$.

active power reference p_{ref} and the converter virtual flux linkage modulus reference $\psi_{1,\text{ref}}$ to the DTC. Therefore, the DTC is used as a modulator, which accepts p_{ref} and $\psi_{1,\text{ref}}$ command signals. The PI control algorithm is a natural choice for the current controllers because it is rather simple and it has proved to perform satisfactorily in vector control applications. The equations of the PI current controllers are

$$\psi_{1,\text{ref}} = -k_{p,d}(i_{1d,\text{ref}} - i_{1d}) - k_{i,d} \int (i_{1d,\text{ref}} - i_{1d}) dt + \psi_{1,n} \quad (4.56)$$

$$p_{\text{ref}} = k_{p,q}(i_{1q,\text{ref}} - i_{1q}) + k_{i,q} \int (i_{1q,\text{ref}} - i_{1q}) dt, \quad (4.57)$$

where $k_{p,d}$, $k_{i,d}$, $k_{p,q}$ and $k_{i,q}$ are the controller parameters and $\psi_{1,n}$ is the nominal value of the converter virtual flux linkage modulus. Typically $\psi_{1,n} = 1$ p.u. The sign of the d-axis controller output is inverted, because the d-axis current is increased by decreasing the converter virtual flux linkage modulus.

Pöllänen (2003) considered tuning of the current controllers of the CFO based line converter by using the internal model control (IMC) approach. In order to be able to use the IMC, Pöllänen (2003) uses a current control structure which is different from the system depicted in Fig. 4.8. Pöllänen (2003) introduces additional digitally implemented compensators between the current controller outputs and the DTC hysteresis control input signals p_{ref} and $\psi_{1,\text{ref}}$. The purpose of these compensators is to make the output of the current controllers to equal the converter voltage vector reference. In effect, the DTC-based hysteresis control is made to appear as a voltage vector reference controlled modulator to the current control system. The tuning of the dc-link voltage controller is also considered in (Pöllänen, 2003). A dc-link control structure, which is based on the estimation and feedforward of the dc-link load current is considered in (Pöllänen et al., 2002) and (Pöllänen, 2003).

4.3.2 Modeling the DTC current control

Let us write the equation of the L-line filter (4.21) in component form in the CFO co-ordinates neglecting the resistances

$$L_1 \frac{di_{1d}}{dt} = u_{2d} - u_{1d} + \omega L_1 i_{1q} \quad (4.58)$$

$$L_1 \frac{di_{1q}}{dt} = u_{2q} - u_{1q} - \omega L_1 i_{1d}, \quad (4.59)$$

where ω is the instantaneous angular frequency of the converter virtual flux linkage vector $\underline{\psi}_1$. Unlike the grid angular frequency ω_s , it is not a constant. Pöllänen (2003) defined the instantaneous angular frequency of the converter virtual flux linkage vector as

$$\omega = \omega_s + \Delta\omega, \quad (4.60)$$

where $\Delta\omega$ is the slip angular frequency of the converter virtual flux linkage vector. The slip angular frequency has a nonzero value if the angle χ between the line and the converter virtual flux linkage vectors is changed.

The line voltage vector \underline{u}_2 in Eq. (4.29) may be expressed in the CFO frame with the assumption $\frac{d\psi_2}{dt} = 0$ as

$$\underline{u}_2^{\text{dq}} = j\omega_s \underline{\psi}_2^{\text{dq}}. \quad (4.61)$$

Further, Eq. (4.32) holds in the CFO frame, that is

$$\underline{\psi}_2^{\text{dq}} = \underline{\psi}_1^{\text{dq}} + L_1 \dot{i}_1^{\text{dq}} . \quad (4.62)$$

Substituting (4.62) in (4.61) and expressing in component form, the grid voltage components in the CFO frame are given as

$$u_{2d} = -\omega_s \psi_{2q} = -\omega_s L_1 i_{1q} \quad (4.63)$$

$$u_{2q} = \omega_s \psi_{2d} = \omega_s \psi_1 + \omega_s L_1 i_{1d} . \quad (4.64)$$

Substituting (4.60), (4.63) and (4.64) in (4.58) and (4.59) the model of an L-filter in the CFO frame is written as

$$L_1 \frac{di_{1d}}{dt} = -u_{1d} + \Delta\omega L_1 i_{1q} \quad (4.65)$$

$$L_1 \frac{di_{1q}}{dt} = -u_{1q} + \omega_s \psi_1 - \Delta\omega L_1 i_{1d} . \quad (4.66)$$

A peculiarity of the CFO frame is that it does not rotate with a constant angular frequency but in every transient where the rotation of the converter virtual flux linkage is accelerated or decelerated the CFO frame accelerates or decelerates as well. This property has a profound impact on the vector control system operating in the CFO frame. This, as pointed out by Pöllänen (2003), may be observed by comparing the L-filter model expressed in the CFO co-ordinates and the L-filter model expressed in the virtual line flux linkage oriented (LFO) co-ordinates. The LFO co-ordinate system is similar to the CFO co-ordinate system but with the exception that the d-axis of the LFO co-ordinates is fixed to the virtual line flux linkage vector instead of the virtual converter flux linkage vector. In the LFO co-ordinate system the components of the line voltage vector are expressed as $u_{2d} = 0$ and $u_{2q} = \omega_s \psi_2$, again assuming that $\frac{d\psi_2}{dt} = 0$. The L-filter model in the LFO co-ordinates is obtained from Eqs. (4.58) and (4.59) by replacing ω with the line angular frequency ω_s , and substituting $u_{2d} = 0$ and $u_{2q} = \omega_s \psi_2$, as

$$L_1 \frac{di_{1d}}{dt} = -u_{1d} + \omega_s L_1 i_{1q} \quad (4.67)$$

$$L_1 \frac{di_{1q}}{dt} = \omega_s \psi_2 - u_{1q} - \omega_s L_1 i_{1d} . \quad (4.68)$$

A comparison between (4.65), (4.66) and (4.67), (4.68) reveals that the cross-coupling terms in the CFO frame are multiplied with $\Delta\omega$ but in the LFO frame with ω_s . Also, $\omega_s \psi_1$ in the CFO frame is replaced with $\omega_s \psi_2$ in the LFO frame. The slip angular frequency, and hence also the cross-coupling in the CFO frame, is zero in steady state. In transients, there exist a cross-coupling in the CFO frame, but, according to (Pöllänen, 2003), it is significantly lower than in the LFO co-ordinates. Pöllänen (2003) further compared the CFO current control to the LFO current control and concluded that in the CFO frame the cross-coupling between the d- and the q-axes is so small that decoupling in the control system is not necessary.

A conventional way to study the control system of a PWM modulated line converter is to assume ideal modulation. In other words, the PWM modulator is assumed to perfectly fulfill its voltage reference, and therefore the modulator has a unity transfer function. This also means that a continuous model is obtained because the switching action of the converter is not modeled. Typically, the reference of the PWM modulator is a voltage vector. In DTC, however,

the references to the voltage vector selection algorithm are the instantaneous power reference p_{ref} and the reference of the converter virtual flux linkage modulus $\psi_{1,\text{ref}}$. The ideal modulation, in the case of the DTC, means that the converter instantaneously fulfills these references. Let us, at first, consider the converter active power in the CFO co-ordinates. By using per unit quantities the scaling constant $\frac{3}{2}$ may be omitted and the converter instantaneous power is given as

$$p = \omega_s(\psi_{1d}i_{1q} + \psi_{1q}i_{1d}) . \quad (4.69)$$

Using (4.53) and (4.54) this is written as

$$p = \omega_s\psi_1 i_{1q} . \quad (4.70)$$

Differentiating with respect to the time t yields

$$\frac{dp}{dt} = \omega_s \frac{d\psi_1}{dt} i_{1q} + \omega_s \psi_1 \frac{di_{1q}}{dt} , \quad (4.71)$$

and solving $\frac{di_{1q}}{dt}$ gives

$$\frac{di_{1q}}{dt} = \frac{1}{\omega_s\psi_1} \frac{dp}{dt} - \frac{1}{\psi_1} \frac{d\psi_1}{dt} i_{1q} . \quad (4.72)$$

Substituting (4.72) into the q-axis model of the L-filter in the CFO co-ordinates (4.66) and solving for u_{1q} yields

$$u_{1q} = \frac{\frac{d\psi_1}{dt} i_{1q} L_1}{\psi_1} - \frac{L_1}{\omega_s\psi_1} \frac{dp}{dt} + \omega_s\psi_1 - \Delta\omega L_1 i_{1d} . \quad (4.73)$$

This represents the q-axis voltage that has to be applied to the L-filter in order to produce the active power p . In CFO co-ordinates the voltage integral (4.27), with resistance neglected, is written as

$$\psi_1^{\text{dq}} = \psi_1 = \int u_{1d} dt , \quad (4.74)$$

from which the d-axis voltage required to produce the virtual converter flux linkage modulus ψ_1 is solved as

$$u_{1d} = \frac{d\psi_1}{dt} . \quad (4.75)$$

Now, substituting voltages (4.73) and (4.75) into the equations of the L-filter (4.65) and (4.66), and assuming an ideal modulation $p = p_{\text{ref}}$ and $\psi_1 = \psi_{1,\text{ref}}$ the continuous model of an L-filter process with DTC modulation is written as

$$\frac{di_{1d}}{dt} = -\frac{1}{L_1} \frac{d\psi_{1,\text{ref}}}{dt} + \Delta\omega i_{1q} \quad (4.76)$$

$$\frac{di_{1q}}{dt} = -\frac{i_{1q}}{\psi_{1,\text{ref}}} \frac{d\psi_{1,\text{ref}}}{dt} + \frac{1}{\omega_s\psi_{1,\text{ref}}} \frac{dp_{\text{ref}}}{dt} . \quad (4.77)$$

The following remarks are made

1. The derivatives of the controller output signals p_{ref} and $\psi_{1,\text{ref}}$ are the input signals to the model.
2. In the q-axis no cross-coupling term $-\Delta\omega i_{1d}$ is present because it is inherently compensated by the active power hysteresis control loop.

3. No rotational voltage $\omega_s \psi_1$ is present in the q-axis because it is too inherently compensated by the active power hysteresis control loop.
4. The d- and the q-axis have different dynamics.

Equation (4.76) may be developed further. The angular frequency of the virtual converter flux linkage vector ω may be written as

$$\omega = \frac{u_{1q}}{\psi_1} . \quad (4.78)$$

Solving u_{1q} from process equation (4.66) yields

$$u_{1q} = -L_1 \frac{di_{1q}}{dt} + \omega_s \psi_1 - \Delta\omega L_1 i_{1d} , \quad (4.79)$$

and substitution to (4.78) gives

$$\omega = -\frac{L_1}{\psi_1} \frac{di_{1q}}{dt} + \omega_s - \frac{\Delta\omega L_1 i_{1d}}{\psi_1} . \quad (4.80)$$

Now, from (4.60) we have $\Delta\omega = \omega - \omega_s$. Substituting (4.80) and solving for $\Delta\omega$, we obtain as a result

$$\Delta\omega = -\frac{L_1 \frac{di_{1q}}{dt}}{\psi_1 + L_1 i_{1d}} . \quad (4.81)$$

Using (4.81) to express $\Delta\omega$ in (4.76) we have

$$\frac{di_{1d}}{dt} = -\frac{1}{L_1} \frac{d\psi_{1,\text{ref}}}{dt} - \frac{L_1 i_{1q}}{\psi_{1,\text{ref}} + L_1 i_{1d}} \frac{di_{1q}}{dt} \quad (4.82)$$

$$\frac{di_{1q}}{dt} = -\frac{i_{1q}}{\psi_{1,\text{ref}}} \frac{d\psi_{1,\text{ref}}}{dt} + \frac{1}{\omega_s \psi_{1,\text{ref}}} \frac{dp_{\text{ref}}}{dt} . \quad (4.83)$$

Eqs. (4.82) and (4.83) are alternative expressions of the continuous-time L-filter process with DTC control. If Eqs. (4.82) and (4.83) are simulated, the derivatives of the input signals p_{ref} and $\psi_{1,\text{ref}}$ may be approximated using a transfer function

$$G_D(s) = \frac{s}{sT_D + 1} , \quad (4.84)$$

where T_D is sufficiently smaller than unity, e.g., $T_D = 0.1 \dots 0.01$. The continuous-time model is, however, nonlinear, because the input signal $\psi_{1,\text{ref}}$ and the state variable i_{1d} are involved in the inverse function. We may further simplify the model (4.82) and (4.83) if we are not particularly interested in the cross-coupling effects but focus on solving how the input signals affect the control quantities, i.e. p_{ref} to i_{1q} and $\psi_{1,\text{ref}}$ to i_{1d} . Considering (4.82) we may state that the significance of the term $-\frac{L_1 i_{1q}}{\psi_{1,\text{ref}} + L_1 i_{1d}} \frac{di_{1q}}{dt}$ is notably smaller compared to the term $-\frac{1}{L_1} \frac{d\psi_{1,\text{ref}}}{dt}$, because it is a cross-coupling term and the typical value for L_1 is about 0.1 p.u. and for $\psi_{1,\text{ref}}$ about 1 p.u. Hence, the model may be simplified by leaving the former term out. Considering (4.83), we may leave the cross-coupling term $-\frac{i_{1q}}{\psi_{1,\text{ref}}} \frac{d\psi_{1,\text{ref}}}{dt}$ out if we consider only how the q-axis current reacts on the q-axis input quantity p_{ref} . Thus, simplified model is written as

$$\frac{di_{1d}}{dt} = -\frac{1}{L_1} \frac{d\psi_{1,\text{ref}}}{dt} + D_d \quad (4.85)$$

$$\frac{di_{1q}}{dt} = \frac{1}{\omega_s \psi_{1,\text{ref}}} \frac{dp_{\text{ref}}}{dt} + D_q , \quad (4.86)$$

where the left-out terms are substituted with the disturbance terms D_d and D_q . Further, we may regard $\psi_{1,\text{ref}}$ as a constant $\psi_{1,\text{ref}0}$ in (4.86) if it is assumed that no d-axis transient is occurring at the same time with a q-axis transient. Laplace transforming (4.85) and (4.86) gives

$$si_{1d}(s) = -\frac{1}{L}s\psi_{1,\text{ref}}(s) + D_d(s) \quad (4.87)$$

$$si_{1q}(s) = \frac{sp_{\text{ref}}(s)}{\omega_s\psi_{1,\text{ref}0}} + D_q(s) . \quad (4.88)$$

Further, Laplace transforming the controller equations (4.56) and (4.57) and considering the transfer characteristics from the reference to the output give

$$\psi_{1,\text{ref}}(s) = -\left(k_{p,d} + \frac{k_{i,d}}{s}\right)(i_{1d,\text{ref}}(s) - i_{1d}(s)) \quad (4.89)$$

$$p_{\text{ref}}(s) = \left(k_{p,q} + \frac{k_{i,q}}{s}\right)(i_{1q,\text{ref}}(s) - i_{1q}(s)) , \quad (4.90)$$

The nominal converter flux linkage modulus $\psi_{1,n}$ in (4.56) is considered as another input signal and disregarded in the analysis from $i_{1d,\text{ref}}$ to i_{1d} . Substituting the controller equations to (4.87) and (4.88) and evaluating the transfer functions we have

$$\frac{i_{1d}(s)}{i_{1d,\text{ref}}(s)} = \frac{sk_{p,d} + k_{i,d}}{s(L_1 + k_{p,d}) + k_{i,d}} \quad (4.91)$$

$$\frac{i_{1q}(s)}{i_{1q,\text{ref}}(s)} = \frac{sk_{p,q} + k_{i,q}}{s(\omega_s\psi_{1,\text{ref}0} + k_{p,q}) + k_{i,q}} . \quad (4.92)$$

Notice that the transfer functions are different but of the same form. Evaluating the roots of the numerator and denominator polynomials the zeros z and poles p are found for the d-axis as

$$z_d = -\frac{k_{i,d}}{k_{p,d}} \quad (4.93)$$

$$p_d = -\frac{k_{i,d}}{L_1 + k_{p,d}} \quad (4.94)$$

and for the q-axis as

$$z_q = -\frac{k_{i,q}}{k_{p,q}} \quad (4.95)$$

$$p_q = -\frac{k_{i,q}}{\omega_s\psi_{1,\text{ref}0} + k_{p,q}} . \quad (4.96)$$

Because always $L_1 > 0$ and $\omega_s\psi_{1,\text{ref}0} > 0$, in both axes the pole is closer to the origin than the zero. Hence, the transfer functions are recognized to have the dynamics of phase-lag compensators. It is desirable to select the controller parameters to give similar current control dynamics in both axes. To achieve this, we have to select the controller parameters that place the zeros and the poles similarly in both axes. In other words, we should have $z_d = z_q$ and $p_d = p_q$. Equating and solving yield the results

$$k_{p,d} = \frac{L_1}{\omega_s\psi_{1,\text{ref}0}}k_{p,q} \quad (4.97)$$

$$k_{i,d} = \frac{L_1}{\omega_s\psi_{1,\text{ref}0}}k_{i,q} . \quad (4.98)$$

Accordingly, having $\omega_s = 1$ p.u. and $\psi_{1,\text{ref}0} = 1$ p.u. and $L_1 = 0.13$ p.u., the controller gain parameters in the d-axis should be chosen to be 0.13 times the controller parameters of the q-axis in order to have similar dynamic performance. Figs. 4.10 and 4.11 show the step responses of both axes with controller parameters chosen to satisfy this condition. The step responses are obtained using the transfer functions (4.91) and (4.92) and a switching model of a current controlled DTC line converter. Also results measured with the practical converter are provided. In the switching model the dc-link voltage is kept constant at $u_{\text{dc}} = 2$ p.u. In the experimental setup another line converter was used to regulate the dc-link voltage to have the same value. In active power steps the other line converter can not maintain a constant dc-link voltage. This affects predominantly only the generating side step in Fig. 4.11(b), in which a decreasing of about 35 V in the dc-link voltage reduces the slope of the current change. The effect is, however, quite small. In the motor side step the dc-link voltage does not have such an effect because zero vectors are used and the slope of the current is not determined by the dc-link voltage. The oscillation in the q-axis current in Fig. 4.10(d) reveals that in the practical converter case the voltage reserve is smaller than in the corresponding simulated case. Ohmic losses in the power switches and in the line filter may contribute to this difference. Overall, the results presented show that the behavior of the DTC current controlled line converter is well represented by the proposed transfer functions. However, the controller parameters used are not selected to provide the desirable or optimal performance but merely to clearly show the phase-lag type characteristics of the control system.

Practical issues

In practical dynamic transients the converter saturation has a significant role. Typically, the dc-link voltage is regulated near the limit of the linear modulation range, $u_{\text{dc}} = \sqrt{3}$ p.u., because the dc-link capacitors and other components are not dimensioned to withstand voltage levels significantly higher than that. The equations of the L-filter in the CFO frame (4.58) and (4.59) may be written as

$$L_1 \frac{di_{1d}}{dt} = \underbrace{u_2 \sin \delta}_{\approx 0} - u_{1d} + \omega L_1 i_{1q} \quad (4.99)$$

$$L_1 \frac{di_{1q}}{dt} = \underbrace{u_2 \cos \delta}_{\approx u_2} - u_{1q} - \omega L_1 i_{1d} . \quad (4.100)$$

The approximations are based on the assumption of the power angle δ being relatively small. The equations show that the negative q-axis current dynamics are most sensitive to the dc-link voltage. That is because the converter has to produce a voltage that annuls the effect of the line voltage and generates a negative voltage across the inductor. In the d-axis the line voltage component is small and no significant amount of available converter voltage is needed to cancel its effect. In the d-axis, however, the location of the virtual flux linkage vector in a sector has an effect on the current control dynamics. As discussed in (Tarkiainen et al., 2003a), the orientation of the two active voltage vectors used in a sector decreases the performance of the negative d-axis current dynamics at the beginning of a sector. Correspondingly, at the end of a sector the positive d-axis dynamic performance is degraded.

The converter saturation occurs if the current controllers generate output signals that the converter can not realize. This causes an integrator windup in the PI-controllers. The integrator windup is a well-known phenomenon, which occurs when the output of the actuator saturates.

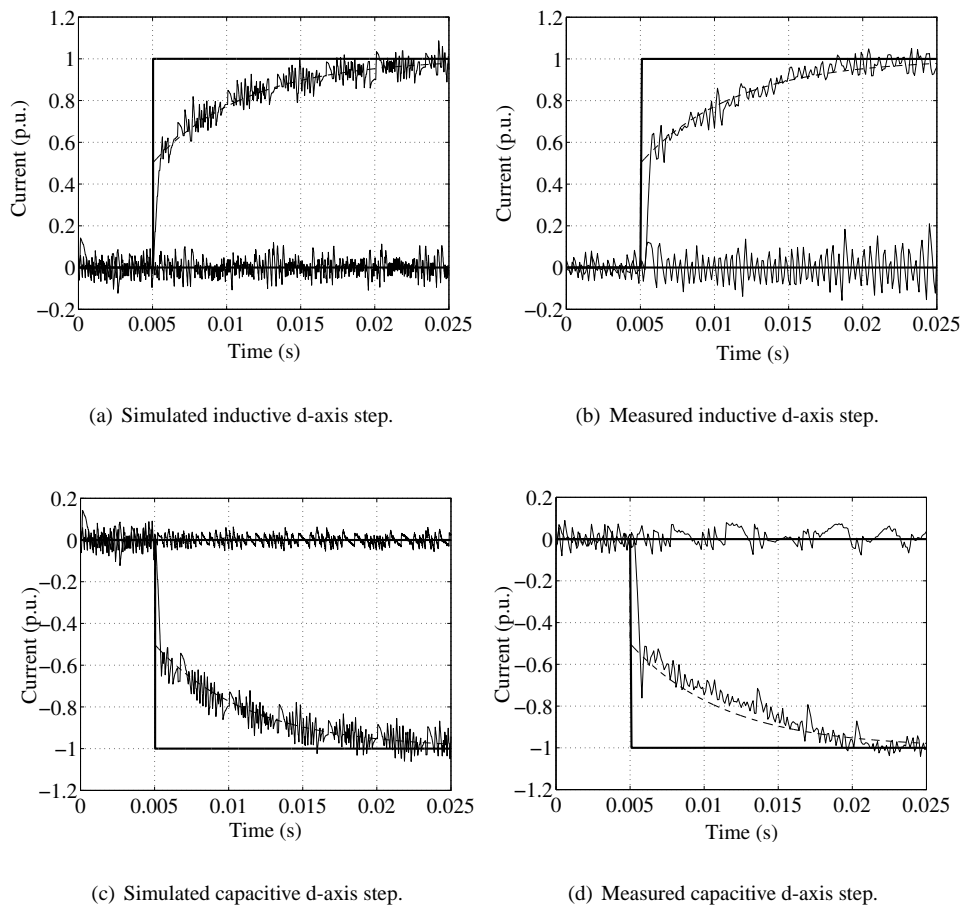
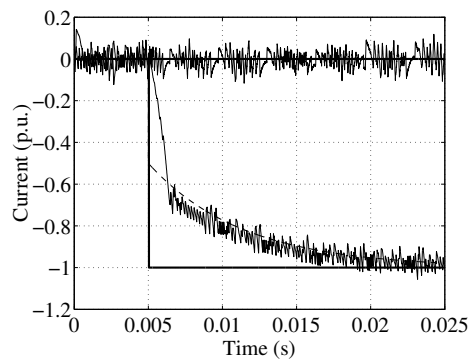
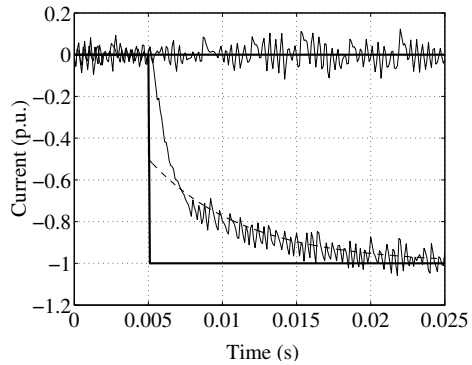


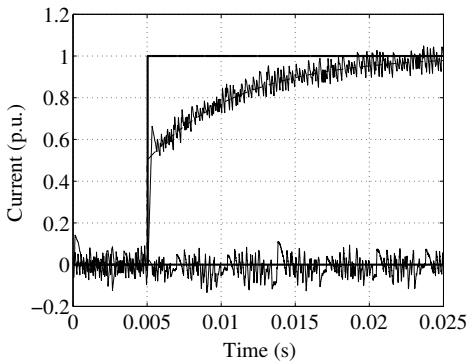
Figure 4.10: Current reference steps of 1 p.u., simulated with a switching line converter model (left) and measured (right). The dashed line shows the response of the transfer function (4.91). The line filter inductance is $L_1 = 0.13$ p.u. and the dc-link voltage was regulated to 2 p.u. Controller parameters $k_{p,d} = 0.13 (= L_1)$ and $k_{i,d} = 0.13 (= L_1)$ were used. In the simulated case the data were sampled with $5 \mu\text{s}$ sample time and in the measured case with $100 \mu\text{s}$ sample time.



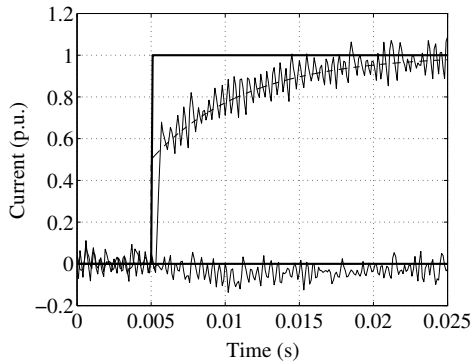
(a) Simulated generating side q-axis step.



(b) Measured generating side q-axis step.



(c) Simulated motoring side q-axis step.



(d) Measured motoring side q-axis step.

Figure 4.11: Current reference steps of 1 p.u., simulated with a switching line converter model (left) and measured (right). The dashed line shows the response of the transfer function (4.92). The line filter inductance is $L_1 = 0.13$ p.u. and the dc-link voltage was regulated to 2 p.u. Controller parameters $k_{p,q} = 1$ and $k_{i,q} = 1$ were used. In the simulated case the data were sampled with $5 \mu\text{s}$ sample time and in the measured case with $100 \mu\text{s}$ sample time.

In the controller the error is still integrated even though it has no effect on the error. As a consequence, the integral may become very large, which is called “winding up”. This may result in degraded control performance and great overshoots. Integrator windup issues are considered and anti-windup methods are presented in (Åström and Hägglund, 1995) and (Hodel and Hall, 2001). In converters with explicit voltage vector reference the saturation condition can be detected by comparing the voltage reference and the maximum voltage that can be synthesized with the current dc-link voltage. Some methods are presented in (Ottersten and Svensson, 2002). In (Pöllänen, 2003) a space-vector limitation method is implemented in a converter virtual flux linkage oriented current control system. In DTC based control where no voltage reference exists, this method is not straightforwardly applicable. It is, however, possible to calculate the implicit voltage command using (4.73) and (4.75), but this would not be very practical because several derivatives would have to be evaluated. A more practical anti-windup method is the conditional integration.

The saturation of the DTC converter can be detected by observing the error signals of the hysteresis controls. If the flux linkage modulus error $|e_{\psi_1}|$ is greater than the limiting value $e_{\psi_1, \text{limit}}$, i.e. $|e_{\psi_1}| > e_{\psi_1, \text{limit}}$ the integration in the d-axis current controller is stopped. Similarly for the power hysteresis control loop, if $|e_p| > e_{p, \text{limit}}$ the integration in the q-axis is stopped. In the practical implementation the limit values were chosen as $e_{\psi_1, \text{limit}} = 0.1L_1 = 0.013$ p.u. and $e_{p, \text{limit}} = 0.1$ p.u. The limit was chosen to be 10% of the control quantity’s variation range corresponding to nominal current step. The conditional integration method may be improved by considering the direction to which the input signal drives the controller output. The integration may be stopped only if the input signal is driving the controller into the direction of increasing saturation and the integration is allowed if the controller is coming out of the saturation even though the actuator is still saturated (Hodel and Hall, 2001; Åström and Hägglund, 1995). This improvement, however, was not implemented in the practical converter.

In the practical control system the converter current components i_{1d} and i_{1q} were low-pass filtered before the PI-regulation. This reduces the chattering of the power reference and the flux linkage modulus reference in the hysteresis control, which, in turn, would induce unnecessary current ripple, thus resulting in disturbances circulating in the control system. The low-pass filters are shown in Fig. 3 in Appended Publication I. The purpose of the low-pass filters is to provide attenuation to switching ripple current components, which primarily reside in frequencies greater than 2 kHz. On the other hand, in the time domain the filter output should be able to swiftly track the current changes associated with dynamic transients. As a practical compromise, a cascade of two first-order infinite impulse response filters were used. The resulting second-order low pass filter has a transfer function

$$H(z^{-1}) = \left(\frac{0.4}{1 - 0.6z^{-1}} \right)^2 = \frac{0.16}{1 - 1.2z^{-1} + 0.36z^{-2}} . \quad (4.101)$$

The filter is computationally rather simple but provides about 20 dB attenuation in the desired frequency range, as shown in Fig. 4.12. In the time domain the settling time is about 1 ms, which is considered reasonable as the fastest current transients have about the same rise time.

Fig. 4.13 shows the current reference step responses with the integrator anti-windups and the current feedback low-pass filtering. The controller parameters were selected to provide the same dynamical properties to both axes. However, the controllers’ parameters were hand-tuned to provide good response in the best case, which is the motoring side q-axis step. In the generating side q-axis step the converter saturates. In the saturation the control system

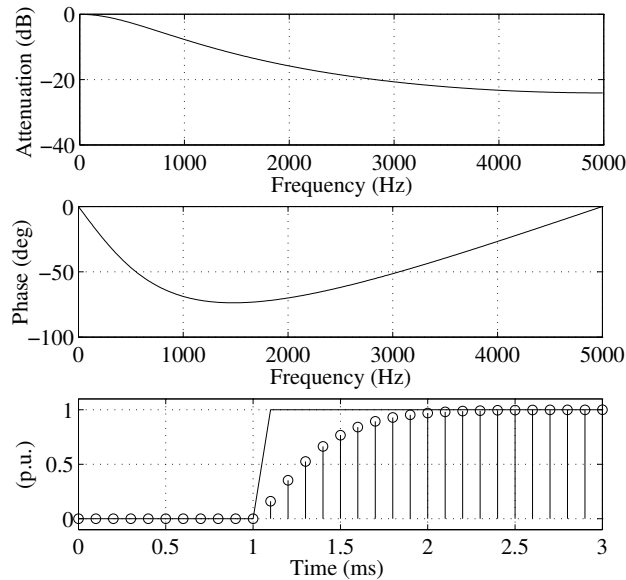
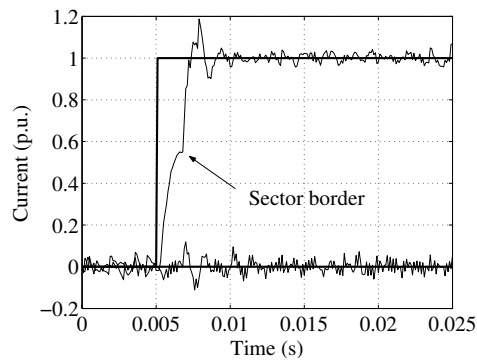


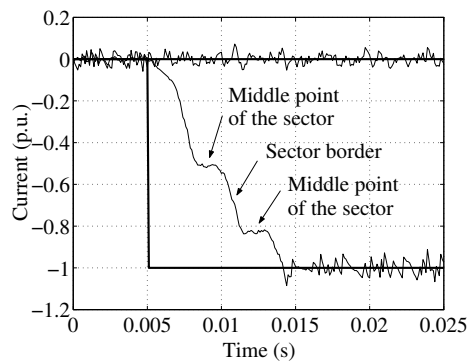
Figure 4.12: Amplitude response (top), phase response (middle) and step response (bottom) of the low pass filter used to attenuate the switching ripple in the synchronous frame current feedback signals.

operates effectively as an open-loop system and the converter is using all available control force to reduce the error. After the reference is reached, the converter leaves the saturation and the closed-loop operation continues. The anti-windup prevents the overshoot from occurring. In the current in Fig. 4.13(b) the effect of the sectors is clearly visible. In the middle point of the sector the q-axis current can not be increased because the dc-link voltage is collapsed so that neither of the voltage vectors can produce negative voltage over the inductor. Near the sector borders one of the voltage vectors can produce negative voltage. In the d-axis saturation also occurs, but it is not as severe as in the generating side q-axis step. Also, in the d-axis current the effect of the sector border can be observed. The capacitive d-axis step was not measured because the used dc-link voltage does not allow operation with nominal capacitive current.

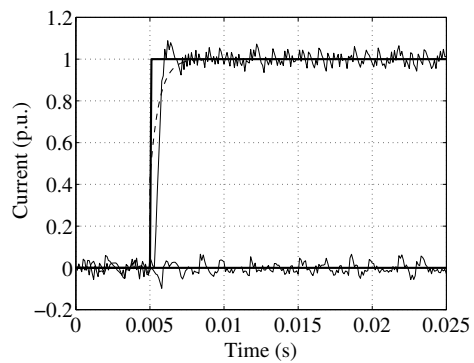
It is concluded that the overall performance of the current control may be improved by allowing the converter to saturate in transients. However, this brings nonlinearity to the control system rendering the straightforward use of linear models impossible. If, e.g., in the case illustrated in Fig. 4.13, linear design methods would be used, the current response time should be chosen according to the worst case performance—about 10 ms. Allowing the converter to saturate, the q-axis response time of 1 ms was achieved in the motoring side. The design, however, involves hand-tuning with the practical converter or with the switching model, which is regarded as a drawback. Anyhow, in the author's opinion, the final result is more important than the method of obtaining it.



(a) Measured inductive d-axis step.



(b) Measured generating side q-axis step.



(c) Measured motoring side q-axis step. Dashed line shows the response of transfer function (4.92).

Figure 4.13: Measured current step responses. The line filter inductance was $L_1 = 0.13$ p.u. and the dc-link voltage was regulated to $u_{dc} = 1.84$ p.u. by other line converter. The controller parameters in the d-axis were $k_{p,d} = 0.75L_1$ and $k_{i,d} = 9L_1$ and in the q-axis $k_{p,q} = 0.75$ and $k_{i,q} = 9$. An anti-windup is implemented in the current controllers.

4.4 Overmodulation characteristics of a DTC converter

4.4.1 Carrier-based and space-vector modulation

The most common methods of pulse width modulation are carrier-based. In ac-applications the PWM is typically used to produce a sinusoidal output voltage with controllable frequency and magnitude. The classical sine-triangle comparison is a carrier-based method, see e.g. (Mohan et al., 1995), where the triangular carrier signal is compared with a sinusoidal control signal. The duty cycles (i.e. the on/off ratios) of the switches are determined according to the intersection times of the carrier and the control signals. The output voltage is not a perfect sine but it contains harmonic components. The fundamental wave, however, ideally has the same amplitude and the same magnitude than the control signal, if the amplitude of the control signal is not higher than the amplitude of the carrier signal. The control signal is, therefore, a reference to the modulation. The frequency of the carrier signal is the switching frequency of the converter bridge. In the three-phase case there are three individual control signals, which are compared with a single carrier.

The maximum achievable fundamental wave magnitude of the output voltage is a rather important figure of merit of a PWM method. The six-step operation represents the absolute maximum fundamental wave output voltage. In this case, the amplitude of the converter fundamental phase voltage is (Holtz, 1994)

$$u_{1, \text{six step, fund}} = \frac{2}{\pi} u_{\text{dc}} . \quad (4.102)$$

This constitutes a good point of reference to the PWM methods. Holtz (1994) defines a modulation index as

$$m = \frac{u_{1, \text{fund}}}{\frac{2}{\pi} u_{\text{dc}}} , \quad (4.103)$$

where $u_{1, \text{fund}}$ is the fundamental phase amplitude of the pulse width modulated switching sequence. Another modulation index based on the amplitude modulation ratio may be defined as

$$m_a = \frac{u_{1, \text{fund}}}{u_{\text{dc}}/2} . \quad (4.104)$$

This definition is based on the maximum output fundamental phase voltage of the classical sine-triangle comparison. With sinusoidal control signals the maximum fundamental phase voltage amplitude is $u_{1, \text{fund}} = \frac{u_{\text{dc}}}{2}$, which is achieved when the ratio of the control signal amplitude and the triangular carrier wave amplitude equals unity. This ratio is called the amplitude modulation ratio (Mohan et al., 1995). In this thesis, Holtz's modulation index is preferred. In a three-phase case, the output fundamental voltage can be increased by adding zero-sequence components into the modulation reference signals. The zero-sequence component cancels out in the line-to-line voltages and do not show up in the phase currents in a three-wire case. The maximum modulation index that can be achieved with the zero-sequence adding technique is $m = \sqrt{3}\pi/6$ (Holtz, 1994). Output fundamental voltages higher than that may be obtained with overmodulation. In the carrier-based PWM, overmodulation is achieved with a control signal which has its amplitude higher than the amplitude of the carrier signal. Overmodulation techniques of the carrier-based PWM methods are analyzed and compared in (Hava et al., 1998).

Space-vector pulse width modulation (SVPWM) method is based on the space-vector representation of the converter voltage. The modulation algorithm approximates the reference space-vector $\underline{u}_{1, \text{ref}}$ in a time averaged sense with three switching states as

$$\underline{u}_{1, \text{ref}} T_0 = \underline{u}_a t_a + \underline{u}_b t_b + u_0 t_0, \quad (4.105)$$

where \underline{u}_a and \underline{u}_b are active voltage vector adjacent to the reference space-vector and u_0 is a zero vector. t_a , t_b and t_0 are on-durations of the switching vectors and T_0 is the subcycle interval

$$T_0 = t_a + t_b + t_0. \quad (4.106)$$

The switching frequency may be given as

$$f_s = \frac{1}{2T_0}. \quad (4.107)$$

In a linear modulation range, that is $m \leq \frac{\sqrt{3}\pi}{6}$, the on-durations are calculated as (Holtz et al., 1993)¹

$$t_a = \frac{\sqrt{3}}{u_{\text{dc}}} u_{\text{ref}} T_0 \sin\left(\frac{\pi}{3} - \alpha\right) \quad (4.108)$$

$$t_b = \frac{\sqrt{3}}{u_{\text{dc}}} u_{\text{ref}} T_0 \sin(\alpha) \quad (4.109)$$

$$t_0 = T_0 - t_a - t_b. \quad (4.110)$$

The angle α is the angle of the reference space-vector, shown in Fig. 4.14. To reach a modulation index higher than $\frac{\sqrt{3}\pi}{6}$ with space-vector modulation, overmodulation methods must be utilized. Holtz et al. (1993) define two operation regions, overmodulation mode 1 and overmodulation mode 2, between the linear modulation range and the six-step mode. These ranges are shown in Fig. 4.14. In the overmodulation mode 1 the reference space-vector locus is partly inside and partly outside the voltage hexagon. In the portions outside the hexagon the on-durations are calculated as (Holtz et al., 1993)

$$t_a = \frac{T_0}{3} \frac{\sqrt{3} \cos \alpha - \sin \alpha}{\sqrt{3} \cos \alpha + \sin \alpha} \quad (4.111)$$

$$t_b = \frac{T_0}{3} - t_a \quad (4.112)$$

$$t_0 = 0. \quad (4.113)$$

In the portions inside the voltage hexagon Eqs. (4.108)–(4.110) are used. As an output, the modulation produces a space-vector that, in the time averaged sense, tracks the sides of the hexagon when the reference locus is outside the hexagon. When the reference locus is inside the hexagon the output space-vector tracks the circular reference locus. As a result, an output space-vector, which has a constant angular frequency but varying modulus, is produced. At the end of overmodulation mode 1 the reference locus is entirely outside the hexagon and the circular portions of the output space-vector locus has degenerated to zero length, resulting in completely hexagonal output space-vector trajectory. In overmodulation mode 2 the constant angular frequency of the output voltage vector is no more retained. Holtz et al. (1993)

¹Note that Holtz et al. (1993) give equations using a normalized dc-link voltage $u_{\text{dc}} = \pi/2$.

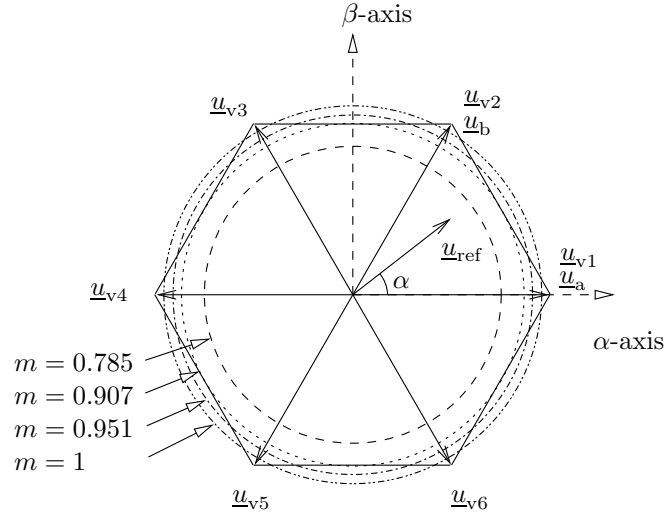


Figure 4.14: Voltage hexagon and sectors used in space-vector modulation. Circles are denoting maximum fundamental waves. Region: $0 < m \leq 0.785$: Carrier based modulation with sinusoidal references. Region $0 < m \leq 0.907$: Linear modulation range. Region $0.907 < m \leq 0.951$: Overmodulation range 1. Region $0.951 \leq m < 1$: Overmodulation range 2. Operation point $m = 1$: Six-step mode.

presented a method for space-vector modulation that covers the overmodulation mode 2 and converges smoothly to the six-step operation.

Bolognani and Zigliotto (1999) derived an analytical form for the amplitude of the fundamental component in overmodulation mode 1. The maximum value is given as

$$u_{1, \text{fund}} = \frac{\sqrt{3} \ln 3}{\pi} u_{dc} , \quad (4.114)$$

and, hence, the maximum modulation index in the overmodulation mode 1 becomes

$$m = \frac{\sqrt{3} \ln 3}{2} \approx 0.951 . \quad (4.115)$$

Interestingly, various sources, e.g., (Holtz, 1994; Holtz et al., 1993; Lee and Lee, 1998; Malinowski, 2000) give the approximation 0.952 as the upper limit of the overmodulation mode 1, which contradicts with the analytical form. The difference, however, is insignificant from the practical point of view. Tab. 4.2 summarizes fundamental wave properties of different PWM methods.

4.4.2 Fundamental voltage of DTC converter

In a DTC converter the modulation process does not try to produce a time average of a reference voltage space-vector. Instead, the converter output voltage space-vector is indirectly determined by the hysteresis control. However, it is worthwhile to ask, what is the maximum

Table 4.2: Fundamental wave properties of PWM methods.

| | Peak-value of the fundamental phase voltage $u_{1, \text{fund}}$ | Holtz's modulation index $m = \frac{u_{1, \text{fund}}}{2u_{\text{dc}}/\pi}$ | Modulation index based on amplitude modulation ratio $m_a = \frac{u_{1, \text{fund}}}{u_{\text{dc}}/2}$ | RMS line-to-line voltage if $u_{\text{dc}} = 566 \text{ V}^\dagger$ |
|---|--|--|---|---|
| Carrier-based PWM with sinusoidal reference signals | $\leq \frac{1}{2} u_{\text{dc}}$ | $\leq \frac{\pi}{4} \approx 0.785$ | ≤ 1 | $\leq 347 \text{ V}$ |
| Carrier-based PWM with zero sequence added to reference signals or space-vector modulation. | $\leq \frac{\sqrt{3}}{3} u_{\text{dc}}$ | $\leq \frac{\sqrt{3}\pi}{6} \approx 0.907$ | $\leq \frac{2\sqrt{3}}{3} \approx 1.155$ | $\leq 400 \text{ V}$ |
| Overmodulation range 1 | $\leq \frac{\sqrt{3} \ln 3}{\pi} u_{\text{dc}}$ | $\leq \frac{\sqrt{3} \ln 3}{2} \approx 0.951$ | $\leq \frac{2\sqrt{3} \ln 3}{2} \approx 1.211$ | $\leq 420 \text{ V}$ |
| Overmodulation range 2 | $< \frac{2}{\pi} u_{\text{dc}}$ | < 1 | $< \frac{4}{\pi} \approx 1.273$ | $< 441 \text{ V}$ |
| Six-step mode | $= \frac{2}{\pi} u_{\text{dc}}$ | $= 1$ | $= \frac{4}{\pi}$ | $= 441 \text{ V}$ |

[†]The dc-link voltage of 566 V corresponds to the line converter's limit of the linear modulation range in a 400 V grid. The dc-link voltage of a diode bridge fed motor converter in load conditions is lower than that.

fundamental wave output voltage, and, hence, also the maximum modulation index that a DTC converter can produce?

First, we define an ideal converter output voltage vector $\underline{u}_{1, \text{id}}$ as the continuous voltage vector that the converter switching process is trying to approximate. Basically, the concept of an ideal output voltage vector, which is free of switching harmonics, is the same that is used in the analysis of the space-vector overmodulation methods in (Holtz et al., 1993) and (Bolognani and Zigliotto, 1999). With SVPWM, the ideal output voltage vector is defined as the actual voltage vector averaged over the subcycle. With DTC, there are no subcycles over which the averaging could be performed, and we have to use a different definition, even though the meaning of the variable is basically the same.

Let us denote the ideal converter output voltage space vector as

$$\underline{u}_{1, \text{id}} = (a\underline{u}_{q+d+} + b\underline{u}_{q+d-}) (1 - z_v) . \quad (4.116)$$

where \underline{u}_{q+d+} and \underline{u}_{q+d-} are the active voltage vectors used in the sector in question. In sector 1, as shown in Fig. 4.15, \underline{u}_{q+d+} and \underline{u}_{q+d-} correspond to voltage vectors \underline{u}_{v2} and \underline{u}_{v3} , respectively. a , b and z_v are all continuous functions of time t . a and b determine how the active voltage vectors are used in constructing the ideal output vector. It holds that

$$a(t) + b(t) = 1 , \quad (4.117)$$

for all t . z_v determines how the zero vectors should be applied relatively to active vectors in order to produce the ideal output voltage. Basically, a and b determine the direction of the ideal output space-vector while z_v scales it to the correct length. In (Tarkainen et al., 2002) a and b are called relative incidences, because they describe the theoretical ratio between the active voltage vectors that the converter should switch in order to produce the ideal output voltage space-vector in time averaged sense. Similarly, z_v could be interpreted as the theoretical ratio between the zero vectors and the all voltage vectors. Let us also define the ideal converter virtual flux linkage vector as

$$\underline{\psi}_{1, \text{id}} = \psi_{1, \text{id}} e^{j\omega t} = \int \underline{u}_{1, \text{id}} dt . \quad (4.118)$$

Then, the equations for a , b and z_v are derived. First, let us write (4.116) in the converter virtual flux linkage oriented dq-frame in component form

$$\begin{aligned} \underline{u}_{1, \text{id}}^{\text{dq}} &= a(1 - z_v)u_{q+d+, d} + b(1 - z_v)u_{q+d-, d} \\ &\quad + j(a(1 - z_v)u_{q+d+, q} + b(1 - z_v)u_{q+d-, q}) \end{aligned} \quad (4.119)$$

The components of the active voltage vectors in the CFO frame, also given in (Tarkainen et al., 2002), are

$$u_{q+d+, d} = \text{Re}\{\underline{u}_{q+d+}\} = \frac{2}{3}u_{\text{dc}} \sin(\gamma) \quad (4.120)$$

$$u_{q+d+, q} = \text{Im}\{\underline{u}_{q+d+}\} = \frac{2}{3}u_{\text{dc}} \cos(\gamma) \quad (4.121)$$

$$u_{q+d-, d} = \text{Re}\{\underline{u}_{q+d-}\} = \frac{2}{3}u_{\text{dc}} \sin(\gamma - \frac{\pi}{3}) \quad (4.122)$$

$$u_{q+d-, q} = \text{Im}\{\underline{u}_{q+d-}\} = \frac{2}{3}u_{\text{dc}} \cos(\gamma - \frac{\pi}{3}) , \quad (4.123)$$

where the angle $\gamma \in [0, \frac{\pi}{3}]$ is the angle of the converter virtual flux linkage vector measured from the sector border, as shown in Fig. 4.15. In steady state, the DTC algorithm maintains the constant modulus of the converter virtual flux linkage vector. Hence, applying (4.75) to (4.119) we may write

$$u_{1d, id} = \text{Re}\{\underline{u}_{1, id}^{dq}\} = a(1 - z_v)u_{q+d+, d} + b(1 - z_v)u_{q+d-, d} = \frac{d\psi_{1, id}}{dt} = 0. \quad (4.124)$$

By taking into account (4.117), (4.120) and (4.122), we may solve the expressions for a and b as

$$a = \frac{\sqrt{3} \cos(\gamma) - \sin(\gamma)}{\sqrt{3} \cos(\gamma) + \sin(\gamma)} \quad (4.125)$$

$$b = \frac{2 \sin(\gamma)}{\sqrt{3} \cos(\gamma) + \sin(\gamma)}. \quad (4.126)$$

To derive the equation for z_v we have to consider the imaginary part of (4.119). Applying (4.78) to ideal quantities, we have $u_{1q, id} = \omega \psi_{1, id}$, and we may write

$$u_{1q, id} = \text{Im}\{\underline{u}_{1, id}^{dq}\} = a(1 - z_v)u_{q+d+, q} + b(1 - z_v)u_{q+d-, q} = \omega \psi_{1, id} \quad (4.127)$$

Substituting (4.121), (4.123), (4.125) and (4.126), and solving for z_v and simplifying gives

$$z_v = 1 - \frac{\sqrt{3} \omega \psi_{1, id}}{u_{dc}} \left(\sin(\gamma) + \cos\left(\gamma + \frac{\pi}{6}\right) \right), \quad (4.128)$$

$\gamma \in [0, \frac{\pi}{3}]$. Obviously, z_v can not have arbitrary values but is bounded as $0 \leq z_v < 1$. The upper limit 1 is a theoretical limit, which is approached if u_{dc} is let to approach infinity. The instantaneous angular frequency of the ideal converter virtual flux linkage vector is

$$\omega = \frac{(au_{q+d+, q} + bu_{q+d-, q})(1 - z_v)}{\psi_{1, id}}. \quad (4.129)$$

When $z_v > 0$ the DTC is controlling the active power and in steady state the DTC maintains the constant phase shift χ in (4.48). This implies that the angular frequencies of the converter and line virtual flux linkages are the same, $\omega_s = \omega$. However, when $z_v = 0$ the DTC does not control the active power but is rotating the virtual converter flux linkage vector with the greatest possible angular frequency, and hence, trying to maximally increase the power transfer from the dc-link to the ac-grid. The angular frequency ω is not constant throughout the sector but, in steady state, its time average value equals the grid frequency, $\omega_{ave} = \omega_s$. In Fig. 4.16 the graphs of a , b and z_v are depicted with three different modulation indices.

Let us consider the maximum output fundamental voltage. The maximum fundamental voltage is produced when no zero vectors are switched at all, and hence $z_v \equiv 0$. Since it holds that

$$\frac{d\gamma}{dt} = \omega, \quad (4.130)$$

we may solve time t as a function of γ as

$$t(\gamma) = \int_0^\gamma \frac{1}{\omega} d\gamma \quad (4.131)$$

$$= \int_0^\gamma \frac{\psi_{1, id}}{au_{q+d+, q} + bu_{q+d-, q}} d\gamma \quad (4.132)$$

$$= \frac{\psi_{1, id}}{u_{dc}} \left(\frac{\sqrt{3}}{2} - \frac{\sqrt{3}}{2} \cos(\gamma) + \frac{3}{2} \sin(\gamma) \right), \quad (4.133)$$

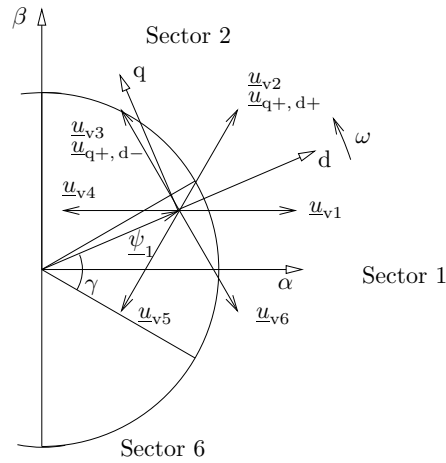


Figure 4.15: Converter virtual flux linkage vector and the converter voltage vectors. In the sector 1 \underline{u}_{v2} equals \underline{u}_{q+d+} and \underline{u}_{v3} equals \underline{u}_{q+d-} .

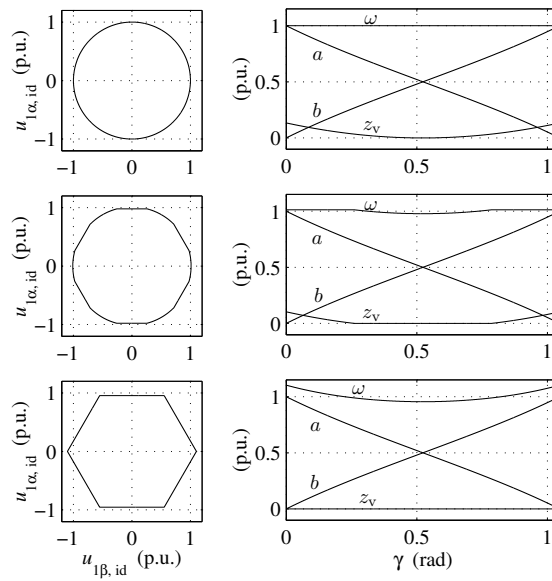


Figure 4.16: Trajectories of the ideal converter output voltage space-vector $\underline{u}_{1,id}$ and a , b and z_v as a function of γ . In all cases, the fundamental output voltage is $u_{1,id,fund} = \psi_{1,id} = 1$ p.u. and the time average of the angular frequency is $\omega_{ave} = 1$ p.u.

First row: The limit of the linear modulation range, $u_{dc} = \sqrt{3}$ p.u., $m \approx 0.907$.

Second row: In the overmodulation range 1, $u_{dc} = \frac{1}{2}(\sqrt{3} + \frac{3\sqrt{3}}{\pi})$, $m \approx 0.928$.

Third row: Maximum modulation index, $u_{dc} = \frac{3\sqrt{3}}{\pi}$, $m \approx 0.950$.

where $\gamma \in [0, \frac{\pi}{3}]$. In order to have the time average frequency of $\omega_{\text{ave}} = 1$ p.u., one sector must equal sixth of the cycle period. Therefore, as $t(0) = 0$, we have to have $t(\frac{\pi}{3}) = \frac{\pi}{3}$ in per unit quantities. Using this result to (4.133) yields

$$u_{\text{dc}} = \frac{3\sqrt{3}\psi_{1,\text{id}}}{\pi} . \quad (4.134)$$

To have the unity fundamental wave output voltage $u_{1,\text{id},\text{fund}} = 1$ p.u., we obviously must have $\psi_{1,\text{id}} = 1$ p.u. Because we have (4.118), the circular locus of the converter virtual flux linkage vector is solely determined by the fundamental wave converter voltage. The harmonic flux linkages, which make $\psi_{1,\text{id}}$ to rotate with variable angular frequency are due to the harmonic converter voltages. The fundamental output voltage $u_{1,\text{id},\text{fund}}$ is given as a function of u_{dc} as

$$u_{1,\text{id},\text{fund}} = \psi_{1,\text{id}} = \frac{\pi}{3\sqrt{3}} u_{\text{dc}} . \quad (4.135)$$

Now, the maximum modulation index for the DTC may be given as

$$m = \frac{u_{1,\text{id},\text{fund}}}{\frac{2}{\pi} u_{\text{dc}}} = \frac{\pi^2}{6\sqrt{3}} \approx 0.950 . \quad (4.136)$$

Comparison to Tab. 4.2 shows that with DTC the overmodulation range 1 is almost completely covered. The fundamental wave amplitude may be calculated with the complex Fourier series as

$$u_{1,\text{id},\text{fund}} = \left| \frac{1}{2\pi} \int_0^{2\pi} \underline{u}_{1,\text{id}}^{\alpha\beta} e^{-j\omega_{\text{ave}} t} d\omega_{\text{ave}} t \right| . \quad (4.137)$$

Since all sectors are identical, it is enough to integrate over one sector

$$u_{1,\text{id},\text{fund}} = \left| \frac{1}{\pi/3} \int_0^{\pi/3} \underline{u}_{1,\text{id}}^{\text{dq}}(\gamma) e^{j\gamma} e^{-j\omega_{\text{ave}} t} d\omega_{\text{ave}} t \right| \quad (4.138)$$

$$\stackrel{\omega_{\text{ave}}=1}{=} \left| \frac{1}{\pi/3} \int_0^{\pi/3} \left(\underbrace{\text{Re} \{ \underline{u}_{1,\text{id}}^{\text{dq}}(\gamma) \}}_{=u_{1,\text{id}}=0} + j \underbrace{\text{Im} \{ \underline{u}_{1,\text{id}}^{\text{dq}}(\gamma) \}}_{=u_{1q,\text{id}}} \right) e^{j\gamma} e^{-jt} dt \right| \quad (4.139)$$

$$= \frac{1}{\pi/3} \int_0^{\pi/3} u_{1q,\text{id}}(\gamma) dt \quad (4.140)$$

To express $u_{1q,\text{id}}$ as a function of the time t instead of the angle γ , we have to invert relation (4.133). This yields

$$\gamma = \frac{\pi}{6} - \arctan \left(\frac{\sqrt{3}\psi_{1,\text{id}} - 2tu_{\text{dc}}}{\sqrt{9\psi_{1,\text{id}}^2 + 4\sqrt{3}\psi_{1,\text{id}}tu_{\text{dc}} - 4t^2u_{\text{dc}}^2}} \right) , \quad (4.141)$$

where $t \in [0, \frac{\pi}{3}]$. An expression for $u_{1q,\text{id}}(t)$ is obtained by substituting (4.141) to (4.121), (4.123), (4.125) and (4.126) and by using (4.127). The fundamental wave integral is then

$$u_{1,\text{id},\text{fund}} = \frac{1}{\pi/3} \int_0^{\pi/3} u_{1q,\text{id}}(t) dt . \quad (4.142)$$

The expression is, however, rather cumbersome. Numerically, it may be evaluated that when $\psi_{1, \text{id}} = 1$, the integral yields $u_{1, \text{id}, \text{fund}} = 1$, precisely when u_{dc} equals (4.134).

In Tarkiainen et al. (2002) the maximum fundamental wave voltage of the DTC is incorrectly calculated as

$$u_{1, \text{id}, \text{fund}} = \left| \frac{1}{\pi/3} \int_0^{\pi/3} \underline{u}_{1, \text{id}}^{\text{dq}}(\gamma) e^{j\gamma} e^{-j\omega t} d\omega t \right| \quad (4.143)$$

$$= \frac{1}{\pi/3} \int_0^{\pi/3} u_{1, \text{id}}(\gamma) d\gamma . \quad (4.144)$$

This is an incorrect result because the unit vector $e^{-j\omega t}$ is not rotating with a constant angular frequency, and therefore, the integral does not represent a Fourier-integral. The result of the integration equals the upper limit of overmodulation mode 1 of the space-vector modulation, shown in (4.114). This is 0.2% higher than the correct value. From the practical viewpoint, the difference is negligible.

In the space-vector modulation the angular frequency ω is a constant. Further, it holds that

$$\gamma = \int \omega dt = \omega t . \quad (4.145)$$

Expressions for a and b may be calculated as

$$a = \frac{t_a}{t_a + t_b} \quad (4.146)$$

$$b = \frac{t_b}{t_a + t_b} . \quad (4.147)$$

Both, the linear modulation range equations (4.108) and (4.109) and the overmodulation mode 1 equations (4.111) and (4.112) yield the same results (4.125) and (4.126) as the DTC. With the SVPWM, different from the DTC, the shapes of $a(t)$ and $b(t)$ are similar to $a(\gamma)$ and $b(\gamma)$, respectively. Only the scaling of the x-axis is changed, if $\omega \neq 1$. Contrary to the DTC, with SVPWM the ideal converter virtual flux linkage amplitude $\psi_{1, \text{id}}$ is not constant, but it is given as

$$\psi_{1, \text{id}} = \frac{(au_{q+d+, q} + bu_{q+d-, q})(1 - z_v)}{\omega} . \quad (4.148)$$

For the SVPWM a figure similar to 4.16 could be drawn, but with the difference that with SVPWM $\psi_{1, \text{id}}$ would behave analogously to behavior of ω in the DTC. Considering (4.23) and (4.46) it may be concluded that in the overmodulation mode 1 the DTC produces oscillations to the instantaneous power, whereas the SVPWM produces oscillations to the reactive power. In a motor drive application the DTC behavior would lead to torque oscillation. The DTC, however, is not intended to operate in the overmodulation region. The ability to do so is more like an endogenous characteristic. For the overmodulation region the DTC algorithm can be modified to cease maintaining of the circular virtual flux linkage locus. E.g., the hexagonal flux linkage trajectory, proposed in (Depenbrock, 1988), allows the torque to be controlled in the overmodulation range.

In line converters overmodulation occurs when the dc-link voltage is lowered below the peak-value of grid line-to-line voltage. The higher the maximum achievable modulation index the lower the dc-link voltage level that can be maintained. From (4.135) the theoretical minimum

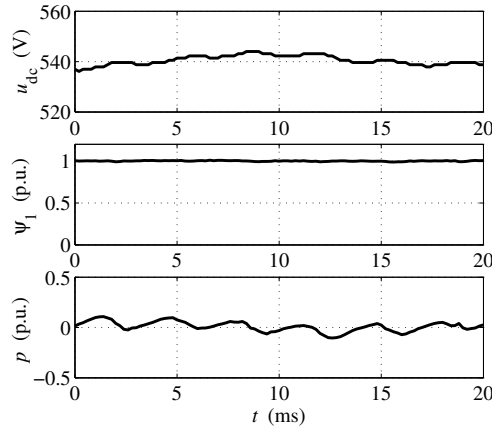


Figure 4.17: Measured maximum modulation index operation of DTC line converter. Top: dc-link voltage u_{dc} , Middle: Converter flux linkage vector modulus ψ_1 , Bottom: Instantaneous active power p . Grid line-to-line voltage is 400 V. Theoretical dc-link voltage level is 540 V.

achievable dc-link voltage of a DTC line converter resulting in unity output voltage is solved as

$$u_{dc, \min} = \frac{3\sqrt{3}}{\pi} . \quad (4.149)$$

In a 400 V grid we have, in terms of absolute values, $u_{dc, \min} = \frac{3\sqrt{3}}{\pi} \text{ p.u.} \cdot 326.6 \frac{\text{V}}{\text{p.u.}} = 540.2 \text{ V}$ as the theoretical minimum achievable dc-link voltage. Fig. 4.17 shows a corresponding measurement, in which the DTC line converter is given a negative active power reference resulting in the minimum dc-link voltage. The measured dc-link voltage oscillates in the near vicinity of the theoretical value, agreeing perfectly with the theoretical result. Also, the anticipated oscillation in the instantaneous active power is clearly observable. The same mechanism may also produce an oscillating power component in generating side transients. An example is shown in Fig. 4.13(b).

4.5 Summary

The chapter considered modeling and control of the line converter. A dynamical model of the line converter was introduced and the typical line converter control methods were reviewed. A new DTC-based current control method was introduced and modeled. A simplified transfer function model was derived and it was shown that, theoretically, the DTC-current control has dynamics of the phase-lag compensator. Tuning of the controllers to achieve similar dynamics in both control axes was presented. Also, the practical issues of the controller tuning, including the converter saturation, were discussed. Finally, the overmodulation characteristics of the DTC converter were considered. An analytical form for the maximum modulation index of the DTC converter was derived. It was found out that the overmodulation range 1 is almost completely covered with the DTC converter.

Chapter 5

Power Quality Improving

In this chapter, line converter is used in power quality improving. Power conditioning system and active filters are introduced. Three different active filtering methods are implemented—a frequency-domain method, a time-domain method and a voltage feedback method. Harmonic control systems are analyzed and designed. The performance and characteristics of different active filtering methods are evaluated using experimental measurements.

5.1 Power conditioning system

Most of the utility power quality problems are caused by voltage sags and short duration interruptions, which last for several cycles to several seconds (Corey, 1999). Custom power and premium power are technological concepts to provide electrical power of high-quality and improved reliability, see e.g. (Corey, 1999; Hingorani, 1995; Lasseter and Piagi, 2000; Stump et al., 1998). The term custom power means the value-added power that electric utilities and other service providers will offer their customers in the future (Hingorani, 1995). Premium power is a concept, which is based on the use of power electronics equipment, multi-utility feeders and uninterruptible power supplies (UPS) to provide power to users having sensitive loads (Lasseter and Piagi, 2000). One technological solution to achieve the improved reliability is depicted in Fig. 5.1. A power conditioning system is connected in parallel with the utility. The utility and the critical loads are separated by a fast static switch. The PCS is equipped with an energy storage, which can be a high-power battery, a flywheel system or a superconducting magnetic energy storage or supercapacitor-based storage system. The critical loads that the PCS is protecting may be industrial or commercial facilities, which need a higher level of reliability than the utility offers. Such critical load could be, e.g., a business park, an automated manufacturing plant or a data processing center.

Probably the most well-known power acceptability standard is the Information Technology Industry Council (ITI) curve, which is formerly known as the Computer Business Equipment Manufacturers Association (CBEMA) curve, see e.g. (Kyei et al., 2002). The ITI curve describes an AC voltage envelope which typically can be tolerated by the information technology equipment. The acceptable voltage envelope is defined in terms of percent change in the line voltage and the duration of the disturbance. Also variable speed drives are sensitive

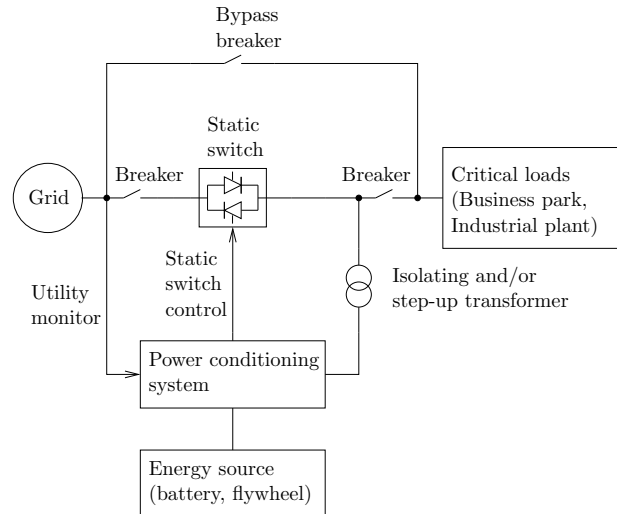


Figure 5.1: Power conditioning system providing uninterruptible power for critical loads. Modified from (Corey, 1999).

to the line voltage variations. The energy storage capacity of the dc-link capacitors is very limited and can support the drive only for a short time. E.g., in the 19 kVA converter, the data of which is listed in Appendix 1, the energy of the dc-link charged to 600 V is consumed in 11 ms in nominal power. In 3 ms the dc-link voltage is dropped to 500 V.

The PCS monitors the utility and when a power quality problem is detected, the static switch is used to disconnect the critical loads from the utility and, concurrently, the PCS starts to supply the loads. In principle, the operation resembles that of a large UPS system. The energy source of the PCS has to be able to deliver energy immediately. This requirement means that a fuel cell or a microturbine alone is not a sufficient energy source because of the slow response. They have to be backed by a fast-response energy storage, which is able to respond to transients. A transformer may be needed in the output of the PCS for isolation and step-up purposes. The transformer prevents the zero-sequence voltage present in the PCS output voltage from affecting the load and also provides a neutral conductor for the single-phase loads. Another reason is that some energy sources have the property that the dc-voltage they produce depends on the load. Some types of batteries and fuel cells exhibit this behavior. In sodium sulfur battery, e.g., the dc-voltage may vary between 325 V and 790 V (Tamyurek et al., 2003). If a voltage source inverter is used in the linear modulation range the dc-link voltage has to be greater than the peak-value of the line-to-line voltage. Therefore, a transformer may be needed to boost the PCS output voltage to a distribution network voltage level. In case of a failure, there is also a possibility to bypass the PCS.

Typically, interruptions or voltage sags and swells are short-lived and caused by circuit breaker automatic re-closings or large loads going on-line or off-line. Hence, even a short-duration back-up power will improve the power quality with respect to the critical loads. If the interruption is long-lasting the back-up power will help to shut down the process in a controlled way. Corey (1999) reports a 2 MW, 10 second PCS system, which utilizes standard off-the-shelf batteries.

When the PCS is supporting the load it is said to be in grid-independent mode. In this mode, the PCS is responsible to control the voltage level and the frequency of the island network to which the critical loads are connected. When the quality of utility power is returned to acceptable levels the PCS may transfer to the grid-connected mode. This involves synchronizing the island and the utility and closing the static switch. In the grid-connected mode, the PCS may be used in reactive power compensation. If the capacity of the storage system is adequate, the PCS may also be used for peak-shaving, that is, the energy storage is charged when the price of the electricity is low (i.e. at night time) and discharged when the rate is higher.

The control principle in the grid-connected mode and in the grid-independent mode has to be different. In the grid-independent mode the converter controls the voltage and the load determines the current. In the grid-connected mode the converter is controlled through active power and reactive power references and conventional line converter control methods may be applied. Appended Publication II considers the grid-independent mode control of the virtual flux linkage-based PCS. Particularly, the article presents a method which may be used to detect and correct the voltage unbalance resulting from unbalanced loading of the island network. Originally, the paper was published in conference proceedings (Tarkiainen et al., 2003c) in a slightly abridged form. The article (Tarkiainen et al., 2003b) shows measurements of mode transfers from grid-connected to grid-independent and from grid-independent to grid-connected.

The author was involved in a larger project, in which a sodium sulfur battery-based energy storage system with UPS functionality was developed. The description of the system and some test results are given in (Tamyurek et al., 2003). The system consists of two sodium sulfur batteries with combined continuous power of 100 kW and peak power of 500 kW. Two DTC-based line converters are used to interface the batteries to the power grid.

5.2 Active filters

The active filter, or active power filter, is a controlled power electronic device that is used to improve power quality. The idea of using the active filters was proposed a couple of decades ago to solve harmonic problems in high voltage DC power transmission, see e.g. (Mohan et al., 1977; Sasaki and Machida, 1971). In the early days, the power electronics were not advanced enough to implement a feasible semiconductor switch-based active filter. In one early configuration an alternator was used to inject a harmonic current (Bird et al., 1969). In 1976 Gyugyi and Strycula (1976) presented measurements with a single-phase power transistor-based active filter. Nowadays, the microprocessor control and controllable high-performance power switches have turned the active filter to practical technology. According to Akagi (2000) over 1000 active filters are in use in Japan.

A shunt active filter, depicted in Fig. 5.2, is the most common active filter configuration. Typically, active filters are used to compensate the harmonic currents of harmonic-producing loads. Traditionally, shunt passive filters have been used to suppress the harmonic currents flowing into the grid. Passive filters are typically tuned LC-filters or high-pass filters. A passive filter exhibits a lower impedance than the grid at the tuned frequency. Hence, the harmonic currents of the nonlinear load are supplied by the passive filter instead of the grid. Passive filters are reported to have the following problems (Akagi, 1994; Dugan et al., 2002; Mohan et al., 1977):

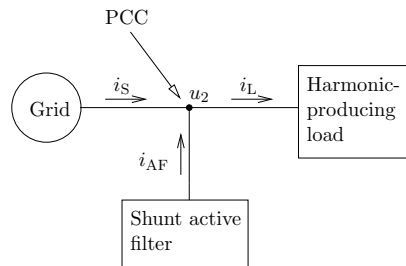


Figure 5.2: Basic principle of shunt active filter.

- The source impedance, which is not accurately known and varies with the system configuration, strongly influences the filtering characteristics.
- The filter is detuned if the filter parameters change with the temperature or age or if the system frequency deviates from its nominal value.
- With suitable excitation the passive filter may resonate with the source impedance.
- A small amount of background voltage in a very strong bus may impose excessive duty on the filter.

The benefit of the active filter is that it is not dependent on the source impedance similarly to the passive filters. One notable exception is the voltage feedback active filter, which is very dependent on the source impedance. The active filter is more costly solution than the passive filter. The cost is probably the most important drawback of the active filter. Also, the number of components is much higher in the active filter than in the passive filter, which may result in lower reliability.

Active filters may be classified according to the harmonic detection approach. In Fig. 5.2, the harmonic detection may be based on the measurement of the load current i_L , supply current i_S or the supply voltage u_2 . In the load current detection, the active filter extracts the harmonics of the load current and feeds them into the point of common coupling so that the harmonics are canceled in the supply current. In the supply current detection, the active filter analyzes the combined supply current of the load and the active filter. The active filter cancels the harmonics of the combined supply current and shapes it sinusoidal. In supply voltage detection, the active filter is used to compensate the voltage harmonics in the PCC.

Active filter control strategies may be classified to time-domain-based or frequency-domain-based methods. The time-domain-based methods typically use the power theory approach to extract the unwanted components of the load current. The detected load current harmonics are given as a reference to the active filter current control system. Ideally, the active filter provides the harmonic currents and the fundamental wave reactive current to the nonlinear load and only the fundamental wave active current is taken from the grid. Implementations and control systems are described e.g. in (Akagi et al., 1984; Buso et al., 1998b; Depenbrock and Skudelny, 1994; Staudt, 1996). The time-domain methods need very good current control performance because the required waveform typically contains sudden slope variations and high di/dt values. Hysteresis current control is, therefore, a natural current control principle

for the time-domain active filters. Buso et al. (1998a) found it to perform better than the other current control techniques included in the comparison.

The frequency-domain methods typically analyze the supply current and extract certain pre-selected harmonics (or harmonic sequences). The control algorithm is used to produce individual active filter current references corresponding to each detected harmonic. This results in closed-loop control of individual harmonic currents. Different from the time-domain active filters, the current control performance is not so critical to the frequency-domain active filters. This is because the harmonic control loops can compensate the errors of the current vector control. Frequency-domain active filters are described e.g. in (Mattavelli, 2001; Sonnenschein and Staudt, 1998). The frequency-domain and the time-domain active filter implementations were compared by Sonnenschein and Weinhold (1999). In contrast to the time-domain methods, the frequency domain methods do not compensate the fundamental wave reactive power of the load. However, if the grid voltage is measured or estimated, it is easy to calculate the fundamental reactive power of the supply current and control it in a closed-loop.

5.3 Active filtering feature of a line converter

The main circuits of the voltage source active filter and the voltage source line converter are basically similar. The only difference is that, in the active filter, there is no load in the dc-link. Nothing, however, prevents one from connecting the load in the active filter dc-link, or from implementing an active filtering feature to the line converter. Several line converter and active filter mergers have been presented in the literature, see e.g. (Abrahamsen and David, 1995; Cichowlas et al., 2003; Kataoka et al., 2000; le Roux and Enslin, 1998; le Roux et al., 1999). A line converter with active filtering feature may be used, e.g., as depicted in Fig. 5.3. The line converter feeds the dc-link of a motor converter and, at the same time, provides harmonic compensation to the diode bridge rectifiers connected to the same PCC. As noted by Abrahamsen and David (1995), several variable speed drives are typically sold and installed at once. Therefore, if low line current harmonics are required, it may be economically rational to equip one or a couple of the drives with line converter bridges with active filtering feature, and use them to compensate the harmonics of the rest.

The harmonic currents required in active filtering reserve a part of the current capacity of the line converter. This leads to derating of the line converter. However, as shown later, the LCL-filter may provide current amplification, which reduces the harmonic current amplitudes in the converter bridge terminals. A more severe limitation is the dc-link voltage level. In line converters the dc-link voltage is typically kept slightly (e.g. 10–30 V) above the peak-value of the grid line-to-line voltage. Typically, the dc-link components are not dimensioned to withstand a long-term voltage level significantly higher than that. Although, in some occasions, it may be possible to use the hardware designed for mains a voltage higher than in the projected site, e.g. a 690 V converter in a 400 V grid. Also, the useful lifetime of the motor insulation may shorten if the dc-link voltage of the motor converter is raised. Active filtering, however, typically needs a higher dc-link voltage than used in the line converters. The extra dc-link voltage is needed to generate harmonic voltages, which, in turn, are needed to produce the harmonic currents. The absolute value of the impedance of the line filter reactors increases with the frequency, which makes the required harmonic voltage for a given harmonic current to increase as well. The LCL-filter, however, may reduce this effect as discussed later on. The

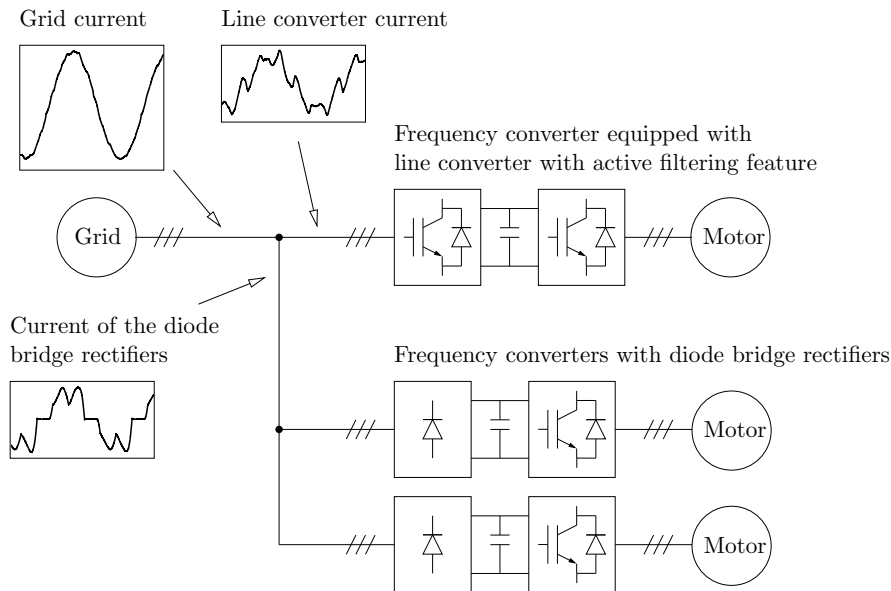


Figure 5.3: Application example of the line converter with active filtering feature.

line filter impedance could be reduced by using smaller inductors, but this would require increasing of the switching frequency. In dedicated active filters switching frequency of at least about 10 kHz is typically used, which is higher than the 2–6 kHz commonly used in industrial line converters. In the line converter with active filtering feature the optimum switching frequency may, perhaps, be higher than in the regular line converter allowing smaller line filter inductors and lower dc-link voltage.

The dc-link voltage requirement of an active filter with L-type line filter is studied in Appended Publication III by taking only two harmonic sequences (5th negative sequence and 7th positive sequence) into consideration. It is found out that the dc-link voltage requirement is not only dependent on the amplitudes of the harmonic sequences but also on their phase shifts. Generally, compensation of the instantaneous power ripple requires more dc-link voltage than the compensation of the corresponding reactive power ripple. Accordingly, the compensation of a nonlinear load with constant power, e.g. a diode bridge with a large dc-inductor, needs less dc-link voltage than the compensation of a nonlinear load with varying instantaneous power, such as a diode bridge converter with a large dc-capacitor.

5.4 The test setup

The practical configurations considered in this chapter are depicted in Fig. 5.4. Frequency-domain, time-domain and voltage feedback active filtering methods are implemented. Fig. 5.4 shows the additional measurements required in each case. In all cases, the converter current vector \underline{i}_1 and the dc-link voltage u_{dc} are measured for the converter current vector control purposes. The time-domain control method is implemented with the L-filter only. The use of the LCL-filter with the time-domain-based method would require a control system, which

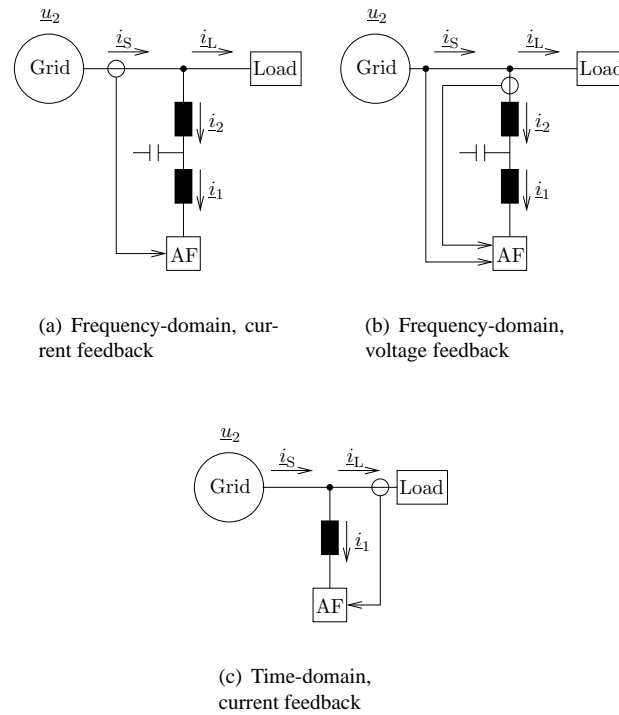


Figure 5.4: Considered active filter configurations. The dc-link voltage u_{dc} and converter current vector \hat{i}_1 are always measured. Cases (a) and (b) can be operated with an L-filter also. In case (c) only an L-filter is used.

take the LCL-filter effects into account and controls the line current i_2 with very high dynamic performance. In the case of the frequency-domain current feedback method also the line voltage was measured, although, that would not have been absolutely necessary. The line voltage measurement was used only in calculation of the combined fundamental wave reactive power of the nonlinear load and the active filter. Alternatively, the line voltage could have been estimated for this purpose by calculating the virtual line flux linkage as shown in section 3.3 in Appended Publication I.

The test setup used in the experiments is shown in Fig. 5.5. The mains transformer has a nominal power of 1 MVA. The line converter 1 is used in the active filtering studies. The nominal values of the line converter are presented in Appendix 1. In order to study the effect of active filtering in weak grid conditions the converter and the nonlinear load are fed through a 380/380 V transformer. The line converter 2 is connected in the same dc-link with the line converter 1 and, in the AC side, to the secondary of the 1 MVA transformer. In the controller tuning (sections 5.5 and 5.6) the line converter 2 is used to regulate the dc-link voltage. By doing so, the effect of the dc-link voltage control to the converter line currents is eliminated. Also, some measurements were performed without the 380/380 V transformer. However, in the active filter performance measurements (section 5.8) the 380/380 V transformer was used and the dc-link was loaded with a resistor and the dc-link voltage was regulated by the line

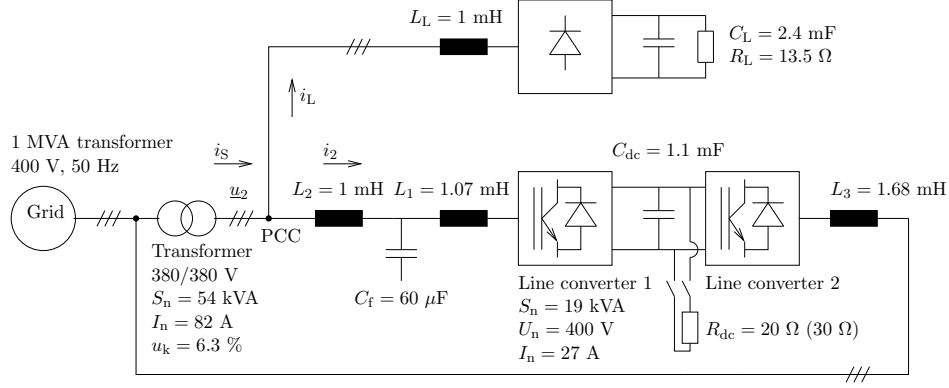


Figure 5.5: Test setup of active filtering experiments. In the L-filter case the filter capacitor was left out. The component values are given by the manufacturers. The base values of the inductance and capacitance are $L_b = 27.2$ mH and $C_b = 0.37$ mF. The short circuit ratio is $SCR_1 = 51$ if only the line converter or the nonlinear load are considered as a load and $SCR_2 = 25$ if both are considered as loads.

converter 1. In section 5.8.3 additional voltage feedback active filtering results are measured with a different setup and 490 kVA line converter.

From the name-plate values, shown in Fig. 5.5, the equivalent series reactance of the 380/380 V transformer is calculated as $X_{trafo} = 0.063 \cdot \frac{380 \text{ V}}{\sqrt{3} \cdot 82 \text{ A}} = 0.167 \Omega$, and the short circuit current as $I_{sc} = \frac{400 \text{ V}/\sqrt{3}}{X_{trafo}} = 1370 \text{ A}$. The nominal current of the line converter and the nonlinear load are the same, $I_n = 27 \text{ A}$. If only the line converter or only the nonlinear load is considered as a load the short circuit ratio is $SCR_1 = \frac{1370 \text{ A}}{27 \text{ A}} = 51$. If both the line converter and the nonlinear load are considered as loads, the short circuit ratio is $SCR_2 = 25$. IEEE recommendation IEEE Std 519–1992 (1993) (Tab. 2.3 on page 26 of this thesis) gives a current TDD limit of 12% for the first case and 8% for the second case.

5.5 Frequency-domain active filtering with DTC controlled line converter

5.5.1 The method of harmonic synchronous reference frames

The frequency selective active filtering was implemented using the method of harmonic synchronous reference frames. Previously, the method has been used in (Bojrup et al., 1999; Mattavelli, 2001; Ponnaluri and Brickwedde, 2001; Yano et al., 1997). The method identifies selected harmonic sequences by transforming them into the harmonic synchronous reference frames. The method is described as a block diagram in Fig. 5.6. The transformation of the supply current vector \underline{i}_S to the 5th negative sequence harmonic synchronous reference frame is calculated as

$$i_{Sd}^{5-} = \text{Re}\{(\underline{s}^{5-})^* \underline{i}_S\} = s_{\alpha}^{5-} i_{S\alpha} + s_{\beta}^{5-} i_{S\beta} \quad (5.1)$$

$$i_{Sq}^{5-} = \text{Im}\{(\underline{s}^{5-})^* \underline{i}_S\} = s_{\alpha}^{5-} i_{S\beta} - s_{\beta}^{5-} i_{S\alpha} \quad (5.2)$$

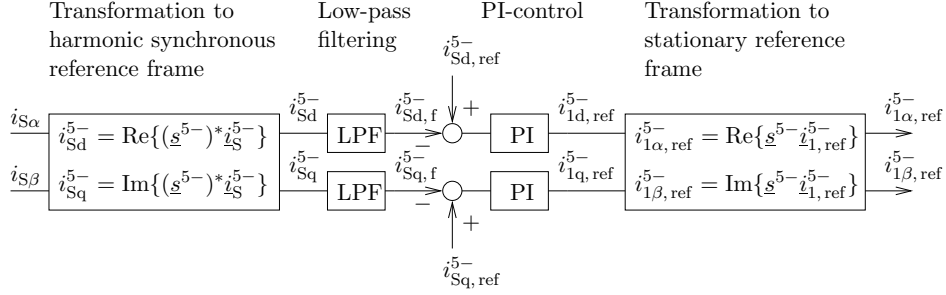


Figure 5.6: Calculation of the negative sequence 5th harmonic $\alpha\beta$ -frame current reference using the method of harmonic synchronous reference frame.

where \underline{s}^{5-} is a unity vector that is calculated in the control software. In the case of the 5th negative sequence, the unity vector is rotated with the angular frequency $5\omega_s$ to the negative direction. Therefore, it is calculated as

$$\underline{s}^{5-} = \cos(-5\omega_s t) + j \sin(-5\omega_s t) . \quad (5.3)$$

The grid angular frequency ω_s has to be estimated continuously because the actual grid frequency slightly deviates from the nominal value. The estimation is implemented by measuring the angular frequency of the converter virtual flux linkage vector $\underline{\psi}_1$. The angle of the converter virtual flux linkage vector is calculated in every millisecond. The angular frequency is estimated as

$$\omega_{s, \text{est}} = \frac{\Delta \arg\{\underline{\psi}_1\}}{\Delta t} , \quad (5.4)$$

where $\Delta \arg\{\underline{\psi}_1\}$ is the change of the virtual converter flux linkage angle between the consecutive evaluations and Δt is 1 ms. Because the converter virtual flux linkage may contain harmonics the estimate is low-pass filtered to find out the average value that corresponds to the fundamental frequency.

In the harmonic synchronous reference frame the harmonic component of the analyzed signal that matches the frequency and the sequence of the synchronous frame appears as a DC signal. Thus, it may be extracted by using a low-pass filter. The fundamental frequency and the other harmonics of the analyzed signal are shifted in the frequency because of the coordinate transformation. In the case of the harmonic synchronous frame corresponding to the negative 5th or the positive 7th harmonic sequence the fundamental frequency appears in the 6th harmonic frequency, which is 300 Hz in a 50 Hz grid. This is the dominating component appearing in the signal transformed to the harmonic synchronous frame and the low-pass filter should be designed to efficiently attenuate this signal component. The characteristics of the low-pass filter are largely determining the potential dynamic performance of the harmonic detection, and further also the dynamic properties of the closed-loop system controlling the harmonic. Therefore, not only the frequency domain but also the time domain characteristics of the low-pass filter are important. The fundamental frequency should be preferably attenuated at least by 60 dB. The cascade of simple discrete filters, where n_c is the number of cascaded filter stages is written as

$$G_{\text{lpf}}(z^{-1}) = \left(\frac{a}{1 - (1 - a)z^{-1}} \right)^{n_c} \quad (5.5)$$

The parameter a and the order of the resulting filter n_c are chosen to provide sufficient attenuation for 300 Hz and to have adequate time domain characteristics. With the sample time $T_s = 200 \mu\text{s}$ and selections $a = 0.008$ and $n_c = 2$, an attenuation of 67 dB at 300 Hz and 96 ms for the 90% rise time are obtained. With the negative 11th (11-) and the positive 13th (13+) harmonic sequences the fundamental frequency is appearing as 600 Hz component and therefore the low-pass filters for these harmonics could be tuned to provide a faster rise time.

The low-pass filtered space-vector components $i_{\text{Sd},f}^{5-}$ and $i_{\text{Sq},f}^{5-}$ represent the detected harmonic current space-vector in the harmonic synchronous frame. Error signals in both directions are calculated by subtracting the detected harmonic components from the corresponding references. Typically, the harmonic supply current references $i_{\text{Sd},\text{ref}}^{5-}$ and $i_{\text{Sq},\text{ref}}^{5-}$ are zeros, but not necessarily, if some predetermined harmonic current is needed. The error signals are fed to the PI-controllers, which produce converter harmonic current references in the harmonic synchronous frame, $i_{1d,\text{ref}}^{5-}$ and $i_{1q,\text{ref}}^{5-}$. These references are then transformed to the stationary $\alpha\beta$ -frame with equations

$$i_{1\alpha,\text{ref}}^{5-} = \text{Re}\{\underline{s}^{5-} \underline{i}_{1,\text{ref}}^{5-}\} = s_{\alpha}^{5-} i_{1d,\text{ref}}^{5-} - s_{\beta}^{5-} i_{1q,\text{ref}}^{5-} \quad (5.6)$$

$$i_{1\beta,\text{ref}}^{5-} = \text{Im}\{\underline{s}^{5-} \underline{i}_{1,\text{ref}}^{5-}\} = s_{\alpha}^{5-} i_{1q,\text{ref}}^{5-} + s_{\beta}^{5-} i_{1d,\text{ref}}^{5-} \quad (5.7)$$

The transformation from the $\alpha\beta$ -frame to the fundamental wave dq-frame is calculated corresponding to Eqs. (4.50) and (4.51)

$$i_{1d,\text{ref}}^{5-(\text{dq}^{1+})} = \frac{\psi_{1\alpha} i_{1\alpha,\text{ref}}^{5-} + \psi_{1\beta} i_{1\beta,\text{ref}}^{5-}}{\psi_1} \quad (5.8)$$

$$i_{1q,\text{ref}}^{5-(\text{dq}^{1+})} = \frac{\psi_{1\alpha} i_{1\beta,\text{ref}}^{5-} - \psi_{1\beta} i_{1\alpha,\text{ref}}^{5-}}{\psi_1} \quad (5.9)$$

where the superscript (dq¹⁺) is used to explicitly indicate that the harmonic component is expressed in the fundamental frequency positive sequence oriented synchronous reference frame. The total current references are calculated by summing the fundamental wave reference components and all harmonic reference components. With four harmonic sequences the total current references are calculated as

$$i_{1d,\text{ref,tot}} = i_{1d,\text{ref}} + i_{1d,\text{ref}}^{5-(\text{dq}^{1+})} + i_{1d,\text{ref}}^{7+(\text{dq}^{1+})} + i_{1d,\text{ref}}^{11-(\text{dq}^{1+})} + i_{1d,\text{ref}}^{13+(\text{dq}^{1+})} \quad (5.10)$$

$$i_{1q,\text{ref,tot}} = i_{1q,\text{ref}} + i_{1q,\text{ref}}^{5-(\text{dq}^{1+})} + i_{1q,\text{ref}}^{7+(\text{dq}^{1+})} + i_{1q,\text{ref}}^{11-(\text{dq}^{1+})} + i_{1q,\text{ref}}^{13+(\text{dq}^{1+})} \quad (5.11)$$

These current references are used in the converter virtual flux linkage oriented current vector system shown in Fig. 4.8 on page 59.

The control of four harmonic sequences, 5-, 7+, 11- and 13+, is implemented to the digital signal processor. The harmonic current reference calculations are implemented in a 200 μs control loop. The 200 μs time level is realized by splitting up the 100 μs time level so that every other cycle new references are calculated to the sequences 5- and 7+ and every other cycle to the sequences 11- and 13+. The current vector control is in 100 μs time level. The calculation of the unit vectors (e.g. (5.3)) is divided in 100 μs and 1 ms time levels. In the 1 ms time level the angle which the unit vector \underline{s}^ν should rotate in 100 μs is calculated with the estimated grid frequency $\omega_{s,\text{est}}$ as

$$\Delta\phi_{\underline{s}^\nu} = \omega_{s,\text{est}} \Delta t \quad (5.12)$$

where Δt is 100 μs . Also, the cosine and sine of the $\Delta\phi_{\underline{s}^\nu}$ are calculated in the 1 ms time level. In the 100 μs time level the corresponding unit vector \underline{s}^ν is in every round rotated for the angle $\Delta\phi_{\underline{s}^\nu}$ as

$$\begin{bmatrix} s_{\alpha, n+1}^\nu \\ s_{\beta, n+1}^\nu \end{bmatrix} = \begin{bmatrix} \cos(\Delta\phi_{\underline{s}^\nu}) & -\sin(\Delta\phi_{\underline{s}^\nu}) \\ \sin(\Delta\phi_{\underline{s}^\nu}) & \cos(\Delta\phi_{\underline{s}^\nu}) \end{bmatrix} \begin{bmatrix} s_{\alpha, n}^\nu \\ s_{\beta, n}^\nu \end{bmatrix}, \quad (5.13)$$

where n is the time index. In (5.13) the rotation direction is positive (i.e. counter-clockwise). The unit vectors are synchronized to the converter virtual flux linkage vector by observing the zero-crossings of the unit vector components and the converter virtual flux linkage vector components. If the unit vector appears to have rotated too much or too little, the rotation angle $\Delta\phi_{\underline{s}^\nu}$ is adjusted by a small offset. The synchronization eliminates slow drifting of the harmonic d- and q-axes with respect to the fundamental d- and q-axes. The drifting, however, is a slow phenomenon and not a problem if zero harmonic references are used. But, if some predetermined harmonic current is injected the synchronism is required to maintain a fixed relation between the harmonic and the fundamental co-ordinate systems, and, thus, between the harmonic and the fundamental waveforms. Instead of the virtual converter flux linkage the harmonic synchronous co-ordinates may also be synchronized to the line voltage or the virtual line flux linkage.

5.5.2 Analysis

Controller tuning

A model of the control system is needed to determine the parameters of the harmonic synchronous frame controllers and to assess the stability of the system. In the harmonic synchronous frame corresponding to the harmonic sequence ν the control process may be described with a block diagram shown in Fig. 5.7. i_S^ν is the instantaneous value of the supply current harmonic sequence. This quantity, however, can not be measured accurately, because in order to find out its value at least one full wave of the corresponding harmonic must be analyzed. The estimation of the harmonic sequence is represented by the low-pass filters $\underline{G}_{\text{lpf}}$ associated with the method of the harmonic synchronous reference frames. The controllers are denoted as $\underline{G}_{\text{PI}}$. The process from the converter current reference $i_{1, \text{ref}}^\nu$ to the line current i_2^ν is represented by $\underline{G}_{\text{proc}}$. This includes the effects of 1) the converter fundamental wave current vector control, 2) equivalent delays associated to sample times of the discrete implementations of the harmonic synchronous frame control and the fundamental wave current vector control, 3) modulation, and 4) the line filter and supply grid. The dynamics of these effects are at least of the order of a magnitude faster than the harmonic current control. The dynamics of the harmonic current control are largely determined by the low-pass filters used in the harmonic detection algorithm (e.g. (5.5)). The rise time of the low-pass filter may be about 100 ms, whereas for the current vector control the rise time of about 5 ms may be easily reached. Therefore, it is justified to use a static model to represent $\underline{G}_{\text{proc}}$. In fact, $\underline{G}_{\text{proc}}$ is modeled as the effective steady-state gain and the effective steady-state phase shift of the actual process. To compensate the gain and the phase shift of the physical process, a compensator $\underline{G}_{\text{comp}}$, which is supposed to approximate $\underline{G}_{\text{proc}}^{-1}$, is introduced.

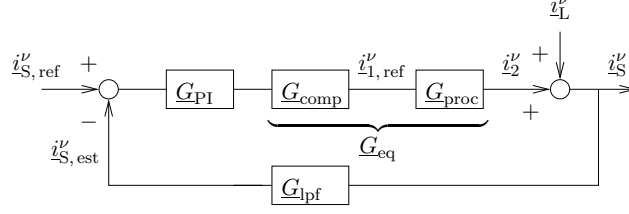


Figure 5.7: Block diagram representing the control process of current harmonic sequence ν in the harmonic synchronous reference frame.

The model of $\underline{G}_{\text{proc}}$ is

$$\underline{G}_{\text{proc}} = G_{\text{proc}} e^{j\gamma_{\text{proc}}} = \begin{bmatrix} G_{\text{proc}} \cos(\gamma_{\text{proc}}) & -G_{\text{proc}} \sin(\gamma_{\text{proc}}) \\ G_{\text{proc}} \sin(\gamma_{\text{proc}}) & G_{\text{proc}} \cos(\gamma_{\text{proc}}) \end{bmatrix}, \quad (5.14)$$

where G_{proc} and γ_{proc} are the effective steady-state gain and the phase shift, respectively. The compensator is

$$\underline{G}_{\text{comp}} = G_{\text{comp}} e^{-j\gamma_{\text{comp}}} = \begin{bmatrix} G_{\text{comp}} \cos(\gamma_{\text{comp}}) & G_{\text{comp}} \sin(\gamma_{\text{comp}}) \\ -G_{\text{comp}} \sin(\gamma_{\text{comp}}) & G_{\text{comp}} \cos(\gamma_{\text{comp}}) \end{bmatrix}. \quad (5.15)$$

The compensated process is

$$\underline{G}_{\text{eq}} = G_{\text{eq}} e^{j\gamma_{\text{eq}}} = \underline{G}_{\text{comp}} \underline{G}_{\text{proc}} = \begin{bmatrix} G_{\text{eq}} \cos(\gamma_{\text{eq}}) & -G_{\text{eq}} \sin(\gamma_{\text{eq}}) \\ G_{\text{eq}} \sin(\gamma_{\text{eq}}) & G_{\text{eq}} \cos(\gamma_{\text{eq}}) \end{bmatrix}, \quad (5.16)$$

where $G_{\text{eq}} = G_{\text{comp}} G_{\text{proc}}$ and $\gamma_{\text{eq}} = \gamma_{\text{proc}} - \gamma_{\text{comp}}$. Obviously, perfect compensation yields $\underline{G}_{\text{eq}}$ as unit matrix, $\underline{G}_{\text{eq}} = \underline{I}$. The low-pass filters are modeled as

$$\underline{G}_{\text{lpf}} = \begin{bmatrix} \frac{1}{(s\tau + 1)^2} & 0 \\ 0 & \frac{1}{(s\tau + 1)^2} \end{bmatrix}, \quad (5.17)$$

where τ is the filter time constant. The controllers with PI-algorithm in standard form are modeled as

$$\underline{G}_{\text{PI}} = \begin{bmatrix} K_p \frac{1 + sT_i}{sT_i} & 0 \\ 0 & K_p \frac{1 + sT_i}{sT_i} \end{bmatrix}, \quad (5.18)$$

where K_p is the controller gain and T_i is the integration time.¹ The PI-algorithm is selected because the integral action removes the steady-state error and the controller zero may be used

¹In section 4.3 PI-controllers were expressed in form $G_{\text{PI}} = k_p + \frac{k_i}{s}$. The parameters in these two forms are related as $k_p = K_p$ and $k_i = \frac{K_p}{T_i}$.

to cancel one pole of the process. The loop transfer function matrix is written as

$$\begin{aligned} \underline{G}_{\text{loop}} &= \underline{G}_{\text{PI}}\underline{G}_{\text{eq}}\underline{G}_{\text{lpf}} \quad (5.19) \\ &= \begin{bmatrix} \frac{K_p(1+sT_i)G_{\text{eq}}\cos(\gamma_{\text{eq}})}{sT_i(s\tau+1)^2} & -\frac{K_p(1+sT_i)G_{\text{eq}}\sin(\gamma_{\text{eq}})}{sT_i(s\tau+1)^2} \\ \frac{K_p(1+sT_i)G_{\text{eq}}\sin(\gamma_{\text{eq}})}{sT_i(s\tau+1)^2} & \frac{K_p(1+sT_i)G_{\text{eq}}\cos(\gamma_{\text{eq}})}{sT_i(s\tau+1)^2} \end{bmatrix}. \quad (5.20) \end{aligned}$$

Let us, at first, consider a perfectly compensated process, that is, $G_{\text{eq}} = 1$ and $\gamma_{\text{eq}} = 0$. In that case, we have

$$\underline{G}_{\text{loop}} = \begin{bmatrix} \frac{K_p(1+sT_i)}{sT_i(s\tau+1)^2} & 0 \\ 0 & \frac{K_p(1+sT_i)}{sT_i(s\tau+1)^2} \end{bmatrix}. \quad (5.21)$$

The integration time T_i is selected to compensate the pole of the process, i.e. $T_i = \tau$. Now, the closed-loop process from the reference to the output is

$$\underline{G}_{\text{cl}} = \frac{i_{\text{S}}^{\nu}}{i_{\text{S,ref}}^{\nu}} = (\underline{I} + \underline{G}_{\text{PI}}\underline{G}_{\text{eq}}\underline{G}_{\text{lpf}})^{-1}\underline{G}_{\text{PI}}\underline{G}_{\text{eq}} \quad (5.22)$$

$$= \begin{bmatrix} \frac{K_p(s\tau+1)^2}{s^2\tau^2+s\tau+K_p} & 0 \\ 0 & \frac{K_p(s\tau+1)^2}{s^2\tau^2+s\tau+K_p} \end{bmatrix}. \quad (5.23)$$

Accordingly, the closed-loop process from the reference to the estimated harmonic current is

$$\underline{G}_{\text{cl,est}} = \frac{i_{\text{S,est}}^{\nu}}{i_{\text{S,ref}}^{\nu}} = (\underline{I} + \underline{G}_{\text{PI}}\underline{G}_{\text{eq}}\underline{G}_{\text{lpf}})^{-1}\underline{G}_{\text{PI}}\underline{G}_{\text{eq}}\underline{G}_{\text{lpf}} \quad (5.24)$$

$$= \begin{bmatrix} \frac{K_p}{s^2\tau^2+s\tau+K_p} & 0 \\ 0 & \frac{K_p}{s^2\tau^2+s\tau+K_p} \end{bmatrix}. \quad (5.25)$$

Rearranging yields

$$\underline{G}_{\text{cl,est}} = \begin{bmatrix} \frac{K_p/\tau^2}{s^2 + \frac{1}{\tau}s + \frac{K_p}{\tau^2}} & 0 \\ 0 & \frac{K_p/\tau^2}{s^2 + \frac{1}{\tau}s + \frac{K_p}{\tau^2}} \end{bmatrix}, \quad (5.26)$$

and by comparing with the standard form of the second order system

$$G_{\text{st}} = \frac{\omega_n^2}{s^2 + 2\zeta\omega_n s + \omega_n^2} \quad (5.27)$$

the natural frequency is recognized as $\omega_n = \frac{\sqrt{K_p}}{\tau}$ and the damping ratio as $\zeta = \frac{1}{2\sqrt{K_p}}$. The transient performance is a compromise between the swiftness of the response and the closeness of the response as presented by the overshoot and settling time. For the standard second

order system Dorf and Bishop (1995) give the peak response as $M_p = 1 + e^{-\zeta\pi/\sqrt{1-\zeta^2}}$. Because the process gain and the phase shift were assumed to be ideally compensated, the damping ratio is conservatively chosen as $\zeta = \frac{1}{\sqrt{2}} \approx 0.707$, yielding $K_p = \frac{1}{2}$. The percent overshoot of the step response is 4.3%. In the instantaneous harmonic line current the overshoot is about 10% due to the additional double zero.

Generally, the perfect compensator $\underline{G}_{\text{comp}}$ can not be obtained, but there is always some nonzero γ_{eq} causing cross-coupling between the d- and the q-axes of the harmonic synchronous frame. In a general case, the closed-loop transfer functions are calculated as in (5.22)–(5.25), but using the general expression (5.16) for the $\underline{G}_{\text{eq}}$. The resulting equations are very cumbersome making the analytical forms impractical. Instead, numerical simulations are used to assess the stability in case of an imperfect compensator.

In Fig. 5.8 1 p.u. direct axis reference steps are simulated in cases where $G_{\text{eq}} = 1$ and $\gamma_{\text{eq}} = 0^\circ, -30^\circ$ and -60° . The negative value of γ_{eq} means that the combined effect of the process and the compensator is causing a phase lag to the harmonic space-vector. The simulation shows, that the controller tuning results in an acceptable performance if we have $\gamma_{\text{eq}} \leq -30^\circ$. In the case of $\gamma_{\text{eq}} = -60^\circ$ the system is stable but poorly damped. Since the dynamics are the same regardless of the sign of γ_{eq} , it is recommended that the compensator is tuned to achieve $-30^\circ \leq \gamma_{\text{eq}} \leq 30^\circ$. The gain G_{eq} affects the loop gain similarly with the controller gain K_p , and to ensure stability, it preferably should not be larger than unity.

The transfer function from the load current i_L^ν to the supply current is given as

$$\frac{i_S^\nu}{i_L^\nu} = (\underline{I} + \underline{G}_{\text{PI}}\underline{G}_{\text{eq}}\underline{G}_{\text{lpf}})^{-1} \quad (5.28)$$

and the corresponding injected line current transfer function as

$$\frac{i_2^\nu}{i_L^\nu} = (\underline{I} + \underline{G}_{\text{PI}}\underline{G}_{\text{eq}}\underline{G}_{\text{lpf}})^{-1} \underline{G}_{\text{PI}}\underline{G}_{\text{eq}}\underline{G}_{\text{lpf}} \ , \quad (5.29)$$

which, in fact, is identical with the closed-loop process from the reference current to the estimated current (5.24). This, also, reveals why it is more practical to tune the controllers using the estimated line current dynamics (5.24) instead of the instantaneous line current dynamics (5.22). From the practical viewpoint, the response to the disturbance is more important than the response to the setpoint change, and, hence, it should be considered in the controller tuning. A simulated d-axis load current step is shown in Fig. 5.9 in a case where $\gamma_{\text{eq}} = -30^\circ$.

The effect of the LCL-filter

For the LCL-filter shown in Fig. 4.1(b) on page 46 the transfer function of the converter voltage to the line current is calculated as

$$\frac{i_2(s)}{u_1(s)} = \frac{1}{s^3 L_1 L_2 C_f + s^2 C_f (L_2 R_1 + L_1 R_2) + s(L_1 + L_2 + R_1 R_2 C_f) + R_1 + R_2} \quad (5.30)$$

and the transfer function from the converter current to the line current as

$$\frac{i_2(s)}{i_1(s)} = \frac{1}{s^2 L_2 C_f + s C_f R_2 + 1} \ . \quad (5.31)$$

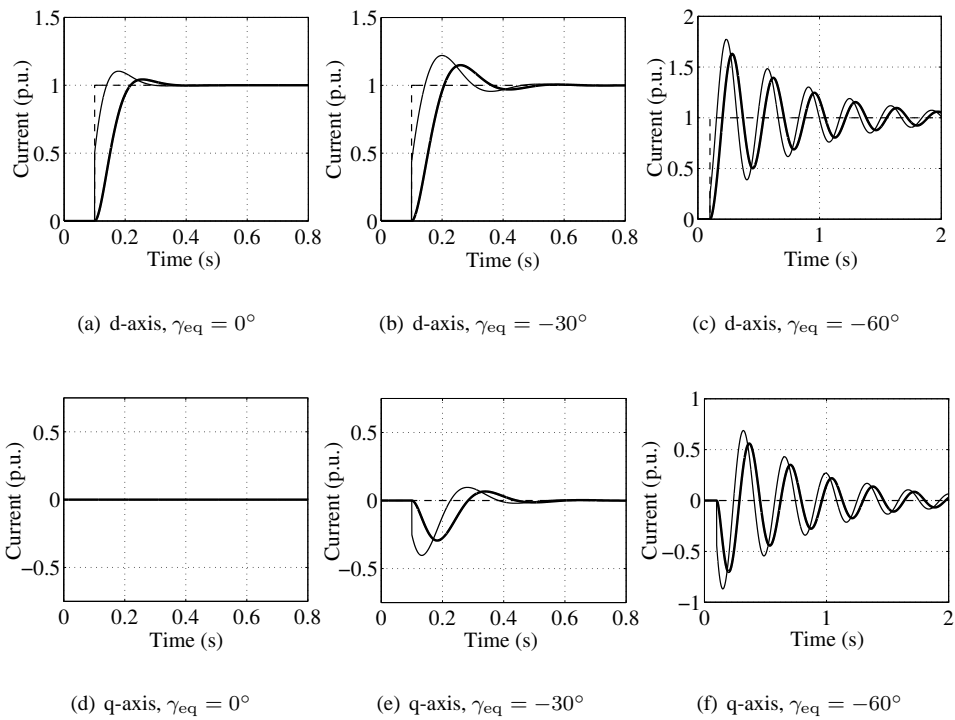


Figure 5.8: Simulated 1 p.u. direct axis steps of the harmonic supply current reference $i_{S,ref}^v$. Top row: d-axis response, Bottom row: q-axis response. Thin: components of supply current i_S^v , Thick: components of estimated supply current $i_{S,est}^v$, Dashed: components of supply current reference $i_{S,ref}^v$. The parameters are $K_p = \frac{1}{2}$, $T_i = 0.025$ s, $\tau = 0.025$ s, $G_{eq} = 1$ and $\gamma_{eq} = 0^\circ, -30^\circ$ and -60° .

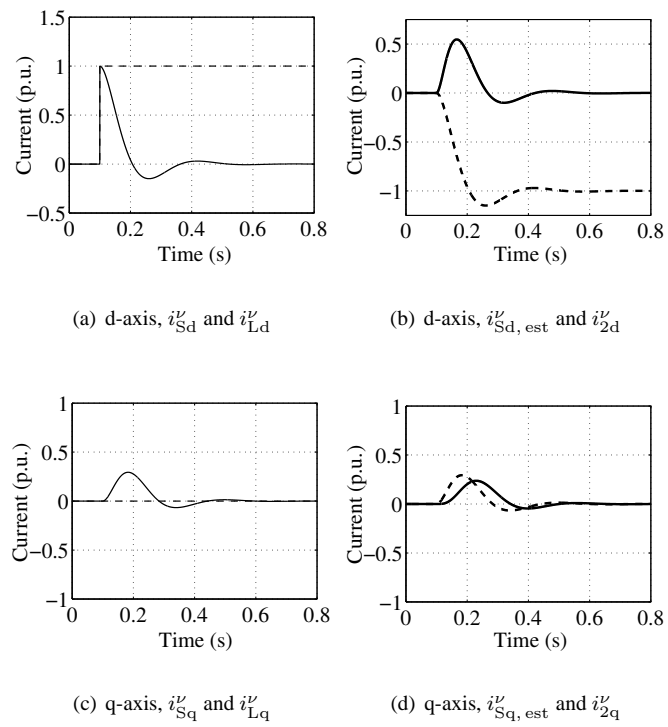


Figure 5.9: Simulated 1 p.u. direct axis step of the load current i_{Ld}' . Thin: components of supply current i_{Sd}' , Thin dashed: components of load current i_{Ld}' , Thick: components of estimated supply current $i_{Sd,est}'$, Thick dashed: components of injected line current i_{2d}' . The parameters are $K_p = \frac{1}{2}$, $T_i = 0.025$ s, $\tau = 0.025$ s, $G_{eq} = 1$ and $\gamma_{eq} = -30^\circ$.

R_1 and R_2 are the equivalent series resistances of the inductors L_1 and L_2 , respectively. The capacitor series resistance was assumed as zero. For the L-filter the transfer functions reduce to

$$\frac{i_2(s)}{u_1(s)} = \frac{1}{sL_1 + R_1} \quad (5.32)$$

and to trivial

$$\frac{i_2(s)}{i_1(s)} \equiv 1, \quad (5.33)$$

since we have $i_2 = i_1$ for the L-filter. The resonance frequencies² are $f_1 = \frac{1}{2\pi\sqrt{\frac{L_1L_2C_f}{L_1+L_2}}}$ in the case of (5.30) and $f_2 = \frac{1}{2\pi\sqrt{L_2C_f}}$ in the case of (5.31). The transfer function from the converter current i_1 to converter voltage u_1 is calculated for LCL-filter as

$$\frac{u_1(s)}{i_1(s)} = \frac{u_1(s)}{i_2(s)} \cdot \frac{i_2(s)}{i_1(s)} \quad (5.34)$$

$$= \frac{s^3L_1L_2C_f + s^2C_f(L_2R_1 + L_1R_2)}{s^2L_2C_f + sC_fR_2 + 1} + \frac{s(L_1 + L_2 + R_1R_2C_f) + R_1 + R_2}{s^2L_2C_f + sC_fR_2 + 1}. \quad (5.35)$$

The resonance occurs at $f_2 = \frac{1}{2\pi\sqrt{L_2C_f}}$ and antiresonance at $f_1 = \frac{1}{2\pi\sqrt{\frac{L_1L_2C_f}{L_1+L_2}}}$. The transfer function (5.35) represents the impedance of the LCL-filter at the converter terminals. The resonance frequency f_1 corresponds to a low-impedance resonance and f_2 to a high-impedance resonance. For the L-filter (5.35) is written as

$$\frac{u_1(s)}{i_1(s)} = sL_1 + R_1. \quad (5.36)$$

The amplitude responses of the transfer functions are graphed in Fig. 5.10. Also the measured points corresponding to the frequencies of the controlled harmonic sequences are shown. The points of $\frac{i_2(s)}{u_1(s)}$ and $\frac{i_2(s)}{i_1(s)}$ were experimentally obtained by using the active filter to generate 0.25 p.u. (6.75 A) harmonic current separately in each controlled harmonic frequency and by measuring the appropriate harmonic currents and voltages with a power analyzer. The points corresponding to $\frac{u_1(s)}{i_1(s)}$ were calculated according to (5.34). The trivial $\frac{i_2(s)}{i_1(s)} \equiv 1$ for the L-filter was not measured. The measurements were performed without the 380/380 V transformer.

The LCL-filter is used to attenuate the frequency components associated to the converter switchings. Typically, the transfer characteristics from the converter voltage to the line current, i.e. Fig. 5.10(a), are considered. For the frequencies higher than the crossing point of the amplitude responses of the L- and LCL-filter, which in Fig. 5.10(a) is about 1285 Hz, the LCL-filter provides a better attenuation than the L-filter. But, for the frequencies lower than that the attenuation of the LCL-filter is lower than that of the L-filter. In the conventional line converter applications, where the sinusoidal line current is desired, this is considered to be a drawback. If there are any lower harmonics, such as 5th, 7th, 11th, etc., present in the

²Here, the resonance frequency (i.e. the frequency corresponding to the maximum value of the frequency response) is approximated with the natural frequency (i.e. the frequency of the natural oscillation if the damping is zero). If the damping is low, which is the case here, the resonance frequency is well approximated by the natural frequency.

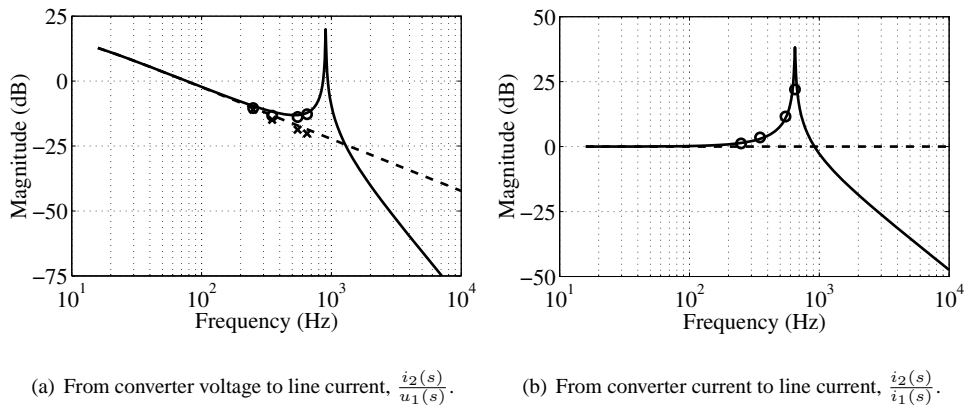
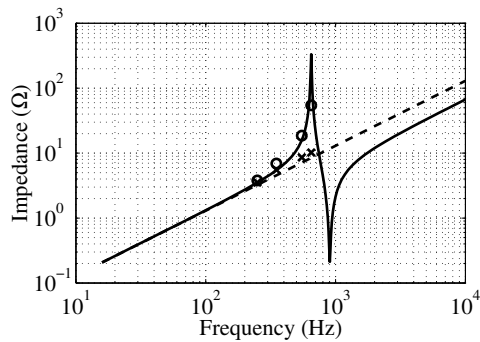
(a) From converter voltage to line current, $\frac{i_2(s)}{u_1(s)}$.(b) From converter current to line current, $\frac{i_2(s)}{i_1(s)}$.(c) From converter current to converter voltage, i.e. impedance at the converter terminals, $\frac{u_1(s)}{i_1(s)}$.

Figure 5.10: Amplitude responses of the LCL-filter (solid line) and the L-filter (dashed line). Measured points corresponding to harmonics 5, 7, 11 and 13 are shown with circles (LCL-filter) and crosses (L-filter). L-filter parameters $L_1 = 2.07$ mH (0.076 p.u.) and $R_1 = 100$ m Ω (0.012 p.u.). LCL-filter parameters $L_1 = 1.07$ mH (0.039 p.u.) and $R_1 = 50$ m Ω (0.0058 p.u.), $C_f = 60$ μ F (0.16 p.u.), $L_2 = 1.0$ mH (0.037 p.u.) and $R_2 = 50$ m Ω (0.0058 p.u.). The resistance values are approximations and used only in the amplitude response calculations. The resonance frequencies are $f_1 = 904$ Hz and $f_2 = 650$ Hz.

modulated voltage the LCL-filter provides less attenuation than the L-filter with equal inductance. In the active filter application, however, the lower attenuation may be regarded also as a positive feature, if the intentionally generated harmonics reside in that area. With the LCL-filter the converter needs to generate a lower amplitude of a harmonic voltage to produce the harmonic line current compared to the L-filter case. It follows that the dc-link voltage that is required to produce a certain line current harmonic is lower with the LCL-filter than with the L-filter.

Let us consider the 13th harmonic. We have measured $\frac{i_2(j2\pi \cdot 50 \cdot 13)}{u_1(j2\pi \cdot 50 \cdot 13)} = 0.23 \frac{\text{A}}{\text{V}}$. Accordingly, in order to generate 6.75 A RMS (0.25 p.u.) of 13th harmonic current, the converter has to generate a corresponding harmonic voltage with the amplitude of $\frac{\sqrt{2} \cdot 6.75 \text{ A}}{0.23 \frac{\text{A}}{\text{V}}} = 42 \text{ V}$. The converter operates in the limit of the linear modulation range if the dc-link voltage is $u_{\text{dc}} = \sqrt{3}(u_2 + 42 \text{ V})$. With a grid peak phase voltage of $u_2 = 327 \text{ V}$ the dc-link voltage corresponding to the linear modulation range is calculated as $u_{\text{dc}} = 639 \text{ V}$. Similarly, for the L-filter, we have $\frac{i_2(j2\pi \cdot 50 \cdot 13)}{u_1(j2\pi \cdot 50 \cdot 13)} = 0.098 \frac{\text{A}}{\text{V}}$ and the corresponding dc-link voltage is found as $u_{\text{dc}} = 735 \text{ V}$. The difference is significant. However, the linear modulation range does not represent the lowest practical active filter dc-link voltage in all cases. As explained in Appended Publication III, a harmonic overmodulation phenomenon may allow the active filter dc-link voltage to be lowered significantly below the linear modulation range limit. In the case above, in practice the converter with the LCL-filter was stable with a dc-link voltage of $u_{\text{dc}} = 600 \text{ V}$ and with the L-filter with $u_{\text{dc}} = 640 \text{ V}$.

The LCL-filter may considerably amplify the harmonic current. This is evident in Fig. 5.10(b). In the frequencies close to the resonance frequency, considerable amplifications are obtained, e.g., for the 13th harmonic the amplification³ is 12.6. The current amplification is advantageous because it diminishes the converter current and reduces associated losses. The impedance of the LCL-filter at the converter terminals is depicted in Fig. 5.10(c). It is seen to increase considerably toward the high-impedance resonance frequency.

5.5.3 Practical verification

The practical verification of the controller tuning was performed with both L- and LCL-filters. The inductance of the L-filter was $L_1 = 2.07 \text{ mH}$ (0.076 p.u.) and the parameters of the LCL-filter were $L_1 = 1.07 \text{ mH}$ (0.039 p.u.), $C_f = 60 \mu\text{F}$ (0.16 p.u.) and $L_2 = 1.0 \text{ mH}$ (0.037 p.u.). The gain and the phase shift of the process model G_{proc} were determined with the open-loop process of the control system in Fig. 5.7. The open-loop system was obtained by disconnecting the feedback loop. With each individual controlled harmonic sequence the gain and the phase shift of the compensator G_{comp} were adjusted to find a perfect compensation in a case where the harmonic d-axis current reference was 0.25 p.u. The measurements were performed with and without the additional 380/380 V transformer shown in Fig. 5.5. The results are shown in Tab. 5.1. Also, the amplitude of the harmonic current reference was varied. The experiments indicated that the gain G_{proc} is dependent on the amplitude of the harmonic current. The gain G_{proc} decreases with the increasing harmonic amplitude, probably because of the nonlinearities associated with the fundamental wave current vector control with oscillating references. In the case of the L-filter and the 5th negative sequence harmonic, G_{proc} was 0.9 with 0.5 p.u. harmonic current reference and 0.75 with 1 p.u. harmonic current reference. Another factors affecting the gain G_{proc} are the undesired converter voltage

³Numerical values are shown later in Tab. 5.2.

harmonics and cross-coupling effects between the generated individual harmonic sequences. Because of these effects in some occasions there may be slightly different loop gains in the d- and q-directions. The modeling uncertainties justify conservative tuning of the controllers.

The additional 380/380 V transformer changes the process. Theoretically, the resonance frequency is brought to lower frequencies because the equivalent transformer series inductance is added to the line filter inductance L_2 . The measurement shown in Tab. 5.2 confirms this. The identified compensator parameters in Tab. 5.1 show that the source impedance affects the tuning of the harmonic controllers. Again, the conservative controller design is emphasized. However, the effect of the source impedance variations may be reduced by leaving more gap between the resonance frequency of the LCL-filter and the highest controlled harmonic.

With the L-filter the gain G_{proc} is approximately unity with all controlled harmonic sequences. With the LCL-filter that is not true. We may characterize G_{proc} as the steady-state gain from the harmonic converter current reference to the harmonic line current, that is

$$G_{\text{proc}} = \frac{i_2(j\omega)}{i_{1,\text{ref}}(j\omega)}. \quad (5.37)$$

The LCL-filter has a high current amplification $\frac{i_2(j\omega)}{i_1(j\omega)}$ near the resonance frequency, as shown in Fig. 5.10(b) and in Tab. 5.2. This amplification shows up only partially in G_{proc} , which may be seen by comparing Tabs. 5.1 and 5.2. Observe that G_{proc} may be divided into the effect of the LCL-filter current amplification and into the effect of the fundamental wave current control, modulation, etc., as

$$G_{\text{proc}} = \frac{i_2(j\omega)}{i_{1,\text{ref}}(j\omega)} = \underbrace{\frac{i_2(j\omega)}{i_1(j\omega)}}_{\text{LCL-filter current amplification}} \cdot \underbrace{\frac{i_1(j\omega)}{i_{1,\text{ref}}(j\omega)}}_{\text{Current control, modulation, etc.}}, \quad (5.38)$$

With the LCL-filter $\frac{i_1(j\omega)}{i_{1,\text{ref}}(j\omega)}$ decreases in harmonic frequencies and partially offsets the gain of $\frac{i_2(j\omega)}{i_1(j\omega)}$. The reason for decreasing $\frac{i_1(j\omega)}{i_{1,\text{ref}}(j\omega)}$ is the increasing impedance, shown in 5.10(c), that the converter experiences in the harmonic frequencies. The increased impedance affects the properties of the current control—with the LCL-filter the converter has to produce more corresponding harmonic voltage than with the L-filter in order to produce a given harmonic converter current. It follows that a given oscillating error signal of the current vector control corresponding to a harmonic frequency produces more harmonic current with the L-filter than with the LCL-filter. In effect, this shows up as the decreasing gain of $\frac{i_1(j\omega)}{i_{1,\text{ref}}(j\omega)}$. This may also be seen by writing

$$\frac{i_1(j\omega)}{i_{1,\text{ref}}(j\omega)} = \underbrace{\frac{i_1(j\omega)}{u_1(j\omega)}}_{\text{Admittance}} \cdot \frac{u_1(j\omega)}{i_{1,\text{ref}}(j\omega)}, \quad (5.39)$$

where the effect of the impedance seen from the converter bridge terminals (written as admittance, i.e. the inverse of the impedance) and the effect of the control system transfer characteristics from the current reference to converter voltage have been separated. The admittance behaves inversely to the impedance shown in 5.10(c) and, hence, decreases in the controlled harmonic frequencies.

Furthermore, substituting (5.39) to (5.38) gives

$$G_{\text{proc}} = \frac{i_2(j\omega)}{i_{1,\text{ref}}(j\omega)} = \frac{i_2(j\omega)}{u_1(j\omega)} \cdot \frac{u_1(j\omega)}{i_{1,\text{ref}}(j\omega)}, \quad (5.40)$$

Table 5.1: Parameters of the process model (5.14) determined with 0.25 p.u. harmonic d-axis current change. Dc-link voltage $u_{dc} = 750$ V was used. In the L-filter case the effect of the 380/380 V transformer was negligible.

| Harmonic sequence | L-filter | | LCL-filter | | LCL-filter [†] | |
|-------------------|------------|-----------------|------------|-----------------|-------------------------|-----------------|
| | G_{proc} | γ_{proc} | G_{proc} | γ_{proc} | G_{proc} | γ_{proc} |
| 5- | 1.0 | -60° | 1.1 | -60° | 1.1 | -75° |
| 7+ | 1.0 | -70° | 1.4 | -80° | 1.3 | -95° |
| 11- | 1.0 | -135° | 2.6 | -175° | 1.8 | -220° |
| 13+ | 1.0 | -165° | 3.6 | -240° | 1.1 | -270° |

[†]Fed through a 54 kVA 380/380 V transformer

Table 5.2: Measured $\frac{i_2(s)}{i_1(s)}$ current amplification of the LCL-filter. The measurement is performed with 6.75 A RMS line current magnitude. LCL-filter parameters are $L_1 = 1.07$ mH (0.076 p.u.), $C_f = 60$ μ F (0.16 p.u.), $L_2 = 1.0$ mH (0.037 p.u.).

| Harmonic sequence | Gain $\frac{i_2(s)}{i_1(s)}$ | Gain $\frac{i_2(s)}{i_1(s)}$ [†] |
|-------------------|------------------------------|---|
| 5- | 1.2 | 1.4 |
| 7+ | 1.5 | 1.8 |
| 11- | 3.8 | 9.4 |
| 13+ | 12.6 | 1.8 |

[†]Fed through a 54 kVA 380/380 V transformer

which shows that G_{proc} may also be expressed using the LCL-filter transfer function from the converter voltage to the line current and the transfer characteristics from the converter current reference to the converter voltage. However, in the control system of the DTC-converter the converter voltage is an implicit quantity, which is not directly controlled or observed.

Fig. 5.11 shows the performance of the closed-loop control in a 0.25 p.u. d-axis reference step change. In Fig. 5.11(a) the compensator is tuned to achieve approximately $G_{eq} = 1$ and $\gamma_{eq} = 0^\circ$. The measurement shows that the response of the control system performance is very accurately represented by the model used in the design. Fig. 5.11(b) shows the case where the 60° phase shift of the process is not compensated, representing the case where $\gamma_{eq} = -60^\circ$. Also in this case, the correspondence between the measurement and the model output is good. A slight difference in the oscillating frequency is observed, which may be caused by the inaccuracies of the process model G_{proc} used, e.g., the nonlinear gain of the actual model. The difference is, however, insignificant from the practical point of view.

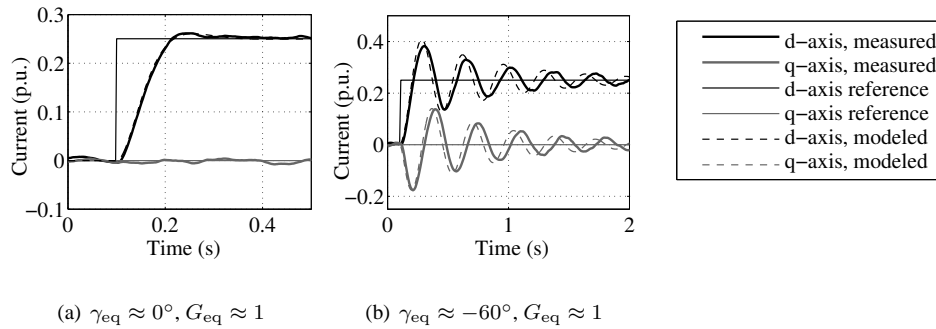


Figure 5.11: Measured 0.25 p.u. d-axis steps of the 5th negative sequence harmonic line current reference. The L-filter and $u_{dc} = 750$ V were used.

5.6 Voltage feedback active filtering

5.6.1 Operation principle of voltage feedback active filter

The voltage feedback active filter focuses on improving the quality of the voltage rather than the quality of the grid current. The voltage feedback active filter analyzes the grid voltage harmonics and injects harmonic line currents that are adjusted to mitigate them. The voltage feedback active filter is discussed in Appended Publications IV and V. Previously, voltage feedback active filtering was proposed by Brogan and Yacamini (1998, 1999, 2000, 2003) and Wheeler et al. (1997). In (Takeshita et al., 2001) and (Takeshita and Matsui, 2003) the manipulation of the converter line current waveform to provide voltage harmonic suppression is proposed but a complete voltage feedback active filter system is not considered. The grid impedance is a very important quantity in the operation of the voltage feedback active filter. The injected harmonic currents flow through the equivalent grid impedance and cause harmonic voltage drops, which are supposed to cancel the existing harmonic voltages. The grid impedance causes a phase shift between the injected current and the resulting voltage drop. This phase shift has to be taken into account in the control system. Appended Publication V introduces a measurement-based method to identify the grid impedance. Also, in the controller tuning the absolute value of the grid impedance has to be taken into account.

The voltage distortion of the PCC has two origins. Typically, the majority of it is originating from the local nonlinear loads. However, if the voltage on the primary side of the transformer is nonsinusoidal, this distortion is transmitted to the secondary side. The distortion that is coming through the transformer is called background distortion. The voltage feedback active filter can compensate both distortions equally. In some cases, however, the compensation of the background distortion may be undesirable, particularly if it is produced by other users of electrical power. Brogan and Yacamini (2003) proposed that the background distortion can be measured and excluded from the compensation. The origins of the distortion and the compensation with the voltage feedback active filter are illustrated in Fig. 5.12.

It is important to notice that with a voltage feedback active filter the supply current is not sinusoidal if the background distortion is compensated. To compensate the background distortion

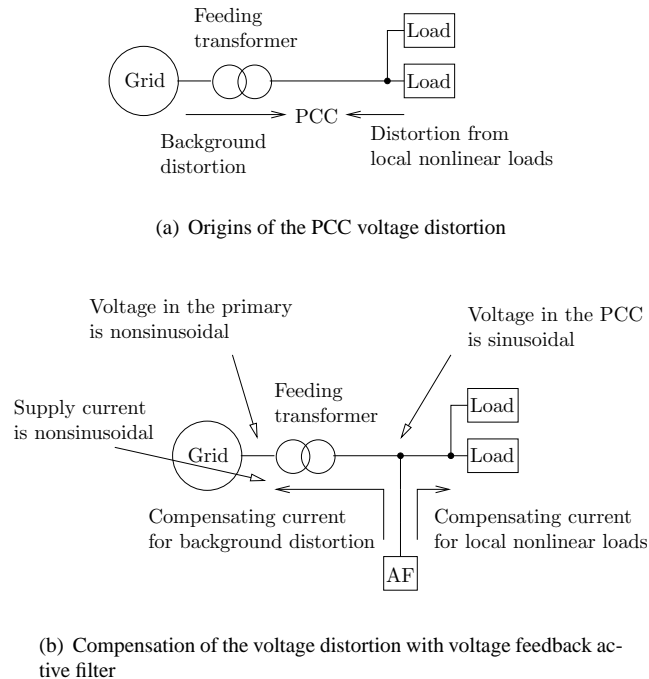


Figure 5.12: The voltage feedback active filter can compensate both the local distortion and the background distortion.

the voltage feedback active filter has to inject harmonic currents through the transformer, which produce suitable compensating voltage drops across the transformer impedance. However, the original cause of the supply current harmonics is the distorted primary voltage. If the magnetizing current is disregarded, the harmonic current flow through the transformer is determined by the differences of the harmonic voltages across the transformer. The supply current harmonics flowing through the transformer are the same regardless of the method by which the secondary voltage is brought sinusoidal. If the primary voltage is sinusoidal the voltage feedback active filter does not inject harmonics through the transformer. Conceptually, the shunt passive filter works similarly to the voltage feedback active filter and reacts to harmonic voltages rather than to harmonic currents. Clearly, if the background distortion is present, it is pointless to assess the supply current harmonics or the supply current THD as a figure of merit in a system comprising a voltage feedback active filter. Hence, the current harmonic standards are not suitable for such systems.

If the short circuit power of the grid is large compared to the nominal power of the active filter (i.e. a strong grid) the voltage feedback concept may not be favored. In such an environment the voltage feedback active filter has only a small effect on the grid voltage. In the same environment, however, the nonlinear loads do not have as big an impact on the voltage quality as in a weaker grid. In the laboratory experiments, the measurements were carried out with the ratio of the grid short circuit power to the active filter nominal power of 51.

Applications of the voltage feedback active filter may be found in industrial environments and

in the area of power distribution. In industrial environment, the voltage feedback approach may be advantageous because the nonlinear load current does not have to be measured. This provides freedom to the selection of the active filter installation site. Moreover, one voltage feedback active filter can compensate several nonlinear loads situated in different locations in the same secondary. This, however, involves transfer of harmonic currents in the power cables. Installation of the voltage feedback active filter in a power distribution system was considered by Akagi (1997). Inzunza and Akagi (2004) proposed a voltage feedback active filter, which is capacitively coupled directly to a 6.6 kV power line. The capacitive coupling eliminates the need of a step-down transformer. Emanuel and Yang (1993) analyzed different compensation strategies in the case of a power system with nonsinusoidal voltage. They believe that the compensation of the voltage harmonics is a better control target than the sinusoidal line current or unity power factor. Further, they suggest that the minimum voltage distortion in a large customer bus may yield minimum harmonic power loss in the system. Interesting applications of voltage feedback active filtering may also be found in the area of distributed generation. Jóos et al. (2000) discussed the potential of distributed generating resources to provide ancillary services such as reactive power generation, or consumption, and harmonic filtering.

5.6.2 Control system analysis

In order to achieve the voltage feedback active filter functionality the method of harmonic synchronous reference frames is applied to the control of voltage harmonics. A block diagram presentation is shown in Fig. 5.13. First, the measured grid voltage is transformed to the harmonic synchronous frame. Then, the low-pass filtering and the PI-control are performed similarly as in the harmonic current control case shown in Fig. 5.6. After the PI-control, the effect of the grid impedance is compensated using a compensator $\underline{G}_{Z_{\text{grid}}}$. The resulting harmonic synchronous frame grid current references $i_{2d, \text{ref}}$ and $i_{2q, \text{ref}}$ are fed as inputs to the harmonic current control system in Fig. 5.6.

The resulting system has a cascaded structure with inner harmonic current control loop and outer harmonic voltage control loop. A block diagram representing the control system of a grid voltage harmonic sequence ν is shown in Fig. 5.14. The low-pass filter $\underline{G}_{\text{lpf}}$ and the PI-controller $\underline{G}_{\text{PI}}$ are similar to the current harmonic control case in (5.17) and (5.18). The controller parameters are, naturally, different, but the same low-pass filtering time constants are used. The active filter-injected line current i_2^ν causes a voltage drop of

$$\Delta \underline{u}_2^\nu = \underline{Z}_{\text{grid}} i_2^\nu, \quad (5.41)$$

where $\underline{Z}_{\text{grid}}$ is the effective grid impedance (Thevenin impedance) seen from the active filter point of connection. If an inductive grid impedance is assumed, the voltage drop vector \underline{u}_2^ν is leading the injected current vector i_2^ν by 90 degrees. Hence, in that case, we have

$$\underline{Z}_{\text{grid}} = Z_{\text{grid}} e^{j\phi_{\text{grid}}} = \begin{bmatrix} Z_{\text{grid}} \cos(\phi_{\text{grid}}) & -Z_{\text{grid}} \sin(\phi_{\text{grid}}) \\ Z_{\text{grid}} \sin(\phi_{\text{grid}}) & Z_{\text{grid}} \cos(\phi_{\text{grid}}) \end{bmatrix} \Big|_{\phi_{\text{grid}} = \frac{\pi}{2}}. \quad (5.42)$$

The electrical dynamics are neglected, as in the case of $\underline{G}_{\text{proc}}$ in (5.14), and the grid impedance is modeled as a steady-state gain and a phase shift. The effect of $\underline{Z}_{\text{grid}}$ on the voltage harmonic control system is analogous to the effect of $\underline{G}_{\text{proc}}$ on the current harmonic control

system. The phase shift causes a cross-coupling between the axes and the gain affects the loop gain and changes the control loop tuning. The effect of the grid impedance is compensated with a compensator $\underline{G}_{Z_{\text{grid}}}$, which is determined to approximate the inverse of the grid impedance $(\underline{Z}_{\text{grid}})^{-1}$. The gain and the phase shift of the grid impedance at the compensated frequencies are obtained with the method presented in Appended Publication V.

From the block diagram of the voltage harmonic control, shown in Fig. 5.14, the transfer function from the reference to the output is calculated as

$$\frac{\underline{u}'_2}{\underline{u}'_{2,\text{ref}}} = (\underline{I} + \underline{G}_{\text{PI}}\underline{G}_{Z_{\text{grid}}}\underline{G}_{\text{cl}}\underline{Z}_{\text{grid}}\underline{G}_{\text{lpf}})^{-1}(\underline{G}_{\text{PI}}\underline{G}_{Z_{\text{grid}}}\underline{G}_{\text{cl}}\underline{Z}_{\text{grid}}), \quad (5.43)$$

and from the reference to the estimated harmonic voltage as

$$\frac{\underline{u}'_{2,\text{est}}}{\underline{u}'_{2,\text{ref}}} = (\underline{I} + \underline{G}_{\text{PI}}\underline{G}_{Z_{\text{grid}}}\underline{G}_{\text{cl}}\underline{Z}_{\text{grid}}\underline{G}_{\text{lpf}})^{-1}(\underline{G}_{\text{PI}}\underline{G}_{Z_{\text{grid}}}\underline{G}_{\text{cl}}\underline{Z}_{\text{grid}}\underline{G}_{\text{lpf}}). \quad (5.44)$$

The transfer function from the disturbance to the output is

$$\frac{\underline{u}'_2}{\underline{u}'_{2,\text{orig}}} = (\underline{I} + \underline{G}_{\text{PI}}\underline{G}_{Z_{\text{grid}}}\underline{G}_{\text{cl}}\underline{Z}_{\text{grid}}\underline{G}_{\text{lpf}})^{-1}. \quad (5.45)$$

In a cascaded control structure the inner loop should be faster than the outer loop. Åström and Hägglund (1995) give the rule of thumb that the average residence times should have a ratio of at least 5. Let us consider the harmonic voltage control process with a perfect compensator, that is, $\underline{G}_{Z_{\text{grid}}} = (\underline{Z}_{\text{grid}})^{-1}$. If the inner current control loop is approximated as the unity transfer function the dynamics of the voltage control loop (5.44) are similar to the current control loop (5.24). To make the voltage control loop slower than the current control loop the controller integration time is selected five times longer than in the current control loop. The same controller gain parameters are used. With this selection the 2% settling time of the voltage control loop is 2 s, which is about ten times longer than the settling time of the current control loop. Also, the voltage control loop is stable if both the current control loop compensator $\underline{G}_{\text{comp}}$ and the voltage control loop compensator $\underline{G}_{Z_{\text{grid}}}$ have a 30° phase error. Further, the stability is not lost if both the current control loop and the voltage control loop have the loop gains doubled.

Fig. 5.15 shows the theoretical and measured voltage control loop responses in the reference step changes of the 5th negative sequence control loop. The line converter was connected to the 380/380 V transformer secondary and the nonlinear load was not present. The magnitude of the identified impedance at the 5th harmonic frequency was about 0.1 p.u. (0.8 Ω) and the phase shift about 90 degrees. The impedance measurements are shown in Fig. 4(a) in Appended Publication V. The correct compensator for the grid impedance is hence $\underline{G}_{Z_{\text{grid}}} = 10e^{-\frac{\pi}{2}}$. Fig. 5.15 shows a step with the correct compensator and a step with a compensator that has a 60° phase error. Also, a step is shown with a compensator, which has a 7 times higher gain than the designed value. In all cases, the voltage control loop is stable, which shows that the design is robust against the parameter variations. Also Fig. 5.15(c) demonstrates that, if needed, the voltage harmonic control may achieve considerably better dynamic performance than what the designed control tuning delivers. However, it is believed that from the practical point of view the robust operation is more important than the utmost dynamic performance. Also, the standards typically regulate the steady-state distortions rather than transients, which supports the choice of conservative design.

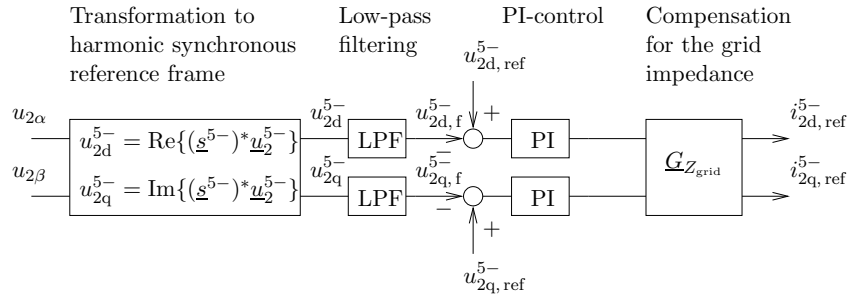


Figure 5.13: Control of the 5th negative sequence grid voltage harmonic with the method of harmonic synchronous reference frames.

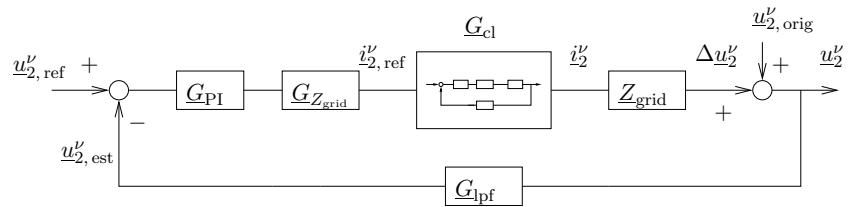


Figure 5.14: Block diagram representing the control process of the voltage harmonic sequence ν in the harmonic synchronous reference frame. The current harmonic control included in block G_{cl} is similar to Fig. 5.7 with the exception that the load current is absent. $u_{2,orig}^{\nu}$ is an intrinsic voltage, which summed with the active filter caused voltage drop Δu_2^{ν} constitutes u_2^{ν} .

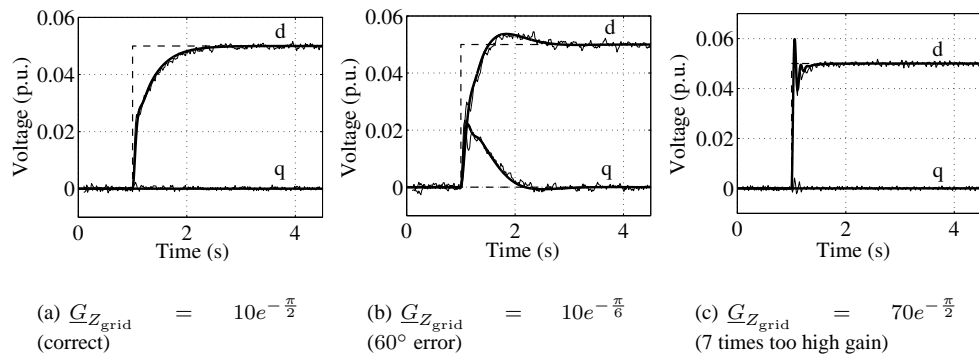


Figure 5.15: 5th harmonic negative sequence line voltage d-axis reference steps of 0.05 p.u. (20 V RMS) with different $G_{Z_{grid}}$ compensators. Thick: theoretical, Thin: measured, Dashed: References. LCL-filter and $u_{dc} = 750$ V were used.

5.7 Time-domain active filtering

5.7.1 Implementation of the control system

The time-domain active filter control was implemented using the FBD-method introduced in section 3.2.1 on page 32. The configuration is presented in Fig. 5.4(c). The unwanted current components are extracted from the load current i_L and the active filter is used to inject the current i_1 , which cancels the unwanted components from the supply current i_S . The active components of the load current are calculated as

$$i_{L\alpha, a} = Gu_{2\alpha} \quad (5.46)$$

$$i_{L\beta, a} = Gu_{2\beta} , \quad (5.47)$$

where the active conductance G shown in (3.35) is estimated as

$$G = \frac{\frac{1}{T} \int_{t-T}^t (u_{2\alpha} i_{L\alpha} + u_{2\beta} i_{L\beta}) dt}{\text{LPF}(u_{2\alpha}^2 + u_{2\beta}^2)} . \quad (5.48)$$

In the nominator, the mean instantaneous collective power $\overline{p_\Sigma(t)}$ is estimated by calculating a moving average over one fundamental cycle (cycle time T). In the denominator, the mean value of the squared collective instantaneous voltage $\overline{u_\Sigma^2}$ is estimated by low-pass filtering the instantaneous value of the squared length of the grid voltage space-vector. A first order low-pass filter with a time constant of 20 ms was used. The calculation of (5.48) was implemented in a 2 ms time level. The moving average calculation was realized using a circular buffer of 10 samples. In the denominator, the moving average calculation was replaced with a low-pass filter in order to achieve a simpler implementation. The simplification is based on the assumption of a relatively stable and slowly varying grid voltage. Because the space-vector representation is used in estimating the active current, the zero-sequence components of the load current are excluded from the analysis. This, however, is not a drawback since a three-phase three-wire active filter can only affect the positive and negative sequence components. The calculation of (5.46) and (5.47) was implemented in a 100 μ s time level. The load current vector \underline{i}_L and the grid voltage vector \underline{u}_2 were measured with 100 μ s sample time.

The nonactive current components of the load current are calculated as

$$i_{L\alpha, na} = i_{L\alpha} - i_{L\alpha, a} \quad (5.49)$$

$$i_{L\beta, na} = i_{L\beta} - i_{L\beta, a} . \quad (5.50)$$

According to (3.37) the nonactive current is composed of the variation current and the zero-power current. The active filter harmonic current reference in the $\alpha\beta$ -co-ordinates is obtained simply by changing the sign of the load nonactive current

$$i_{1\alpha, href} = -i_{L\alpha, na} \quad (5.51)$$

$$i_{1\beta, href} = -i_{L\beta, na} . \quad (5.52)$$

The harmonic current references are transformed to the synchronous frame similarly with the fundamental current references (4.50) and (4.51) on page 58,

$$i_{1d, href} = \frac{\psi_{1\alpha} i_{1\alpha, href} + \psi_{1\beta} i_{1\beta, href}}{\psi_1} \quad (5.53)$$

$$i_{1q, href} = \frac{\psi_{1\alpha} i_{1\beta, href} - \psi_{1\beta} i_{1\alpha, href}}{\psi_1} . \quad (5.54)$$

In the synchronous frame the total current references are calculated by summing the fundamental and harmonic current references

$$\dot{i}_{1d, \text{ref}, \text{tot}} = \dot{i}_{1d, \text{ref}} + \dot{i}_{1d, \text{href}} \quad (5.55)$$

$$\dot{i}_{1q, \text{ref}, \text{tot}} = \dot{i}_{1q, \text{ref}} + \dot{i}_{1q, \text{href}} \quad (5.56)$$

The total current references are passed to the current vector control. The current reference calculation was implemented in the 100 μs time level. The calculation of the harmonic current references is graphically shown in Fig. 5.16(b).

In the time-domain method the control delay has a very big impact on the performance of the active filter. Because of the discrete sampling of the load current and the time needed to calculate the current reference, the active filter current reference is always realized later than needed. Methods to compensate the control delay has been presented, e.g., in (Svensson and Ottersten, 1999) and (Sensarma et al., 2000). In steady state, the control delay may be compensated by storing samples of the previous cycle and using them in prediction of the load current at the time instant needed. In the practical implementation, no delay compensation was used, which degrades the steady-state compensation performance.

5.7.2 Hysteresis current control

The dynamic performance of the DTC-based current control, described in section 4.3, is based on the PI current controllers. In the active filtering application the current references contain a significant amount of harmonics. The PI-controllers do not perform satisfactorily if the setpoint is not a constant in steady state (Harnefors, 1997; Rowan and Kerkman, 1986). Hence, as proposed by Buso et al. (1998a), a hysteresis current control was used.

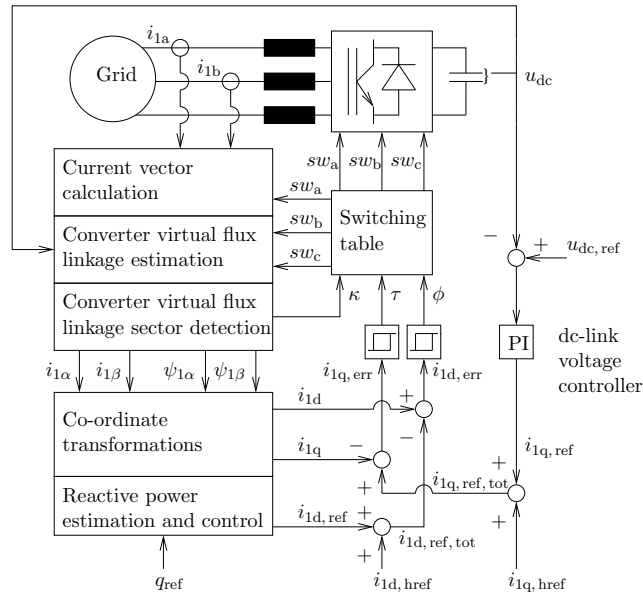
The hysteresis current control was implemented with the DTC hysteresis comparators as described in (Tarkiainen et al., 2003a). The idea of the hysteresis current control in the synchronous frame is presented previously, e.g., by Kaźmierkowski et al. (1991). Kaźmierkowski et al. (1991), however, use a rotor flux linkage orientation instead of the CFO and a switching table that is different from the switching table used with DTC.

The measured converter current vector is transformed to the CFO frame corresponding to (4.50) and (4.51). Current errors are calculated as

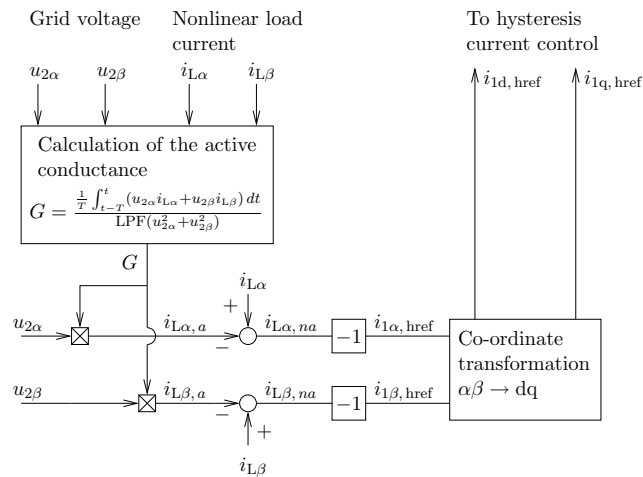
$$\dot{i}_{1d, \text{err}} = -(\dot{i}_{1d, \text{ref}} - \dot{i}_{1d}) \quad (5.57)$$

$$\dot{i}_{1q, \text{err}} = \dot{i}_{1q, \text{ref}} - \dot{i}_{1q} \quad (5.58)$$

In the d-direction the sign of the output is inverted correspondingly to the PI current controller output in (4.56) on page 61. The error signals are fed to the hysteresis comparators. In the 25 μs time level the switch combination is determined similarly with the DTC method, but with the exception that the flux linkage amplitude error and the instantaneous power (or torque) error are replaced with the d- and the q-axis current errors, respectively. The block diagram representation of the current hysteresis control is shown in 5.16(a).



(a) Hysteresis current control



(b) Calculation of the harmonic current references with the FBD-method.

Figure 5.16: Time-domain active filter control system.

5.8 Experimental results of the active filtering

5.8.1 Steady-state measurements

"Today's scientists have substituted mathematics for experiments, and they wander off through equation after equation, and eventually build a structure which has no relation to reality."

– Nikola Tesla in Modern Mechanix and Inventions, July, 1934

Steady-state measurements were carried out with the test setup shown in Fig. 5.5. All three control approaches, the frequency-domain, voltage feedback and time-domain-based methods were measured. The dc-link voltage reference of 630 V was used except in two voltage feedback measurements (Figs. 5.24 and 5.25), in which the dc-link voltage setpoint was 680 V. In the voltage feedback measurements the background distortion was compensated in addition to the nonlinear load originating distortion. This required increasing of the magnitudes of the injected harmonic currents, which, in turn, required a higher dc-link voltage. All cases were measured with and without the dc-load of the active filter. The cases without the dc-load correspond to the conventional use of the active filters, in which the only purpose of using the active filter is to compensate deficiencies of nonlinear load current. The cases measured with the dc-load represent the application where the active filtering is an add-on feature to the line converter. The primary task is to regulate the dc-link voltage and supply dc-loads but, additionally, harmonic currents can be injected to compensate nonlinear load harmonics. The dc-load used was a 20 Ω resistor, which with 630 V dc-link voltage correspond to a 20 kW load power. In cases where the dc-link voltage was 680 V, the dc-load resistor was increased to 30 Ω to prevent severe overloading of the line converter. The 30 Ω resistor imposed a 15 kW load to the line converter. An average switching frequency of 4 kHz was used, except in the time-domain active filtering where the switching frequency was about 3 kHz even though the hysteresis bands were set to have zero widths. In the cases of the frequency-domain method and the time-domain method the fundamental wave reactive power of the nonlinear load was compensated as well. With the voltage feedback method this is impossible because the load current is not measured. In the case of the voltage feedback method the active filter fundamental wave reactive power was controlled to zero.

The following 11 measurements were performed:

1. Grid voltage with both nonlinear load and active filter disconnected: Fig. 5.17
2. Grid voltage with nonlinear load connected and active filter disconnected: Fig. 5.18
3. Frequency-domain active filtering, LCL-filter: Fig. 5.19
4. Frequency-domain active filtering with dc-load, LCL-filter: Fig. 5.20
5. Frequency-domain active filtering, L-filter: Fig. 5.21
6. Frequency-domain active filtering with dc-load, L-filter: Fig. 5.22
7. Voltage feedback active filtering, compensation of the background distortion, LCL-filter: Fig. 5.23
8. Voltage feedback active filtering, compensation of the nonlinear load and background distortion, LCL-filter: Fig. 5.24
9. Voltage feedback active filtering with dc-load, compensation of the nonlinear load and background distortion, LCL-filter: Fig. 5.25

10. Time-domain active filtering, L-filter: Fig. 5.26
11. Time-domain active filtering with dc-load, L-filter: Fig. 5.27

Measurements 1 and 2 serve as reference points. Measurement 1 shows the background distortion, which is transmitted through the 380/380 V transformer and is present in the primary side voltage. The measured case represents a very typical background distortion in the laboratory establishment in question. The feeding 1 MVA transformer was only lightly loaded and, evidently, the background distortion comes from the medium voltage network. Measurement 2 presents the case where no active filtering actions were taken. Note, that in the measurements 1 and 2 the LCL-filter was also disconnected from the grid.

Measurements 3–6 may be used to evaluate the effect of the active filter LCL-line filter. Measurements 5, 6, 10 and 11 may be compared to evaluate the steady-state performance of the frequency-domain and the time-domain control approaches. Measurements 3 and 8 may be compared to evaluate the effects of the voltage feedback approach. Also, measurements 4 and 9 may be compared noting that the dc-loads are different (20 kW in measurement 4 versus 15 kW in measurement 9).

The data were sampled with a 250 kHz sample rate and a record length of 400 ms (i.e. 20 fundamental cycles) using a Yokogawa PZ4000 power analyzer. Current transformers (Goerz Electro GE 4461, 100 A/5 A) were used in the current measurements. The current transformers used have found to perform acceptably in measurements involving inverter-fed motors. Manula (1999) measured the accuracy of current transformers used in LUT with 1 A primary current in frequencies 50–5000 Hz and with 10 A primary current in frequencies 50 Hz and 1000 Hz. The results indicate very small errors ($\leq 0.1\%$). The measured current transformers were not the same that was used in the measurements of this dissertation, but the measured accuracy indicates that current transformers may be accurate in frequencies higher than the power frequency.

The frequency-domain representations were calculated by applying DFT to the sample of 20 cycles. A rectangular window was used. As a result, frequency components from 0 to 125 kHz with 2.5 Hz separation were obtained. The components corresponding to the harmonic frequencies were picked up from the DFT output. Each measured waveform is portrayed in the time-domain and in the frequency-domain. In the time-domain presentations two fundamental cycles are shown. The frequency-domain figures show harmonics up to the 40th component.

Five numerical parameters were calculated from the data samples. The total harmonic distortions up to the 40th harmonic (THD_{40}) and up to the 200th harmonic (THD_{200}) were evaluated using (2.19) on page 24. The fundamental wave amplitude was obtained directly from the DFT output and the fundamental wave RMS (FW RMS) was calculated by dividing it by $\sqrt{2}$. The true RMS value was calculated using (2.25) with $T_{\text{end}} = 0.4$ s. From the fundamental wave RMS value and the true RMS value the THD' was evaluated using (2.24). Several THD indices help in assessing where the distortion is located in the frequency-domain. The THD_{40} and the THD_{200} represent the harmonic distortion up to 2 kHz and 10 kHz, respectively. The THD' covers all harmonic distortion and all interharmonic distortion. The difference between THD_{40} and THD_{200} reveals that there is harmonic distortion in the frequency band 2–10 kHz. If the THD' is almost similar to the THD_{200} there is no harmonic distortion over 10 kHz and no interharmonic distortion at all.

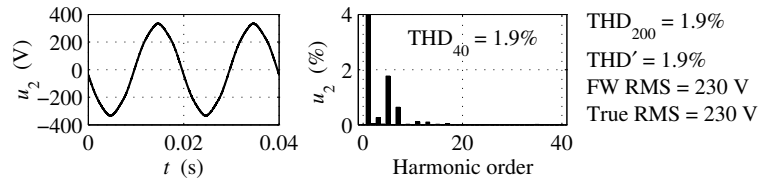


Figure 5.17: Grid phase voltage with both nonlinear load and active filter disconnected. (Measurement 1)

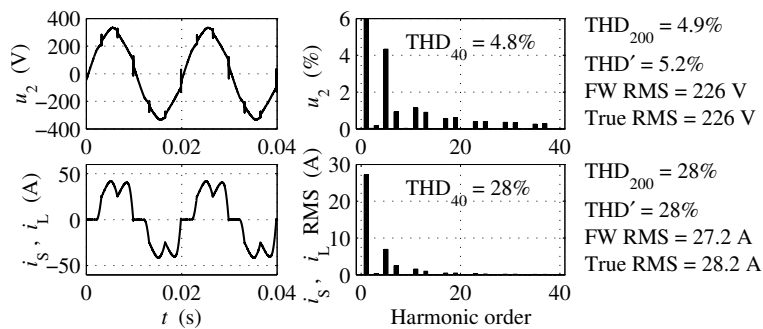


Figure 5.18: Nonlinear load connected, active filter disconnected. Top: Grid voltage, Bottom: Nonlinear load current. (Measurement 2)

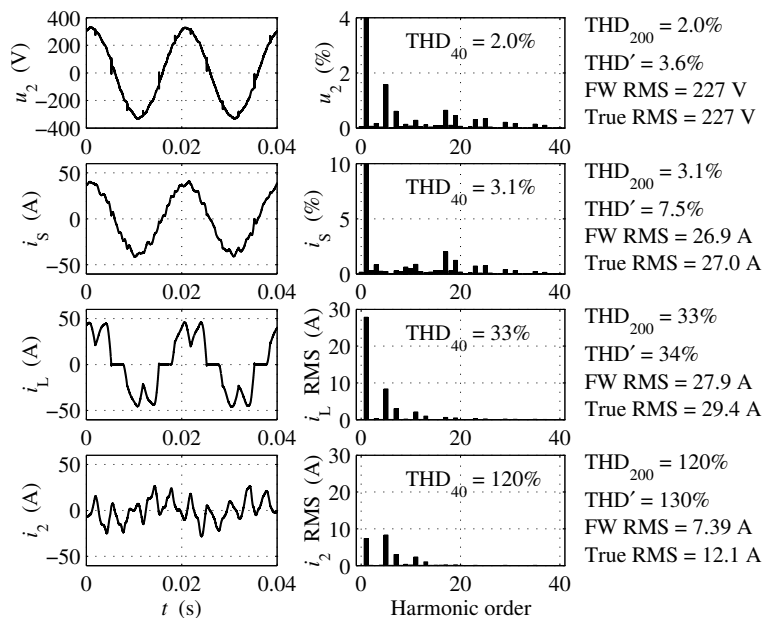


Figure 5.19: Frequency-domain active filtering, LCL-filter. Top to Bottom: Grid voltage, Supply current, Nonlinear load current, Active filter current. (Measurement 3)

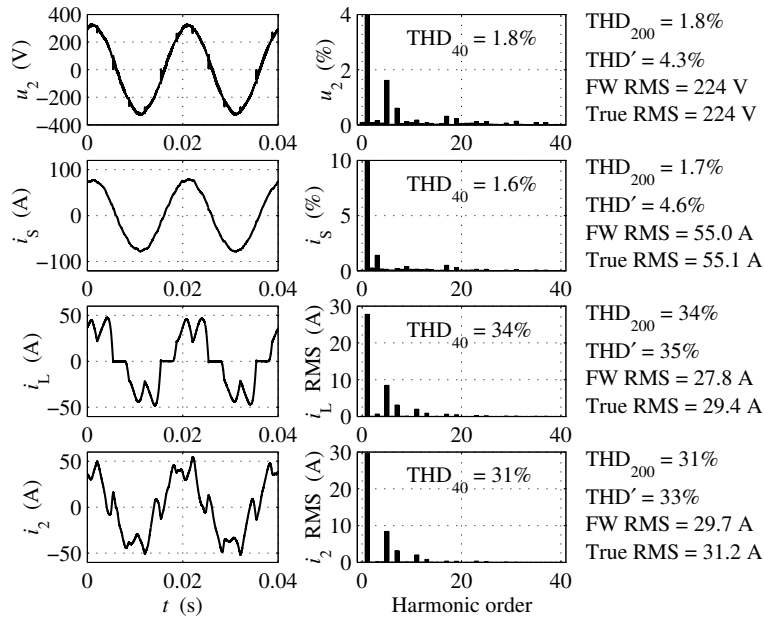


Figure 5.20: Frequency-domain active filtering, LCL-filter, Dc-load. Top to Bottom: Grid voltage, Supply current, Nonlinear load current, Active filter current. (Measurement 4)

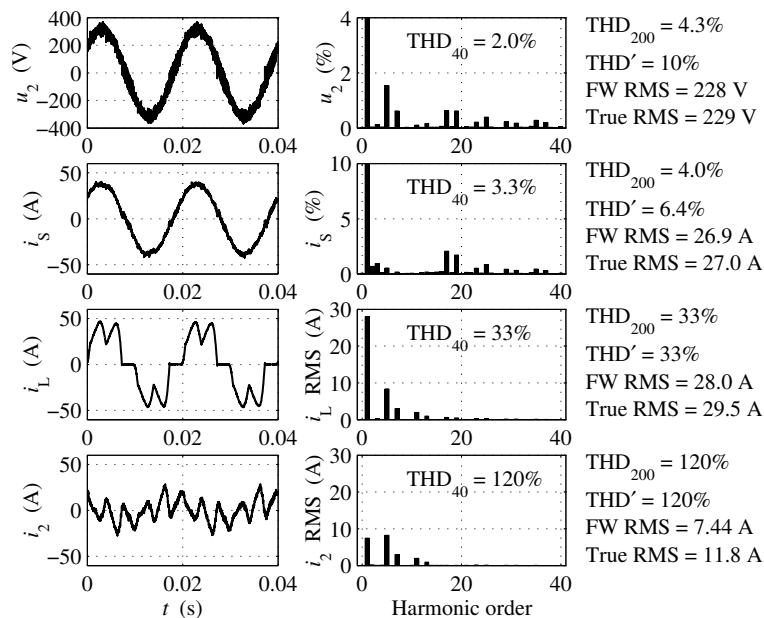


Figure 5.21: Frequency-domain active filtering, L-filter. Top to Bottom: Grid voltage, Supply current, Nonlinear load current, Active filter current. (Measurement 5)

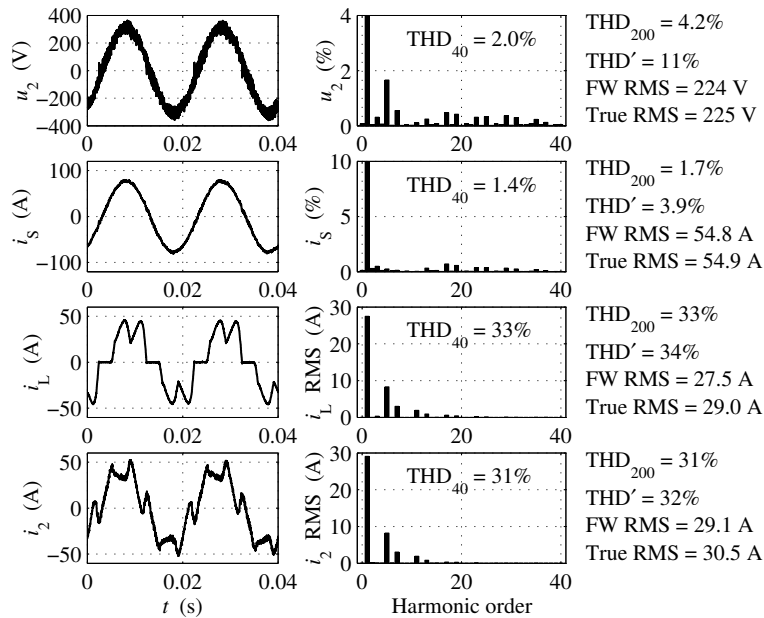


Figure 5.22: Frequency-domain active filtering, L-filter, Dc-load. Top to Bottom: Grid voltage, Supply current, Nonlinear load current, Active filter current. (Measurement 6)

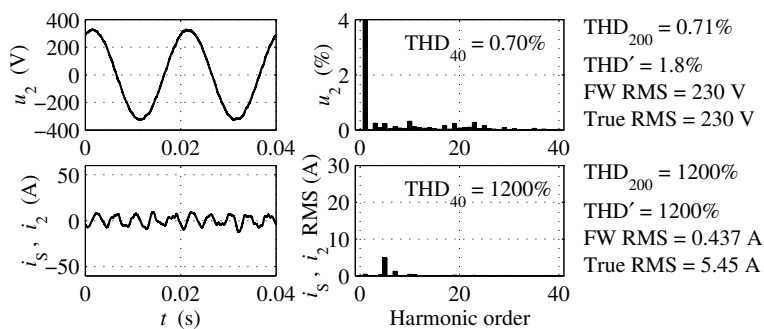


Figure 5.23: Voltage feedback active filtering, compensation of background distortion, nonlinear load is disconnected, LCL-filter. Top: Grid voltage, Bottom: Supply current (which is also active filter current). (Measurement 7)

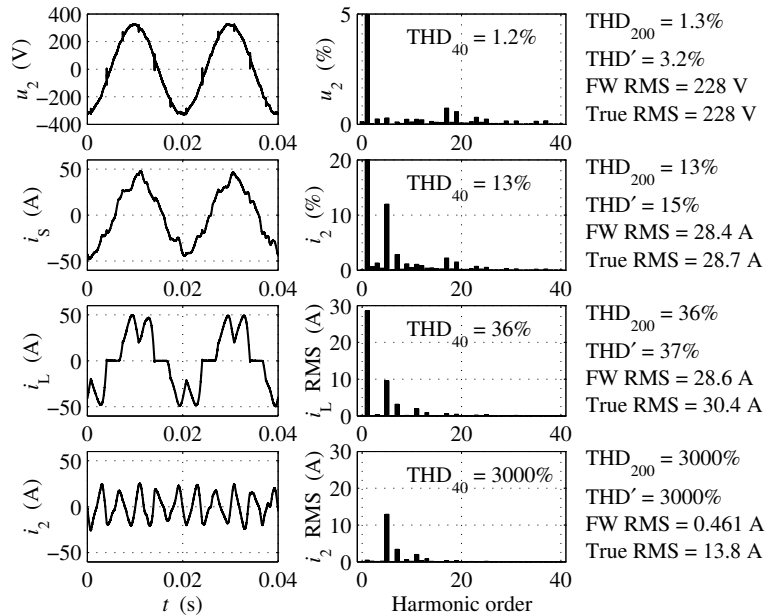


Figure 5.24: Voltage feedback active filtering, compensation of nonlinear load distortion and background distortion, LCL-filter. Top to Bottom: Grid voltage, Supply current, Nonlinear load current, Active filter current. (Measurement 8)

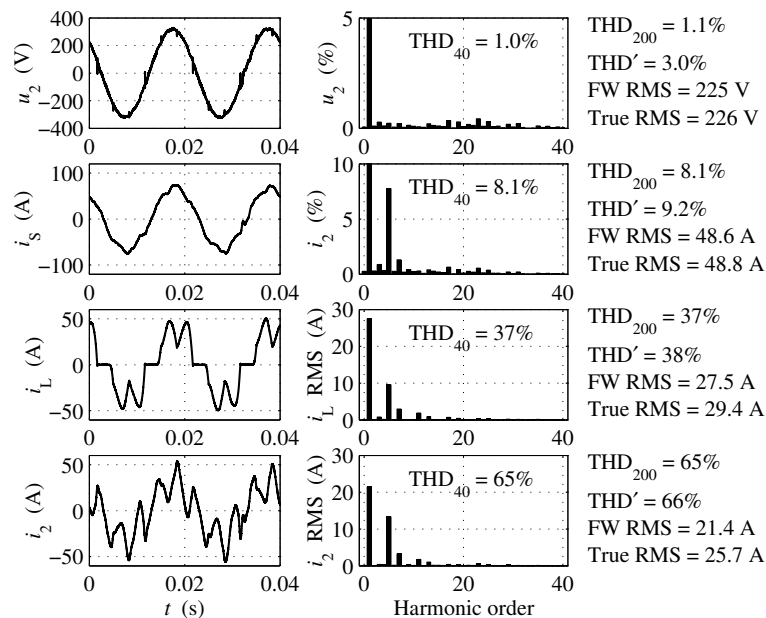


Figure 5.25: Voltage feedback active filtering, compensation of nonlinear load distortion and background distortion, LCL-filter, Dc-load. Top to Bottom: Grid voltage, Supply current, Nonlinear load current, Active filter current. (Measurement 9)

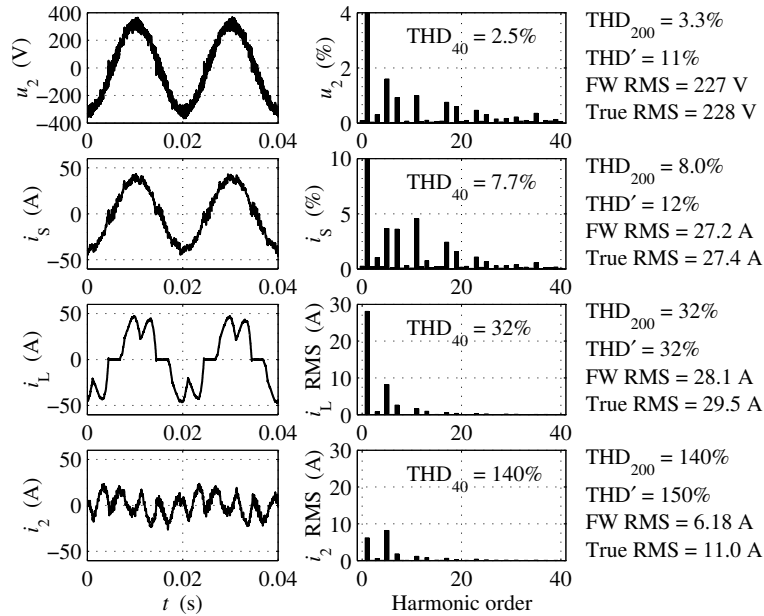


Figure 5.26: Time-domain active filtering, L-filter. Top to Bottom: Grid voltage, Supply current, Non-linear load current, Active filter current. (Measurement 10)

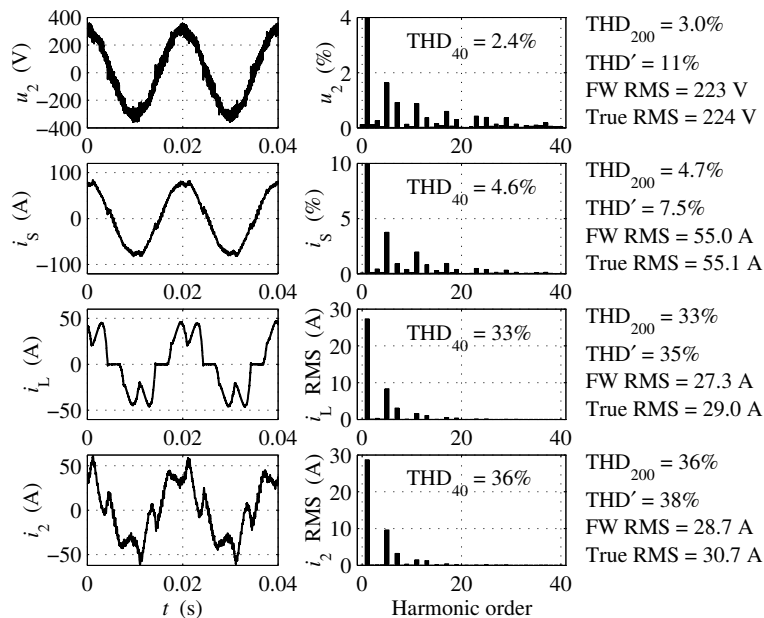


Figure 5.27: Time-domain active filtering, L-filter, Dc-load. Top to Bottom: Grid voltage, Supply current, Nonlinear load current, Active filter current. (Measurement 11)

5.8.2 Dynamic performance

To assess the dynamic performance of the active filtering methods, waveforms were recorded at the instant where the nonlinear load was switched on. The frequency-domain and time domain active filtering methods were measured. In the frequency-domain method both the L- and the LCL-filters were used, the results are shown in Figs. 5.28 and 5.29. The time-domain active filtering result is shown in Fig. 5.30. The measurement setup is similar to that in the steady-state measurements. Each channel was sampled with a sample rate of 25 kHz. The total record length was 4 seconds. The dynamic performance of the voltage feedback method is of an order slower than that of the frequency-domain method and it may be assessed using Fig. 5.15.

5.8.3 Measurements with a 490 kVA line converter with voltage feedback active filtering function

The frequency-domain active filtering function was tested with a 490 kVA / 690 V line converter unit. The line converter was fed with a 1 MVA 0–690 V variable voltage transformer system comprising a fixed turn 10 / 0.4 kV transformer and a variable turn transformer providing adjustable voltage level. No other loads were connected on the secondary of the transformer. There was no load connected to the dc-link. Hence, the active power loading of the line converter was not possible. Measurements to demonstrate the individual control of line current harmonics and grid voltage harmonics were carried out. A dc-link voltage of 1100 V were used. The nominal values of the line converter are listed in Appendix 1.

The individual control of the line current harmonics is demonstrated in Fig. 5.31. In the first case, an inductive fundamental wave current with an RMS value of 200 A (0.49 p.u.) is supplied into the grid. Subsequently, each of the controlled harmonics is individually given a 40 A RMS (0.098 p.u.) reference. Finally, all harmonics are given a 40 A RMS reference at the same time. The phase angles of the harmonics are selected to produce a maximum to the α -axis, which in the time-domain means that the top of the fundamental wave and the top of the harmonic wave are coinciding.

In Fig. 5.32 the individual control of grid voltage harmonics is demonstrated. As in the previous case, an inductive fundamental wave current of 200 A RMS is supplied into the grid. In the first case, the control of the voltage harmonics is disabled, and the 2% grid voltage THD is caused by the background distortion. In the second case, the background distortion is compensated by enabling the harmonic voltage control with zero references. The resulting THD is very good, 0.6%. Next, each of the controlled grid voltage harmonics is given a 5% reference, and finally all harmonics are given a 5% reference at once. Similar to the current harmonic case, the phase angles of the harmonics are selected to produce a maximum in the α -axis.

5.8.4 Discussion on the active filtering results

The distortion levels are evaluated according to the IEEE Std 519–1992 (1993) limits shown in Tab. 2.3 on page 26. The standard (IEEE Std 519–1992, 1993) is used only to provide a generally accepted point of comparison. The local standards and requirements may differ

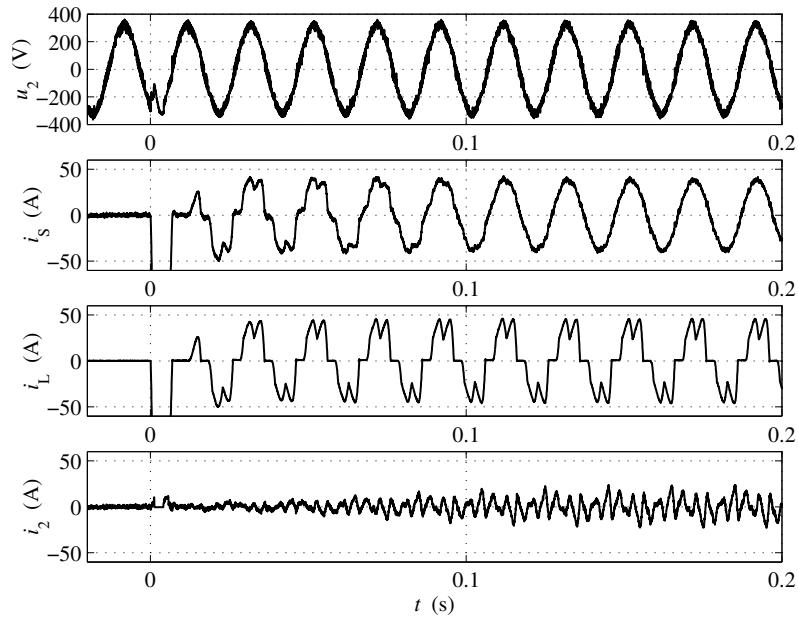


Figure 5.28: Dynamic performance of frequency-domain active filtering with L-filter. The nonlinear load is switched on at $t = 0$ s. Top to Bottom: Grid voltage, Supply current, Nonlinear load current, Active filter current

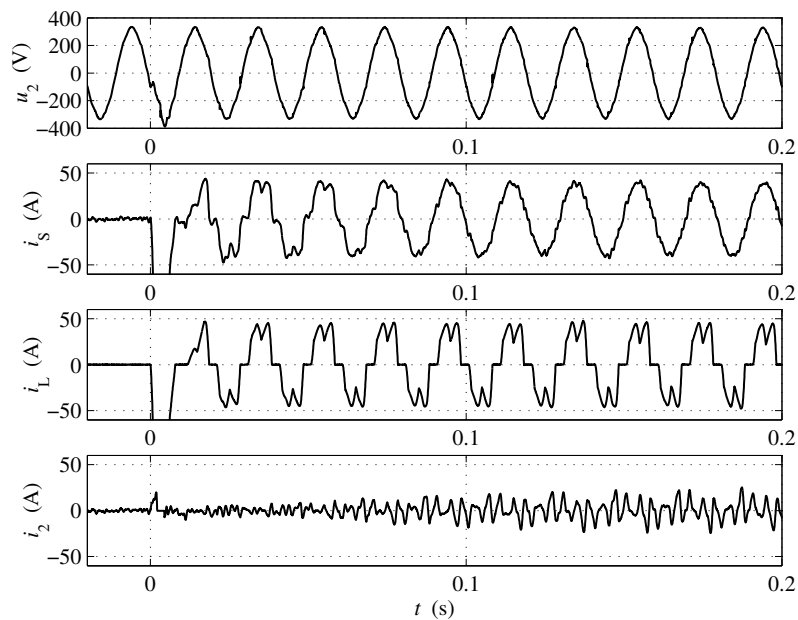


Figure 5.29: Dynamic performance of frequency-domain active filtering with LCL-filter. The nonlinear load is switched on at $t = 0$ s. Top to Bottom: Grid voltage, Supply current, Nonlinear load current, Active filter current

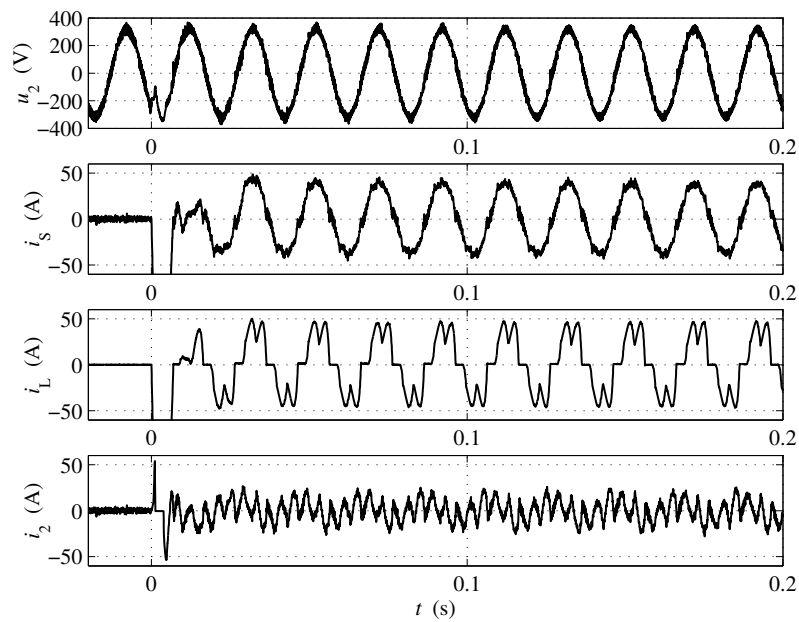


Figure 5.30: Dynamic performance of time-domain active filtering with L-filter. The nonlinear load is switched on at $t = 0$ s. Top to Bottom: Grid voltage, Supply current, Nonlinear load current, Active filter current

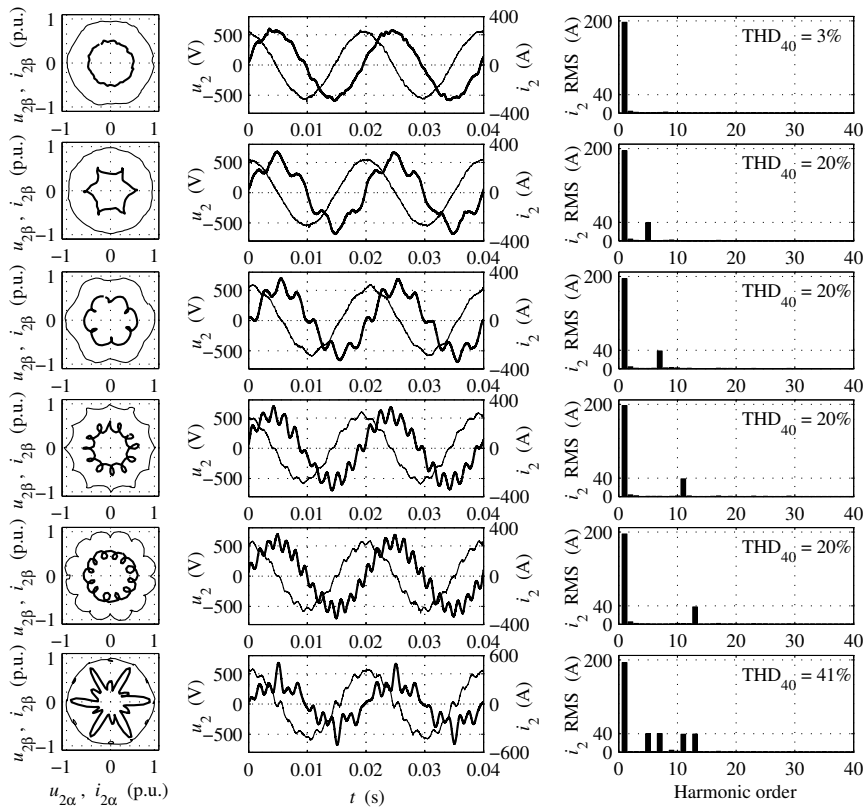


Figure 5.31: Individual control of converter line current harmonics with a 490 kVA line converter. Converter line current (thick) and grid voltage (thin) in the $\alpha\beta$ -frame and in the time domain (phase quantities), line current in the frequency domain. First row: Fundamental wave only, Second row: 5-harmonic, Third row: 7+ harmonic, Fourth row: 11- harmonic, Fifth row: 13+ harmonic, Sixth row: All of the above harmonics. Each individual harmonic is 40 A in magnitude and the phase angles are selected to produce a maximum in the α -axis.

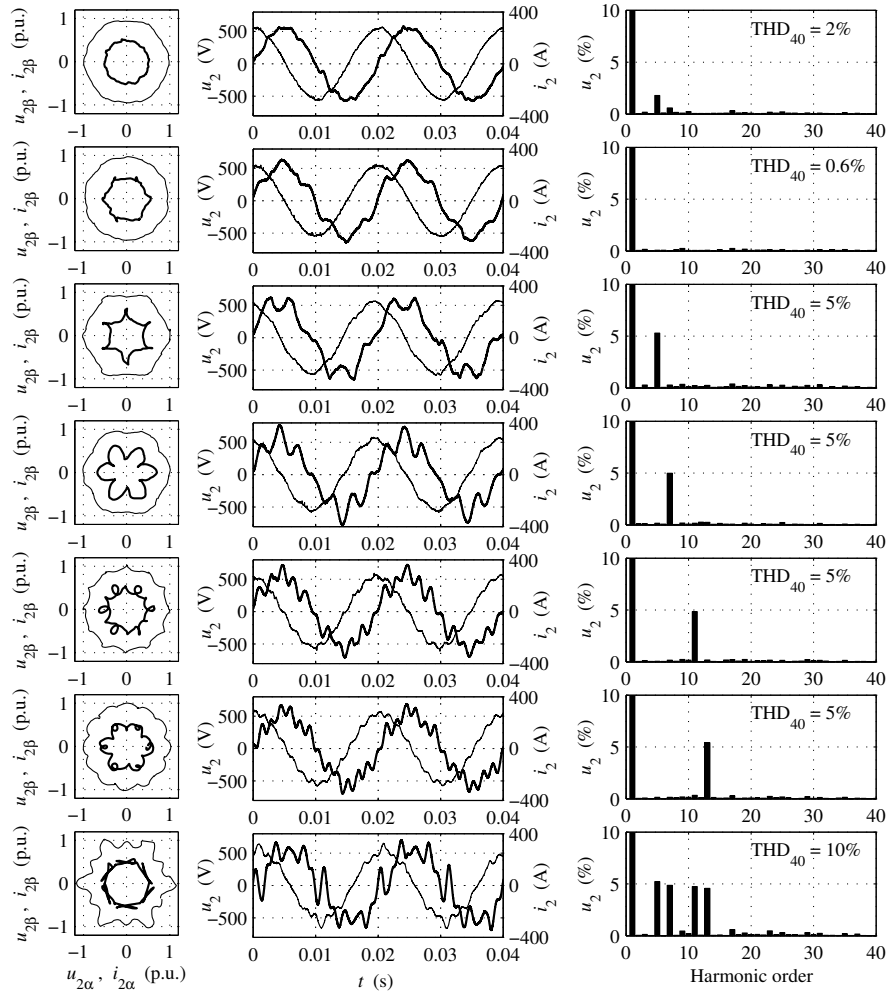


Figure 5.32: Individual control of grid voltage harmonics with a 490 kVA line converter. Converter line current (thick) and grid voltage (thin) in the $\alpha\beta$ -frame and in the time domain (phase quantities), grid voltage in the frequency domain. First row: Voltage harmonic control disabled, Second row: Zero harmonic references (background distortion compensated), Third row: 5% of 5-harmonic, Fourth row: 5% of 7+ harmonic, Fifth row: 5% of 11-harmonic, Sixth row: 5% of 13+ harmonic, Seventh row: All of the above harmonics. The harmonic phase angles are selected to produce a maximum in the α -axis.

from IEEE Std 519–1992 (1993). The purpose of the evaluation is not to show agreement or disagreement with this particular standard.

The current distortion limits stipulated in Tab. 2.3 are 12% for systems with SCR of 51 and 8% for systems with SCR of 25, corresponding the cases without and with the dc-load, respectively. The measurements with the dc-load are, except in the voltage feedback case, performed approximately in the nominal active power load conditions but the fundamental wave reactive power and the harmonics result in approximately 110% converter line current. This 10% current overloading results in slightly lower THD values than what the corresponding TDD values would be. However, the difference is rather small.⁴ The TDD in IEEE Std 519–1992 (1993) is defined up to harmonics of infinite order. With an LCL-filter, practically no harmonic distortion exists over the 200th harmonic, so the THD₂₀₀ may be used to approximate the THD calculated to infinite harmonic order. In the L-filter cases, the current THD increased typically by 0.1 %-unit and the voltage distortion by 1 %-unit when the included harmonics were increased from 200 to 800 (10 kHz to 40 kHz). In this frequency band, however, the current transformers probably do not give reliable results.

The THD₂₀₀ of the nonlinear load current was 28%, which caused a voltage THD₂₀₀ of 4.9% (Fig. 5.18). The current distortion exceeds the limit of TDD = 12%. The voltage THD₂₀₀ is just under the 5% limit at which Tab. 2.3 aims. The amplitude of the 5th harmonic voltage is 4.3%, which, according to Tab. 2.4, is higher than a single harmonic that one customer should cause (i.e. 1.0%–1.5%). However, the background distortion in this case is 1.9% (Fig. 5.17). Altogether, it is concluded that the situation is not acceptable according to IEEE Std 519–1992 (1993).

In all active filtering cases where the sinusoidal supply current was pursued, the THD₂₀₀ of the current complies with the TDD limits in Tab. 2.3. The frequency-domain method gives very good results with THD₂₀₀ < 3% with dc-load and THD₂₀₀ ≤ 4% without dc-load. The time-domain method reduces the supply current distortion considerably but less than the frequency domain method—THD₂₀₀ = 8% and THD₂₀₀ = 5% are obtained without and with the dc-load, respectively. In the measured cases, the THD' may be significantly higher than the THD₂₀₀. This implies that there is interharmonic distortion present. Interharmonic distortion is a known feature of the hysteresis current control methods, see e.g. (Holtz, 1994; Rahman et al., 1997), and hence, it is expected to be present also if DTC-based methods are used.

The effect of the LCL-filter is most clearly seen by examining the voltage waveforms. In the case of the L-filter, the voltage is heavily distorted by the converter switchings. Although the current ripple resulting from the switchings is of a relatively low amplitude it produces a significant voltage distortion. The reason is the inductive grid impedance, which is due to the transformer, and the high frequency of the current ripple. The amplitude of the voltage ripple across the inductance is proportional to the frequency of the current ripple that is causing it. In the measured L-filter cases, the voltage THD₂₀₀ is about 4% and the THD' is about 10%. The high voltage distortion practically renders the L-filter unusable in the weak grid conditions. This is important because the weak grids are most vulnerable to the harmonics and, therefore, they represent a potential condition in which the active filtering technologies may be needed.

⁴E.g., consider a 2.1 p.u. supply current composed of 1 p.u. nonlinear load current and 1.1 p.u. active filter current, and having a THD of 5%. Assuming unity fundamental wave power factors for both units, the reduction of the active power of the active filter by 0.1 p.u. to 1 p.u. leads to 2 p.u. supply current and to THD of (2.1/2)·5% = 5.25%. Increase of 0.25 percentage units.

Frequency-domain active filtering with a LCL-filter (Figs. 5.19 and 5.20) reduces the voltage distortion considerably. The original THD_{200} of 4.9% (Fig. 5.18) is reduced to about 2%. By taking into account that the THD_{200} of the background distortion is about the same, this is considered to be a good result. The active filter with sinusoidal supply current does not improve the voltage quality below the background distortion level because it does not provide a low impedance shunt path at the harmonic frequencies.

The voltage feedback active filtering method provides a way to reduce the background distortion, as shown in Fig. 5.23. The THD_{200} is improved from 1.9% (Fig. 5.17) to 0.71%. The supply current contains only harmonics and practically no power frequency component at all, which makes the THD considerations irrational. Even with the nonlinear load connected the voltage feedback method can maintain the voltage THD_{200} at about 1% level, which is below the background distortion level. Hence, even though the nonlinear load is present the voltage has a higher quality than what is available in the neighboring parts of the local grid. The supply current has a high harmonic content, e.g. in the case of Fig. 5.24 the THD_{200} is 13%. This is because at the harmonic frequencies the active filter provides a low, theoretically zero, impedance shunt path, which sinks the harmonic currents and annuls the corresponding harmonic voltages. The supply current is not in accordance with Tab. 2.3, even though the voltage quality, which is the basis of the current harmonic limits, is excellent. Clearly, the current harmonic limits are not applicable to voltage feedback compensated system when background distortion is present.

The measurements with a 490 kVA line converter (Figs. 5.31 and 5.32) demonstrate the control of individual line current harmonics and voltage feedback approach with a power level closer to the practical industrial or distributed generation applications. Also, the measurements demonstrate the possibility of generating a predetermined harmonic distortion in the grid. This could be used in studying the behavior of electrical apparatuses in a known distortion environment.

The dynamic performance measurements (Figs. 5.28–5.30) show the response when the nonlinear load is abruptly connected in the grid. At the switching moment the nonlinear load takes a large inrush current to charge the dc-capacitor. In practical applications charging circuits are used to charge the dc-capacitors without a high inrush current. In the case of the frequency-domain method, the supply current is beginning to have the appearance of a sine wave after 5 cycles and after 10 cycles the waveform looks similar to the steady-state waveform. The time-domain method responds more quickly—after 1 cycle the current is shaped sinusoidal.

In typical applications the dynamic performance of the frequency domain method is acceptable. A couple of non-perfect cycles in transients are typically allowed. However, in special applications where the nonlinear load current is constantly changing, the dynamic performance of the frequency-domain method may be insufficient. Or, if the distortion is not condensed in some specific frequencies, the time-domain method, which is effective to all distortion within the dynamic range, may be preferred to the frequency-selective approach that is effective only in some predetermined harmonic sequences. An example of such difficult nonlinear load is an arc furnace. The arc furnace current has a spread of frequencies and the levels of individual frequency components vary with the time (Arrillaga and Watson, 2003). Recently, Wrede and Staudt (2004) proposed an FBD-method-based compensation of the arc furnace originating flicker.

The properties of the implemented frequency-domain and time-domain active filtering systems are compared in Tab. 5.3. In the literature, one may find methods, which improve some

Table 5.3: Comparison of the implemented frequency-domain and time-domain active filtering methods.

| | Frequency-domain method | Time-domain method |
|---|--------------------------------|--|
| Complexity | Complex | Simple |
| Control loops that require tuning | Yes | No |
| Current control dynamics requirement | Moderate | Very high |
| Mode of operation | Closed loop | Open loop |
| Filtering is effective to | Preselected harmonic sequences | Fundamental wave reactive power and all harmonics within the dynamic range |
| Additional measured current | Supply current | Load current |
| Required sample rate of additional current measurement | Moderate | High |
| Steady-state performance | Very good | Average |
| Dynamic performance | Average | Very good |
| Possible to use LCL-filter | Yes | No |
| Possible to implement voltage feedback active filtering functionality | Yes | No |

aspects of the control systems. In particular, the performance of the time-domain method could be improved by compensating the control delays. Moreover, in steady state, the samples stored in the previous cycle can be used to improve the time-domain filtering performance. It is possible to combine the frequency-domain and the time-domain methods by using the frequency-domain method as a feedback control and the time-domain method as an open-loop control. The combined method was implemented and it improved the dynamic performance of the frequency-domain method. But, the overall advantages gained were too modest to justify the inclusion in the comparison. Also, in voltage feedback active filter, it is possible to connect the nonlinear load between the line side filter inductor and the line side current measurement. In this case, the combined supply current i_S is measured instead of the active filter line current i_2 . Basically, the configuration is similar to 5.4(a) but with additional line voltage measurement. In this configuration, the dynamics of the nonlinear load current harmonic compensation are similar to the frequency-domain active filter, but the ability of voltage harmonic compensation is retained. Experimental measurements indicated that the steady-state performance is similar to the voltage feedback active filter measurements presented in section 5.8.1. This configuration may be useful if, e.g., the response time requirement of harmonic compensation is higher with one particular load than with the others. The nonlinear load which needs the higher compensation dynamics may be connected between the line side filter inductor and the current measurement, and, be compensated with the harmonic current control, while the rest of the nonlinear loads and the background distortion are compensated with the harmonic voltage control.

Chapter 6

Conclusions

This dissertation studied the virtual converter flux linkage-based voltage source line converter and extended its application area to the field of power quality improving. After introducing the line converter and the concepts related to electrical power and power quality, the modeling and the control of the line converter was considered. The most typical line converter control methods were reviewed and a new DTC-based current control method was introduced. A model of the DTC-based current control was derived and compared with simulation and experimental results. It was concluded that, theoretically, the DTC-based current control exhibits the dynamics of a phase-lag compensator. Based on the model, the gains of the current controllers were selected to generate similar dynamic characteristics in both control axes. The overmodulation characteristics of the DTC converter were studied and an analytical equation for the maximum modulation index of the DTC was derived.

Subsequently, power quality improving was considered. First, the power conditioning system, the active filters and the concept of the line converter with integrated active filtering features were introduced. The practical test setup configuration was also presented. Three different active filtering methods were presented and implemented—the frequency-domain, the voltage feedback and the time-domain method. The control systems of the frequency-domain and the voltage feedback methods were analyzed and, based on the analysis, the controllers were designed. For the time-domain control method a hysteresis current control system employing the DTC structure was implemented. A measurement-based method using the control system of the voltage feedback active filter to identify the grid impedance was proposed. The importance of having a correct grid impedance estimate in the voltage feedback active filter control system was discussed.

The performance of all three active filtering methods were experimentally verified. Both the L-type and the LCL-type line filters were used. It was found out that the LCL-filter is superior to the L-filter, if the line voltage quality is concerned. Moreover, the voltage feedback method was found to perform better than the other methods in respect of the voltage quality. The supply current of the voltage feedback compensated system may differ considerably from the sinusoid if the background voltage distortion is present. Therefore, it was concluded that the supply harmonic current limits should not be applied to such cases. The voltage feedback active filtering was also tested with a 490 kVA line converter. In the dynamic performance measurements the time-domain method was found to perform better than the

frequency-domain method. Finally, the results of the active filtering were discussed and the properties and requirements of the implemented systems were compared.

Suggestions for future work

During the research work the author identified the following subjects, in which more study should be conducted than included in this work.

The grid-independent mode of the PCS control system implemented was based on the converter voltage control and not on the converter current control. Alternatively, it would have been possible to establish the island grid voltage control through the converter current vector control. Research is needed to find out whether the current control approach is suitable and what would be its characteristics. It is anticipated that in situations where the current capacity of the PCS is temporarily exceeded, e.g. in the induction motor start, the current limiting and avoiding the overcurrent trip is more easily realized with the current control approach. Further, the operation in case of nonlinear load in the island grid should be researched. The voltage controlled PCS will provide harmonic currents if the load is nonlinear, but, because of the line filter impedance, the nonlinear load will distort the island voltage. Research should be conducted to find out how the active filtering methods should be applied to the PCS to ensure the good voltage quality also in case of nonlinear load. Is it possible to apply the time-domain-based methods, and how should the load impedance be taken into account?

A feasible concept of the line converter with active filtering feature is another subject for further study. How should the LCL-filter be designed for active filtering and what switching frequency should be used? Can the resonances of the LCL-filter be taken advantage of, as suggested in this study?

Practical means to limit the harmonic currents should be implemented in the voltage feedback active filter. This feature would prevent the active filter from tripping overcurrent if the grid is too strong or the distortion too severe to be fully compensated. Preferably, the active filter should include a line current management control, which allocates the current capacity to the active, reactive and harmonic currents. If the current capacity is exceeded, the tasks are prioritized and the most important tasks are preferred. Also, it would be convenient to limit and prioritize the individual harmonic currents. The robustness of the voltage feedback active filter against grid impedance variations should be researched. Also, methods to exclude the background distortion from the compensation should be studied.

The market potential and the application areas of the line converter with active filtering feature and the voltage feedback active filter should be investigated. How will future development of power electronics affect the feasibility of these concepts?

References

- Abrahamsen, F., and David, A. (1995), "Adjustable speed drive with active filtering capability for harmonic current compensation," in *Proc. IEEE 26th Annual Power Electronics Specialists Conference*, Atlanta, GA, USA, vol. 2, pp. 1137–1143.
- Akagi, H. (1994), "Trends in active power line conditioners," *IEEE Transactions on Power Electronics*, vol. 9, no. 3, pp. 263–268.
- Akagi, H. (1996), "New trends in active filters for power conditioning," *IEEE Transactions on Industry Applications*, vol. 32, no. 6, pp. 1312–1322.
- Akagi, H. (1997), "Control strategy and site selection of a shunt active filter for damping of harmonic propagation in power distribution systems," *IEEE Transactions on Power Delivery*, vol. 12, no. 1, pp. 354–362.
- Akagi, H. (2000), "Active filters and energy storage systems operated under non-periodic conditions," in *Power Engineering Society Summer Meeting*, Seattle, WA, USA, vol. 2, pp. 965–970.
- Akagi, H., Kanazawa, Y., and Nabae, A. (1983), "Generalized theory of the instantaneous reactive power in three-phase circuits," in *Proc. International Power Electronics Conference*, Tokyo, Japan, pp. 1375–1386.
- Akagi, H., Kanazawa, Y., and Nabae, A. (1984), "Instantaneous reactive power compensators comprising switching devices without energy storage components," *IEEE Transactions on Industry Applications*, vol. IA-20, no. 3, pp. 625–630.
- Akagi, H., Ogasawara, S., and Kim, H. (1999), "The theory of instantaneous power in three-phase four-wire systems: a comprehensive approach," in *Proc. IEEE 34th IAS Annual Meeting*, vol. 1, pp. 431–439.
- Arrillaga, J., Bollen, M. H. J., and Watson, N. R. (2000), "Power quality following deregulation," *Proceedings of the IEEE*, vol. 88, no. 2, pp. 246–261.
- Arrillaga, J., and Watson, N. R. (2003), *Power System Harmonics*, John Wiley & Sons, Chichester, UK, second ed., 399 p.
- Bhattacharya, S., Veltman, A., Divan, D. M., and Lorenz, R. D. (1996), "Flux-based active filter controller," *IEEE Transactions on Industry Applications*, vol. 32, no. 3, pp. 491–502.
- Bird, B. M., March, J. F., and McLellan, P. R. (1969), "Harmonic reduction in multiplex convertors by triple-frequency current injection," *Proc. IEE*, vol. 116, no. 10, pp. 1730–1734.

- Blaschke, F. (1972), "The principle of field orientation as applied to the new transvektor closed-loop control system for rotating-field machines," *Siemens Review*, no. 5, pp. 217–220.
- Bojrup, M., Karlsson, P., Alaküla, M., and Gertmar, L. (1999), "A multiple rotating integrator controller for active filters," in *Proc. 8th European Conference on Power Electronics and Applications*, Lausanne, Switzerland, 9 p., cd-rom.
- Bollen, M. H. J. (2002), "Definitions of voltage unbalance," *IEEE Power Engineering Review*, vol. 22, no. 11, pp. 49–50.
- Bolognani, S., and Zigliotto, M. (1999), "Space vector Fourier analysis of SVM inverters in the overmodulation range," in *Proc. International Conference on Power electronics, Drives and Energy Systems for Industrial Growth*, New Delhi, India, vol. 1, pp. 319–324.
- Brogan, P., and Yacamini, R. (1998), "An active filter based on voltage feedback," in *Proc. IEE 7th International Conference on Power Electronics and Variable Speed Drives*, pp. 1–4.
- Brogan, P., and Yacamini, R. (1999), "Stability of an active filter based on voltage feedback," in *Proc. 8th European Conference on Power Electronics and Applications*, Lausanne, Switzerland, 5 p., cd-rom.
- Brogan, P., and Yacamini, R. (2000), "Stability of selective harmonic active filters," in *Proc. IEE 8th International Conference on Power Electronics and Variable Speed Drives*, pp. 416–421.
- Brogan, P., and Yacamini, R. (2003), "Harmonic control using an active drive," *IEE Proceedings Electric Power Applications*, vol. 150, no. 1, pp. 14–20.
- Buso, S., Malesani, L., and Mattavelli, P. (1998a), "Comparison of current control techniques for active filter application," *IEEE Transactions on Industrial Electronics*, vol. 45, no. 5, pp. 722–729.
- Buso, S., Malesani, L., Mattavelli, P., and Veronese, R. (1998b), "Design and fully digital control of parallel active filters for thyristor rectifiers to comply with IEC-1000-3-2 standards," *IEEE Transactions on Industry Applications*, vol. 34, no. 3, pp. 508–517.
- Cichowlas, M., Malinowski, M., Kazmierkowski, M. P., and Blaabjerg, F. (2003), "Direct power control for three-phase PWM rectifier with active filtering function," in *Proc. IEEE 18th Annual Applied Power Electronics Conference and Exposition*, vol. 2, pp. 913–918.
- Corey, G. P. (1999), "Energy storage solutions for premium power," *IEEE Transactions on Aerospace and Electronic Systems*, vol. 11, no. 6, pp. 41–44.
- Czarnecki, L. S. (1987), "What is wrong with the Budeanu concept of reactive and distortion power and why it should be abandoned," *IEEE Transactions on Instrumentation and Measurement*, vol. IM-36, no. 3, pp. 834–837.
- Depenbrock, M. (1971), *Wirk- und Blindleistungen periodischer Ströme in Ein- und Mehrphasensystemen mit periodische Spannungen beliebiger Kurvenform*, ETG-Fachberichte 6, pp. 17–59.

- Depenbrock, M. (1985), "Direkte Selbstregelung (DSR) für hochdynamische Drehfeldantriebe mit Stromrichterspeisung," *etzArchiv*, Bd. 7, pp. 211–218.
- Depenbrock, M. (1988), "Direct self-control (DSC) of inverter-fed induction machine," *IEEE Transactions on Industry Applications*, vol. 3, no. 4, pp. 420–429.
- Depenbrock, M. (1993), "The FBD-method, a generally applicable tool for analyzing power relations," *IEEE Transactions on Power Systems*, vol. 8, no. 2, pp. 381–387.
- Depenbrock, M., and Skudelny, H.-C. (1994), "Dynamic compensation of non-active power using the FBD method—basic properties demonstrated by benchmark examples," *European Transactions on Electrical Power*, vol. 4, no. 5, pp. 381–388.
- Depenbrock, M., and Staudt, V. (1996), "Practical definitions for powers in systems with non-sinusoidal waveforms and unbalanced loads: a discussion," *IEEE Transactions on Power Delivery*, vol. 11, no. 1, pp. 89–90.
- Depenbrock, M., and Staudt, V. (1998), "The FBD-method as tool for compensating total non-active currents," in *Proc. 8th International Conference on Harmonics and Quality of Power*, Athens, Greece, vol. 1, pp. 320–324.
- Depenbrock, M., Staudt, V., and Wrede, H. (2003), "A theoretical investigation of original and modified instantaneous power theory applied to four-wire systems," *IEEE Transactions on Industry Applications*, vol. 39, no. 4, pp. 1160–1167.
- Dorf, R. C., and Bishop, R. H. (1995), *Modern Control Systems*, Addison-Wesley, Reading, MA, USA, seventh ed., 807 p.
- Dugan, R., McGranaghan, M. F., Santoso, S., and Beaty, H. W. (2002), *Electrical Power Systems Quality*, McGraw-Hill, New York, NY, USA, second ed., 528 p.
- Emanuel, A. E. (1990), "Powers in nonsinusoidal situations a review of definitions and physical meaning," *IEEE Transactions on Power Delivery*, vol. 5, no. 3, pp. 1377–1383.
- Emanuel, A. E., and Yang, M. (1993), "On the harmonic compensation in nonsinusoidal systems," *IEEE Transactions on Power Delivery*, vol. 8, no. 1, pp. 393–399.
- EN 50160 (1999), *Voltage characteristics of electricity supplied by public distribution systems*, European Committee for Electrotechnical Standardization, Brussels, Belgium, European standard, 19 p.
- Ferrero, A., and Superti-Furga, G. (1990), "A unified approach to unbalanced three-phase systems under non-sinusoidal conditions: some definitions," in *Proc. 4th International Conference on Harmonics in Power Systems*, Budapest, Hungary, pp. 31–37.
- Ferrero, A., and Superti-Furga, G. (1991), "A new approach to the definition of power components in three-phase systems under nonsinusoidal conditions," *IEEE Transactions on Instrumentation and Measurement*, vol. 40, no. 3, pp. 568–577.
- Filipski, P. S., Baghzouz, Y., and Cox, M. D. (1994), "Discussion of power definitions contained in the IEEE dictionary," *IEEE Transactions on Power Delivery*, vol. 9, no. 3, pp. 1237–1243.

- Fourier, J. (1822), *Théorie analytique de la chaleur*, Reprint, Éditions Jacques Gabay, 1988, Sceaux, France, 639 p.
- Fryze, S. (1932), “Wirk-, Blind- und Scheinleistung in elektrischen Stromkreisen mit nichtsinusförmigem Verlauf von Strom und Spannung,” *Elektrotechnische Zeitschrift*, no. 25, 26 and 29, pp. 596–599, 625–627 and 700–702.
- Grady, W. M., and Santoso, S. (2001), “Understanding power system harmonics,” *IEEE Power Engineering Review*, vol. 21, no. 11, pp. 8–11.
- Green, A. W., Boys, J. T., and Gates, G. F. (1988), “3-phase voltage sourced reversible rectifier,” *IEE Proceedings B, Electric Power Applications*, vol. 135, no. 6, pp. 362–370.
- Gunther, E. W. (2001), “Interharmonics in power systems,” in *Proc. IEEE Power Engineering Society Summer Meeting*, vol. 2, pp. 813–817.
- Gyugyi, L., and Strycula, E. C. (1976), “Active AC power filters,” in *Proc. IEEE Industry Applications Society Annual Meeting*, pp. 529–535.
- Harnefors, L. (1997), *On Analysis, Control and Estimation of Variable-Speed Drives*, Doctoral dissertation, Royal Institute of Technology, Stockholm, Sweden, 269 p.
- Hava, A. M., Kerkman, R. J., and Lipo, T. A. (1998), “Carrier-based PWM-VSI overmodulation strategies: Analysis, comparison, and design,” *IEEE Transactions on Power Electronics*, vol. 13, no. 4, pp. 674–689.
- Heydt, G. T. (1991), *Electric power quality*, Stars in a Circle Publication, West LaFayette, IN, USA, second ed., 462 p.
- Heydt, G. T. (1998), “Electric power quality: a tutorial introduction,” *IEEE Computer Applications in Power*, vol. 11, no. 1, pp. 15–19.
- Heydt, G. T. (2000), “Problematic power quality indices,” in *Proc. IEEE Power Engineering Society Winter Meeting*, Singapore, vol. 4, pp. 2838–2842.
- Heydt, G. T., and Jewell, W. T. (1998), “Pitfalls of electric power quality indices,” *IEEE Transactions on Power Delivery*, vol. 13, no. 2, pp. 570–578.
- Hingorani, N. G. (1995), “Introducing custom power,” *IEEE Spectrum*, vol. 32, no. 6, pp. 41–48.
- Hodel, A. S., and Hall, C. E. (2001), “Variable-structure PID control to prevent integrator windup,” *IEEE Transactions on Industrial Electronics*, vol. 48, no. 2, pp. 442–451.
- Holmes, D. G., and Lipo, T. A. (2003), *Pulse Width Modulation for Power Converters*, IEEE Press, Piscataway, NJ, USA, 724 p.
- Holtz, J. (1994), “Pulsewidth modulation for electronic power conversion,” *Proceedings of the IEEE*, vol. 82, no. 8, pp. 1194–1214.
- Holtz, J., Lotzkat, W., and Khambadkone, A. M. (1993), “On continuous control of PWM inverters in the overmodulation range including the six-step mode,” *IEEE Transactions on Power Electronics*, vol. 8, no. 4, pp. 546–553.

- IEC Std 60050-551-20 (2001), *International Electrotechnical Vocabulary Part 551-20: Power electronics – Harmonic analysis*, International Electrotechnical Commission, Geneva, Switzerland, IEC Standard, 21 p.
- IEC Std 61800-4 (2002), *Adjustable speed electrical power drive systems – Part 4: General requirements – Rating specifications for a.c. power drive systems above 1000 V a.c. and not exceeding 35 kV*, International Electrotechnical Commission, Geneva, Switzerland, IEC Standard, 219 p.
- IEEE Std 100–1984 (1984), *IEEE Standard Dictionary of Electrical and Electronics Terms*, American National Standards Institute / The Institute of Electrical and Electronics Engineers, 1173 p.
- IEEE Std 519–1992 (1993), *Recommended Practices and Requirements for Harmonic Control in Electrical Power Systems*, The Institute of Electrical and Electronics Engineers, New York, USA, IEEE Standard, 100 p.
- IEEE Working Group on Nonsinusoidal situations (1996), “Practical definitions for powers in systems with nonsinusoidal waveforms and unbalanced loads: a discussion,” *IEEE Transactions on Power Delivery*, vol. 11, no. 1, pp. 79–87.
- Inzunza, R., and Akagi, H. (2004), “A 6.6 kV transformerless shunt hybrid active filter for installation on a power distribution system,” in *Proc. IEEE 35th Annual Power Electronics Specialists Conference*, Aachen, Germany, pp. 4630–4636.
- Jahns, T. M., and Owen, E. L. (2001), “AC adjustable-speed drives at the millennium: How did we get here?” *IEEE Transactions on Power Electronics*, vol. 16, no. 1, pp. 17–25.
- Jenkins, N., Allan, R., Crossley, P., Kirschen, D., and Strbac, G. (2000), *Embedded Generation*, The Institution of Electrical Engineers, Stevenage, UK, 273 p.
- Jóos, G., Morán, L., and Ziogas, P. (1991), “Performance analysis of a PWM inverter VAR compensator,” *IEEE Transactions on Power Electronics*, vol. 6, no. 3, pp. 380–391.
- Jóos, G., Ooi, B. T., McGillis, D., Galiana, F. D., and Marceau, R. (2000), “The potential of distributed generation to provide ancillary services,” in *Proc. Power Engineering Society Summer Meeting*, Seattle, WA, USA, vol. 3, pp. 1762–1767.
- Kataoka, T., Fuse, Y., Nakajima, D., and Nishikata, S. (2000), “A three-phase voltage-type PWM rectifier with the function of an active power filter,” in *Proc. 8th International Conference Power on Electronics and Variable Speed Drives*, London, UK, pp. 386–391.
- Kaukonen, J. (1999), *Salient pole synchronous machine modelling in an industrial direct torque controlled drive application*, Doctoral dissertation, Lappeenranta University of Technology, Lappeenranta, Finland, 138 p.
- Kaźmierkowski, M. P., Dzieniakowski, M. A., and Sulkowski, W. (1991), “Novel space vector based current controllers for PWM-inverters,” *IEEE Transactions on Power Electronics*, vol. 6, no. 1, pp. 158–166.
- Kovács, K. P., and Rácz, I. (1959), *Transiente Vorgänge in Wechselstrommaschinen, Band I*, Verlag der Ungarischen Akademie der Wissenschaften, Budapest, Hungary, 514 p.

- Kreyszig, E. (1993), *Advanced Engineering Mathematics*, John Wiley & Sons, New York, NY, USA, seventh ed., 1271 p.
- Kyei, J., Ayyanar, R., Heydt, G., Thallam, R., and Blevins, J. (2002), "The design of power acceptability curves," *IEEE Transactions on Power Delivery*, vol. 17, no. 3, pp. 828–833.
- Lasseter, R., and Piagi, P. (2000), "Providing premium power through distributed resources," in *Proc. 33rd Annual Hawaii International Conference on Systems Sciences*, 9 p.
- Lee, D.-C., and Lee, G.-M. (1998), "A novel overmodulation technique for space-vector PWM inverters," *IEEE Transactions on Power Electronics*, vol. 13, no. 6, pp. 1144–1151.
- Luukko, J. (2000), *Direct torque control of permanent magnet synchronous machines – analysis and implementation*, Doctoral dissertation, Lappeenranta University of Technology, Lappeenranta, Finland, 172 p.
- Luukko, J., Niemelä, M., and Pyrhönen, J. (2003), "Estimation of the flux linkage in a direct-torque-controlled drive," *IEEE Transactions on Industrial Electronics*, vol. 50, no. 2, pp. 283–287.
- Malinowski, M. (2000), *Sensorless Control Strategies for Three-Phase PWM Rectifiers*, Ph.D. thesis, Warsaw University of Technology, Warsaw, Poland, 127 p.
- Malinowski, M., Kazmierkowski, M. P., Hansen, S., Blaabjerg, F., and Marques, G. D. (2001), "Virtual flux-based direct power control of three-phase PWM rectifiers," *IEEE Transactions on Industry Applications*, vol. 37, no. 4, pp. 1019–1027.
- Manninen, V. (1995), "Application of direct torque control modulation technology to a line converter," in *Proc. 6th European Conference on Power Electronics and Applications*, Sevilla, Spain, vol. 1, pp. 1292–1296.
- Manula, T. (1999), *Defining the Most Significant Characteristics of Induction Motor with Laboratory Measurements (in Finnish)*, B.Sc. thesis, South Carelia Polytechnic, Imatra, Finland, 41 p.
- Mattavelli, P. (2001), "A closed-loop selective harmonic compensation for active filters," *IEEE Transactions on Industry Applications*, vol. 37, no. 1, pp. 81–89.
- McGranaghan, M., Kennedy, B. W., and Samotyj, M. (1998), "Power quality contracts in a competitive electric utility industry," in *Proc. 8th International Conference on Harmonics and Power Quality*, vol. 1, pp. 170–175.
- Mohan, N., Peterson, H. A., Long, W. F., Dreifuerst, G. R., and Vithayathil, J. J. (1977), "Active filters for ac harmonic suppression," in *Proc. IEEE Power Engineering Society Winter Meeting*, pp. 1–7.
- Mohan, N., Undeland, T. M., and Robbins, W. P. (1995), *Power Electronics*, John Wiley & Sons, Inc., New York, NY, USA, second ed., 802 p.
- Nabae, A., Nakano, H., and Togasawa, S. (1995), "An instantaneous distortion current compensator without any coordinate transformation," in *Proc. IEEJ International Power Electronics Conference*, Yokohama, Japan, pp. 1651–1655.

- Niemelä, M. (1999), *Position sensorless electrically excited synchronous motor drive for industrial use based on direct flux linkage and torque control*, Doctoral dissertation, Lappeenranta University of Technology, Lappeenranta, Finland, 142 p.
- Noguchi, T., Tomiki, H., Kondo, S., and Takahashi, I. (1998), "Direct power control of PWM converter without power-source voltage sensors," *IEEE Transactions on Industry Applications*, vol. 34, no. 3, pp. 473–479.
- Ollila, J. (1993), *Analysis of PWM-Converters using Space Vector Theory*, Doctoral dissertation, Tampere University of Technology, Tampere, Finland, 179 p.
- Ooi, B. T., and Wang, X. (1990), "Voltage angle lock loop control of the boost type PWM converter for HVDC application," *IEEE Transactions on Power Electronics*, vol. 5, no. 2, pp. 229–235.
- Ottersten, R., and Svensson, J. (2002), "Vector current controlled voltage source converter—deadbeat control and saturation strategies," *IEEE Transactions on Power Electronics*, vol. 17, no. 2, pp. 279–285.
- Park, R. H. (1929), "Two-reaction theory of synchronous machines. Generalized method of analysis—Part I," *A. I. E. E. Transactions*, vol. 48, pp. 716–727.
- Pillay, P., and Manyage, M. (2001), "Definitions of voltage unbalance," *IEEE Power Engineering Review*, vol. 21, no. 5, pp. 50–51.
- Ponnaluri, S., and Brickwedde, A. (2001), "Overriding individual harmonic current control with fast dynamics for active filtering," in *Proc. IEEE 32nd Annual Power Electronics Specialists Conference*, Vancouver, BC, Canada, vol. 3, pp. 1596–1601.
- Pretorius, J.-H. C., van Wyk, J. D., and Swart, P. H. (2000), "An evaluation of some alternative methods of power resolution in a large industrial plant," *IEEE Transactions on Power Delivery*, vol. 15, no. 3, pp. 1052–1059.
- Proakis, J. G., and Manolakis, D. G. (1996), *Digital Signal Processing*, Prentice-Hall, Upper Saddle River, NJ, USA, third ed., 968 p.
- Pöllänen, R. (2003), *Converter-flux-based current control of voltage source PWM rectifiers – analysis and implementation*, Doctoral dissertation, Lappeenranta University of Technology, Lappeenranta, Finland, 165 p.
- Pöllänen, R., Tarkiainen, A., Niemelä, M., and Pyrhönen, J. (2002), "A novel load current feedforward control for direct torque control based AC-DC-AC converters," in *Proc. 15th International Conference on Electrical Machines*, Bruges, Belgium, 6 p., cd-rom.
- Pöllänen, R., Tarkiainen, A., Niemelä, M., and Pyrhönen, J. (2003), "Supply voltage sensorless reactive power control of DTC modulation based line converter with L- and LCL-filters," in *Proc. 10th European Conference on Power Electronics and Applications*, Toulouse, France, 10 p., cd-rom.
- Rahman, M. A., Radwan, T. S., Osheiba, A. M., and Lashine, A. E. (1997), "Analysis of current controllers for voltage-source inverter," *IEEE Transactions on Industrial Electronics*, vol. 44, no. 4, pp. 477–485.

- le Roux, A. D., and Enslin, J. H. R. (1998), "Integrated active rectifier and power quality compensator," in *Proc. 8th International Conference on Harmonics And Quality of Power*, Athens, Greece, vol. 1, pp. 337–341.
- le Roux, A. D., du Toit, J. A., and Enslin, J. H. R. (1999), "Integrated active rectifier and power quality compensator with reduced current measurement," *IEEE Transactions on Industrial Electronics*, vol. 46, no. 3, pp. 504–511.
- Rowan, T. M., and Kerkman, R. J. (1986), "A new synchronous current regulator and an analysis of current-regulated PWM inverters," *IEEE Transactions on Industry Applications*, vol. IA-22, no. 4, pp. 678–690.
- Råde, L., and Westergren, B. (1993), *Beta mathematics handbook*, Chartwell-Bratt, Lund, Sweden, second ed., 494 p.
- Sasaki, H., and Machida, T. (1971), "A new method to eliminate AC harmonic currents by magnetic flux compensation—considerations on basic design," *IEEE Transactions on Power Apparatus and Systems*, vol. PAS-90, pp. 2009–2019.
- Sensarma, P. S., Padiyar, K. R., and Ramanarayanan, V. (2000), "A comparative study of harmonic filtering strategies for a shunt active filter," in *Proc. IEEE Industry Applications Conference*, Rome, Italy, vol. 4, pp. 2509–2516.
- Sonnenschein, M., and Staudt, V. (1998), "Evaluation of a shunt active filter using frequency identification," in *Proc. 8th International Conference on Harmonics and Quality of Power*, Athens, Greece, vol. 2, pp. 617–622.
- Sonnenschein, M., and Weinhold, M. (1999), "Comparison of time-domain and frequency-domain control schemes for shunt active filters," *European Transactions on Electrical Power*, vol. 9, no. 1, pp. 5–16.
- Staudt, V. (1996), "Dynamic parallel compensation of active non-linear loads using the FBD-method," in *Proc. 7th International Conference on Harmonics and Quality of Power*, Las Vegas, NV, USA, pp. 21–26.
- Stump, M. D., Keane, G. J., and Leong, F. K. S. (1998), "The role of custom power products in enhancing power quality at industrial facilities," in *Proc. International Conference on Energy Management and Power Delivery*, Singapore, vol. 2, pp. 507–517.
- Svensson, J., and Ottersten, R. (1999), "Shunt active filtering of vector current-controlled VSC at a moderate switching frequency," *IEEE Transactions on Industry Applications*, vol. 35, no. 5, pp. 1083–1090.
- Takahashi, I., and Noguchi, T. (1986), "A new quick-response and high-efficiency control strategy of an induction motor," *IEEE Transactions on Industry Applications*, vol. IA-22, no. 5, pp. 820–827.
- Takeshita, T., Masuda, T., and Matsui, N. (2001), "Current waveform control of distributed generation system for harmonic voltage suppression," in *Proc. IEEE 32nd Annual Power Electronics Specialists Conference*, Vancouver, BC, Canada, vol. 2, pp. 516–521.
- Takeshita, T., and Matsui, N. (2003), "Current waveform control of PWM converter system for harmonic suppression on distribution system," *IEEE Transactions on Industrial Electronics*, vol. 50, no. 6, pp. 1134–1139.

- Tamyurek, B., Nichols, D. K., and Demirci, O. (2003), "The NAS battery: A multi-functional energy storage system," in *Proc. IEEE Power Engineering Society General Meeting*, vol. 4, pp. 1991–1996.
- Tarkiainen, A., Pöllänen, R., Niemelä, M., and Pyrhönen, J. (2002), "Optimum switching table based synchronous co-ordinate modulation method for voltage source inverter," in *Proc. 15th International Conference on Electrical Machines*, Bruges, Belgium, 6 p., cd-rom.
- Tarkiainen, A., Pöllänen, R., Niemelä, M., and Pyrhönen, J. (2003a), "Converter flux linkage oriented current vector control using synchronous co-ordinate vector modulation," in *Proc. 10th European Conference on Power Electronics and Applications*, Toulouse, France, 10 p., cd-rom.
- Tarkiainen, A., Pöllänen, R., Niemelä, M., and Pyrhönen, J. (2003b), "DTC based power conditioning system capable of grid-connected and grid-independent operation," in *Proc. 10th European Conference on Power Electronics and Applications*, Toulouse, France, 8 p., cd-rom.
- Tarkiainen, A., Pöllänen, R., Niemelä, M., Pyrhönen, J., and Vertanen, M. (2003c), "Compensating the island network voltage unsymmetry with DTC-modulation based power conditioning system," in *Proc. IEEE International Electric Machines and Drives Conference*, Madison, WI, USA, pp. 987–993.
- Tiitinen, P., Pohjalainen, P., and Lalu, J. (1995), "The next generation motor control method: Direct torque control (DTC)," *EPE Journal*, vol. 5, no. 1, pp. 14–18.
- Vas, P. (1992), *Electrical Machines and Drives*, Oxford University Press., New York, USA, 808 p.
- Veltman, A., and Duarte, J. (1995), "Fish method based on-line optimal control for PWM rectifiers," in *Proc. IEEE 26th Annual Power Electronics Specialists Conference*, Atlanta, Georgia, USA, vol. 1, pp. 549–555.
- Wei, T., Li, Y., Hu, G., and Zhu, H. (2003), "Modeling and control of circulating current in parallel three-phase PWM converters," in *Proc. 5th International Conference on Power Electronics and Drive Systems*, vol. 2, pp. 910–914.
- Weinhold, M. (1991), "A new control scheme for optimal operation of a three-phase voltage dc link PWM converter," in *Proc. 19th International Intelligent Motion Conference*, Nürnberg, Germany, pp. 371–383.
- Wheeler, N. J., Fraser, M. E., Alexander, T., and Davies, T. S. (1997), "Three-phase regenerative front-ends for induction motor drives," in *IEE Colloquium, Update on New Power Electronic Techniques (Digest No:1997/091)*, pp. 6/1–6/6.
- Willems, J. L. (1992), "A new interpretation of the Akagi-Nabae power components for nonsinusoidal three-phase situations," *IEEE Transactions on Instrumentation and Measurement*, vol. 41, no. 4, pp. 523–527.
- Wilson, T. G. (2000), "The evolution of power electronics," *IEEE Transactions on Power Electronics*, vol. 15, no. 3, pp. 439–446.

- Wrede, H., and Staudt, V. (2004), "Optimized feed forward control of STATCOM with limited energy storage capability for flicker compensation," in *Proc. IEEE 35th Annual Power Electronics Specialists Conference*, Aachen, Germany, pp. 3157–3163.
- Yano, M., Kuramochi, S., and Nanaumi, N. (1997), "New control method of harmonic current compensation using individual rotating P-Q frame of corresponding frequency," in *Proc. 7th European Conference on Power Electronics and Applications*, vol. 4, pp. 4842–4847.
- Ye, Z., Boroyevich, D., Choi, J.-Y., and Lee, F. C. (2000), "Control of circulating current in parallel three-phase boost rectifiers," in *Proc. IEEE 15th Annual Applied Power Electronics Conference and Exposition*, New Orleans, LA, USA, vol. 1, pp. 506–512.
- Åström, K., and Hägglund, T. (1995), *PID Controllers: Theory, Design, and Tuning*, Instrument Society of America, Research Triangle Park, NC, USA, second ed., 343 p.

Appendix 1

The data of the line converters used in experiments

The following tables provide information of the 19 kVA and 490 kVA line converter units used in experiments. Both line converters use the same control software. The digital signal processor used is Motorola 56002 running at 80 MHz clock frequency. The control algorithms were programmed with assembler language. The switch combination of the power stage is determined in every 25 μ s. The minimum pulse width is also 25 μ s.

Table A1.1: Data of 19 kVA line converter

| Nominal values | |
|---|------------------------|
| Nominal apparent power, S_n | 18.7 kVA |
| Nominal input voltage, U_{2n} | 400 V |
| Nominal current, I_{1n} | 27 A |
| Nominal line frequency, f_s | 50 Hz |
| Average switching frequency | 1–4 kHz (controllable) |
| Base values of the per unit system | |
| Voltage, u_{base} | 327 V |
| Current, i_{base} | 38.2 A |
| Frequency, ω_{base} | 100π rad/s |
| Impedance, Z_{base} | 8.55 Ω |
| Inductance, L_{base} | 27.2 mH |
| Capacitance, C_{base} | 0.372 mF |
| Flux, ψ_{base} | 1.04 Wb |
| Apparent power, s_{base} | 18.7 kVA |
| Line filter and dc-link parameters | |
| L-filter inductance, L_1 | 2.07 mH (0.0760 p.u.) |
| LCL-filter converter side inductance, L_1 | 1.07 mH (0.0393 p.u.) |
| LCL-filter line side inductance, L_2 | 1.00 mH (0.0367 p.u.) |
| LCL-filter capacitor [†] , C_f | 60 μ F (16.1 p.u.) |
| Dc-link capacitor, C_{dc} | 1.1 mF (2.96 p.u.) |

[†]Star connection equivalent value

Table A1.2: Data of 490 kVA line converter

| Nominal values | |
|---|---------------------------|
| Nominal apparent power, S_n | 490 kVA |
| Nominal input voltage, U_{2n} | 690 V |
| Nominal current, I_{1n} | 410 A |
| Nominal line frequency, f_s | 50 Hz |
| Average switching frequency | 1–4 kHz (controllable) |
| Base values of the per unit system | |
| Voltage, u_{base} | 563 V |
| Current, i_{base} | 580 A |
| Frequency, ω_{base} | 100π rad/s |
| Impedance, Z_{base} | 0.972 Ω |
| Inductance, L_{base} | 3.09 mH |
| Capacitance, C_{base} | 3.28 mF |
| Flux, ψ_{base} | 1.79 Wb |
| Apparent power, s_{base} | 490 kVA |
| Line filter and dc-link parameters | |
| LCL-filter converter side inductance, L_1 | 186 μ H (0.0601 p.u.) |
| LCL-filter line side inductance, L_2 | 124 μ H (0.0401 p.u.) |
| LCL-filter capacitor [†] , C_f | 450 μ F (13.7 p.u.) |
| Dc-link capacitor, C_{dc} | 7.83 mF (2.39 p.u.) |

[†]Star connection equivalent value

Publication I

A. TARKIAINEN, R. PÖLLÄNEN, M. NIEMELÄ, AND J. PYRHÖNEN

Current Controlled Line Converter Using Direct Torque Control Method

European Transactions on Electrical Power, vol. 14, no 5, Sept./Oct. 2004, pp. 277–291.

Copyright © 2004 John Wiley & Sons Limited. Reproduced with permission.

The manuscript was sent to the publisher in 2001 and accepted for publication in 2002.

Current controlled line converter using direct torque control method

Antti Tarkkiainen^{*†}, Riku Pöllänen, Markku Niemelä and Juha Pyrhönen

Lappeenranta University of Technology, P.O. Box 20, FIN-53851 Lappeenranta, Finland

SUMMARY

The control system of a current controlled line converter is implemented using the direct torque control (DTC) method. Implementation of the converter flux linkage orientated control system combines the DTC method with the conventional field orientated vector control principle. The same physical structure of the control system as in DTC motor control can be used with the line converter without extra measurements. Both L- and LCL-topologies are used as line filters. Experimental results demonstrate the validity and the high dynamic performance of the control system. Copyright © 2004 John Wiley & Sons, Ltd.

KEY WORDS: direct torque control; line converter; power conversion; variable speed drive

1. INTRODUCTION

Line converters have become attractive in industrial applications because of a number of favourable properties. They provide constant or controllable dc-link voltage, almost sinusoidal input current, controllable power factor and regeneration capability. Line converters are used as part of high-performance electrical drives or as stand-alone supply units with common dc-bus. In order to achieve nearly sinusoidal input current and fast dc-bus voltage control advanced current vector control principle is usually recommended. Conventionally the pulse width modulation (PWM) method or current hysteresis control have been used to control the power switches. In this paper it is shown that the current control of the line converter can also be implemented using the direct torque control (DTC) method. It is also shown that a low line current distortion level can be achieved with a relatively small line filter and with a switching frequency that is in a typical range of industrial frequency converters. The experiments performed with the laboratory prototype converter show that the dynamic performance of the dc-bus voltage control with DTC is very good.

2. LINE CONVERTER WITH DTC METHOD

The DTC modulation method was initially developed for induction motor (IM) control [1]. Later the same or the same kind of control methods have been applied to control of the line converter [2,3]. The basic principle of the DTC controlled line converter is shown in Figure 1. The hardware can be,

^{*}Correspondence to: Antti Tarkkiainen, Lappeenranta University of Technology, P.O. Box 20, FIN-53851 Lappeenranta, Finland.
[†]E-mail: Antti.Tarkkiainen@lut.fi

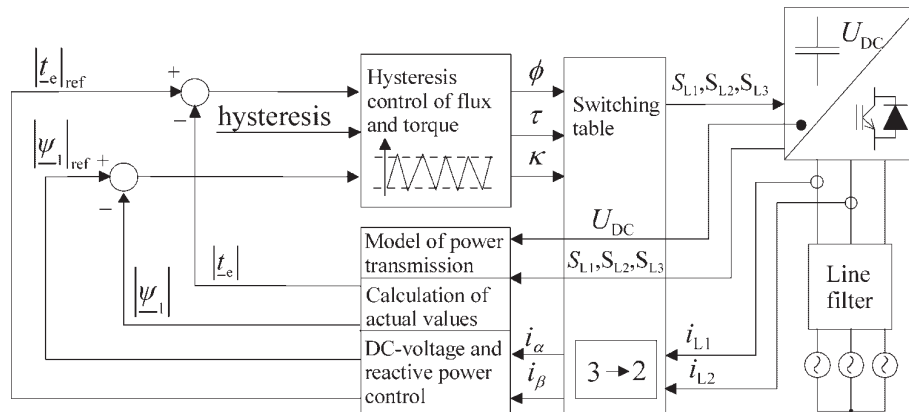


Figure 1. Principle of the direct torque controlled line converter.

in fact, exactly the same as in the IM drive application. Only the dc-bus voltage and two-phase current measurements are needed.

The primary task of the control system is to stabilize the dc-bus voltage. Also the reactive power of the converter is controlled. Primary control variables are the absolute value of the converter flux linkage vector and the calculatory torque. In the line converter application the torque should be understood as a calculatory quantity that is proportional to the active power. With the conventional DTC method, in contrast to most traditional line converter control methods, the converter current is not directly controlled.

The line filter is used to reduce the line current distortion. Commonly the three-phase series inductance (L-filter) has been used as a line filter. Recently the LCL-filter has become a very attractive alternative because a lower line current harmonic distortion can be obtained, at least in theory, at low switching frequencies [4] and with smaller total inductance compared to an L-filter [5].

In practice, however, owing to resonances in the LCL-filter, the line current harmonic distortion tends to be higher than with the L-filter. Therefore, it should be emphasized that the main benefit of using an LCL-filter is the lower line voltage distortion compared to the L-filter. This is a very important feature especially when the short circuit ratio (SCR) at the point of common coupling (PCC) is small. Both L- and LCL-filter topologies are considered in this paper.

3. MATHEMATICAL MODELLING

3.1. Two-axis model

Line converters with L- and LCL-filters are shown in Figure 2. By transforming the voltages and currents of the AC side into the d - q -coordinate reference frame rotating synchronously with the network angular frequency ω_s , the voltage equations can be expressed in state-space form

$$\dot{\mathbf{x}}(t) = \mathbf{A}\mathbf{x}(t) + \mathbf{B}\mathbf{u}(t) \quad (1)$$

where matrices and vectors for the L-filter case are

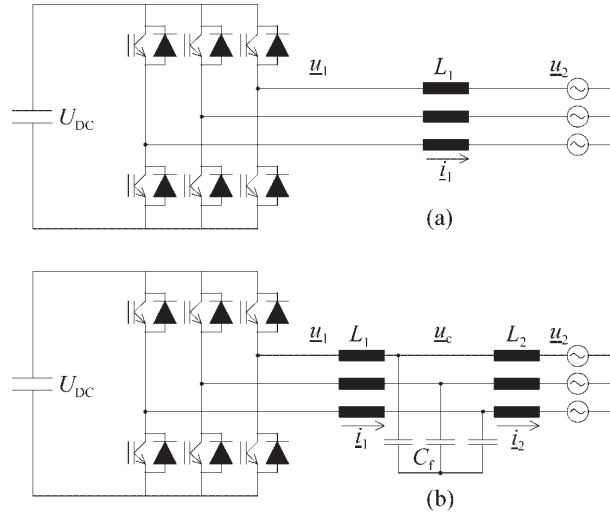


Figure 2. Line converter connected to the grid through (a) an L-filter and (b) an LCL-filter.

$$\mathbf{x}_L = [i_{1d} \quad i_{1q}]^T \quad (2a)$$

$$\mathbf{u}_L = [u_{1d} \quad u_{1q} \quad u_{2d} \quad u_{2q}]^T \quad (2b)$$

$$\mathbf{A}_L = \begin{bmatrix} -\frac{R_1}{L_1} & \omega_s \\ -\omega_s & -\frac{R_1}{L_1} \end{bmatrix} \quad (2c)$$

$$\mathbf{B}_L = \begin{bmatrix} \frac{1}{L_1} & 0 & -\frac{1}{L_1} & 0 \\ 0 & \frac{1}{L_1} & 0 & -\frac{1}{L_1} \end{bmatrix} \quad (2d)$$

and the matrices and vectors for the LCL-filter case are

$$\mathbf{x}_{LCL} = [i_{1d} \quad i_{1q} \quad i_{2d} \quad i_{2q} \quad u_{cd} \quad u_{cq}]^T \quad (2e)$$

$$\mathbf{u}_{LCL} = [u_{1d} \quad u_{1q} \quad u_{2d} \quad u_{2q}]^T \quad (2f)$$

$$\mathbf{A}_{LCL} = \begin{bmatrix} -\frac{R_1}{L_1} & \omega_s & 0 & 0 & -\frac{1}{L_1} & 0 \\ -\omega_s & -\frac{R_1}{L_1} & 0 & 0 & 0 & -\frac{1}{L_1} \\ 0 & 0 & -\frac{R_2}{L_2} & \omega_s & \frac{1}{L_2} & 0 \\ 0 & 0 & -\omega_s & -\frac{R_2}{L_2} & 0 & \frac{1}{L_2} \\ \frac{1}{C_f} & 0 & -\frac{1}{C_f} & 0 & 0 & \omega_s \\ 0 & \frac{1}{C_f} & 0 & -\frac{1}{C_f} & -\omega_s & 0 \end{bmatrix} \quad (2g)$$

and

$$\mathbf{B}_{\text{LCL}} = \begin{bmatrix} \frac{1}{L_1} & 0 & 0 & 0 \\ 0 & \frac{1}{L_1} & 0 & 0 \\ 0 & 0 & -\frac{1}{L_2} & 0 \\ 0 & 0 & 0 & -\frac{1}{L_2} \\ 0 & 0 & 0 & 0 \\ 0 & 0 & 0 & 0 \end{bmatrix} \quad (2\text{h})$$

respectively. Usually the d -axis of the d - q -frame is fixed to the network voltage vector \underline{u}_2 or the network flux linkage vector $\underline{\psi}_2$. This means that the network voltage has to be measured. In the DTC controlled line converter this measurement can be avoided by fixing the d - q -frame to the fictitious line converter flux linkage vector $\underline{\psi}_1$ estimated with the voltage model

$$\underline{\psi}_1 = \int \underline{u}_1 dt + \underline{\psi}_{\text{init}} \quad (3)$$

where $\underline{\psi}_{\text{init}}$ is the initial value of the integral identified by the control system during the synchronization. Coordinate transformations between the rotating reference frame (d - q) and the stationary reference frame (α - β) are also easily calculated without trigonometric functions using the scalar and vector products and the absolute value of the converter flux linkage vector

$$i_{1d} = \frac{\underline{\psi}_1 \cdot \underline{i}_1}{|\underline{\psi}_1|} \quad \text{and} \quad i_{1q} = \frac{\underline{\psi}_1 \times \underline{i}_1}{|\underline{\psi}_1|} \quad (4)$$

As a drawback of the reference frame selection the power factor control becomes slightly more complex when the reference frame is fixed to the $\underline{\psi}_1$ instead of \underline{u}_2 or $\underline{\psi}_2$.

3.2. Power transmission model

Let us derive the equations of the power transmission between the converter and the network when an L-filter is used. The same equations apply also to the LCL-filter when the power transfer through the converter side inductance L_1 is only considered. Actually the equations for the active power hold also for the whole LCL-filter if the resistances of the filter components are assumed to be negligible.

The transferred active power in the steady state is calculated as

$$p = \frac{3}{2} \text{Re}\{\underline{u}_2 \underline{i}_1^*\} = \frac{3}{2} \text{Re}\{j\omega_s \underline{\psi}_2 \underline{i}_1^*\} = \frac{3}{2} \omega_s (\psi_{2d} i_{1q} - \psi_{2q} i_{1d}) \quad (5)$$

The last expression can be interpreted as a calculatory torque t_e , which can also be determined using the converter flux linkage vector

$$\underline{p} = \frac{3}{2} \omega_s (\underline{\psi}_2 \times \underline{i}_1) = \frac{3}{2} \omega_s (\underline{\psi}_1 \times \underline{i}_1) = t_e \omega_s \quad (6)$$

where the (calculatory) torque of the line converter is

$$t_e = \frac{3}{2} (\underline{\psi}_1 \times \dot{i}_1) \quad (7)$$

In d - q -coordinates fixed to the converter flux linkage vector the quadratic component ψ_{-1q} is zero and the direct component is equal to the length of converter flux linkage vector so Equation (7) becomes simply

$$t_e = \frac{3}{2} (\psi_{1d} i_{1q} - \psi_{1q} i_{1d}) = \frac{3}{2} |\underline{\psi}_1| i_{1q} \quad (8)$$

Referring to Equations (6) and (8) the quadratic current component i_{1q} and the active power can be controlled with the torque of the line converter.

Reactive power can be calculated as

$$q = \frac{3}{2} \text{Im}\{\underline{u}_2 \dot{i}_1^*\} = \frac{3}{2} \text{Im}\{j\omega_s \underline{\psi}_2 \dot{i}_1^*\} = \frac{3}{2} \omega_s (\psi_{2d} i_{1d} + \psi_{2q} i_{1q}) \quad (9)$$

where the last expression can be expressed as the scalar product

$$q = \frac{3}{2} \omega_s (\underline{\psi}_2 \cdot \dot{i}_1) \quad (10)$$

From Figure 2(a) it is seen that the network flux linkage vector can be calculated as

$$\underline{\psi}_2 = \underline{\psi}_1 - L_1 \dot{i}_1 \quad (11)$$

Substituting Equation (11) into Equation (10) gives

$$q = \frac{3}{2} \omega_s [(\underline{\psi}_1 - L_1 \dot{i}_1) \cdot \dot{i}_1] = \frac{3}{2} \omega_s (|\underline{\psi}_1| i_{1d} - L_1 |\dot{i}_1|^2) \quad (12)$$

From Equation (12) it is seen that the reactive power and thus the power factor of the line converter can be controlled with the length of the converter flux linkage vector. Also, the amplitude of the converter flux linkage can be used to control the current component i_{1d} .

3.3. Reactive power estimation with LCL-filter

The calculation of the reactive power in the network becomes more complicated than Equation (12) when an LCL-filter is used. The reason is that the current \dot{i}_2 flowing through the line side inductance L_2 is not measured. It is, however, needed to determine the network flux linkage vector, which can be expressed as

$$\underline{\psi}_2 = \underline{\psi}_1 - L_1 \dot{i}_1 - L_2 \dot{i}_2 \quad (13)$$

In order to use Equation (13) the line current i_2 has to be estimated from the measured current i_1 , estimated converter flux linkage $\underline{\psi}_1$ and the known filter parameters. Because we are mainly interested in controlling the power factor, i.e. the reactive power related to the fundamental frequency, appropriate equations for line current estimation are found from the d - q -frame state equations of the LCL-filter corresponding to the steady state. If the resistances are negligible the following steady state relations between converter and line currents may be solved from Equations (1) and (2e)–(2h)

$$i_{2d} = (1 - \omega_s^2 L_1 C_f) i_{1d} + \omega_s C_f u_{1q} \quad (14)$$

and

$$i_{2q} = (1 - \omega_s^2 L_1 C_f) i_{1q} - \omega_s C_f u_{1d} \quad (15)$$

Furthermore, if it is assumed that

$$\underline{u}_1 = j\omega_s \underline{\psi}_1 = -\omega_s \psi_{1q} + j\omega_s \psi_{1d} = j\omega_s |\underline{\psi}_1| \quad (16)$$

Equations (14) and (15) can be rewritten as

$$i_{2d} = (1 - \omega_s^2 L_1 C_f) i_{1d} + \omega_s^2 C_f |\underline{\psi}_1| \quad (17)$$

and

$$i_{2q} = (1 - \omega_s^2 L_1 C_f) i_{1q} \quad (18)$$

Substituting Equation (13) into Equation (10) and writing the result in synchronous coordinates gives the reactive power estimate

$$q = \frac{3}{2} \omega_s \left[(|\underline{\psi}_1| - L_1 i_{1d}) i_{2d} - L_1 i_{1q} i_{2q} - L_2 |\dot{i}_2|^2 \right] \quad (19)$$

where the line current components i_{2d} and i_{2q} are estimated with Equations (17) and (18).

4. CURRENT CONTROL USING DTC

The conventional DTC based control system of the line converter, shown in Figure 1, has some advantageous properties. The control system is rather simple because coordinate transformations are unnecessary and the hysteresis control loops are very fast and do not need any controller parameters to be determined. Very good dc-link control dynamics may be obtained and thus modest dc-link capacitors can be used. The grid currents, however, are not actively controlled but are indirectly determined by the torque and the flux control loops. In a line converter application the shape of the currents is more important than in a motor drive application. Often the shape of the currents and the total harmonic distortion (THD) are used as a figure of merit. A good line converter control system, in this respect, draws sinusoidal grid currents that correspond to the requested active and reactive power transfer. This also implies that the line converter should draw sinusoidal currents even if the grid voltage is not purely sinusoidal. This objective is achieved by controlling the converter currents actively.

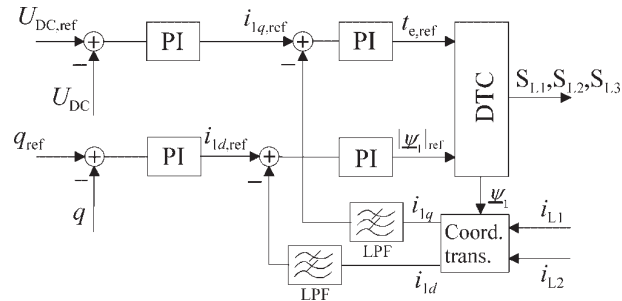


Figure 3. Block diagram of the current control principle with the DTC method.

In Figure 3 the proposed current control principle of the DTC line converter is shown. The synchronous reference frame of the current control is fixed to the converter flux linkage vector. Previously this reference frame has been used in induction motor control [6,7] and the concept of line converter flux linkage has been used previously in Reference 8, where the line converter flux linkage was not used in a control system. Conventional line converter vector control systems require a network voltage measurement for the field orientation. With DTC the converter flux linkage vector is always available and by using it as a basis of the synchronous reference frame the field orientated control can be realized without network voltage measurement. Sometimes a line converter control without network voltage measurement is called sensorless control [3,9].

The idea of controlling current components i_{1d} and i_{1q} with DTC is based on the equations given in the previous section. Conventionally the current controllers in Figure 3 give the d - q -components of the converter voltage vector reference. These voltage references are then transformed to stationary coordinates and further to gate signals of the power switches using some PWM modulation method.

With DTC these coordinate transformations are unnecessary because current controllers produce the torque reference and the converter flux linkage amplitude reference directly. The converter voltage vector to be switched is determined according to normal DTC principles using hysteresis comparators and the optimal switching table [10]. Measured current components are low-pass filtered to prevent the switching ripple from disturbing the control.

The DTC control method is a stationary reference frame control method. However, one may find similarities between the DTC and the converter flux linkage oriented control. According to Equation (8) the instantaneous torque is directly proportional to the quadrature component of the current vector expressed in the converter flux linkage orientated reference frame. Further, the absolute value of the converter flux linkage vector is the integral of the direct component of the converter voltage in the converter flux orientated reference frame

$$|\underline{\psi}_1| = \int u_{1d} dt \quad (20)$$

This article shows that the field oriented control principle and the DTC method can be combined. The synchronous coordinate current control may use the DTC as a high performance modulator, which has the torque and the flux linkage amplitude references as the input quantities.

The reactive power control can be implemented either as open-loop control or as closed-loop control. In the closed-loop control the estimated network reactive power is controlled with a controller

producing the direct axis converter current reference $i_{1d,\text{ref}}$. In the open-loop control the d -axis current reference producing the desired reactive power can be solved for L- and LCL-filter cases from Equations (12) and (19), respectively. With the L-filter, for example, the direct axis current reference, which produces unity power factor, is calculated as

$$i_{1d,\text{ref}} = \frac{|\psi_1| - \sqrt{|\psi_1|^2 - 4L_1^2 i_{1q,\text{ref}}^2}}{2L_1} \quad (21)$$

where $i_{1q,\text{ref}}$ is the output of the dc-link voltage controller. With the LCL-filter the closed-loop reactive power control is preferable because the open-loop equation for $i_{1d,\text{ref}}$ will become very cumbersome. Instead, it is quite easy to estimate the reactive power using Equations (17)–(19) and control it with the controller. Of course this means that a couple of the new controller parameters must be determined, but in this case the tuning of the controller is simple because the control system is required more to reduce the steady-state error than to provide good tracking properties in transient situations. Moreover, when the controller has an integral action, the steady state error in the reactive power depends on the accuracy of the line filter parameters in the reactive power estimation scheme and not on the controller parameters.

5. EXPERIMENTAL RESULTS

The introduced current control method was implemented in a digital signal processor (DSP) and tested with a 55 kVA line converter prototype. Other nominal values of the converter were $U_n = 400$ V, $I_n = 77$ A. These nominal values and the fundamental frequency 50 Hz were used in calculating the base values of the per unit (pu) system. DC-link capacitance was 2.3 mF (2.2 pu) and the inductances L_1 and L_2 of the line filter were 810 μ H (0.08 pu) and 500 μ H (0.05 pu), respectively. Line filter capacitance C_f was 60 μ F (0.05 pu). The average switching frequency was about 4 kHz. The total harmonic distortion of the supply voltage when the line converter was not connected to the grid was 2.3%, calculated with the first 40 harmonic components. The most significant harmonic component was the 5th harmonic, the amplitude of which was 2.2%.

The line converter was used as a supplying unit for a laboratory test set-up consisting of an induction motor supplied by a voltage source inverter, a DC load machine with a 4-quadrant drive and a flexible coupling between the machines. Owing to the test arrangement both the DC-drive and the line converter were distorting the line voltage since they were connected to the same transformer.

5.1. Steady-state operation

Figure 4 shows measured line currents under unity power factor and rated power operation in steady state when L- and LCL-filters are used. Figure 5 shows the corresponding phase voltages. The calculated line current spectrums are shown in Figure 6. The total harmonic distortions are found to be excellent, 1.8% for the L-filter and 3.0% for the LCL-filter, calculated with the first 40 harmonic components. It is seen that the LCL-filter effectively removes the high-frequency current components that are the most harmful for the line voltage. The higher THD-value in the case of the LCL-filter is due to low-order harmonics. Still, no harmonic current amplitude exceeds 2% of the fundamental component amplitude. Figure 6 also shows that there is no distinct switching frequency component in the spectrum when the DTC principle is used.

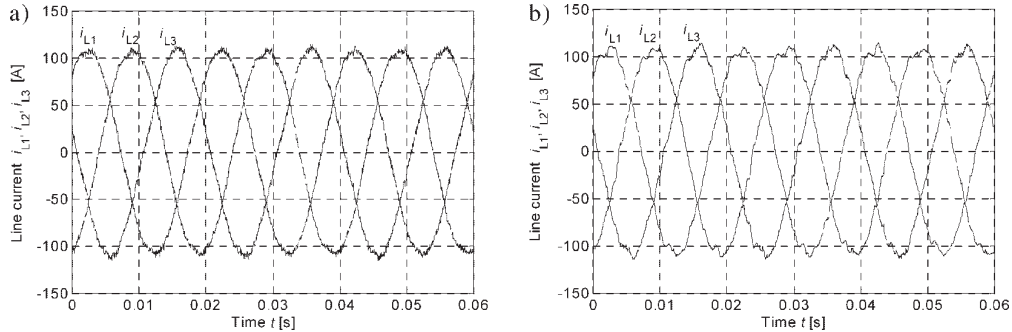


Figure 4. Measured line currents in rectifying mode when $P = 55$ kW and (a) the L-filter, and (b) the LCL-filter are used.

In Figure 5 it is seen that the high-frequency voltage distortion is absent when the LCL-filter is used. The apparent power of the mains transformer is 1000 kVA and it is thus rather large compared to the line converter. In weaker networks the effect of the LCL-filter is emphasized still. Figures 5 also shows, that the thyristor bridge of the dc-drive has a considerable distorting effect on the network voltage.

5.2. Dynamic performance

The dynamic performance of the dc-link voltage control was tested with a dc-voltage reference step change and a load step. Figure 7 shows a step response of the dc-voltage when the reference is changed from 570 V to 670 V under nominal load conditions in rectifying mode. The q -direction current changes from 1 pu to 2.3 pu in 1 ms. The torque reference limit limits the q -direction current to that value. The d -axis current does not experience a large change and thus the current control is seen to have good decoupling even though no synchronous frame decoupling has been used.

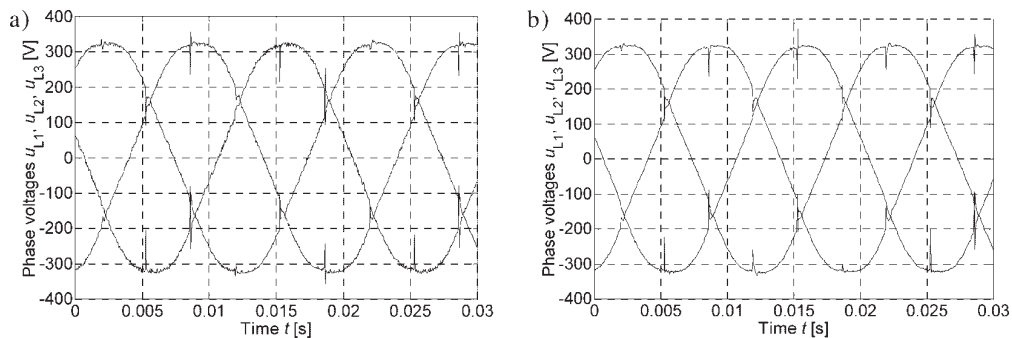


Figure 5. Measured network phase voltages with (a) the L-filter, and (b) LCL-filter. The line converter is rectifying at nominal power $P = 55$ kW and the dc-drive is inverting the power back to the grid. The apparent power of the mains transformer is 1000 kVA.

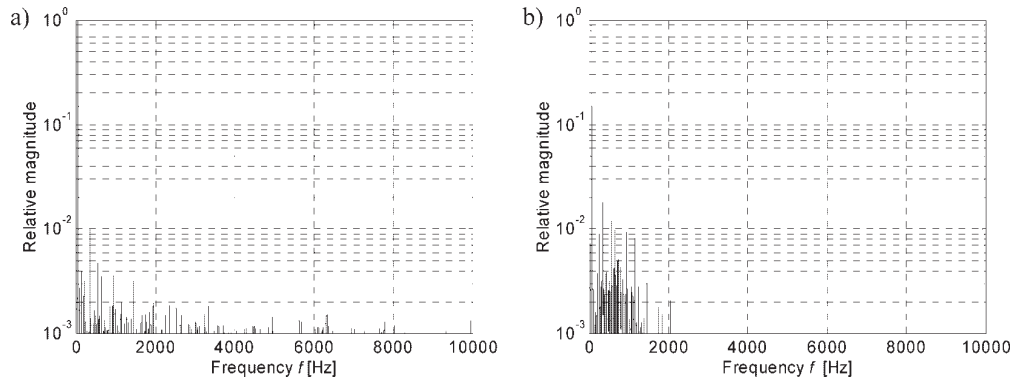


Figure 6. Line current spectra when (a) the L-filter, and (b) the LCL-filter are used. The total harmonic distortions are 1.8% and 3.0%, respectively.

Figure 8 shows the line converter phase currents and the dc-link voltage during the load step test. The load step was generated by changing the torque reference of the motor converter stepwise from 0% to 100%. The dc-link voltage is observed to deviate less than 5% from the 600 V reference value.

The closed loop reactive power control with LCL-filter was tested in the transient situation by ramping the active power of the line converter from rectifying mode to inverting mode in 400 ms under zero reactive power reference. The result of the measurement is shown in Figure 9. It is seen that in the beginning of the transient situation the reactive power deviates slightly from the reference value but is rapidly corrected. The small steady state error is mostly due to parameter inaccuracies in the reactive power estimation scheme.

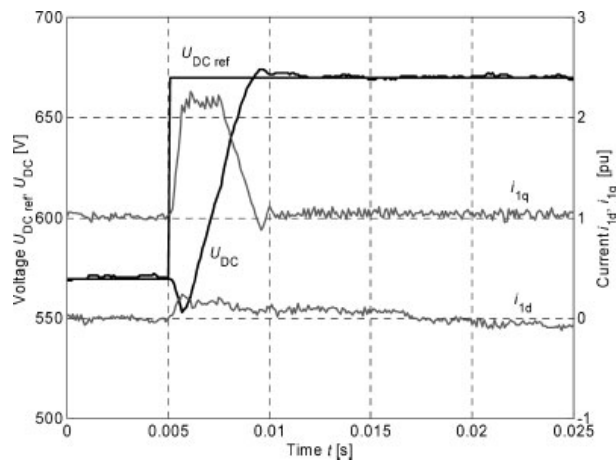


Figure 7. A measured 100 V dc-voltage step at the time instant $t = 0.005$ s. Line converter d - and q -axis currents are also shown.

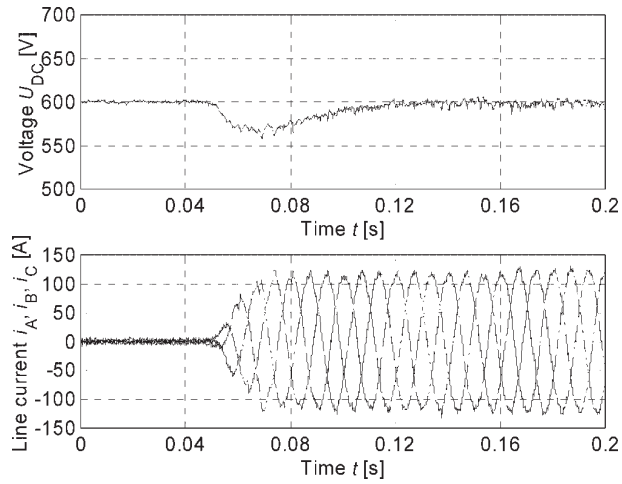


Figure 8. Measured load step responses from no-load to rated power.

5.3. Comparison of the conventional DTC and the current control DTC

The conventional DTC control of the line converter provides good dynamic performance but does not actively control the grid currents. The measured conventional DTC method is generally outlined in Figure 1. The dc-bus voltage controller produces torque reference directly and the reactive power controller sets the reference of the flux linkage amplitude. This paper shows that the high-performance DTC method can be used to control the grid currents similarly to the field orientated control methods.

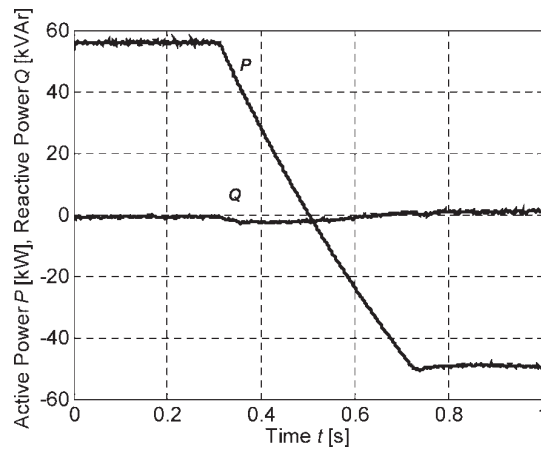


Figure 9. Measured active and reactive power in active power ramp from rectifying mode to inverting mode.

Good dynamic properties are maintained and better current waveforms are obtained. Table I shows the measured phase current THD values of the line converter using the conventional DTC method and the current control DTC. Two different L-filters and an LCL-filter were used and measurements were conducted with dc-link voltages ranging from 560 V to 600 V. The dc-link voltage determines the voltage reserve of the line converter. With 400 V mains voltage the converter is operating in the linear modulation range if the dc-link voltage is higher than 565 V. If the reactive power of the line filter is to be compensated for the unity power factor the dc-link voltage limit is somewhat higher. Table I shows that the current THD is rapidly increasing when the over-modulation range is approached. The grid current THD with the current control DTC is always smaller than with the conventional DTC. It is expected that the difference is emphasized with more distorted supply voltage.

The performance in unsymmetrical supply was also tested. The unsymmetrical supply condition was made by adding a 500 μH series inductor in one of the supply phases. At nominal power rectifying this yielded a 5% unsymmetry in supply voltages. Line currents were measured using the conventional DTC method and current control DTC. Figure 10 shows that the current control DTC can maintain rather sinusoidal currents even in an unsymmetrical supply.

6. CONCLUSIONS

The line converter control system that combines the high dynamic performance of the direct torque control method and sinusoidal input current of the conventional current control method was introduced and experimentally verified. Measurements show that the converter grid currents with the proposed method are more sinusoidal than with the conventional DTC method. In demanding supply conditions, such as unsymmetrical supply voltage, the benefits of the proposed method are emphasized. The control system may be used with either the L- or the LCL-line filter. The input current THD-value is slightly lower with the L-filter than with the LCL-filter. In spite of that the LCL-filter is preferred because of lower line voltage disturbance. The reactive power control was investigated using both

Table I. Total harmonic distortion of the measured converter phase current with different control methods, line filter configurations and dc-link voltage levels. The THD values are calculated with the 40 first harmonic components. L-filter 1: $L_1 = 1310 \mu\text{H}$, L-filter 2: $L_1 = 810 \mu\text{H}$, LCL-filter: $L_1 = 810 \mu\text{H}$, $C_f = 60 \mu\text{F}$, $L_2 = 500 \mu\text{H}$.

| Line filter and control method | Grid current THD [%] | | | | |
|--------------------------------|----------------------|-------|-------|-------|-------|
| | Dc-link voltage | | | | |
| | 560 V | 570 V | 580 V | 590 V | 600 V |
| L-filter 1 | | | | | |
| Conventional DTC | 5.0 | 3.9 | 3.0 | 2.3 | 2.3 |
| Current control DTC | 2.7 | 1.8 | 1.9 | 1.8 | 1.7 |
| L-filter 2 | | | | | |
| Conventional DTC | 9.9 | 7.2 | 5.0 | 4.5 | 4.3 |
| Current control DTC | 8.2 | 5.3 | 3.2 | 3.0 | 2.9 |
| LCL-filter | | | | | |
| Conventional DTC | 6.1 | 4.1 | 3.3 | 3.6 | 3.4 |
| Current control DTC | 4.7 | 2.9 | 2.8 | 2.8 | 2.8 |

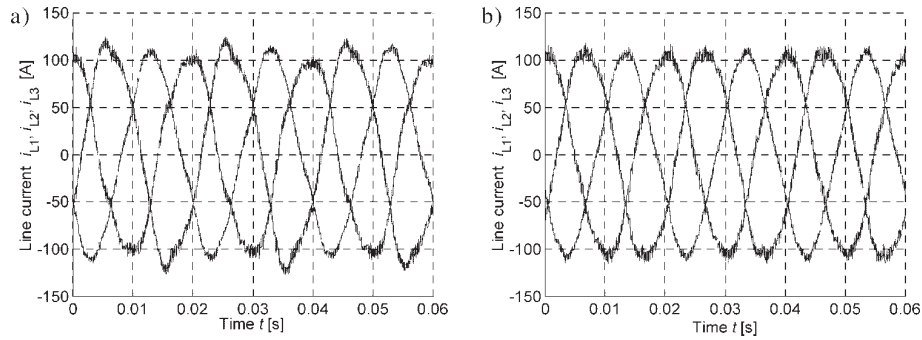


Figure 10. Measured line currents with unsymmetrical supply voltage. The line converter is rectifying at nominal power. L-filter $L_1 = 810 \mu\text{H}$ is used. (a) Conventional DTC, (b) current control DTC.

line filter topologies. The implemented converter flux orientated control algorithm uses only simple calculations and allows a relatively small line filter and dc-link capacitor to be used. Only three measurements are needed in the control system—two converter phase currents and the dc-link voltage.

7. LIST OF SYMBOLS AND ABBREVIATIONS

Symbols

| | |
|-------------------|---|
| \mathbf{A} | state matrix |
| \mathbf{B} | coefficient matrix of input vector |
| C_{dc} | dc-link capacitance |
| C_f | line filter capacitance |
| i | current |
| \dot{i}_1 | converter current space-vector |
| \dot{i}_2 | network current space-vector |
| L_1 | line filter inductance, converter side |
| L_2 | line filter inductance, network side |
| p | converter active power |
| \underline{p} | converter active power, space-vector representation |
| q | converter reactive power |
| t_e | converter calculatory torque |
| \underline{t}_e | converter calculatory torque, space-vector representation |
| R_1 | resistance of the line filter inductance, converter side |
| R_2 | resistance of the line filter inductance, network side |
| t | time |
| \mathbf{u} | input vector |
| \underline{u}_1 | converter voltage space-vector |
| \underline{u}_2 | network voltage space-vector |
| \underline{u}_c | line filter capacitor voltage space-vector |
| \mathbf{x} | state vector |
| κ | sector bits |
| τ | torque bits |

| | |
|----------------------|-------------------------------------|
| ϕ | flux bits |
| ψ | flux linkage |
| $\underline{\psi}_1$ | converter flux linkage space-vector |
| $\underline{\psi}_2$ | network flux linkage space-vector |
| ω_s | network angular frequency |

Subscripts

| | |
|-----------------|---|
| α, β | stationary reference frame quantity |
| 1 | converter side quantity |
| 2 | network side quantity |
| DC | direct current link |
| d | direct axis quantity (parallel with converter flux linkage space-vector) |
| init | initial value |
| L | L-filter |
| LCL | LCL-filter |
| ref | reference value |
| q | quadrature axis quantity (perpendicular with converter flux linkage space-vector) |

Abbreviations

| | |
|-----|---------------------------|
| DC | direct current |
| DSP | digital signal processor |
| DTC | direct torque control |
| IM | induction motor |
| PCC | point of common coupling |
| pu | per unit |
| PWM | pulse width modulation |
| SCR | short circuit ratio |
| THD | total harmonic distortion |

REFERENCES

1. Tiitinen P, Pohjalainen P, Lalu J. The next generation motor control method: direct torque control (DTC). *EPE Journal* 1995; **5**:14–18.
2. Manninen V. Application of direct torque control modulation technology to a line converter. *6th European Conference on Power Electronics and Applications (EPE)*, vol. 1–19, Sevilla, Spain, 1995; 1292–1296.
3. Noguchi T, Tomiki H, Kondo S, Takahashi I. Direct power control of PWM converter without power-source voltage sensors. *IEEE Transactions on Industry Applications* 1998; **34**:473–479.
4. Lindgren M, Svensson J. Connecting fast switching voltage source converters to the grid—harmonic distortion and its reduction. *IEEE Stockholm Power Tech Conference*, Stockholm, Sweden, 1995; 191–195.
5. Ollila J. A PWM-rectifier without current measurement. *EPE Journal* 1994; **4**(2):14–19.
6. Xu X, Novotny DW. Implementation of direct stator flux orientation on a versatile DSP based system. *IEEE Transactions on Industry Applications* 1991; **27**:694–700.
7. Kazmierkowski MP, Malinowski M, Sobczuk DL, Blaabjerg F, Pedersen JK. Simplified stator flux oriented control. *IEEE International Symposium on Industrial Electronics*, vol. 2, Bled, Slovenia, 1999; 474–479.
8. Weinhold M. A new control scheme for optimal operation of a three-phase voltage DC link PWM converter. *19th International Intelligent Motion Conference (PCIM)*, Nürnberg, Germany, 1991; 371–383.
9. Hansen S, Malinowski M, Blaabjerg F, Kazmierkowski MP. Sensorless control strategies for PWM rectifier. *15th Applied Power Electronics Conference and Exposition (APEC)*, vol. 1, New Orleans, U.S.A., 2000; 832–838.
10. Takahashi I, Noguchi T. A new quick-response and high-efficiency control strategy of an induction motor. *IEEE Transactions on Industry Applications* 1986; **1A**–22:820–827.

AUTHORS' BIOGRAPHIES



Antti Tarkiainen (born in 1975) received his M.Sc. degree in electrical engineering from Lappeenranta University of Technology (LUT) in 2000. He is a member of the Finnish Graduate School of Electric Engineering and is working as a research engineer in the Department of Electrical Engineering. His research work is in the area of electric drives, particularly in the line converter applications.



Riku Pöllänen (born in 1975) received his M.Sc. and D.Sc. degrees in electrical engineering from Lappeenranta University of Technology (LUT) in 1999 and 2003 respectively. He is currently working as a researcher in the Department of Electrical Engineering. His areas of interest are the modelling and control of electric drives, especially line converters.



Markku Niemelä (born in 1968) obtained his B.Sc. degree in electrical engineering from Helsinki Institute of Technology in 1990. He obtained his M.Sc. degree in 1995 and his Doctor of Science degree in 1999 from LUT. Currently he is a senior researcher in LUT. His research activities are on electric machines and drives.



Juha Pyrhönen (born in 1957) received his M.Sc. degree in electrical engineering from Lappeenranta University of Technology (LUT) in 1982. He received his Licentiate of Science (Technology) degree from LUT in 1989 and his degree of Doctor of Science (Technology) from LUT in 1991. Juha Pyrhönen became Associate Professor in Electric Engineering at LUT in 1993 and Professor in Electrical Machines and Drives in 1997. He is currently working as Head of the Department of Electrical Engineering. He is engaged in electric motor and electric drive research and development. He is also the leader of the Carelian Drives and Motor Centre which in co-operation with Finnish ABB Company develops new electric motors and drives.

Publication II

A. TARKIAINEN, R. PÖLLÄNEN, M. NIEMELÄ, J. PYRHÖNEN, AND M. VERTANEN

Compensating the Island Network Voltage Unsymmetry with DTC-Modulation-Based Power Conditioning System

IEEE Transactions on Industry Applications, vol. 40, no. 5, Sept./Oct. 2004, pp. 1398–1405.

Copyright © 2004 IEEE. Reprinted with permission.

Compensating the Island Network Voltage Unsymmetry With DTC-Modulation-Based Power Conditioning System

Antti Tarkiainen, *Student Member, IEEE*, Riku Pöllänen, *Member, IEEE*, Markku Niemelä, Juha Pyrhönen, and Mikko Vertanen

Abstract—An algorithm for compensating island network voltage unsymmetry with a direct torque control modulation-based scalar-controlled power conditioning system is introduced and experimentally verified. The proposed method consists of two separate stages where at first the unsymmetry is detected and then a compensating negative-sequence system is calculated. Experimental results show that the proposed method fully compensates the voltage unsymmetry resulting from unbalanced load. Both the magnitude and the phase angle unsymmetry are compensated.

Index Terms—DC-AC power conversion, power converters, unbalanced load.

I. INTRODUCTION

THIS PAPER concerns a power conditioning system (PCS) that is used in grid-independent island mode. The PCS is a power converter that is used to connect distributed energy resources, such as windmills, fuel cells, large batteries, and microturbines into an electric grid. Typically, the PCS is operated in grid-connected mode to supply power into the utility grid. Grid-independent operation mode is needed if the network is permanently isolated from the utility or if some part of the utility network is operated as an island because of interruption or degraded power quality in the power distribution. Also, the variable-speed constant-frequency power converters used in aerospace industry [1] or naval power generation systems operate as island networks.

Operation modes may be realized by having different operation mode specific control systems and a controllable switch that is used to disconnect the island network and the utility network. The change from grid-connected to grid-independent and resynchronization from grid-independent to grid-connected mode may be realized without significant delays and thus the system may appear similar to a large uninterruptible power supply (UPS). The basic circuit of an insulated gate bipolar

Paper IPCSD-04-045, presented at the 2003 IEEE International Electric Machines and Drives Conference, Madison, WI, June 1–4, and approved for publication in the IEEE TRANSACTIONS ON INDUSTRY APPLICATIONS by the Industrial Drives Committee of the IEEE Industry Applications Society. Manuscript submitted for review June 1, 2003 and released for publication June 15, 2004.

A. Tarkiainen, R. Pöllänen, M. Niemelä, and J. Pyrhönen are with the Department of Electrical Engineering, Lappeenranta University of Technology FIN-53851 Lappeenranta, Finland (e-mail: Antti.Tarkiainen@lut.fi; Riku.Pollanen@lut.fi; Markku.Niemela@lut.fi; Juha.Pyrhonen@lut.fi).

M. Vertanen is with ABB Oy, FIN-00381 Helsinki, Finland (e-mail: Mikko.Vertanen@fi.abb.com).

Digital Object Identifier 10.1109/TIA.2004.834059

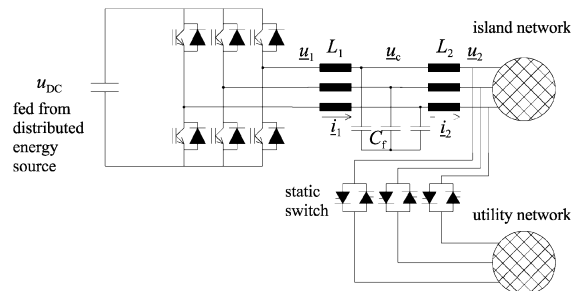


Fig. 1. A power conditioning system with an LCL filter. The inductor L_2 may be replaced with a transformer.

transistor (IGBT) voltage-source-converter-based PCS is shown in Fig. 1. An LCL filter is used to attenuate the high-frequency IGBT switching ripple.

The output impedance of the PCS is rather high because in high-power converters the switching frequency cannot be very high; it typically varies between 2–6 kHz and, therefore, the line filter reactors have to be quite large. In grid-independent mode the nonlinear or unbalanced load can easily distort the output voltage and result in unsatisfactory power quality in the island network. One approach to cope with this is to focus on reducing the output impedance of the converter [2]. Another approach is to control the converter so that it actively compensates the voltage distortions.

This paper proposes a feedback control for compensating voltage unsymmetry in the grid-independent mode. Because of the space-vector approach, the method is intended for three-wire systems. If a four-wire system is needed a delta/wye transformer can be used in place of the inductor L_2 . Single-phase loads are connected to the neutral of the transformer secondary. The proposed method is based on steady-state unsymmetry and control of the converter negative-sequence voltage directly on basis of the detected negative-sequence island voltage. This limits the dynamic performance of the method and typically couple of seconds are needed to carry out the compensation.

Previously methods and systems to compensate voltage nonidealities in the grid-connected mode have been studied in [3], [4]. Control systems for active filters directly compensating voltage harmonics have also been presented in [5]–[8]. Such “bus conditioning mode” of an active filter could be applied

in a PCS operating in grid-connected mode. An interesting space-vector and repetitive-control-based control method to compensate both the voltage unsymmetry and the harmonics in the UPS grid-independent operation has been recently reported in [9]. Methods developed for selective voltage harmonic compensation in UPS grid-independent mode could also be used in compensating the unsymmetry. Typically these methods concentrate on specific harmonic voltage sequences, and because the unsymmetry is caused by a fundamental frequency negative sequence, it could be included in the compensation. Selective harmonic voltage compensating methods for uninterruptible power supply (UPS) systems have been proposed, e.g., in [10]–[13].

II. SCALAR CONTROL WITH DIRECT TORQUE CONTROL (DTC) MODULATION

The grid-connected mode control system is based on the DTC method, which was originally developed for induction motor control [14], [15]. Later, the same principle was successfully applied to control line converters [16] and synchronous machines [17], [18]. The DTC control method is based on the hysteresis control of the motor torque and the flux linkage amplitude. In applications, such as a line converter, which do not include a motor, the torque is understood as a quantity proportional to the active power and the flux linkage as time integral of the converter voltage. Other control systems using the concept of the flux linkage have been proposed in [19]–[22]. For line converters the inventors of the DTC have introduced a principle of direct power control (DPC) [23]. Later, DPC based on virtual-flux estimation was presented in [24].

The fundamental equation of the DTC is the voltage integral

$$\underline{\psi}_1 = \int \underline{u}_1 dt \quad (1)$$

where \underline{u}_1 is a converter voltage vector and $\underline{\psi}_1$ is a quantity that is often called the converter flux linkage vector. Outside the motor control application it should be understood as an integral of the converter terminal voltage and without any relation to a physical magnetic flux. The converter voltage vector is conveniently calculated with the measured dc-link voltage and the known switching state.

In the conventional DTC control [14], [15] the motor torque is calculated with the motor stator flux linkage vector and the converter current vector

$$t_e = \frac{3}{2}(\underline{\psi}_1 \times \underline{i}_1). \quad (2)$$

In the case of an actual motor (1) is modified to take into account the voltage drop in the stator resistance. The torque and the flux linkage amplitude $|\underline{\psi}_1|$ are hysteresis compared with their respective references. The switched converter voltage vector is looked up from the optimum switching table according to the outputs of the torque and the flux linkage hysteresis comparators and the sector of the flux linkage vector. The flux plane is divided into six sectors and the sector information for the optimum switching table is, thus, a discretized location of the flux linkage vector $\underline{\psi}_1$.

In the grid-independent mode the intention is not to control the active and the reactive power of the converter but to maintain sinusoidal balanced voltages with fixed frequency and voltage level. In grid-independent mode the output voltage of the converter is controlled through the hysteresis control of converter flux linkage vector. This control method is referred to as DTC-modulation-based scalar control because previously it has been used in implementing a scalar control of an induction motor with a DTC inverter. It is briefly presented in [18].

In steady state the fundamental converter voltage \underline{u}_1 , the fundamental angular frequency ω , and the fundamental flux linkage $\underline{\psi}_1$ have a relation

$$\underline{u}_1 = j\omega\underline{\psi}_1 \quad (3)$$

and, thus, the fundamental converter voltage follows the same locus as the fundamental flux linkage but in 90° phase advance. This justifies the control of the converter voltage through the converter flux linkage. The flux linkage reference vector $\underline{\psi}_{1ref}$ is defined as

$$\underline{\psi}_{1ref} = \psi_{1ref,\alpha} + j\psi_{1ref,\beta}. \quad (4)$$

The angle of the flux linkage reference vector $\underline{\psi}_{1ref}$ is calculated in stationary $\alpha\beta$ reference frame with sine and cosine functions according to the given frequency reference. This sets the frequency in the island network. The magnitude of the fundamental flux linkage reference controls the voltage level of the island. The magnitude of the flux linkage reference vector is set by a proportional plus integral (PI) controller regulating the voltage level of the island network.

The magnitude of the converter flux linkage $|\underline{\psi}_1|$ is hysteresis controlled similarly to the conventional DTC [14], [15] and its reference is calculated from the flux linkage reference components

$$|\underline{\psi}_{1ref}| = \sqrt{\psi_{1ref,\alpha}^2 + \psi_{1ref,\beta}^2}. \quad (5)$$

The other hysteresis control loop is, however, quite different from the conventional DTC. The controlled quantity is the vector product of the converter flux linkage vector and the reference flux linkage vector

$$\delta = \underline{\psi}_1 \times \underline{\psi}_{1ref}. \quad (6)$$

This quantity represents a phase angle difference between the actual and the reference converter flux linkage vectors and hysteresis control is used to control it to zero. Individual voltage vectors are looked up from the optimum switching table according to DTC principle using the outputs of the hysteresis comparators and the sector of the flux linkage vector. Thus in the DTC scalar mode the hysteresis control loops are used to force the converter flux linkage vector to follow the reference vector. The hysteresis comparison is performed in 25- μ s control loop and the reference calculation in 100- μ s control loop. The minimum pulse width is also 25 μ s. The switching frequency is controlled using suitable tolerance bands in the hysteresis controllers.

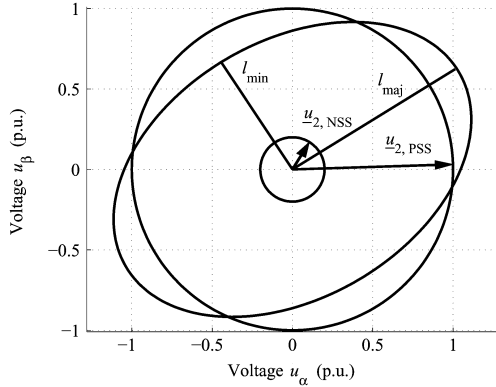


Fig. 2. Positive- and negative-sequence voltage vectors and the circular loci of the vector tips. The locus of the tip of the sum vector draws an ellipse. Major and minor half-axes of the ellipse are also shown. The magnitudes are 1 per unit for the PSS vector and 0.2 per unit for the NSS vector. Positive direction is counterclockwise.

III. UNSYMMETRICITY IN ISLAND NETWORK VOLTAGE

A. Unsymmetry and Negative-Sequence System (NSS)

The island network can be loaded with an unsymmetrical three-phase load or a single-phase load. Because of the line filter reactors the grid-independent supply created with the PCS can not be very rigid and thus the unbalanced load leads to the unbalanced voltage. Unsymmetry in the voltage is a consequence of the NSS. If the zero sequence component is absent the total fundamental voltage is a sum of the positive-sequence system (PSS) rotating in the positive direction and the NSS rotating in the negative direction. The trajectory of the sum voltage vector tip is an ellipse as shown in Fig. 2. The island network voltage vector may be represented as

$$\underline{u}_2 = u_{2,PSS} e^{j\omega t} + u_{2,NSS} e^{-j(\omega t - \phi_2)} \quad (7)$$

where ϕ_2 is an initial phase difference between the PSS and the NSS. The major axis angle of the ellipse is the angle $\alpha_{2,maj}$ where the PSS and the NSS vectors have the same angle. Thus, on the major axis we have

$$e^{j\alpha_{2,maj}} = e^{-j(\alpha_{2,maj} - \phi_2 - n2\pi)} \quad (8)$$

and

$$\alpha_{2,maj} = \phi_2/2 + n\pi. \quad (9)$$

The length of the ellipse major half-axis is the sum of the PSS and the NSS vector magnitudes

$$l_{maj} = u_{2,PSS} + u_{2,NSS}. \quad (10)$$

The angle of the ellipse minor axis is perpendicular to the major one

$$\alpha_{2,min} = \phi_2/2 - \pi/2 + n\pi \quad (11)$$

and the length of the minor half-axis is the difference

$$l_{min} = u_{2,PSS} - u_{2,NSS}. \quad (12)$$

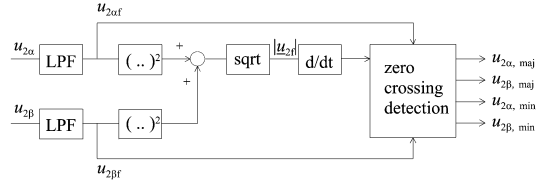


Fig. 3. Detection of voltage ellipse major and minor half-axis components.

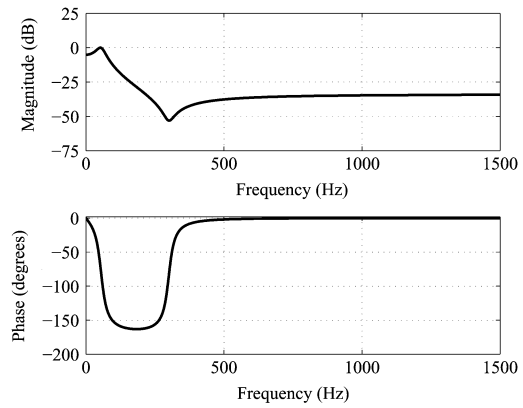


Fig. 4. Frequency response of the digital filter used in voltage ellipse detection algorithm.

The relative unsymmetry is calculated as a ratio of the magnitudes of the NSS and the PSS vectors

$$u = \frac{u_{2,NSS}}{u_{2,PSS}} = \frac{l_{maj} - l_{min}}{l_{maj} + l_{min}} \quad (13)$$

and also the PSS and the NSS magnitudes may be given in terms of the ellipse half-axes

$$u_{2,PSS} = (l_{maj} + l_{min})/2 \quad (14)$$

$$u_{2,NSS} = (l_{maj} - l_{min})/2. \quad (15)$$

Thus by measuring the length of the ellipse half-axes we may deduce the magnitudes of the PSS and the NSS and the relative unsymmetry. By detecting the angle of the ellipse axes we may deduce the phase shift ϕ_2 between the PSS and the NSS.

B. Detection of Unsymmetry

The characteristics of the voltage ellipse may be detected with a system depicted in Fig. 3. First the measured island network voltage components are low-pass filtered so that only the fundamental component remains. The phase shift of the filter does not introduce any drawbacks since it does not affect the orientation of the ellipse. In the practical implementation actually a bandpass filter was used. The frequency response of the filter used is shown in Fig. 4. The attenuation at the 0 Hz frequency is beneficial since it rejects the dc offset that might be present in the measurement and thus keeps the voltage trajectory origin centered. The filter was designed to pass the fundamental frequency and to attenuate harmonics, particularly the 5th and the

7th that are typically the largest harmonics in three-phase power systems. The filter is a two-pole two-zero filter and it was implemented as a second order direct form II realization with two memory blocks. The transfer function of the filter is

$$H(z^{-1}) = \frac{0.0202 - 0.0392z^{-1} + 0.0198z^{-2}}{1 - 1.98z^{-1} + 0.980z^{-2}}. \quad (16)$$

The exact type of the filter is not a crucial part of the algorithm and other filters may be employed.

The voltage ellipse axes are detected by calculating the length of the island network voltage vector and searching the extreme values with a basic derivative test. The discrete algorithm is as follows.

- 1) Calculate the length of the fundamental voltage vector $|\underline{u}_{2f}|_k$.
- 2) Approximate the derivative with difference $d_k = (|\underline{u}_{2f}|_k - |\underline{u}_{2f}|_{k-1})/T_s$.
- 3) Test the extremes
 - if $d_k < 0$ and $d_{k-1} > 0$ the maximum (major axis) is found
 - if $d_k > 0$ and $d_{k-1} < 0$ the minimum (minor axis) is found
- 4) If maximum or minimum was found store $u_{2\alpha f,k}$ and $u_{2\beta f,k}$ to $\underline{u}_{2,maj}$ or $\underline{u}_{2,min}$ components, respectively.

The time index of the discrete system is k and the sample time is T_s . Step 3) is actually a zero-crossing detection of the derivative signal. The extremes are classified according to the direction of the zero crossing, which is analogous with classifying the extremes of the continuous functions with a second derivative test. The ellipse detection is the only time critical part of the algorithm. In the test setup it was programmed in the 100- μ s control loop. In practical implementation the calculation of square root may be left out from the calculation of $|\underline{u}_{2f}|$ in step 1) (see Fig. 3), since square root is a monotonic function and does not affect the occurrence of the extreme values. Also, the division with the sample time T_s in step 2) may be left out. In the practical implementation step 4) was modified so that only $\underline{u}_{2,maj}$ or $\underline{u}_{2,min}$ that located in the right-half plane was saved. Thus, in a cycle only one major and minor axis is found. The most time-consuming part is the filtering of the measured voltage components. Simpler filters may well be used if it is known that no significant harmonics will exist.

The rest of the calculations may be carried out in a slower control loop and in the test setup a 1-ms control loop was used. The ellipse major and minor axes are calculated as

$$l_{maj} = \sqrt{u_{2\alpha,maj}^2 + u_{2\beta,maj}^2} \quad (17)$$

$$l_{min} = \sqrt{u_{2\alpha,min}^2 + u_{2\beta,min}^2} \quad (18)$$

and the angle of the minor axis as

$$\alpha_{2,min} = \arctan\left(\frac{u_{2\beta,min}}{u_{2\alpha,min}}\right). \quad (19)$$

The magnitude of the NSS is calculated with (15). The block diagram representation is shown in Fig. 5.

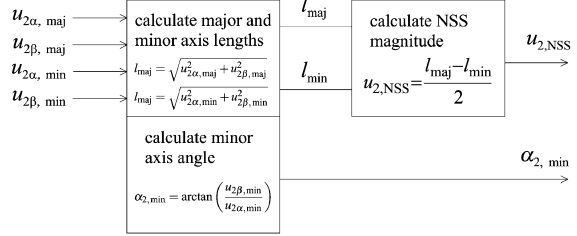


Fig. 5. Calculation of voltage NSS.

C. Compensating the Unsymmetry

The unsymmetry of the island network voltage may be remedied by adding a compensating NSS into the converter voltage \underline{u}_1 . With flux-linkage-based scalar control using DTC modulation the compensating NSS is added to the flux linkage reference. Thus, the flux linkage reference is composed of the sum of the PSS and the NSS references

$$\underline{\psi}_{1ref} = \underline{\psi}_{1ref,PSS} + \underline{\psi}_{1ref,NSS}. \quad (20)$$

$\underline{\psi}_{1ref,PSS}$ is calculated with sine and cosine functions and its magnitude is set by the island network voltage amplitude controller. $\underline{\psi}_{1ref,NSS}$ is used to cancel the NSS voltage component from the island network. The flux linkage NSS is easily constructed from the PSS component by complex conjugating and multiplying with a complex scaling coefficient \underline{k}

$$\underline{\psi}_{1ref,NSS} = \underline{k}\underline{\psi}_{1ref,PSS}^*. \quad (21)$$

Because of the complex conjugation the NSS reference vector is rotating in the opposite direction than the PSS vector. The coefficient $\underline{k} = k_\alpha + jk_\beta$ scales the magnitude of the NSS and sets the phase angle in relation to the PSS.

The unsymmetry in the island network is compensated when the converter voltage \underline{u}_1 is driven unsymmetric so that the NSS of the island network voltage \underline{u}_2 is canceled. Therefore, the major axis of the converter voltage ellipse should be aligned with the minor axis of the island network voltage ellipse. By applying (9) to the converter voltage we see that the converter voltage major axis location $\alpha_{1,maj}$ is set by the initial phase difference ϕ_1 between the converter voltage PSS and NSS

$$\phi_1 = 2\alpha_{1,maj} - n2\pi. \quad (22)$$

This angle is set by the complex scaling coefficient \underline{k} . Thus, the angle of \underline{k} is chosen to two times the minor axis angle of the island voltage ellipse $\alpha_{2,min}$. The magnitude of \underline{k} is scaled with the estimated island network NSS magnitude $u_{2,NSS}$. Thus, \underline{k} is calculated as

$$k_\alpha = u_{2,NSS} \cos(2\alpha_{2,min}) \quad (23)$$

$$k_\beta = u_{2,NSS} \sin(2\alpha_{2,min}). \quad (24)$$

In the practical realization k_α and k_β are low-pass filtered and PI regulated before the NSS of the flux linkage reference is calculated with (21); see Fig. 6. The low-pass filtering is advisable because it guarantees that short defects, e.g., in ellipse axis detection, do not severely distort the calculated NSS. Moreover,

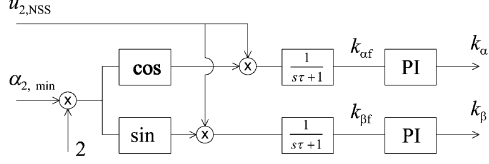


Fig. 6. Calculation of the NSS scaling parameter $\underline{k} = k_\alpha + jk_\beta$. The NSS flux linkage reference is calculated with (21) and the final flux linkage reference with (20).

$u_{2,NSS}$ and $\alpha_{2,min}$ are obtained only once in a cycle and the low-pass filtering smoothes the effects of the discrete nature of the unsymmetry detection algorithm. In the test setup the filtering time constant $\tau = 1000$ ms was used. PI controllers are used to remove steady state errors, and in Fig. 6 they control k_α and k_β so that the inputs k_{af} and k_{bf} become zeros. This means that the controllers adjust the magnitude and the phase shift of the converter flux linkage NSS so that eventually no NSS can be detected from the island network voltage. It is worth noting that the choice to generate the converter voltage major axis to align with the island voltage minor axis is only a selection to begin with. Ultimately, the closed-loop process determines how the NSS is generated in the converter voltage.

IV. MODEL OF THE CONTROL SYSTEM

The dynamical performance of the compensation method is not very high because the voltage ellipse axes are detected only once in a cycle. The NSS detection algorithm finds out the steady-state NSS of the island voltage and therefore very fast response is impossible to obtain. As the compensation is designed to a slow process the PI controllers do not have strict dynamical performance requirements. Instead, the controllers should be tuned to ensure stable operation and to minimize the steady-state error.

Let us present a model for the control system, which can be used in studying and assessing the dynamical properties of the system. The negative-sequence detection system processes the elliptical trajectory of voltage (7) to find out the vector $u_{2,NSS}e^{-j\phi_2}$. Let us denote it as

$$\mathbf{u}_{2,NSS} = u_{2,NSS}e^{-j\phi_2}. \quad (25)$$

This is a nonrotating vector representing the NSS in a cycle. The control system generates a converter voltage NSS, which is supposed to mitigate the island voltage unsymmetry. The converter voltage NSS may be expressed also as a nonrotating vector $\mathbf{u}_{1,NSS}$. Because the control system operates with the nonrotating steady state quantities the electrical dynamics may be disregarded in modeling. This is justified because the electrical dynamics are of order of magnitude faster than the dynamics of the control system. Hence, the simplified model of the electrical process may be given as

$$\mathbf{u}_{2,NSS,conv} = \mathbf{G}(j\omega)\mathbf{u}_{1,NSS} \quad (26)$$

where $\mathbf{u}_{2,NSS,conv}$ is the converter-induced NSS component of the island voltage and $\mathbf{G}(j\omega)$ represents the steady-state transfer characteristics of the electrical process. The electrical process

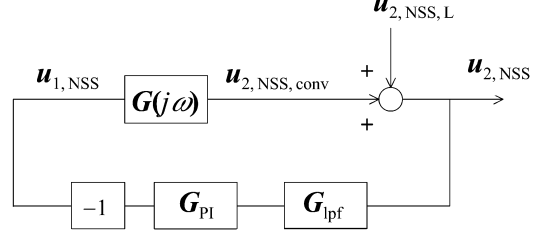


Fig. 7. Model of the control process. $\mathbf{u}_{2,NSS}$ is the island network NSS, which is composed of the converter-originating component $\mathbf{u}_{2,NSS,conv}$ and the unbalanced load-originating component $\mathbf{u}_{2,NSS,L}$. $\mathbf{G}(j\omega)$ is the model of the process transferring the converter voltage NSS $\mathbf{u}_{1,NSS}$ to the corresponding island voltage NSS.

describes how the converter NSS voltage is transferred to island NSS voltage. The steady-state transfer characteristics are modeled as a gain and a phase shift. The actual island voltage NSS $\mathbf{u}_{2,NSS}$ is composed of the converter-induced component and an unbalanced load-originating component $\mathbf{u}_{2,NSS,L}$

$$\mathbf{u}_{2,NSS} = \mathbf{u}_{2,NSS,conv} + \mathbf{u}_{2,NSS,L}. \quad (27)$$

The block diagram presentation of the control system model is depicted in Fig. 7. The low-pass filtering is modeled as

$$\mathbf{G}_{lpf} = \begin{bmatrix} 1/(s\tau + 1) & 0 \\ 0 & 1/(s\tau + 1) \end{bmatrix} \quad (28)$$

and the PI controllers as

$$\mathbf{G}_{PI} = \begin{bmatrix} k_p + k_i/s & 0 \\ 0 & k_p + k_i/s \end{bmatrix} \quad (29)$$

where s is the Laplace variable and k_p and k_i are the gain parameters of the PI controllers. The electrical process is described as

$$\mathbf{G}(j\omega) = |G|e^{j\gamma} = \begin{bmatrix} |G|\cos\gamma & -|G|\sin\gamma \\ |G|\sin\gamma & |G|\cos\gamma \end{bmatrix} \quad (30)$$

where $|G|$ is the steady-state gain of the electrical process and γ the corresponding phase shift. The closed-loop system is given as

$$\mathbf{u}_{2,NSS} = [\mathbf{I} + \mathbf{G}_{lpf}\mathbf{G}_{PI}\mathbf{G}(j\omega)]^{-1}\mathbf{u}_{2,NSS,L} \quad (31)$$

where \mathbf{I} is the unity matrix. In component form the system is written as

$$\begin{bmatrix} u_{2,NSS,\alpha} \\ u_{2,NSS,\beta} \end{bmatrix} = \left[\begin{bmatrix} 1 & 0 \\ 0 & 1 \end{bmatrix} + \begin{bmatrix} \frac{1}{(s\tau+1)} & 0 \\ 0 & \frac{1}{(s\tau+1)} \end{bmatrix} \cdot \begin{bmatrix} k_p + \frac{k_i}{s} & 0 \\ 0 & k_p + \frac{k_i}{s} \end{bmatrix} \cdot \begin{bmatrix} |G|\cos\gamma & -|G|\sin\gamma \\ |G|\sin\gamma & |G|\cos\gamma \end{bmatrix} \right]^{-1} \cdot \begin{bmatrix} u_{2,NSS,L,\alpha} \\ u_{2,NSS,L,\beta} \end{bmatrix}. \quad (32)$$

It is seen that the closed-loop dynamics are dependent on $|G|$ and γ . These quantities are dependent on the NSS impedance of the line filter and the NSS impedance of the unbalanced load. Because the unbalanced load may be unknown and varying

the closed loop dynamics are uncertain. Hence, the controllers should be tuned to ensure stable operation over wide range of $|G|$ and γ . E.g., with parameters $k_p = 1$ and $k_i = 0.5$ and time constant $\tau = 1$ the system is stable if $-\pi/2 < \gamma < \pi/2$. This may be verified by calculating the roots of the characteristic polynomial of (32). A nonzero phase shift γ causes a cross coupling between the axes of the control system, which degrades the stability of the system.

The multiplication with -1 in Fig. 7 results from the generation of converter voltage ellipse axes vice versa compared to those of the island voltage ellipse. Further, it means that the converter voltage NSS vector is generated in 180° phase shift with respect to island voltage NSS vector. If $\gamma = 0$, this leads fully decoupled control axes. If we have $\gamma \neq 0$, the resulting cross coupling may be reduced by introducing a compensator G_c . It is favorable to determine the compensator to approximate the inverse of the electrical process $G_c \approx G(j\omega)^{-1}$, which means that in order to determine the compensator the electrical process should be known or, at least, be appreciable. It may be possible to modify the control system to identify the electrical process. If the feedback control is disabled a known converter voltage NSS can be generated. The resulting change in the island voltage NSS is measured and the $G(j\omega)$ may be calculated from (26). Similar idea of steady-state transfer characteristics has been successfully used in [25] to identify the grid impedance. In the practical system, however, neither the compensator nor the identification procedure was implemented because in the intended operating environment no stability problems were encountered.

The dependence on the load impedance is a drawback of all control systems where the converter voltage NSS is produced solely on the basis of the island voltage NSS. Therefore, this kind of control system should be designed to adapt to a wide range of different load impedances.

V. EXPERIMENTAL RESULTS

The proposed unsymmetry compensation method was programmed in a digital signal processor and tested with a 19-kVA IGBT frequency converter. In the laboratory setup the distributed energy source was replaced with a line converter feeding power from the utility grid to the dc-link capacitor and regulating the dc-link voltage to 600 V. An island network with 400-V mains voltage and 50-Hz frequency was generated. The nominal values of the power conditioner were $U_n = 400$ V, $I_n = 27$ A. These nominal values and the fundamental frequency 50 Hz were used in calculating the base values of the per unit (p.u.) system. The parameters of the *LCL* filter were $L_1 = 2$ mH (0.074 p.u.), $C_f = 56$ μ F (0.15 p.u.) (Y-connection), and $L_2 = 1$ mH (0.037 p.u.). The average switching frequency was 4 kHz. A Yokogawa PZ4000 power analyzer was used as an external measurement device.

An unbalanced load condition was generated by connecting an 11-kW resistive load between phases L2 and L3. The phases L2 and L3 were in nominal 27-A load and the phase L1 was without current. The island network voltages before compensation are shown in Fig. 8. The relative unsymmetry is about 9%. The phase angle of the voltage L1–L2 was $\varphi_{L1-L2} = 249.8^\circ$ and

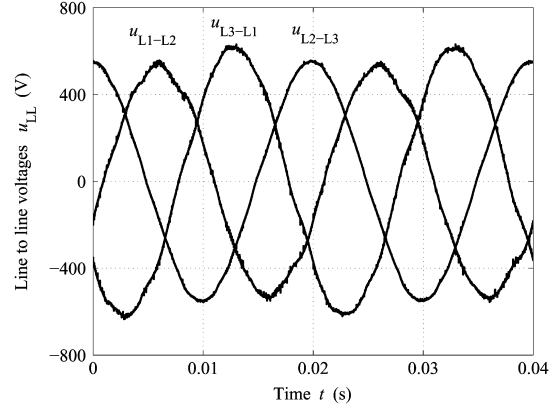


Fig. 8. Island network line-to-line voltages with unbalanced load. $U_{L1-L2} = 376.2$ V, $U_{L2-L3} = 384.4$ V, $U_{L3-L1} = 435.4$ V, $\varphi_{L1-L2} = 249.8^\circ$, $\varphi_{L1-L3} = 124.1^\circ$.

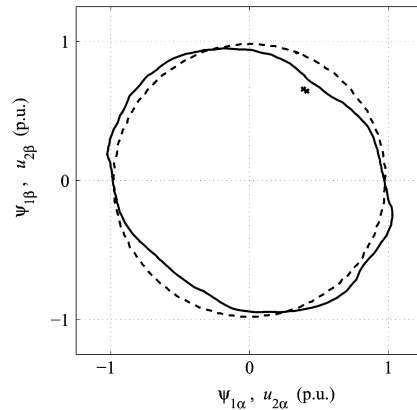


Fig. 9. Converter flux linkage vector locus (dashed line) and island network voltage vector locus (solid line). Compensation is not enabled. Crosses are marking the direction of the detected voltage ellipse minor axis. In total, 20 minor axis direction estimations have been performed. Positive direction is counterclockwise.

the phase angle of the voltage L1–L3 was $\varphi_{L1-L3} = 124.1^\circ$. Thus, the phase angles deviated 4° to 10° from the balanced case. Fig. 9 shows the trajectories of the converter flux linkage vector tip and the island network voltage vector tip. Because of the unsymmetry the island network voltage has also a negative sequence and the trajectory of the voltage vector tip is an ellipse. The crosses show the direction of the estimated minor axis. By eye it is seen that the algorithm finds the minor axis rather correctly and all 20 estimations point in the same direction.

Figs. 10 and 11 show the compensated case. Fig. 10 shows the line-to-line voltages with compensation turned on. It may be seen that practically no unsymmetry exists anymore. Also, the unsymmetry in the phase angles was corrected. Fig. 11 shows the trajectory of the converter flux linkage vector tip, which is driven ellipse to compensate the unsymmetry in the island voltage. In Fig. 11 the fundamental trajectory of the compensated voltage vector is circular. The estimated minor axis directions are spread rather equally in the right-half plane. This

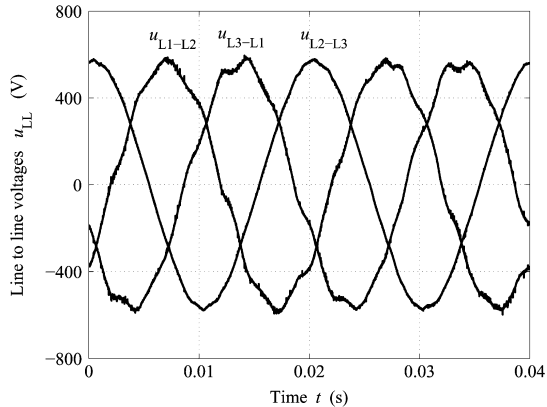


Fig. 10. Compensated island network line to line voltages with unbalanced load. $U_{L1-L2} = 399.4$ V, $U_{L2-L3} = 399.4$ V, $U_{L3-L1} = 399.5$ V, $\varphi_{L1-L2} = 240.1^\circ$, $\varphi_{L1-L3} = 120.0^\circ$. It may be seen that there are harmonics present in the voltages. Harmonics may be reduced with other control methods or by increasing damping in the *LCL* filter.

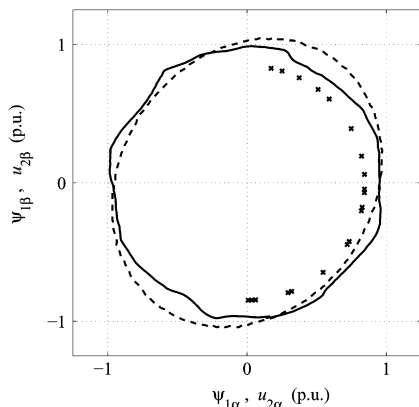


Fig. 11. Converter flux linkage vector locus (dashed line) and island network voltage vector locus (solid line). Unsymmetry compensation is enabled. Crosses showing the estimated voltage ellipse minor axis directions are spread in the right-half plane indicating that compensation have been successful. Positive direction is counterclockwise.

indicates that the compensation has been successful and the algorithm cannot determine the direction of the ellipse axes anymore. From Fig. 10 it may be seen that even though the unsymmetry has been compensated there are still harmonics left. The harmonics may be compensated by other control methods but this is not in the scope of this paper. Also, damping resistors may be included in the *LCL* filter to reduce the harmonics originating from the filter.

VI. CONCLUSION

The algorithm for compensating island network voltage unsymmetry with DTC-modulation-based scalar-controlled PCS was introduced and experimentally verified. Using a DTC-modulated PCS in supplying island networks with unbalanced loads is made possible by the method presented.

Even though the method was presented using a DTC-modulation-based converter the method may also be adapted in converters using other control principles. The method detects the negative sequence of the island voltage according to the major and the minor axes of the voltage ellipse and determines corrective negative sequence of the converter voltage in a closed control loop. The converter voltage is controlled through the converter flux linkage using hysteresis control loops and the optimum switching table. To the authors' knowledge, this kind of control system for unsymmetry compensation has not been previously proposed. Laboratory measurements show that both the magnitude and the phase angle unsymmetries are well compensated.

REFERENCES

- [1] M. E. Elbuluk and M. D. Kankam, "Potential starter/generator technologies for future aerospace applications," *IEEE Aerosp. Electron. Syst. Mag.*, vol. 12, pp. 24–31, May 1997.
- [2] M. A. Boost and P. D. Ziogas, "Toward zero-output impedance UPS system," *IEEE Trans. Ind. Appl.*, vol. 25, pp. 408–418, May/June 1989.
- [3] K. Kanazawa *et al.*, "Development of multi-functional power conversion system," in *Proc. IEEE PESC'01*, vol. 1, 2001, pp. 193–198.
- [4] D. Casadei, G. Grandi, and C. Rossi, "Effects of supply voltage nonidealities on the behavior of an active power conditioner for cogeneration systems," in *Proc. IEEE PESC'00*, vol. 3, 2000, pp. 1312–1317.
- [5] P. Brogan and R. Yacamini, "An active filter based on voltage feedback," in *Conf. Pub. 456, 7th Int. IEE Conf. Power Electronics and Variable Speed Drives*, 1998, pp. 1–4.
- [6] —, "Measurements and simulation of an active filter based on voltage feedback," in *Proc. 8th Int. Conf. Harmonics and Quality of Power*, vol. 2, 1998, pp. 1113–1118.
- [7] —, "Stability of an active filter based on voltage feedback," in *Proc. 8th Eur. Conf. Power Electronics and Applications*, 1999 [CD ROM].
- [8] —, "Stability of selective harmonic active filters," in *Conf. Pub. 475, 8th Int. IEE Conf. on Power Electronics and Variable Speed Drives*, 2000, pp. 416–421.
- [9] U. Borup, P. N. Enjeti, and F. Blaabjerg, "A new space-vector-based control method for UPS systems powering nonlinear and unbalanced loads," *IEEE Trans. Ind. Appl.*, vol. 37, pp. 1864–1870, Nov./Dec. 2001.
- [10] A. von Jouanne, P. N. Enjeti, and D. J. Lucas, "DSP control of high-power UPS systems feeding nonlinear loads," *IEEE Trans. Ind. Electron.*, vol. 43, pp. 121–125, Feb. 1996.
- [11] Y. Byun, K. Joe, S. Park, and C. Kim, "DSP control of three-phase voltage source UPS inverter with software controlled harmonic conditioners," in *Conf. Rec. Telecommunications Energy Conf.*, 1997, pp. 195–200.
- [12] S. Ponnaluri, A. Brickwedde, and R. W. De Doncker, "Overriding individual harmonic current control with fast dynamics for UPS with nonlinear loads," in *Proc. IEEE PEDS'01*, vol. 2, 2001, pp. 527–532.
- [13] P. Mattavelli, "Synchronous-frame harmonic control for high-performance AC power supplies," *IEEE Trans. Ind. Appl.*, vol. 37, pp. 864–872, May/June 2001.
- [14] I. Takahashi and T. Noguchi, "A new quick-response and high-efficiency control strategy of an induction motor," *IEEE Trans. Ind. Appl.*, vol. 1A-22, pp. 820–827, Sept./Oct. 1986.
- [15] P. Tiitinen, P. Pohjalainen, and J. Lalu, "The next generation motor control method: Direct torque control (DTC)," *EPE J.*, pp. 14–18, Mar. 1995.
- [16] V. Manninen, "Application of direct torque control modulation technology to a line converter," in *Proc. 6th Eur. Conf. Power Electronics and Applications*, vol. 1, 1995, pp. 1292–1296.
- [17] J. Pyrhönen, O. Pyrhönen, M. Niemelä, J. Luukko, J. Kaukonen, and P. Pohjalainen, "Direct torque control of synchronous motor drives for dynamically demanding applications," *Eur. Trans. Elect. Power*, vol. 10, pp. 297–304, Sept./Oct. 2000.
- [18] M. Niemelä, "Position Sensorless Electrically Excited Synchronous Motor Drive for Industrial Use Based on Direct Flux Linkage and Torque Control," Doctoral dissertation, Dept. Elect. Eng., Lappeenranta Univ. of Technology, Lappeenranta, Finland, 1999.

- [19] M. Weinhold, "A new control scheme for optimal operation of a three-phase voltage DC link PWM converter," in *Proc. PCIM'91*, 1991, pp. 371–383.
- [20] X. Xu and D. W. Novotny, "Implementation of direct stator flux orientation on a versatile DSP based system," *IEEE Trans. Ind. Applicat.*, vol. 27, pp. 694–700, July/Aug. 1991.
- [21] S. Bhattacharya, A. Veltman, D. M. Divan, and R. D. Lorenz, "Flux-based active filter controller," *IEEE Trans. Ind. Applicat.*, vol. 32, pp. 491–500, May/June 1996.
- [22] M. P. Kazmierkowski, M. Malinowski, D. L. Sobczuk, F. Blaabjerg, and J. K. Pedersen, "Simplified stator flux oriented control," in *Proc. IEEE Int. Symp. Industrial Electronics*, vol. 2, 1999, pp. 474–479.
- [23] T. Noguchi, H. Tomiki, S. Kondo, and I. Takahashi, "Direct power control of PWM converter without power-source voltage sensors," *IEEE Trans. Ind. Applicat.*, vol. 34, pp. 473–479, May/June 1998.
- [24] M. Malinowski, M. P. Kazmierkowski, S. Hansen, F. Blaabjerg, and G. D. Marques, "Virtual-flux-based direct power control of three-phase PWM rectifiers," *IEEE Trans. Ind. Applicat.*, vol. 37, pp. 1019–1027, July/Aug. 2001.
- [25] A. Tarkiaimen, R. Pöllänen, M. Niemelä, and J. Pyrhönen, "Identification of grid impedance for purposes of voltage feedback active filtering," *IEEE Power Electron. Lett.*, vol. 2, pp. 6–10, Mar. 2004.



Antti Tarkiaimen (S'04) received the M.Sc. degree in electrical engineering in 2000 from Lappeenranta University of Technology (LUT), Lappeenranta, Finland, where he is currently working toward the D.Sc. degree.

He is also currently a Researcher in the Department of Electrical Engineering at LUT. His research interests are in the area of electric drives control, in particular, line converters and active filter applications.



Riku Pöllänen (S'01–M'04) received the M.Sc. and D.Sc. degrees in electrical engineering from Lappeenranta University of Technology (LUT), Lappeenranta, Finland, in 1999 and 2003, respectively.

He is currently a Senior Researcher in the Department of Electrical Engineering at LUT. He is engaged in teaching control engineering and his research interests include the control of electric drives, in particular, PWM rectifiers and active magnetic bearings.



Markku Niemelä received the B.Sc. degree in electrical engineering from Helsinki Institute of Technology, Helsinki, Finland, in 1990, and the M.Sc. and D.Sc. degrees from Lappeenranta University of Technology (LUT), Lappeenranta, Finland, in 1995 and 1999, respectively.

He is currently a Senior Researcher in the Carelian Drives and Motor Centre, LUT, which, in cooperation with the Finnish ABB Company, develops new electric motors and drives. His current interests include control of line converters, sensorless control, and design of synchronous machines.



Juha Pyrhönen received the M.Sc. degree in electrical engineering, the Licentiate of Science (Technology) degree, and the Ph.D. degree (Technology) from Lappeenranta University of Technology (LUT), Lappeenranta, Finland, in 1982, 1989, and 1991, respectively.

He became an Associate Professor of Electric Engineering at LUT in 1993 and a Professor of Electrical Machines and Drives in 1997. He is currently Head of the Department of Electrical Engineering.

He is engaged in electric motor and electric drive research and development. He is also the leader of the Carelian Drives and Motor Centre which in cooperation with Finnish ABB Company develops new electric motors and drives. Synchronous motors and drives, switched reluctance motors and drives, induction motors and drives, solid-rotor high-speed induction machines and drives, as well as active network bridge control, are included in his current interests. He is leading the research work of several postgraduate research groups working in these target areas.



Mikko Vertanen received the M.Sc. degree in electrical engineering from Tampere University of Technology, Tampere, Finland, in 1995.

He is currently a Senior Design Engineer in the Technology Department of ABB Oy, Helsinki, Finland. His areas of interest are modeling and control of electric drives.

Publication III

A. TARKIAINEN, R. PÖLLÄNEN, M. NIEMELÄ, AND J. PYRHÖNEN

DC-link Voltage Effects on Properties of a Shunt Active Filter

*in Proceedings of IEEE 35th Annual Power Electronics Specialists Conference, Aachen
Germany, 20–25 June, 2004, pp. 3169–3175.*

Copyright © 2004 IEEE. Reprinted with permission.

DC-Link Voltage Effects on Properties of a Shunt Active Filter

Antti Tarkkiainen, Riku Pöllänen, Markku Niemelä, and Juha Pyrhönen
Lappeenranta University of Technology, Department of Electrical Engineering
P.O. Box 20, FIN-53851, Lappeenranta, Finland
Antti.Tarkkiainen@lut.fi

Abstract—The effect of the dc-link voltage on the compensation characteristics of a shunt active filter is studied focusing on 5th negative and 7th positive harmonic sequences. It is shown that the type of the harmonic load has a great impact on the required dc-link voltage. According to theoretical derivation there exist harmonic current sequence pairs yielding the minimum dc-link voltage requirement. Analytical equations concerning the 5th negative and the 7th positive harmonic sequences are proposed. Theoretical results are confirmed with measurements using a 19 kVA active front-end converter with active filtering capabilities.

I. INTRODUCTION

Active filters (AFs) are used in reducing the harmonic pollution of electric grids. Shunt AFs are typically installed in parallel to harmonic-producing loads to inject compensating harmonic currents into the point of common coupling (PCC). With voltage source inverter (VSI) topology the harmonic current production capability is dependent on the voltage level of the intermediate dc-link. If active filtering capabilities are incorporated into an active front-end of four-quadrant variable speed drive (VSD), as in [1] and [2], the dc-link voltage can not be selected with such a freedom as in the dedicated active filters. Typically, the dc-link voltage of a four-quadrant VSD is kept close to its minimum value, which is the peak-value of the grid line-to-line voltage. If the line converter is desired to double as an AF, the dc-link voltage has to be risen in order to provide voltage reserve for harmonic current injection. With this perspective, it is interesting to know what kind of active filtering performance could be expected with a certain dc-link voltage level. And further, does the type of the compensated harmonic-producing load affect the dc-link voltage requirement? Previously, a study on the AF compensation characteristics under different nonlinear loads has been carried out in [3], and the subject is also discussed in [4] and [5], but the dc-link voltage have not been taken into consideration.

In this paper this subject is theoretically approached by considering the compensation of harmonic distortion with only two harmonic sequences – the negative 5th (5⁻) and the positive 7th (7⁺). The reason for the limitation is twofold. Firstly, in the combined VSD and AF the mitigation of the largest typical harmonics are of most importance. Secondly, limiting the consideration to only two harmonic sequences the analytical manipulations are more manageable. The paper studies how the AF dc-link voltage requirement depends on the type of the nonlinear load. It is shown, that certain pairs of the 5th and the 7th current harmonics yields the minimum dc-link voltage requirement. Experimental measurements validating the theoretical results are carried out with an industrial VSD line converter with active filtering capabilities.

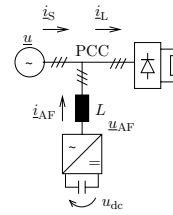


Fig. 1. A shunt active filter and a nonlinear load. The active filter is connected to a grid through an L-filter.

II. ACTIVE FILTER AC VOLTAGE

Let us consider a shunt AF system shown in Fig. 1, and define the grid voltage vector rotating with angular frequency ω as

$$\underline{u} = u^{1+} e^{j\omega t}, \quad (1)$$

containing only the positive sequence fundamental component with amplitude of u^{1+} . Let us further assume that the current space-vector of the nonlinear load \underline{i}_L is composed of the fundamental positive sequence \underline{i}^{1+} and the 5th negative and 7th positive harmonic sequences \underline{i}^{5-} and \underline{i}^{7+} as

$$\begin{aligned} \underline{i}_L &= \underline{i}^{1+} + \underline{i}^{5-} + \underline{i}^{7+} \\ &= i^{1+} e^{j(\omega t - \varphi)} + i^{5-} e^{-j(5\omega t - \rho_5)} \\ &\quad + i^{7+} e^{j(7\omega t - \rho_7)}. \end{aligned} \quad (2)$$

The angle φ determines the fundamental wave power factor. The angles ρ_5 and ρ_7 determine the initial phase angles of the fundamental grid voltage and the harmonic current sequence space-vectors in respect to the α -axis of the stationary coordinates. According to the so called p - q -theory, which is introduced in [6] and used, e.g., in [7], the instantaneous active power p and the instantaneous reactive power q may be calculated as

$$p = \frac{3}{2} (u_\alpha i_\alpha + u_\beta i_\beta) \quad (3)$$

$$q = \frac{3}{2} (u_\beta i_\alpha - u_\alpha i_\beta), \quad (4)$$

where α and β are denoting components of a space-vector in the stationary $\alpha\beta$ -reference frame. Applying (3) and (4) to (1) and (2) the instantaneous power components of the nonlinear load are given as

$$\begin{aligned} p &= \frac{3}{2} u^{1+} i^{1+} \cos(\varphi) + \frac{3}{2} u^{1+} i^{5-} \cos(6\omega t - \rho_5) \\ &\quad + \frac{3}{2} u^{1+} i^{7+} \cos(6\omega t - \rho_7) \end{aligned} \quad (5)$$

TABLE I
CONSIDERED NONLINEAR LOAD CURRENTS

| | Case 1 | Case 2 |
|-------------------|---------------------|----------------------|
| i^{1+}, φ | 1 p.u., 0 rad | 1 p.u., 0 rad |
| i^{5-}, ρ_5 | 1/5 p.u., π rad | 1/5 p.u., π rad |
| i^{7+}, ρ_7 | 1/7 p.u., π rad | 1/7 p.u., 2π rad |
| ρ | 0 rad | π rad |

$$q = \frac{3}{2}u^{1+}i^{1+} \sin(\varphi) + \frac{3}{2}u^{1+}i^{5-} \sin(6\omega t - \rho_5) - \frac{3}{2}u^{1+}i^{7+} \sin(6\omega t - \rho_7) . \quad (6)$$

Power components associated with the fundamental wave quantities are constant if the amplitudes u^{1+} and i^{1+} are constants. The power components associated with the harmonic currents are oscillating with the angular frequency of 6ω . Depending on the harmonic current space-vectors the amplitude of the oscillation may be different in the p and the q components. Particularly, if $\rho_7 - \rho_5 = 0$ the active power components of 5- and 7+ harmonic sequences are in-phase and summing up, and the reactive power components are in opposite phase and canceling each other. In the case $\rho_7 - \rho_5 = \pm\pi$ the opposite occurs. Let us define the phase angle difference $\rho_7 - \rho_5$ as

$$\rho = \rho_7 - \rho_5 . \quad (7)$$

We consider two cases with slightly different nonlinear load currents, which are shown in Tab. I. The only difference between the cases is that in the first case $\rho = 0$ and in the second case $\rho = \pi$. These cases are depicted in Fig. 2. The vectors shown in the figures are drawn at the time instant $t = 400 \mu\text{s}$. The synchronous dq-frame is fixed to the line voltage. Initially, at $t = 0 \mu\text{s}$ the d- and the α -axes and the q- and the β -axes are aligning.

Let us consider the AF in Fig. 1 compensating the nonlinear load taking the current (2) from the grid. The AF must inject harmonic currents to the PCC that are equal to the harmonics of the nonlinear load current, $\underline{i}_{\text{AF}} = \underline{i}^{5-} + \underline{i}^{7+}$. Therefore, the AF has to produce voltage

$$\begin{aligned} \underline{u}_{\text{AF}} &= \underline{u} + L \frac{d\underline{i}_{\text{AF}}}{dt} \\ &= u^{1+} e^{j\omega t} - j5\omega L i^{5-} e^{-j(5\omega t - \rho_5)} \\ &\quad + j7\omega L i^{7+} e^{j(7\omega t - \rho_7)} \\ &= u^{1+} e^{j\omega t} + 5\omega L i^{5-} e^{-j(5\omega t + \pi/2 - \rho_5)} \\ &\quad + 7\omega L i^{7+} e^{j(7\omega t + \pi/2 - \rho_7)} \\ &= \underline{u}^{1+} + \underline{u}^{5-} + \underline{u}^{7+} . \end{aligned} \quad (8)$$

In a voltage source converter any voltage vector within the voltage hexagon may be synthesized using a suitable modulation algorithm. The overmodulation range is not favored because of increased harmonic production, and the operation is usually limited to the linear modulation range. Especially, if an LCL-type line filter is used the excess voltage harmonics can not be tolerated because of the filter resonances. In the linear modulation range the maximum modulus of the AF voltage space-vector that can be synthesized is

$$|\underline{u}_{\text{AF, max}}| = u_{\text{AF, max}} = \frac{u_{\text{dc}}}{\sqrt{3}} . \quad (9)$$

By finding the maximum of (8) we may calculate from (9) how high dc-link voltage is needed to compensate the given i^{5-} , i^{7+} harmonic pair while still remaining in the linear modulation range. Hence, finding the minimum required dc-link voltage is turned to finding the maximum AF voltage vector that is needed to be synthesized.

Fig. 3 illustrates the cases where an AF with $L = 0.1$ p.u. is compensating the harmonic currents shown in Tab. I and Fig. 2. The trajectories of the compensating AF voltage vector are shown in the $\alpha\beta$ - and the dq-frame. Figs. 3(b) and 3(f) show how the AF voltage vector is constructed in the synchronous reference frame from the fundamental and the harmonic components. In the cases shown the voltage vector trajectories in the synchronous frame are degenerated to line segments. Generally, the trajectory is an ellipse. The orientation of the ellipse is determined by the angle difference ρ and the lengths of the axes by the amplitudes of the harmonics. Figs. 3(c) and 3(g) depict the trajectories of the compensating AF voltage vector. The linear modulation range is shown as a circle touching the sides of the voltage hexagon. Figs. 3(d) and 3(h) show the active filter voltage in time domain.

The maximum AF voltages in the considered cases are easily calculated. In the case 1 we have from the Fig.3(b)

$$\begin{aligned} u_{\text{AF, max}} &= u^{1+} + u^{5-} + u^{7+} \\ &= 1 + 5\omega L i^{5-} + 7\omega L i^{7+} \\ &= 1 + 0.1 + 0.1 = 1.200 \text{ p.u.} , \end{aligned} \quad (10)$$

from which the minimum required dc-link voltage for the linear modulation range yields

$$u_{\text{dc, min}} = \sqrt{3} \cdot 1.200 \approx 2.078 \text{ p.u.} . \quad (11)$$

In the case of Fig. 3(f) we have

$$\begin{aligned} u_{\text{AF, max}} &= \sqrt{(u^{1+})^2 + (u^{5-} + u^{7+})^2} \\ &\approx 1.020 \text{ p.u.} \end{aligned} \quad (12)$$

and

$$u_{\text{dc, min}} \approx 1.766 \text{ p.u.} . \quad (13)$$

The example above means that an AF operating in a 400 V and 50 Hz network needs at least 680 V dc-link voltage to remain in the linear modulation range in the first case, but only about 580 V in the second case. Moreover, this indicates very clearly that distortions with equal harmonic magnitudes may be totally different cases when active filtering is considered.

Fig. 4 shows how the maximum required AF voltage $u_{\text{AF, max}}$ varies in the function of the injected 7th harmonic current amplitude and the phase shift ρ , when the amplitude of the injected 5th harmonic current is kept constant at $i^{5-} = 0.2$ p.u.. In other words, the 5th harmonic AF voltage is kept constant at $u^{5-} = 5\omega L i^{5-} = 0.1$ p.u. and the amplitude and the phase of the 7th harmonic AF voltage are varied. The arrow 1 in Fig. 4 corresponds to the example case shown in Figs. 3(a)–(d) and the arrow 2 corresponds to the case in Figs. 3(e)–(h). It is interesting to notice that with larger values of ρ it may happen that actually less AF voltage is needed when the amplitude of the injected 7th harmonic current is

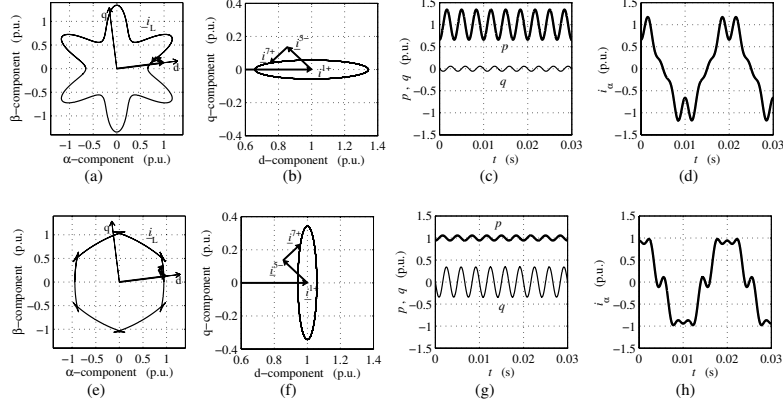


Fig. 2. (a-d): Case 1, (e-h): Case 2. (a) and (e) The locus of the current vector i_L and synchronous dq-frame. Positive direction is counter-clockwise. (b) and (f) The current vector locus in the synchronous dq-frame. (c) and (g) Instantaneous active power p and reactive power q . (d) and (h) Current in the α -axis i_{α} .

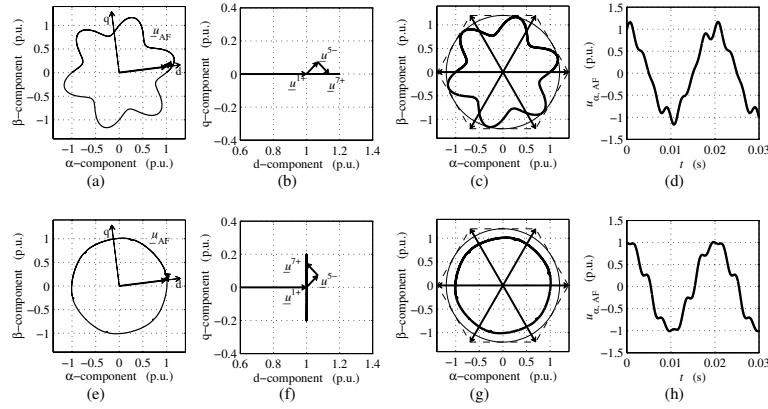


Fig. 3. Compensating AF voltage (a-d): Case 1, (e-h): Case 2. (a) and (b) Locus of the AF voltage vector \underline{u}_{AF} . (b) and (f) AF voltage vector locus in the synchronous dq-frame. (c) and (g) AF voltage hexagon spanned by the discrete voltage vectors, drawn according to $u_{dc} = 680$ V. The AF voltage vector locus (thick) and the limit of the linear modulation range (thin). (d) and (h) AF voltage $u_{\alpha, AF}$ in the time domain.

increased. The harmonic sequence phase angle difference ρ affects both the AF voltage requirement and the division of the instantaneous power oscillation to the active and the reactive power components. Accordingly, the compensation of the active power oscillation requires more dc-link voltage than compensation of similar reactive power oscillation.

III. REQUIRED DC-LINK VOLTAGE

The minimum dc-link voltage resulting in linear modulation range operation is determined by the maximum length of AF voltage space-vector that has to be synthesized. A general equation in the example case with two harmonic sequences may be given as

$$u_{AF, \max} = \max \left(\left| u^{1+} e^{j\omega t} - j5\omega L i^{5-} e^{-j(5\omega t - \rho_5)} + j7\omega L i^{7+} e^{j(7\omega t - \rho_7)} \right| \right), \quad (14)$$

from which the maximum may be searched numerically. However, we may develop this further. Let us present (8) in synchronous dq-co-ordinates, that is $\underline{u}_{AF}^s = \underline{u}_{AF} e^{-j\omega t}$, as follows

$$\underline{u}_{AF}^s = u^{1+} + u^{5-} e^{-j(6\omega t + \pi/2 - \rho_5)} + u^{7+} e^{j(6\omega t + \pi/2 - \rho_7)}. \quad (15)$$

In the synchronous dq-frame the trajectory is generally an ellipse, the center of which is at $(u^{1+}, 0)$. On the major axis the space-vectors of the harmonics are pointing in the same direction. The direction of the major axis is found by solving t_{maj} from

$$e^{-j(6\omega t_{\text{maj}} + \pi/2 - \rho_5)} = e^{j(6\omega t_{\text{maj}} + \pi/2 - \rho_7)}, \quad (16)$$

and by substituting in either one of the exponentials in (16). We obtain the angle between the major axis and the d-axis as

$$\alpha_{\text{maj}} = \frac{\rho_5 - \rho_7}{2} = -\frac{\rho}{2}, \quad (17)$$

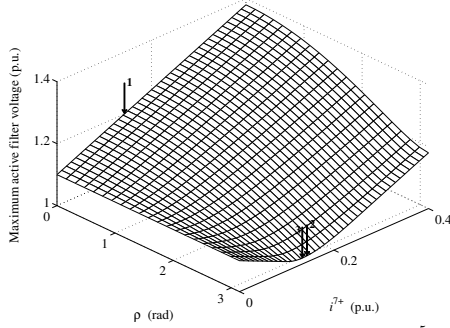


Fig. 4. Maximum required active filter voltage $u_{AF, \max}$ when i^{5-} is kept constant at 0.2 p.u. and i^{7+} and ρ are varied. Arrows 1 and 2 correspond to example cases and arrow 3 is the minimum of the surface.

and the angle between the minor axis and the d-axis is

$$\alpha_{\min} = \alpha_{\text{maj}} + \frac{\pi}{2} . \quad (18)$$

The lengths of the major semi-axis and the minor semi-axis are

$$l_{\text{maj}} = u^{5-} + u^{7+} \quad (19)$$

$$l_{\text{min}} = |u^{5-} - u^{7+}| . \quad (20)$$

With this information we may specify the properties of the trajectory ellipse according to the harmonics in question and reformulate the problem in (14) in Euclidean xy -space. The tilted ellipse centered at $(u^{1+}, 0)$ is translated to origin $(0,0)$ and rotated so that its axes are aligning with the co-ordinate axes, and therefore its equation is

$$\left(\frac{x}{a}\right)^2 + \left(\frac{y}{b}\right)^2 = 1 . \quad (21)$$

The required active filter voltage may be obtained by calculating the distance r between the origin centered ellipse (21) and a point $(u, v) = (-u^{1+} \cos(\alpha), -u^{1+} \sin(\alpha))$, where α is the rotation angle of the ellipse (i.e. either α_{maj} or α_{min}). The geometrical rotation and the translation are applied to simplify mathematical equations. The extremes of the distance between the point (u, v) and the ellipse point (x, y) may be calculated by introducing a normal vector to the ellipse, which is also a vector parallel to a gradient vector, and is calculated as

$$\mathbf{n} = \frac{x}{a^2} \mathbf{i} + \frac{y}{b^2} \mathbf{j} , \quad (22)$$

where \mathbf{i} and \mathbf{j} are unit vectors in xy -plane and a and b are ellipse semi-axes. The extreme of the distance r is encountered when a ray drawn from the point (u, v) intersects the ellipse in right angle and therefore is parallel to the ellipse normal. This condition is depicted in Fig. 5 and may be expressed mathematically as

$$x\mathbf{i} + y\mathbf{j} + k \left(\frac{x}{a^2} \mathbf{i} + \frac{y}{b^2} \mathbf{j} \right) = u\mathbf{i} + v\mathbf{j} , \quad (23)$$

from which we may solve

$$x = \frac{a^2 u}{a^2 + k} \quad (24)$$

$$y = \frac{b^2 v}{b^2 + k} . \quad (25)$$

Substitution to ellipse equation (21) yields

$$\left(\frac{au}{k+a^2}\right)^2 + \left(\frac{bv}{k+b^2}\right)^2 = 1 , \quad (26)$$

which may be presented as

$$a^2 u^2 (k+b^2)^2 + b^2 v^2 (k+a^2)^2 - (k+a^2)^2 (k+b^2)^2 = 0 . \quad (27)$$

This quartic equation may be solved for k and the corresponding (x, y) co-ordinates are obtained from (24) and (25). At most four real roots are obtained. No feasible analytical formula for solving the general case is found and numerical solutions should be employed. The distances corresponding to the extremes may be calculated as $r = \sqrt{(x-u)^2 + (y-v)^2}$ and the largest r equals $u_{AF, \max}$.

A. Special case $u^{1+} = 1$ and $\rho = 0$ or $\rho = \pi$

Let us consider a special case $(u, v) = (-1, 0)$, which covers the cases shown in Fig. 3. We found $k_1 = -a^2 - a$, $k_2 = -a^2 + a$ and $k_{3,4} = -b^2$ as solutions for (27). By substituting to (24) we find the x-co-ordinates of the ellipse points corresponding to the extremes as

$$x_1 = a \quad (28)$$

$$x_2 = -a \quad (29)$$

$$x_{3,4} = \frac{-a^2}{a^2 - b^2} , \quad (30)$$

Further, substitution to (21) yields the y-co-ordinates as

$$y_{1,2} = 0 \quad (31)$$

$$y_{3,4} = \pm \frac{b\sqrt{-a^2 - 2a^2b^2 + b^4 + a^4}}{a^2 - b^2} . \quad (32)$$

The distances r corresponding to the extreme points are then

$$r_1 = 1 + a \quad (33)$$

$$r_2 = 1 - a \quad (34)$$

$$r_{3,4} = \sqrt{\frac{(a^2 - 1 - b^2)b^2}{a^2 - b^2}} . \quad (35)$$

r_1 and r_2 are the obvious maximum and minimum, respectively, in the x-axis. Solutions $r_{3,4}$ are both maxima, and they exist when

$$-a^2 - 2a^2b^2 + b^4 + a^4 > 0 \text{ and } a \neq b . \quad (36)$$

From (36) we may solve the appropriate existence condition as

$$b > \sqrt{a^2 + a} . \quad (37)$$

Moreover, it may be calculated that whenever the maxima $r_{3,4}$ exist they are also global maxima and determine $u_{AF, \max}$. The ellipse point corresponding to the maximum $r_{3,4}$ with positive y-co-ordinate is depicted in Fig. 5 as the point (x, y) .

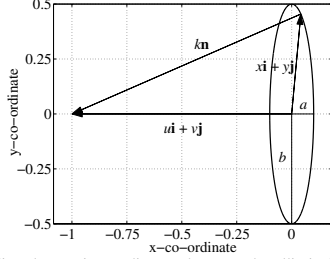


Fig. 5. Finding the maximum distance between the elliptical trajectory and point $(u, v) = (-1, 0)$. Semi-axes are $a = 0.1$, $b = 0.5$.

B. Harmonic pair requiring minimum dc-voltage

It may be asked that with a given AF voltage harmonic, let us say \underline{u}^{5-} , how the harmonic \underline{u}^{7+} should be generated in order to minimize the dc-link voltage requirement? The question is interesting from the theoretical point of view, but it is of limited practical value because the nonlinear load dictates the harmonic voltages that the active filter needs to generate. It is quite obvious that the major axis of the voltage ellipse should be perpendicular to the d-axis of the synchronous frame, i.e. $\rho = \pi$, as in Fig. 3(f). To answer the question, we should find \underline{u}^{7+} so that the greatest of maxima (33) and (35) is minimized. Also, we know that whenever the maximum corresponding to (35) exists it is the greatest maximum. Let us assume

$$u^{5-} > u^{7+} . \quad (38)$$

Then the ellipse semi-axis are

$$a = u^{5-} - u^{7+} \quad (39)$$

$$b = u^{5-} + u^{7+} . \quad (40)$$

Substituting to (35) and squaring and simplifying yields

$$r_{3,4}^2 = \frac{(4u^{5-}u^{7+} + 1)(u^{5-} + u^{7+})^2}{4u^{5-}u^{7+}} . \quad (41)$$

Differentiating (41) with respect to u^{7+} and solving for u^{7+} yields a positive solution

$$u^{7+} = \frac{-1 + \sqrt{1 + 32(u^{5-})^2}}{16u^{5-}} , \quad (42)$$

which gives the magnitude of u^{7+} for given u^{5-} that minimizes the AF dc-link voltage requirement. By substituting (39) and (40) into (37) it may be found out that the solution (42) always satisfies the condition (37) and therefore is always existing. Hence, the minimum of the maximum (35) is always the solution yielding the minimum dc-link voltage requirement.

The magnitude of u^{5-} for given u^{7+} minimizing the AF voltage requirement may be obtained by inverting the relation (42) or alternatively differentiating (41) with respect to u^{5-} and solving for u^{5-} . Either way we obtain

$$u^{5-} = \frac{-u^{7+}}{-1 + 8(u^{7+})^2} . \quad (43)$$

Expressing the amplitudes of the harmonic voltages using harmonic currents as in (8), e.g. $u^{5-} = 5L\omega i^{5-}$, we may

state (42) and (43) as

$$i^{7+} = \frac{-1 + \sqrt{1 + 800\omega^2 L^2 (i^{5-})^2}}{560\omega^2 L^2 i^{5-}} \quad (44)$$

$$i^{5-} = \frac{-7i^{7+}}{-5 + 1960\omega^2 L^2 (i^{7+})^2} . \quad (45)$$

The minimum in Fig. 4 is found by substituting $i^{5-} = 0.2$, $\omega = 1$ and $L = 0.1$ into (44) resulting $i^{7+} \approx 0.1330$ p.u.. In Fig. 4 this minimum is shown with arrow 3. Correspondingly, the AF voltage components are calculated as $u^{5-} = 0.1$ p.u. and $u^{7+} = 0.0931$ p.u. and substitution to (41) and taking a square root yields $r_{3,4} = u_{AF, \max} \approx 1.019$ p.u.. The minimum dc-link voltage is obtained as $u_{dc, \min} = \sqrt{3} \cdot 1.019 \approx 1.765$ p.u., which indeed is smaller than the value obtained in (13).

Considering the case with the assumption (38) inverted,

$$u^{7+} > u^{5-} , \quad (46)$$

we obtain solutions similar to (42) and (43) but u^{5-} and u^{7+} vice versa

$$u^{7+} = \frac{-u^{5-}}{-1 + 8(u^{5-})^2} \quad (47)$$

$$u^{5-} = \frac{-1 + \sqrt{1 + 32(u^{7+})^2}}{16u^{7+}} . \quad (48)$$

Also solutions corresponding to (44) and (45) are obtained with i^{5-} and i^{7+} transposed.

C. Worst case dimensioning

Generally, the minimum required dc-link voltage for the linear modulation range may be found by solving an equation of form (14), which includes all the compensated harmonic sequences. In the worst case the maxima of all harmonic current sequences are coinciding, and therefore the dc-link voltage requirement for the linear modulation range is

$$u_{dc, \min} = \sqrt{3} \cdot \left(u_{AF}^{1+} + \sum_{\nu} \nu \omega L i^{\nu} \right) , \quad (49)$$

where ν is denoting a harmonic sequence. The AF fundamental wave voltage u_{AF}^{1+} is typically about 1 p.u.. However, it is higher if the fundamental reactive power compensation is needed. The network fundamental reactive power may be calculated as

$$q = \frac{3}{2L\omega} (u_{AF}^{1+} u^{1+} \cos(\delta) - (u^{1+})^2) , \quad (50)$$

where δ is the power angle, i.e. the angle between the fundamental components of the AF voltage vector and the grid voltage vector. The AF fundamental voltage is solved as

$$u_{AF}^{1+} = \frac{2qL\omega}{3u^{1+} \cos(\delta)} + \frac{u^{1+}}{\cos(\delta)} . \quad (51)$$

Usually some voltage reserve is left, e.g. 5–10 %, to ensure a sufficient response to dynamical transients.

TABLE II
PROPERTIES OF TWO NONLINEAR LOADS

| | RC-load | RL-load |
|---|---------|---------|
| Fundamental wave current RMS | 21 A | 37 A |
| 5 th harmonic current RMS | 14 A | 7.8 A |
| 7 th harmonic current RMS | 9.2 A | 4.3 A |
| Harmonic sequence phase angle diff. ρ | 2 deg | 180 deg |
| Current THD without compensation [†] | 78 % | 28 % |
| AF linear range u_{dc} limit ($L=0.08$ p.u.) | 791 V | 582 V |

[†]THD calculated up to 40th harmonic

IV. EXPERIMENTAL RESULTS

A. The Measuring Setup

The AF setup used in practical measurement is similar to Fig. 1. The coupling inductor was $L = 2.17$ mH (0.08 p.u.). The nominal values of the AF used in experiments were $U_n = 400$ V, $I_n = 27$ A, $S_n = 19$ kVA and $f_n = 50$ Hz. The base values of the peak-value scaled per unit system were $U_b = 326$ V, $I_b = 38$ A, $\omega_b = 314$ rad/s. The used active filtering algorithm is a frequency selective, and it compensates harmonic current sequences i^{5-} and i^{7+} . The AF control system analyzes the supply current, and therefore the magnitude and the phase shift information of the individual harmonic current sequences are available.

The control system of the AF does not have an explicit voltage vector reference. An off-line filtering was used to find out the fundamental and the harmonic voltage waveforms the AF was producing. A non-causal zero phase shift digital filter was designed to filter out all harmonics above the 7th. This proved to be a very good way to visualize and study the harmonic components of the AF PWM voltage output. With a sample long enough, e.g. 100 cycles used in this case, the off-line filtering can be done without any significant distortion to the fundamental wave or the studied harmonics, and, in the same time, effectively removing all the unwanted frequency components. The external data acquisition and measuring device used was Yokogawa PZ4000 and the off-line filtering was performed in a PC computer.

B. Required dc-link voltage

The effect of the dc-link voltage on the operation of the AF was tested by filtering the 5- and the 7+ harmonic current sequences of the nonlinear load, and by measuring the total harmonic distortion (THD) of the supply current as a function of the dc-link voltage. Two nonlinear loads were measured, which were six-pulse diode bridges with RC- and RL-type loads in the dc-side. The properties of the nonlinear loads and the calculated dc-link voltage limits for the linear modulation range of the compensating AF are presented in Tab. II.

The result of the measurement is shown in Fig. 6. With the RL-type load THD is very stable when the dc-link voltage is lowered. Soon, after the limit of the linear modulation range is met the control system becomes unstable and the AF is tripped. The stability is lost because the current references can not be fulfilled anymore. The behavior with the RC-type load is quite different. In the measured case the limit of the linear modulation range is 791 V but the dc-link voltage can be lowered below this point without problems. After 750 V the THD starts to gradually increase, indicating that even though

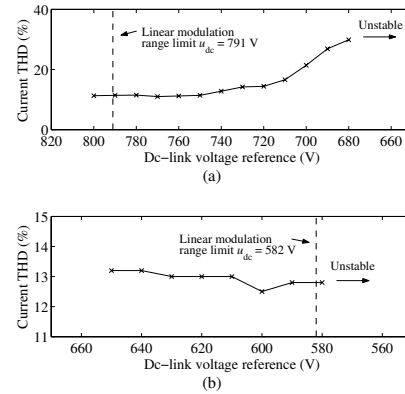


Fig. 6. Measured supply current THD as a function of AF dc-link voltage reference. AF compensates 5th and 7th harmonics. (a) RC-type load (b) RL-type load

the 5th and the 7th harmonic are compensated the AF increases the levels of higher harmonic currents. The control system becomes unstable after the dc-link voltage reference is lowered below 680 V. The reason for this behavior may be understood by looking Fig. 7, which shows the measured voltage hexagon and the trajectory of the AF voltage vector containing only fundamental wave and the 5th and the 7th harmonics. The trajectory was obtained using the off-line filtering described above. Fig. 7(a) shows a measurement with RC-type load and the dc-link voltage set to the theoretically calculated limit of the linear modulation range. The peaks of the voltage vector trajectory are on the circle denoting the linear modulation range. This confirms the theoretical calculation of the dc-link voltage level required for that condition. Fig. 7(b) shows the case where the dc-link voltage is lowered to 690 V. It is seen that the trajectory containing the harmonic sequences actually extends outside the voltage hexagon. This overmodulation phenomenon explains why the AF can compensate the harmonic distortion with a dc-link voltage that, at the first glance, may seem to be way too low.

Fig. 7(c) shows the case with the RL-type load and the AF dc-link voltage very close to the lowest value ensuring stable operation. The voltage trajectory needed to compensate the RL-type nonlinear load does not have similar far extending peaks causing the overmodulation as in the RC-case, and therefore the linear modulation range predicts quite accurately the limit of the stable operation range.

A conclusion is that with an RC-type load the AF may operate with dc-link voltages notably lower than what is needed for the linear modulation range. However, this leads to overmodulation which eventually begins to increase current distortion levels. With an LCL-type coupling filter this probably happens sooner than with the L-type filter, and in that case the linear modulation range may be a good design point.

C. Harmonic pair requiring minimum dc-link voltage

It was theoretically derived that with a given harmonic AF current i^{5-} , there exists a harmonic current i^{7+} , the amplitude of which is given by (44), which minimizes the AF dc-

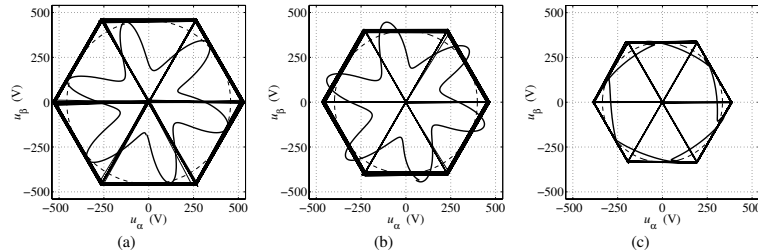


Fig. 7. Measured AF voltage hexagon and the voltage vector trajectory containing the fundamental wave and the 5th and the 7th harmonic. Limit of the linear modulation range is shown as a dashed circle. (a) RC-load, $u_{dc} = 791$ V, (b) RC-load, $u_{dc} = 690$ V, (c) RL-load, $u_{dc} = 580$ V

link voltage requirement. Measurements were performed to confirm this theoretical result. The AF control system used in experiments allows us to give a reference to individual harmonic currents. Both the magnitude and the phase shift of a given harmonic may be controlled. A series of measurements were performed with several i^{5-} , i^{7+} pairs, changing the magnitudes but keeping the phase shift difference constant at $\rho = \pi$. With each pair the maximum value of the AF voltage, including only the fundamental wave and the harmonics up to the 7th, was extracted using the off-line filtering. The result is shown in Fig. 8 as the line with crosses. Theoretical curves calculated with (14) are shown with thin solid line. The curves were measured around the presumed minimum points. The supply voltage has 2 % of the 5th harmonic voltage and 0.5 % of the 7th harmonic voltage, which have some influence on the experimental results. Therefore, theoretical curves were also calculated taking the network harmonics into account by including them into the grid voltage \underline{u} in (8). Theoretical curves including the supply harmonics effect are drawn in Fig. 8 with solid thick lines.

Overall correspondence with the experimental and the theoretical results is fairly good. The theoretical curves calculated with supply harmonics match pretty closely the shape of the measured ones, but as the magnitudes of the current harmonics increase an offset is beginning to develop, and at largest it is about 15 V. One reason for this may be the coupling filter, which was not properly designed for the large harmonic currents. On the bottom of the Fig. 8 equation (44) is graphed to indicate the theoretical location of the AF minimum voltage corresponding the case where no supply harmonics have been taken into account.

As a conclusion it is noted that the experimental results confirm the existence of the harmonic pair yielding the minimum AF voltage, and that the measured minima are pretty close to the theoretically obtained ones. However, it is anticipated that correspondence could be enhanced by having a pure sinusoidal supply voltage and a coupling filter designed for higher frequencies.

V. CONCLUSIONS

The effect of the dc-link voltage level on the operation of a voltage source shunt active filter was considered. Consideration focused on two harmonic sequences – the negative 5th and the positive 7th. It was shown that the dc-link voltage requirement of an active filter is dependent on both the

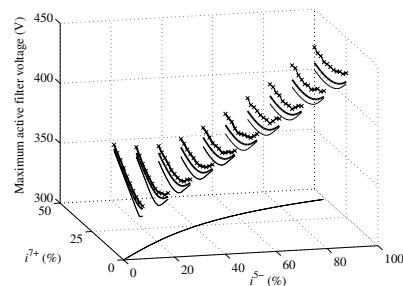


Fig. 8. Maximum AF voltage $u_{AF, \max}$ as a function of injected harmonic current amplitudes. Phase angle difference is $\rho = \pi$. Experimental (crosses), theoretical taking the supply harmonics into account (solid thick), theoretical with sinusoidal supply voltage (solid thin). Graph of (44) denoting the minima of the sinusoidal supply case is drawn on the bottom.

amplitudes and the phase angles of the harmonics. Experimental results showed that an AF with an L-type coupling filter may compensate RC-type nonlinear load with dc-link voltages considerably lower than what is required for the linear modulation range. Theoretical considerations indicated that there exist pairs of the 5th and the 7th harmonic current sequences that can be produced with the least AF dc-link voltage. Analytical equation for these pairs were proposed. Experimental results confirming the result was performed and the correspondence between theoretical and measured results was fairly good.

REFERENCES

- [1] F. Abrahamsen and A. David, "Adjustable speed drive with active filtering capability for harmonic current compensation," in *Proc. IEEE PESC'95*, vol. 2, 1995, pp. 1137–1143.
- [2] P. Brogan and R. Yacimini, "Harmonic control using an active drive," *IEE Proc.-Electr. Power Appl.*, vol. 150, pp. 14–20, Jan. 2003.
- [3] J. Liu, Y. He, H. Li, F. Zhuo, and Z. Wang, "Quantitative analysis of shunt active filter compensation characteristics under different load situations," in *Proc. IEEE ISIE'02*, vol. 4, 2002, pp. 1241–1246.
- [4] F. Z. Peng, "Application issues of active power filters," *IEEE Ind. Appl. Mag.*, vol. 4, pp. 21–30, Sept/Oct. 1998.
- [5] S. Bhattacharya, A. Veltman, D. M. Divan, and R. D. Lorenz, "Flux-based active filter controller," *IEEE Trans. Ind. Applicat.*, vol. 32, pp. 491–500, May/June 1996.
- [6] H. Akagi, Y. Kanazawa, and A. Nabae, "Instantaneous reactive power compensators comprising switching devices without energy storage components," *IEEE Trans. Ind. Applicat.*, vol. IA-20, pp. 625–630, May/June 1984.
- [7] S. Chen and G. Joós, "Direct power control of three phase active filter with minimum energy storage components," in *Proc. IEEE APEC'01*, vol. 1, 2001, pp. 570–576.

Publication IV

A. TARKIAINEN, R. PÖLLÄNEN, M. NIEMELÄ, AND J. PYRHÖNEN

Mitigating Grid Voltage Harmonics using a Line Converter with Active Filtering Feature

Electrical Engineering (in press)

Mitigating Grid Voltage Harmonics Using a Line Converter with Active Filtering Feature

Antti Tarkkiainen, Riku Pöllänen, Markku Niemelä, and Juha Pyrhönen

Lappeenranta University of Technology, Finland

Abstract A line converter equipped with an LCL-line filter is used as an active filter directly compensating grid voltage harmonics. The control of four individual grid voltage harmonics is implemented using an individual control of corresponding harmonic line currents. The knowledge of the grid impedance is essential to efficient control of the grid voltage harmonics. To overcome the problem of an unknown grid impedance an identification method is used. The method uses the converter control system to measure the grid impedance at selected frequencies. The active voltage harmonic cancellation is tested with a 19 kVA line converter by compensating background voltage distortion and distortion caused by a nonlinear load.

Key words Active filters, Voltage feedback active filtering, Power system harmonics, Harmonic distortion, Variable speed drives

1 Introduction

Harmonic pollution of electrical grids is becoming an ever increasing problem. The primary reason for this is the proliferation of power electronic nonlinear loads. Harmonic-producing loads may be classified to unidentified and identified sources of distortion [1]. A large industrial rectifier is an example of an identified harmonic-producing load. Unidentified sources of distortion are typically low power consumer electronic devices such as personal computers, television sets or cell phone battery chargers. Even though the distortion caused by a single such device is negligible, a vast number of these devices dispersed in a grid may severely distort the grid voltage.

A different approach to mitigate the harmonic distortion caused by these two types of distortion source has to be taken. An identified source of distortion, such as a large industrial rectifier, is perfectly localized and remedying actions – typically active or passive filtering – should be carried out in that site. With unidentified source no single begetter of the distortion exists and the corrective measures should be done in a power distribution level. However, it may be that, e.g., in an industrial facility there exist several perfectly identified sources of distortion but it would be economically impractical to install a filter for each one of them. Instead, it may be preferable to treat the distortion as a whole and compensate it as the source would be of unidentified type. A shunt active filter operates by

Correspondence to: Antti Tarkkiainen, Department of Electrical Engineering, Lappeenranta University of Technology, P.O. Box 20, FIN-53851 Lappeenranta, Finland. tel. +358-5-621-6719, fax +358-5-621-6799, e-mail: Antti.Tarkkiainen@lut.fi

injecting harmonic currents into the grid. To generate a reference for the injected harmonic current the active filter has to detect the unwanted harmonics that are to be mitigated. The harmonic detection may be based on load current detection, supply current detection or voltage detection [1], [2]. The detection methods based on current information are suitable for active filters installed near one or more harmonic producing loads. The voltage detection is suitable for active filters dispersively installed on distribution systems [1].

Line converters (also known as PWM rectifiers) have gained popularity in industrial applications where four-quadrant operation or low line current harmonics are needed. A typical application is an active front-end of a motor drive. Industrial line converters with active filtering capabilities have been proposed in [3] with current feedback and in [4] with voltage feedback. This paper proposes a control strategy adding a voltage feedback active filtering feature to an industrial line converter, making the active grid voltage harmonic mitigation possible. Clear distinction between the previously reported systems and the proposed one is that in the proposed system an LCL-line filter is used to filter the high frequency switching noise. This is very important especially in weak grids, where L-type line filter is practically unusable because of severe high frequency distortion to grid voltage. Because weak grids are benefiting the most from the active voltage harmonic mitigation the importance of having an LCL-filter is underscored. The underlying converter current vector control system is based on virtual converter flux linkage vector orientation and direct torque control (DTC) type hysteresis control. In greater details it is presented in [5] and in [6]. Another novelty of the proposed system is that it can measure the grid impedance and adapt to the grid impedance variations. This is an important feature if, for example, power factor compensation capacitors are used in the same grid with the active filter unit. A control strategy using a voltage feedback is particularly vulnerable to changing grid impedances, as was reported in [7] and [8].

2 Overview of the system

2.1 Control system

In the control system proposed the harmonic voltages are controlled through harmonic currents. An overview of the control system is depicted in Fig. 1. Harmonic currents are controlled with a frequency domain method based on harmonic synchronous reference frames. Four harmonic sequences are controlled, namely 5⁻, 7⁺, 11⁻ and 13⁺, where the sign is denoting the rotation direction with respect to the fundamental wave. The method of harmonic synchronous reference frames is also applied to the analysis of line voltage harmonics. References for the line current harmonics are calculated according to the detected voltage harmonics and the knowledge of grid impedance angles at harmonic frequencies. The control system can perform a measurement of the grid impedance for each harmonic frequency. The harmonic current references $i_{1d, \text{href}}$ and $i_{1q, \text{href}}$ are summed with the fundamental wave current references and passed to the current control. The power switches are controlled with hysteresis control more closely presented in [5] and [6]. The converter control system without active filtering features needs only converter current vector i_1 and dc-link voltage u_{dc} measurements. The line current vector i_2 and grid voltage vector u_2 are measured for the purposes of harmonic current control and harmonic voltage control.

2.2 Application areas

The voltage feedback active filter does not represent a customary level of technology but an emerging one. The voltage harmonic mitigation may be very advantageous from the power system point of view. As reported in [9] the minimum voltage distortion at a large customer bus in a network may also yield minimum harmonic power loss in the system. And further,

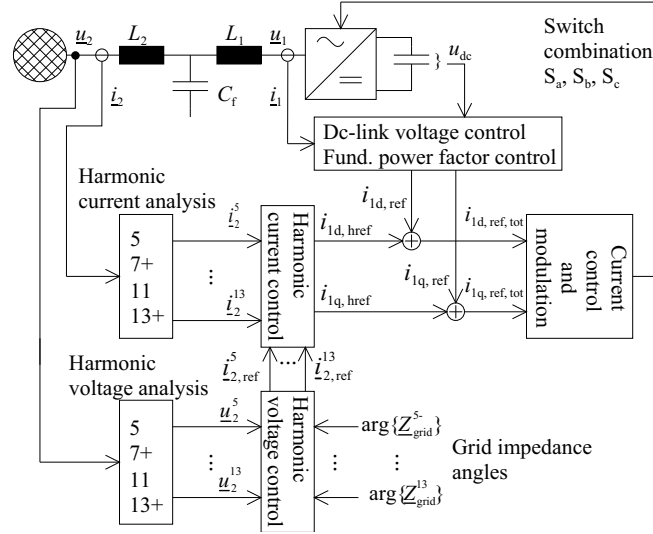


Fig. 1 Overview of the control system.

in [9] the voltage harmonic minimization is believed to be better compensation strategy than sinusoidal line current or unity power factor operation. However, a clear limitation of the voltage feedback active filter concept is that if the rating of the active filter is small compared to the short circuit power of the grid, the active filter has only a negligible effect on the grid voltage. A principle of active power line conditioning has been known for a long time [10], but today's series produced line converter hardware is bringing the system cost down making it more feasible than before. One application for the system proposed is an active filter system dedicated to harmonic compensation. The installation site could be a feeder of a power distribution system, as proposed in [2], or a facility where nonlinear loads are present. Another application area is proposed in [4] – a variable speed drive with grid voltage compensation capability. The current capacity of four-quadrant drives that is not needed in active power transfer may be utilized in harmonic voltage compensation. Another interesting application area is found in the field of the distributed power generation. In wind mills there exist line converter units that typically operate partially loaded for long periods of time. Could this spare current processing capacity be harnessed to improve the voltage quality?

3 Harmonic Current Control

3.1 Converter Current Vector Control

The converter current vector control system is based on a virtual converter flux linkage vector orientation. Only a brief presentation of the converter current control system is included here. A detailed presentation is found in [5] and [6]. The fundamental equation of the control system is the voltage integral

$$\underline{\psi}_1 = \int \underline{u}_1 dt, \quad (1)$$

where \underline{u}_1 is the converter voltage vector and $\underline{\psi}_1$ is the virtual converter flux linkage vector. A synchronous reference frame used in the current vector control is fixed to $\underline{\psi}_1$ so that the direct axis is aligned with $\underline{\psi}_1$ and the quadrature axis is perpendicular to that. Co-ordinate

transformation of the converter current vector i_1 from the stationary $\alpha\beta$ -co-ordinates to the fundamental wave synchronous dq-co-ordinates is calculated as

$$i_{1d} = \frac{\psi_{1\alpha}i_{1\alpha} + \psi_{1\beta}i_{1\beta}}{|\underline{\psi}_1|} \quad (2)$$

$$i_{1q} = \frac{\psi_{1\alpha}i_{1\beta} - \psi_{1\beta}i_{1\alpha}}{|\underline{\psi}_1|} . \quad (3)$$

The synchronous frame current components are compared with the respective references and the power switch combination is determined with DTC-type hysteresis control. However, the harmonic compensation control system is independent of this particular current vector control and other methods may be employed as well.

3.2 Harmonic current control

The control of individual harmonic current sequences is realized by using the method of harmonic synchronous reference frames. This method has been proposed, e.g., in [11] and [12]. To control four harmonic sequences four unit vectors \underline{s}^{5-} , \underline{s}^{7+} , \underline{s}^{11-} and \underline{s}^{13+} are defined. Each vector is rotated with an angular frequency and to the direction of the corresponding harmonic. For the fifth negative harmonic sequence (5-) the unit vector is calculated as

$$\underline{s}^{5-} = \cos(5\omega_s t) - j \sin(5\omega_s t) , \quad (4)$$

where ω_s is the angular frequency of the grid. In the control system ω_s is continuously estimated by calculating the angular frequency of the virtual converter flux linkage vector $\underline{\psi}_1$. The negation of the imaginary part in (4) makes the unit vector to rotate in the negative direction. The d-axis of the harmonic synchronous frame is aligned with the corresponding unit vector and the q-axis is oriented as a normal to that.

The converter line current vector i_2 is transformed to the harmonic synchronous frame. For the harmonic 5- we have the transformation as

$$i_{2d}^{5-} = \text{Re}\{(\underline{s}^{5-})^* i_2\} = s_\alpha^{5-} i_{2\alpha} + s_\beta^{5-} i_{2\beta} \quad (5)$$

$$i_{2q}^{5-} = \text{Im}\{(\underline{s}^{5-})^* i_2\} = s_\alpha^{5-} i_{2\beta} - s_\beta^{5-} i_{2\alpha} , \quad (6)$$

where the asterisk is denoting a complex conjugate. The harmonic component ν of the converter line current vector matching the frequency and the sequence of the unit vector \underline{s}^ν is appearing as a dc-signal in the synchronous frame and therefore it can be efficiently extracted by low-pass filtering. Low-pass filtered components represent the detected harmonic current space-vector in the harmonic synchronous frame. Error signals are calculated in both the d- and the q-directions with corresponding references. PI-controllers are operating on the error signals and producing references $i_{1d, \text{ref}}^{5-}$ and $i_{1q, \text{ref}}^{5-}$ for the fifth harmonic converter current vector i_1^{5-} in the harmonic synchronous frame. The harmonic synchronous frame current references are transformed to $\alpha\beta$ -frame as

$$i_{1\alpha, \text{ref}}^{5-} = \text{Re}\{\underline{s}^{5-} i_{1, \text{ref}}^{5-}\} = s_\alpha^{5-} i_{1d, \text{ref}}^{5-} - s_\beta^{5-} i_{1q, \text{ref}}^{5-} \quad (7)$$

$$i_{1\beta, \text{ref}}^{5-} = \text{Im}\{\underline{s}^{5-} i_{1, \text{ref}}^{5-}\} = s_\alpha^{5-} i_{1q, \text{ref}}^{5-} + s_\beta^{5-} i_{1d, \text{ref}}^{5-} . \quad (8)$$

In the block diagram in Fig. 2 the harmonic synchronous frame co-ordinate transformations and synchronous frame PI-controllers are shown. From the $\alpha\beta$ -frame the harmonic current

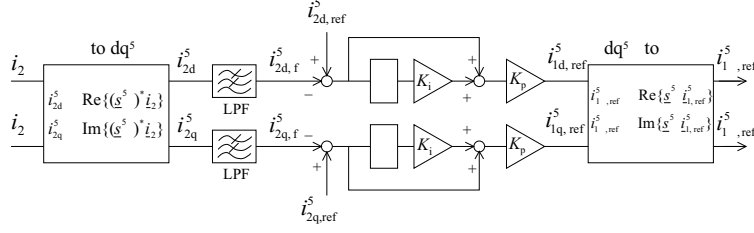


Fig. 2 Calculation of the negative sequence 5th harmonic $\alpha\beta$ -frame converter current reference. K_p and K_I are the parameters of the PI-controllers.

reference is transformed to the fundamental dq-reference frame (dq^{1+}) similar to Eqs. (2) and (3)

$$i_{1d,ref}^{5-(dq^{1+})} = \frac{\psi_{1\alpha} i_{1\alpha,ref}^{5-} + \psi_{1\beta} i_{1\beta,ref}^{5-}}{|\psi_1|} \quad (9)$$

$$i_{1q,ref}^{5-(dq^{1+})} = \frac{\psi_{1\alpha} i_{1\beta,ref}^{5-} - \psi_{1\beta} i_{1\alpha,ref}^{5-}}{|\psi_1|}, \quad (10)$$

where the superscript (dq^{1+}) is indicating that the harmonic component is expressed in other synchronous frame than its natural one. The total reference for the fundamental frame current control is calculated by summing the harmonic references and the fundamental wave references

$$i_{1d,ref,tot} = i_{1d,ref} + i_{1d,ref}^{5-(dq^{1+})} + i_{1d,ref}^{7+(dq^{1+})} + i_{1d,ref}^{11-(dq^{1+})} + i_{1d,ref}^{13+(dq^{1+})} \quad (11)$$

$$i_{1q,ref,tot} = i_{1q,ref} + i_{1q,ref}^{5-(dq^{1+})} + i_{1q,ref}^{7+(dq^{1+})} + i_{1q,ref}^{11-(dq^{1+})} + i_{1q,ref}^{13+(dq^{1+})}. \quad (12)$$

The harmonic synchronous frames are synchronized to the grid voltage with a phase locked loop. This makes it possible to control the phase angles of the harmonic currents with respect to the line voltage. Therefore, any combination of harmonic current space-vectors, within the limit of the converter's ability to produce harmonic currents, can be given as a reference and injected to the grid.

4 Compensating Grid Voltage Harmonics

4.1 Harmonic voltage control

Controllable current harmonics can be used to alter the harmonic voltages of the grid. Harmonic currents injected into the point of common coupling (PCC) flow through the grid impedance and cause a harmonic voltage drop. The voltage quality can be improved by selecting the harmonic currents so that the defects of the voltage are canceled and the voltage waveform is shaped more sinusoidal by the harmonic voltage drops. This approach can be considered as an active filtering based on voltage feedback.

The implemented control system for harmonic voltages employs the method of harmonic synchronous reference frames and has similarities with the harmonic current control system. In Fig. 3 the control system for a general grid voltage harmonic ν is depicted. The control system has a cascaded structure consisting of the inner current control loop and the outer voltage control loop. The grid impedance has an important role in a voltage feedback based active filter. The change in the grid voltage caused by an injected current harmonic i_2^ν is

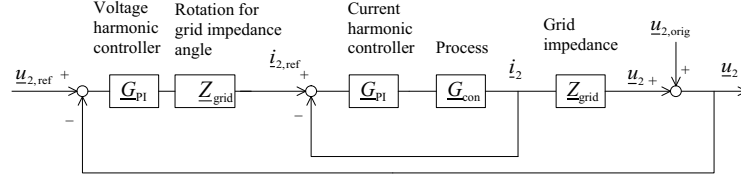


Fig. 3 Control system of a grid voltage harmonic u_2^v . $u_{2,orig}^v$ is an intrinsic voltage, which summed with the active filter caused voltage drop Δu_2^v constitutes u_2^v .

$$\Delta u_2^v = Z_{grid}^v i_2^v . \quad (13)$$

The grid impedance Z_{grid}^v causes a phase shift between the active filter harmonic current and the resulting voltage drop. This phase shift results in cross-coupling between the harmonic d- and the q-axes of the harmonic voltage control system. A strong cross-coupling impairs the stability of the control system and may lead to unstable operation. Therefore, it is suggested that the cross-coupling is decoupled by rotating the harmonic current reference to the opposite direction of the phase shift caused by the grid impedance. Typically the grid impedance is inductive and may be approximated with the feeding transformer's short circuit inductance L_{trafo} . In this case the resulting voltage drop vector Δu_2^v is leading the injected current vector i_2^v by 90 degrees. Therefore, in the control system the reference current vector should be lagged for the same angle to neutralize the effect of the grid impedance phase shift. However, it may be that other loads or, for example, a power factor correction capacitors alter the effective grid impedance seen by the active filter. A wrong presumption of an inductive grid impedance may lead to an unstable operation. A way to obtain an estimate of the grid impedance is necessary.

The main steps of the grid voltage harmonic control are summarized as follows:

1. Transform the grid voltage vector u_2 to the harmonic synchronous frame (Eqs. similar to (5) and (6)).
2. Eliminate unwanted frequency components by low-pass filtering and perform PI-control in the harmonic synchronous frame (similar to Fig. 2). Outputs of the PI-controllers are the reference components for the corresponding harmonic line current (e.g. $i_{2d,ref}^{5-}$ and $i_{2q,ref}^{5-}$ for the harmonic 5-).
3. Rotate the current reference vector to compensate the phase shift caused by the grid impedance.
4. Feed the rotated current vector reference to the harmonic current control system.

4.2 Estimation of Grid Impedance

As a solution to the unknown grid impedance we use a measurement-based method to identify the grid impedance. The method is introduced in [13]. The method uses the control system to identify the grid impedance at selected harmonic frequencies and determines the correct rotation angle to decouple the harmonic voltage control system. In Fig. 4 a simplified grid model, where L_{trafo} is denoting a transformer short circuit impedance and C_c and R_c are denoting a power factor compensator, is presented. The active filter is denoted with a current source i_2 .

The grid impedance is estimated using the control system in Fig. 3 with the outer feedback loop disconnected. Hence, only the current control loop is active and the voltage control loop is disabled. The grid impedance may be estimated by introducing a change $\Delta i_{2,ref}^v$ to the harmonic line current reference vector and by measuring the resulting change in the

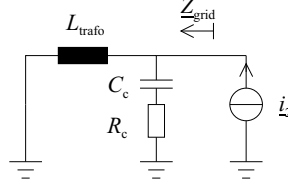


Fig. 4 A simplified model for the grid impedance.

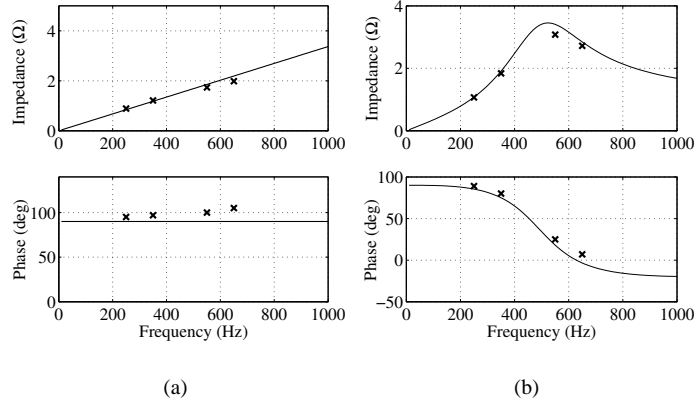


Fig. 5 Impedance of the grid, theoretical results (solid) and measured results (crosses). (a) Only a transformer with $L_{\text{trafo}} = 540 \mu\text{H}$. (b) Power factor correction capacitor with $C_c = 180 \mu\text{H}$ and $R_c \approx 1 \Omega$ added.

harmonic grid voltage Δu_2^ν . The grid impedance at this frequency is calculated by

$$Z_{\text{grid}}^\nu = \frac{\Delta u_2^\nu}{\Delta i_{2,\text{ref}}^\nu}. \quad (14)$$

Because of the integral type control the actual harmonic line current vector equals very accurately the reference vector in steady state. In Fig. 5 the results of an impedance measurement with the proposed method in two different cases are presented. In the first case, shown in Fig. 5(a), no other loads were connected to the transformer secondary. The impedance measurement was performed with 0.2 p.u. (5.4 A RMS) current magnitude change. From the transformer name plate values the short circuit inductance was calculated as $L_{\text{trafo}} = 540 \mu\text{H}$. The values measured by the converter agree quite well with the theoretical curve obtained with this simple transformer model. In the second case, shown in Fig. 5(b), a power factor correction capacitor with a series resistor was connected to the transformer secondary. The transformer short circuit inductance and the capacitor form a resonant circuit with the resonance frequency of 510 Hz. The measured points agree well with the theoretical curve calculated with $R_c = 1 \Omega$ resistance value. The result is very acceptable, the bulk resistors used were measured to have resistance values ranging from 0.8 to 1.1 Ω .

The importance of having a correct grid impedance angle in the control system is illustrated in Fig. 6. A d-axis grid voltage reference step of 5 % (or 20 V RMS) in magnitude is applied to the negative sequence 11th harmonic voltage when a power factor correction capacitor with $C_c = 180 \mu\text{H}$ and $R_c \approx 1 \Omega$ is connected at the transformer secondary. In the first case the grid impedance is erroneously assumed as inductive and in the second case the identified grid impedance angle is used in the control system. The measurement shows that in a first case a strong cross-coupling between the axes is present and the control

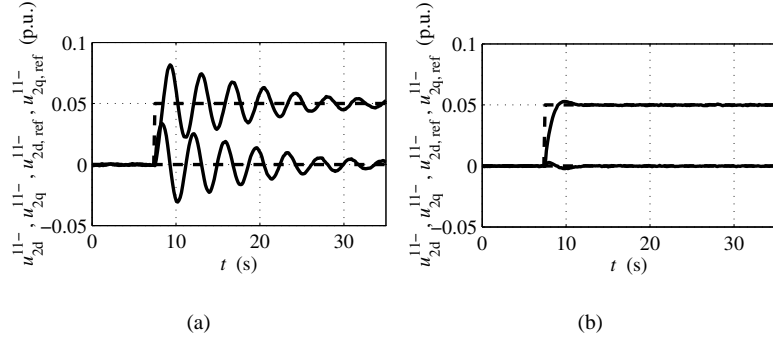


Fig. 6 Measured 5 % step in d-axis voltage reference $u_{2d,ref}^{11-}$ at $t = 7.5$ s. (a) Inductive grid impedance angle $\arg\{\underline{Z}^{11-}\} = 90^\circ$ assumed. (b) Identified impedance angle $\arg\{\underline{Z}^{11-}\} = 24^\circ$ is used to decouple the d- and the q-axes.

system is barely stable. In a second case only a slight cross-coupling and no oscillations are observed. The identification of grid impedance angle greatly enhanced the stability of the system. The identification method is based on direct measurement and therefore the voltage harmonic compensation is not dependent on knowledge of the parameters constituting the grid impedance, such as series inductance and shunt capacitance. This can be considered as a benefit in comparison to prior voltage feedback based active filter implementation such as [7] and [8]. A limitation of the off-line identification method is that it can not detect variations of the grid impedance while the active filtering operation is ongoing. Therefore, a change in the grid impedance, e.g., due to the capacitor switching, may drive the voltage harmonic control to unstable or oscillatory operating mode. To avoid the overcurrent tripping a mechanism to detect these undesired modes is needed. One approach is described in [13].

5 Active Filtering Performance

5.1 Measurement setup

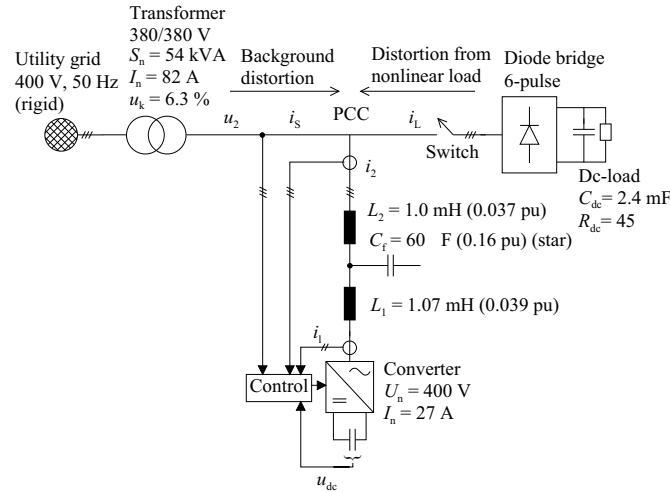
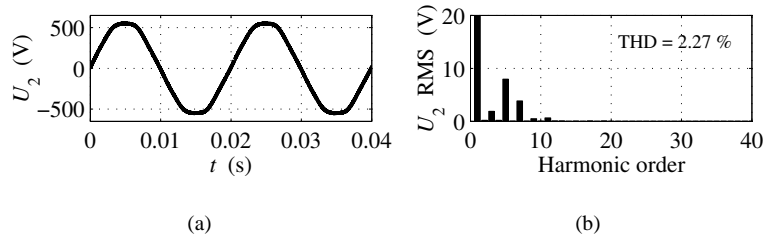
The measurement setup is depicted in Fig. 7. The nominal values of the converter and the base values of the peak-value scaled per unit (p.u.) system used are shown in Tab. 1. The control algorithms were programmed to Motorola 56002 digital signal processor in assembler language. In experiments an average switching frequency of 4 kHz was used. A nonlinear load is connected to the PCC through a switch. The voltage distortion in the PCC has two origins. A portion of it is coming from the primary side of the transformer and it is called a background distortion. The rest are originating from the local nonlinear loads connected to the transformer secondary. The voltage feedback based approach does not separate the source of the voltage distortion and both can be compensated equally. In measurements Yokogawa PZ4000 power analyzer was used as an external data acquisition device.

5.2 Background distortion

In Fig. 8 the measured line-to-line voltage in no-load situation is presented, showing the typical locally available voltage quality. The harmonic content is mainly composed of the 5th and the 7th harmonics and the total harmonic distortion (THD) calculated with the first

Table 1 Nominal values of the active filter and the base values of the per unit system.

| | Nominal value | Base value |
|----------------|---------------|------------|
| Voltage | 400 V | 326 V |
| Current | 27 A | 38 A |
| Apparent power | 19 kVA | 19 kVA |
| Frequency | 50 Hz | 50 Hz |

**Fig. 7** Measurement setup**Fig. 8** Measured line-to-line voltage with no loads connected to a transformer secondary (a) in time domain and (b) in frequency domain.

40 harmonics is about 2 %. Fig. 9(a) shows the voltage when the active filter is controlling the voltage harmonics to zero. As a result of the compensation the THD is reduced to 0.6 %, which means very high voltage quality. Fig. 9(c) shows the supply current that the active filter is feeding through the transformer in order to achieve the harmonic voltage compensation. The frequency domain representation reveals that the active filter is injecting the 5th and the 7th harmonic currents.

5.3 Distortion from nonlinear load

The steady state performance of the voltage feedback based active filter system was further tested by connecting a nonlinear load to the transformer secondary. In that case both the background distortion and the distortion from the nonlinear load are present. The nonlinear

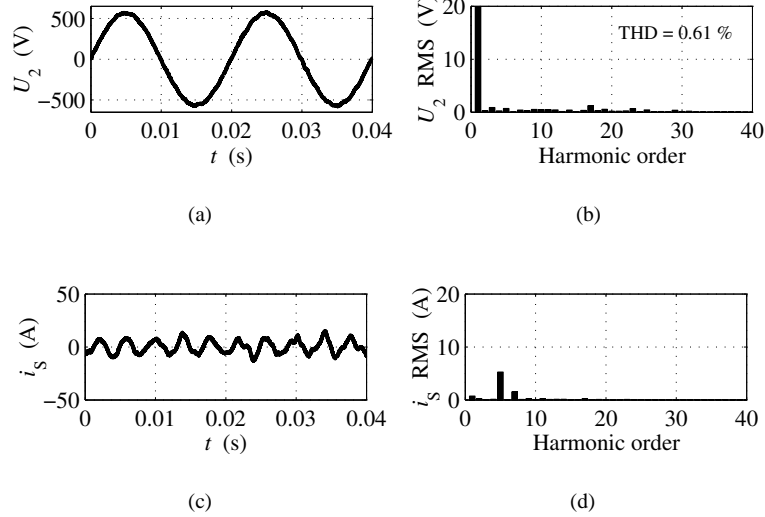


Fig. 9 Background distortion compensated by active filter. (a) and (b) Line-to-line voltage. (c) and (d) Supply current, which is equal to active filter injected current ($i_S = i_2$).

load was a six-pulse diode bridge with RC-type load in the dc-side. No ac-inductors were used. The measurement in Fig. 10(a) shows that the voltage in the PCC is severely distorted having a THD of 5.3 %. The nonlinear load current causing the voltage distortion is shown in Fig. 10(c).

The compensated case is shown in Fig. 11. Fig. 11(a) shows the line-to-line voltage, the THD of which is reduced to 1.7 %, which is better than the locally available utility voltage shown in Fig. 8. The frequency domain figure shows that the levels of the compensated harmonics (5th, 7th, 11th and 13th) are very low. To achieve a THD lower still the compensation should be extended to higher harmonics such as 17th, 19th, 23th and 25th. The nonlinear load current in Fig. 11(c) is different from the uncompensated case. This is because in the compensated case the network impedance appearing to the nonlinear load at the compensated frequencies is very low, theoretically zero, which increases the levels of the corresponding harmonic currents. In these frequencies the active filter is providing the harmonic currents in lieu of the grid. The compensation also rises the voltage of the dc-link capacitor C_{dc} of the nonlinear load and therefore increases the power consumed in the parallel connected load resistor R_{dc} . Hence, a slight increase in the fundamental current of the nonlinear load is also expected. Fig. 11(e) shows the current that the active filter is injecting to the PCC. Naturally, it contains mainly the frequencies of controlled harmonics. The supply current in Fig. 11(g) is the sum of the active filter injected current and the nonlinear load current. It differs from the sinusoidal shape because the harmonics are needed to compensate the background distortion. By looking only the THD, which is 51 %, one might judge this as a very unfavorable supply current waveform, although in reality the harmonics are ‘good harmonics’, which are beneficial to the voltage quality. This indicates very clearly, that in all cases the supply current waveform does not tell much about the goodness or the badness of the load. In [14] this weakness of THD is also noted.

5.4 Adjustable voltage harmonics

Undoubtedly, the most common aim is to lower the voltage harmonic levels and to improve the quality of power. However, the control system proposed can be used to generate

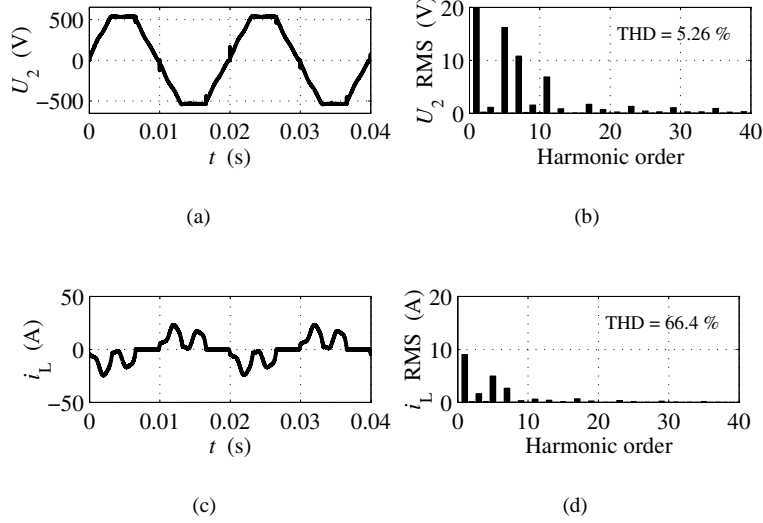


Fig. 10 A measurement with nonlinear load connected. (a) and (b) Line-to-line voltage. (c) and (d) Nonlinear load current.

a predefined voltage distortion if needed. This is accomplished by giving a nonzero voltage harmonic reference $\underline{u}_{2,\text{ref}}^v$. One reason to do this could be a need to test electrical apparatuses in a known distortion environment. A measurement was carried out to demonstrate the individual control of voltage harmonics. The results are shown in Fig. 12. First, all harmonics are given zero references, so that the converter is compensating the background distortion. Subsequently, a 5 % harmonic voltage reference is individually given to each of the harmonics 5-, 7+, 11- and 13+. Finally, all harmonics are given a 5 % reference at the same time. The phase angles of the voltage harmonics were selected to produce a maximum into the α -axis. In the time domain this means that the top of the fundamental wave and the top of the harmonic component are coinciding. The frequency domain presentations in Fig. 12 were calculated from the sample of 20 cycles. In the last case a dc-link voltage of 820 V was needed to inject necessary harmonic currents. In the other cases $u_{\text{dc}} = 780$ V was used and the minimum dc-link voltage resulting to stable operation was about 700 V.

6 Conclusions

An active control of grid voltage harmonics with a line converter equipped with an LCL-filter was proposed. The LCL-filter provides efficient suppression of switching noise, which is a necessity if a good voltage quality is strived for. The control of harmonic voltages was realized through individually controlled harmonic line currents. A frequency domain method utilizing the harmonic synchronous frames of reference was used in implementing the control of individual current and voltage harmonics. The converter current vector control was based on virtual converter flux linkage orientation and DTC-type hysteresis control. However, the control structures proposed are not bound to this specific control method but can be equally applied to converters employing other control methods.

Varying or unknown grid impedance poses a problem to the voltage feedback based active filter control. A method to measure the grid impedance at certain frequencies using the converter control system was proposed as a solution to this problem. It was shown by the measurements that the method can be used in estimating the grid impedance. Further,

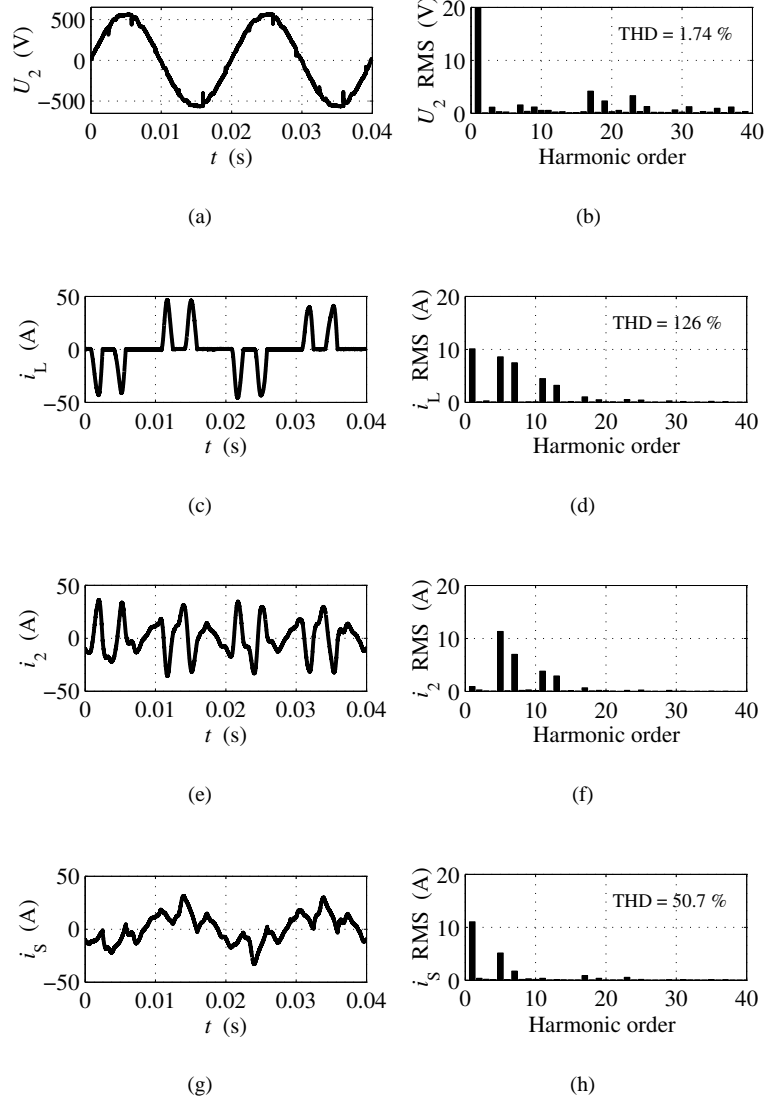


Fig. 11 Background distortion and nonlinear load originated distortion compensated by active filter. (a) and (b) Line-to-line voltage. (c) and (d) Nonlinear load current. (e) and (f) Active filter current. (g) and (h) Supply current.

the measured grid impedance angles were used to decouple the control of the d- and the q-components of harmonic voltage in the harmonic synchronous frame. This resulted in a greatly enhanced system stability as demonstrated in a dynamic step change. The steady state performance of the system was tested by compensating the background voltage distortion and the distortion caused by a nonlinear load. In both cases the active harmonic compensation yielded a significant improvement in the voltage quality and a reduction of the THD below 2 % level. Finally, the capabilities and the power of the individual harmonic control was demonstrated by generating predetermined voltage distortions.

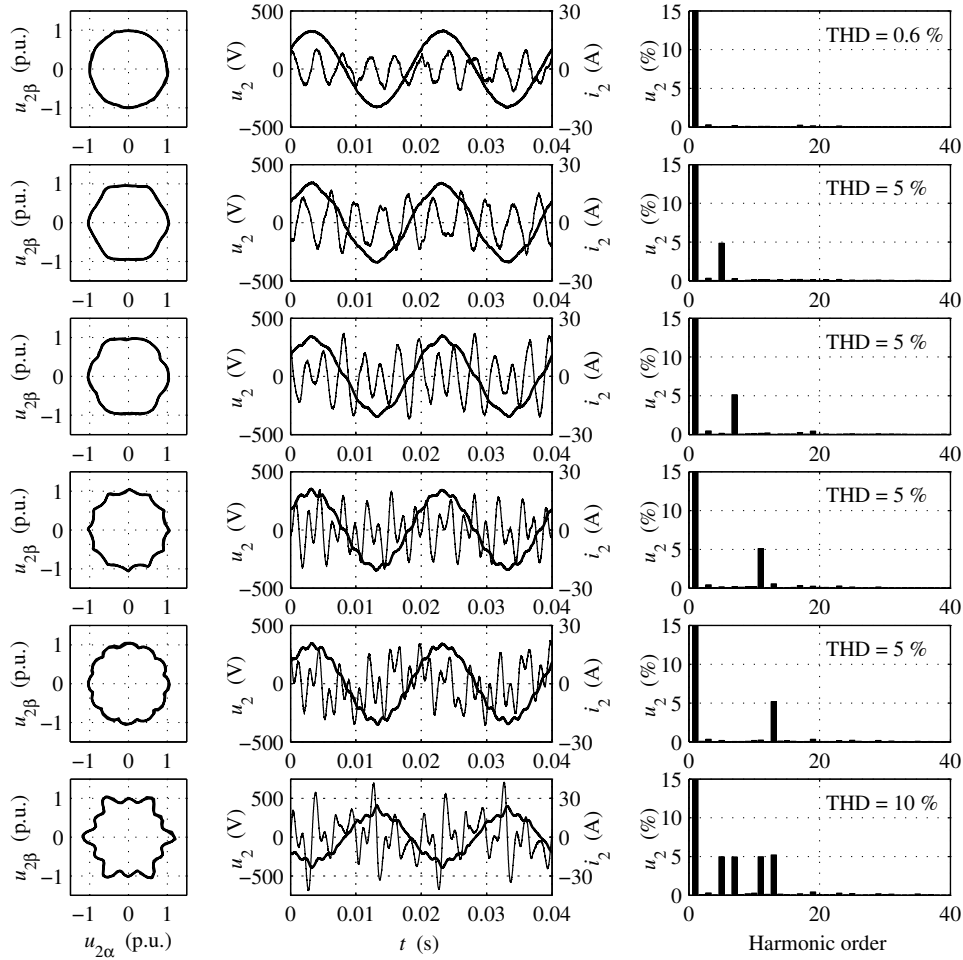


Fig. 12 A measurement demonstrating individual control of grid voltage harmonics. Grid voltage u_2 is presented in the $\alpha\beta$ -axis, in the time domain (phase voltage) and in the frequency domain. Converter line current i_2 is presented in the time domain (thin line). First row: zero harmonic references, background distortion compensated. Second row: 5 % of 5– harmonic. Third row: 5 % of 7+ harmonic. Fourth row: 5 % of 11– harmonic. Fifth row: 5 % of 13+ harmonic. Sixth row: All of the above. The harmonic phase angles were selected to produce a maximum in the α -axis.

References

1. Akagi H (1996) New Trends in Active Filters for Power Conditioning. IEEE Trans. on Industry Appl. 32(6): 1312–1322
2. Akagi H (1997) Control Strategy and Site Selection of a Shunt Active Filter for Damping of Harmonic Propagation in Power Distribution Systems. IEEE Trans. on Power Delivery. 12(1): 354–362
3. Abrahamsen F, David A (1995) Adjustable Speed Drive with Active Filtering Capability for Harmonic Current Compensation. In: Proc. of IEEE Power Electronics Specialists Conf. pp. 1137–1143
4. Brogan P, Yacamini R (2003) Harmonic Control Using an Active Drive. IEE Proc.-Electr. Power Appl. 150(1): 14–20
5. Tarkainen A, Pöllänen R, Niemelä M, Pyrhönen J (in press) Current Controlled Line Converter Using Direct Torque Control Method. European Transactions on Electrical Power

6. Pöllänen R, Tarkiainen A, Niemelä M, Pyrhönen J (2003) Supply Voltage Sensorless Reactive Power Control of DTC Modulation Based Line Converter with L- and LCL-filters. In: Proc. of 10th European Conference on Power Electronics and Applications
7. Brogan P, Yacamini R (1999) Stability of an Active Filter Based on Voltage Feedback. In: Proc. of 8th European Conference on Power Electronics and Applications
8. Brogan P, Yacamini R (2000) Stability of Selective Harmonic Active Filters. In: Proc. of 8th International Conference on Power Electronics and Variable Speed Drives. pp. 416–421
9. Emanuel AE, Yang M (1993) On the Harmonic Compensation in Nonsinusoidal Systems. *IEEE Trans. on Power Delivery* 8(1): 393–399
10. Grady WM, Samotyj MJ, Noyola AH (1990) Survey of Active Power Line Conditioning Methodologies. *IEEE Trans. on Power Delivery*. 5(3): 1536–1542
11. Yano M, Kuramochi S, Nanaumi N (1997) New Control Method of Harmonic Current Compensation Using Individual Rotating P-Q Frame of Corresponding Frequency. in Proc. of 7th European Conference on Power Electronics and Applications, pp. 4842–4847
12. Mattavelli P (2001) A Closed-Loop Selective Harmonic Compensation for Active Filters. *IEEE Trans. on Industry Appl.* 37(1): 81–89
13. Tarkiainen A, Pöllänen R, Niemelä M, Pyrhönen J (2004) Identification of Grid Impedance for Purposes of Voltage Feedback Active Filtering. *IEEE Power Electronics Letters*. 2(1): 6–10
14. Arrillaga J, Bollen MHJ, Watson NR (2000) Power Quality Following Deregulation. *Proceedings of the IEEE*. 88(2): 246–261

Publication V

A. TARKIAINEN, R. PÖLLÄNEN, M. NIEMELÄ, AND J. PYRHÖNEN

Identification of Grid Impedance for Purposes of Voltage Feedback Active Filtering

IEEE Power Electronics Letters, vol. 2, no. 1, March 2004, pp. 6–10.

Copyright © 2004 IEEE. Reprinted with permission.

Identification of Grid Impedance for Purposes of Voltage Feedback Active Filtering

Antti Tarkkiainen, Riku Pöllänen, *Member, IEEE*, Markku Niemelä, and Juha Pyrhönen

Abstract—A voltage feedback active filter is vulnerable to unknown grid impedance. To overcome this problem we propose an identification method, which uses the control system of a frequency selective active filter to measure the grid impedance at selected frequencies. The usefulness of the method is experimentally demonstrated with a 19 kVA active rectifier with a voltage feedback active filtering function. The voltage feedback active filtering is performed in a case in which the active filter control is not stable before the impedance is identified with the method proposed. It is shown that the use of the measured grid impedance in the control system greatly enhances the dynamic stability of the system. Also, the grid impedance measurements are provided in two cases.

Index Terms—Active filters, harmonic distortion, power system harmonics, variable speed drives.

I. INTRODUCTION

AN ACTIVE filter with voltage feedback analyzes the grid voltage harmonics and injects harmonic currents, which are adjusted to mitigate the voltage distortion. The injected harmonic current flows through the grid impedance and the resulting voltage drop cancels the original harmonic voltage resulting in a more sinusoidal voltage waveform. To achieve this, the grid impedance has to be taken into account when calculating the harmonic current references from the measured harmonic voltages. In [1], it is shown that the voltage distortion minimization in a large customer bus may lead to minimum harmonic power loss, and it is believed to be a better compensation strategy than the sinusoidal line current, or the unity power factor operation. The inherent limitation of the voltage feedback active filter is that if the grid impedance is very small compared to the active filter rating, the injected current has only a negligible impact on the voltage. The clear benefit, however, is that the current of the local nonlinear load, or loads if multiple distorting units are present, does not need to be measured. This gives more freedom in siting the active filter unit, which may be advantageous in industrial environments. And further, the exact source of the distortion need not necessarily be known. The voltage distortion in the secondary side of the feeding transformer is composed of the local distortion, originating from local nonlinear loads, and the background distortion, which is coming from the primary side of the transformer. The voltage feedback active filter treats both voltage distortions equally. In some cases, it may be undesirable for the active filter to compen-

Manuscript received December 23, 2003; revised March 26, 2004. Recommended by Associate Editor L. M. Tolbert.

The authors are with the Department of Electrical Engineering, Lappeenranta University of Technology, FIN-53851 Lappeenranta, Finland (e-mail: Antti.Tarkkiainen@lut.fi).

Digital Object Identifier 10.1109/LPEL.2004.828442

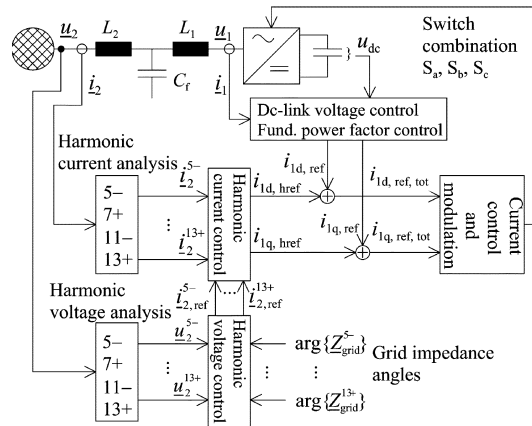


Fig. 1. Overview of the control system. Controlled harmonic line currents are used in mitigating the harmonic grid voltages.

sate for the background distortion, especially if it is produced by the other users of electrical power. In such an environment the voltage feedback active filter may not be favored, although, in [2] it is proposed that the background distortion can be measured and excluded from the compensation.

In order to operate, the voltage feedback active filter needs to know the grid impedance. In a previously proposed solution [3], [4] the grid impedance is modeled with a series inductance and a shunt capacitance. These parameters are used in the control system to model the grid for the purposes of harmonic current reference calculation. In real grids these parameter values may be unknown and difficult to obtain. Moreover, it may be that such a grid model is not accurate enough to describe the impedance in all necessary frequencies. This letter proposes a measurement-based method to identify the grid impedance. The method uses the control system of the active filter to measure the grid impedance at frequencies that are selected for harmonic compensation.

II. ACTIVE FILTER CONTROL SYSTEM

The active filter used in the experiments is a 19-kVA industrial IGBT line converter typically used in four-quadrant variable speed drives. The description of the line converter control system may be found in [5]. The active filtering is provided as an add-on feature to this converter control system. An overview of the control system is shown in Fig. 1. The fundamental wave line converter control needs to measure only the dc-link voltage u_{dc} and the converter current vector \underline{i}_1 . The active filtering control

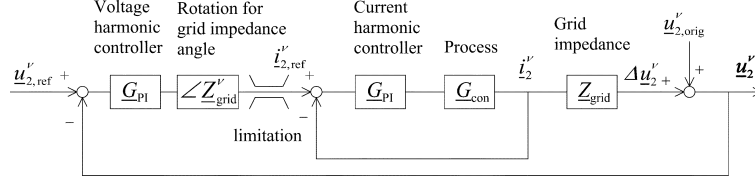


Fig. 2. Control system of a grid voltage harmonic u_2^ν . $u_{2,orig}^\nu$ is an intrinsic voltage, which summed with the active filter caused voltage drop Δu_2^ν constitutes u_2^ν . The process G_{con} includes the converter current vector control and the physical modulation process.

measures the converter line current vector i_2 and the grid voltage vector u_2 . The nominal values of the converter are $U_n = 400$ V, $I_n = 27$ A, $S_n = 27$ kVA and $f_n = 50$ Hz. An average switching frequency of 4 kHz is used. Four individual harmonic sequences are controlled: 5-, 7+, 11-, and 13+, where the sign denotes the rotation direction. Control algorithms are implemented to the Motorola 56002 digital signal processor in assembler language.

The analysis and the control of the harmonics are realized with the method of harmonic synchronous reference frames, used previously, e.g., in [6] and [7]. Each individual harmonic sequence is transformed to a corresponding synchronous frame, where frequency components other than the interesting one, which is appearing as a dc-signal, are filtered out. The direct and the quadrature components of a harmonic are controlled with PI-controllers in a harmonic synchronous frame, resulting in a closed loop control of individual harmonic sequences. The control system of a single grid voltage harmonic is depicted in Fig. 2.

The ν^{th} active filter-injected current harmonic i_2^ν produces a voltage drop

$$\Delta u_2^\nu = Z_{grid}^\nu i_2^\nu \quad (1)$$

across the grid impedance Z_{grid}^ν . The grid impedance causes a phase shift between the active filter-injected harmonic current and the resulting voltage drop. Typically, the grid impedance is inductive and it may be approximated with the transformer's short circuit inductance L_{trafo} . In this case, the resulting voltage drop vector Δu_2^ν is leading the injected current vector i_2^ν by 90° . Therefore, in the control system, the reference current vector should be lagged by the same angle in order to neutralize the effect of the grid impedance phase shift. However, it may be that other loads, or, e.g., a power factor correction capacitor, will alter the effective grid impedance seen by the active filter. In the harmonic synchronous frame a wrong grid impedance angle causes a cross-coupling between the d- and the q-axes. A strong cross-coupling will lead to unstable operation. A method to estimate the grid impedance is needed.

III. IDENTIFICATION OF GRID IMPEDANCE

In Fig. 3, a simplified grid impedance model, where L_{trafo} denotes a transformer short circuit impedance, and C_c and R_c a power factor compensator, is presented. The active filter is denoted with a current source i_2 . The grid impedance is estimated using the control system in Fig. 2 with the outer feedback loop disconnected. Hence, only the current control loop is active and

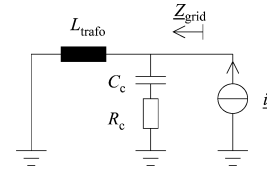


Fig. 3. Simplified model of a grid impedance.

the voltage control loop is disabled. The grid impedance may be estimated by introducing a change of $\Delta i_{2,ref}^\nu$ to the harmonic line current reference vector and by measuring the resulting change in the harmonic grid voltage Δu_2^ν . The grid impedance at this frequency is calculated by

$$Z_{grid}^\nu = \frac{\Delta u_2^\nu}{\Delta i_{2,ref}^\nu} \quad (2)$$

Due to the integral-type control, the actual harmonic current vector very accurately reflects the reference vector in steady-state and we may assume that $i_2^\nu = i_{2,ref}^\nu$. In Fig. 4 the results of the impedance measurement with the proposed method is presented in two cases. In the first case, shown in Fig. 4(a), no other loads were connected to the transformer secondary. The impedance measurement was performed with a 0.2 p.u. (or 5.4 A RMS) current magnitude change. From the transformer name plate values, the short circuit inductance was calculated as $L_{trafo} = 540 \mu\text{H}$. As shown in Fig. 4(a), the values measured by the converter agree quite well with the theoretical curve obtained with this simple transformer model. In the second case, shown in Fig. 4(b), a power factor correction capacitor with a series resistor was connected to the transformer secondary as shown in Fig. 3. The transformer short-circuit inductance and the capacitor form a resonant circuit with a resonance frequency of 510 Hz. The theoretical impedance curves in Fig. 4(b) are drawn with three different values of R_c , namely, 0.5 Ω , 0.75 Ω , and 1 Ω . The correspondence improves when the resistance is increased, showing that the impedance of such a resonance circuit is quite sensitive to the amount of damping. It is not surprising that the simplified impedance model in Fig. 3 is not very accurate, and that in the real system the damping is greater than in the model. Further, the bulk resistors used for R_c were not very accurate either. Despite the nominal resistance of 0.5 Ω , resistances ranging from 0.8 to 1.1 Ω could be measured when the resistors were hot. The active filter, however, works very well with the identified grid impedance as shown later in Figs. 5 and 7. This result supports the proposition that it is more practical to measure the effective grid impedance than to attempt to

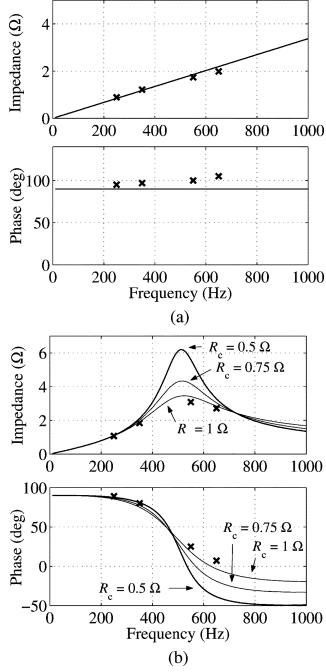


Fig. 4. Impedance of the grid, theoretical results (solid) and measured results (crosses). (a) Only a transformer with $L_{\text{trafo}} = 540 \mu\text{H}$. (b) Power factor correction capacitor with $C_c = 180 \mu\text{H}$ and $R_c = 0.5 \Omega$ connected to the transformer secondary. Theoretical curves are drawn with three different values of R_c .

model it, particularly in real world cases, which will be much more complicated than this example.

IV. OPERATION WITH IDENTIFIED GRID IMPEDANCE

The importance of having a correct grid impedance angle in the control system is illustrated in Fig. 5. A d-axis reference step of 0.05 p.u. (or 20 V RMS) in magnitude is applied to the 11th negative sequence (11-) grid voltage harmonic u_2^{11-} , when a power factor correction capacitor with $C_c = 180 \mu\text{H}$ and $R_c = 0.5 \Omega$ is connected at the transformer secondary. In the first case, the grid impedance is erroneously assumed as inductive and in the second case, the identified grid impedance angle is used in the control system. The measurement shows that in the first case a strong cross-coupling between the axes is present and the control system is barely stable. In the second case only a slight cross-coupling and no oscillations are observed. The identification of the grid impedance angle greatly enhanced the stability of the system.

Figs. 6 and 7 show the effect of the voltage feedback active filter. The measurement setup is depicted in Fig. 8. The power factor correction capacitor is connected in the same terminals with the nonlinear load. Therefore the load current i_L also includes the capacitor current. Fig. 6 shows the case where the active filter is not modulating. The nonlinear load and the background distortion constitute a voltage distortion with total harmonic distortion (THD) of about 5%. The THD of the local

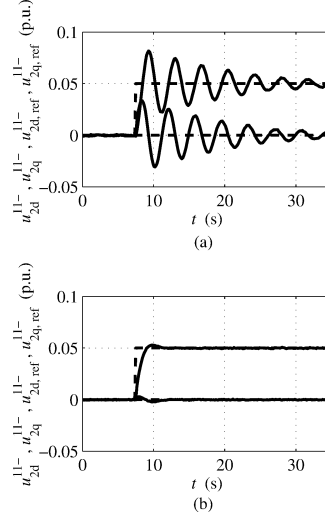


Fig. 5. Measured 0.05 p.u. step in the 11th negative sequence d-axis grid voltage reference $u_{2d,\text{ref}}^{11-}$ at $t = 7.5 \text{ s}$. (a) Inductive grid impedance angle $\arg\{Z^{11-}\} = 90^\circ$ assumed. (b) Identified impedance angle $\arg\{Z^{11-}\} = 24^\circ$ is used to decouple the d- and the q-axes.

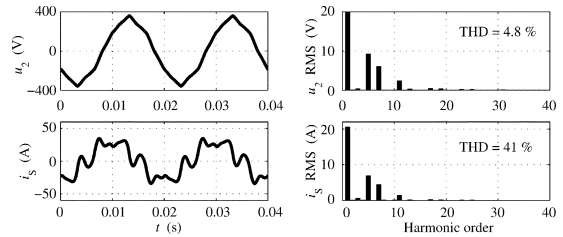


Fig. 6. Not compensated. Top: grid phase voltage, bottom: supply current.

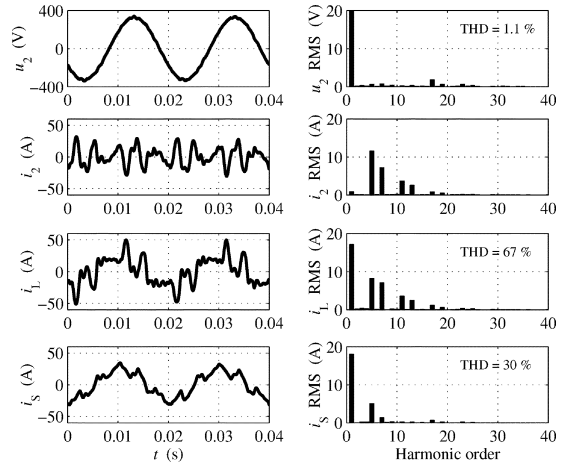


Fig. 7. Compensated. First row: grid phase voltage, second row: active filter current, third row: nonlinear load and power factor correction capacitor current, fourth row: supply current. Supply current waveform differs from the sinusoid because the harmonics are needed to compensate the background voltage distortion.

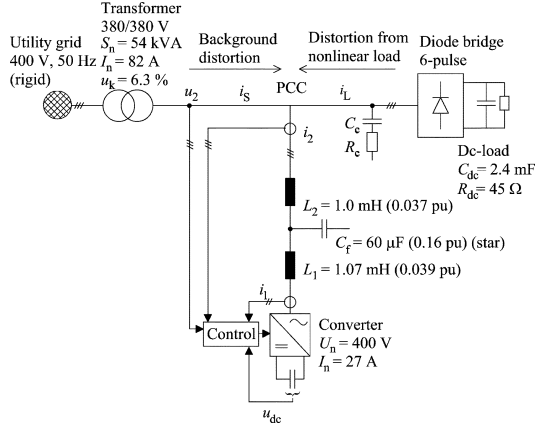


Fig. 8. Measurement setup. Voltage distortion in the point of common coupling (PCC) is composed of the background distortion coming from the primary side of the transformer and the distortion that is caused by the nonlinear load.

utility grid is about 2%, and in the test setup this represents the background distortion, which is coming from the primary side of the transformer. The compensated case is shown in Fig. 7. The voltage THD is reduced to about 1%, which is a lower value than what can be measured from the local rigid utility grid. In the load current the diode bridge current spikes are superimposed in the capacitor current and are clearly visible. In the uncompensated case, the spikes are not so clear because the weak grid cannot feed such harmonic currents. The supply current in the compensated case differs from the sinusoid because the harmonics are needed for compensating the background voltage distortion. When the power factor correction capacitor was connected, the system was unstable if an inductive grid impedance was erroneously presumed. After the grid impedance angles were identified and updated into the control system, no stability problems were encountered.

V. DETECTION OF OSCILLATORY MODES

The inherent disadvantage of the proposed offline identification method is that it cannot perceive the changes in the grid impedance while the active filtering operation is ongoing. Therefore, changes in the operation environment, e.g., switching the capacitors on, may drive a voltage control loop to unstable, or, oscillatory operation mode. A simple method to detect oscillations in the voltage control loop is to calculate the time integral of the squared length of the voltage error vector. The squared value is used to avoid the calculation of square-root in the practical implementation. For the 11th negative sequence the error integral is calculated as

$$(e^{11-})^2 = \int \left(u_{2d}^{11-} - u_{2d,\text{ref}}^{11-} \right)^2 + \left(u_{2q}^{11-} - u_{2q,\text{ref}}^{11-} \right)^2 dt. \quad (3)$$

The integral is zeroed regularly in every T_z s. When the active filter is operating correctly, the value of the integral remains relatively small. If the voltage control loop begins to oscillate, or, is going unstable, the value of the integral increases rapidly. If

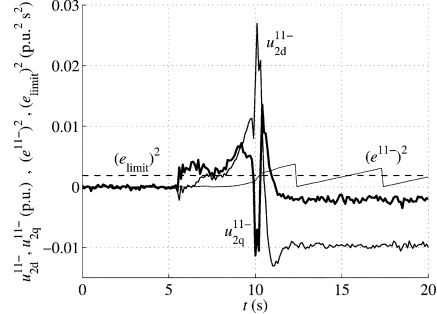


Fig. 9. Detection of unstable mode. The capacitors are switched on at $t = 5.5$ s and the voltage control loop is disabled at $t = 10.2$ s in order to stop the incipient unstable operation. The limiting value is $(e_{\text{limit}})^2 = 0.001875$ p.u.²s².

the integral reaches the predetermined value $(e_{\text{limit}})^2$, the control loop is concluded to be unstable and it is instantaneously disabled by setting the gain parameters of the voltage harmonic controller to zero. The limiting value $(e_{\text{limit}})^2$ should be chosen such that normal transients do not trip the voltage controllers but, at the same time, incipient unstable oscillations are detected before they make the active filter trip to overcurrent.

The operation was tested by switching the power factor correction capacitor ($C_c = 180$ μ F, $R_c = 0$ Ω) on while the active filter was compensating. To aggravate the situation, the series resistors were left out of the capacitors. The measurement showing the operation at the switching moment is shown in Fig. 9. The signals were sampled from the control board with a 0.1 s sample time and the error integral was zeroed in every 5 s. Hence, we have $T_z = 5$ s. The capacitor is switched on at $t = 5.5$ s, making the components of the harmonic voltage vector u_{2d}^{11-} and u_{2q}^{11-} to deviate from the references, which are kept at zero all the time. The active filter reacts by injecting more harmonic current but, as a consequence of the changed grid impedance, the harmonic voltage is not mitigated but amplified. Concurrently, the error integral $(e^{11-})^2$ begins to grow and it crosses the limit $(e_{\text{limit}})^2 = 0.001875$ p.u.²s² at $t = 10.2$ s, making the voltage control loop cease operation. The developing unstable oscillation dies out and the harmonic voltage vector components return to the values corresponding to the distortion from the nonlinear load. Also, the harmonic voltage control loop 13+ was tripped in the capacitor switching but the active filter continued operation with the voltage control loops 5- and 7+, which remained stable. After running the grid impedance identification for the 11- and 13+ harmonic sequences, the active filter operated stably with all voltage harmonic control loops enabled, even though the damping of the power system was rather low.

The low damping condition is obviously a challenging operating environment for the voltage feedback active filter. In order to diminish the risk of resonances, it may be better not to compensate problematic resonant frequencies. Moreover, at the frequencies of high impedance resonances, the grid impedance measurement should be performed with relatively low harmonic current magnitude, because, due to the resonance, the amplitude of the resulting harmonic voltage can be high and severely distort the voltage. The stability of the voltage control loops is

further affected by the tuning of the harmonic voltage and the harmonic current control loops. In a cascaded control structure the inner control loop is recommended to be at least ten times faster than the outer one.

VI. CONCLUSIONS

An identification method of the grid impedance for the frequency selective voltage feedback active filter was proposed. The identification method uses the active filter control system and it is based on direct measurement. Therefore, the voltage harmonic compensation is not dependent on knowledge of the parameters constituting the grid impedance, such as series inductance and shunt capacitance. The identification method measures the grid impedance in certain harmonic sequences, e.g., the fifth negative sequence. For active filtering purposes, common harmonic sequences were selected, but, if needed, the impedances in uncommon sequences, such as the fifth positive sequence, can be measured as well. The identification method was validated experimentally and the importance of knowing the correct impedance was demonstrated. An active filtering performance was presented in a case in which the operation would not have been possible without the correct

impedance information obtained with the proposed method. Finally, a method to detect unstable oscillatory modes of the voltage control loops was described. The method helps avoid the overcurrent tripping of the active filter if the grid impedance changes while the active filter is operating.

REFERENCES

- [1] A. E. Emanuel and M. Yang, "On the harmonic compensation in non-sinusoidal systems," *IEEE Trans. Power Delivery*, vol. 8, pp. 393–399, Jan. 1993.
- [2] P. Brogan and R. Yacamini, "Harmonic control using an active drive," *Proc. Inst. Elect. Eng., Electr. Power Appl.*, vol. 150, pp. 14–20, Jan. 2003.
- [3] —, "Stability of an active filter based on voltage feedback," in *Proc. 8th Eur. Conf. Power Electronics Applications*, 1999.
- [4] —, "Stability of selective harmonic active filters," in *Proc. 8th Int. Conf. Power Electronics Variable Speed Drives*, 2000, pp. 416–421.
- [5] R. Pöllänen, A. Tarkainen, M. Niemelä, and J. Pyrhönen, "Supply voltage sensorless reactive power control of DTC modulation based line converter with L- and LCL-filters," in *Proc. 10th Eur. Conf. Power Electronics Applications*, 2003.
- [6] M. Yano, S. Kuramochi, and N. Nanaumi, "New control method of harmonic current compensation using individual rotating P-Q frame of corresponding frequency," in *Proc. 7th Eur. Conf. Power Electronics Applications*, vol. 4, 1997, pp. 4842–4847.
- [7] P. Mattavelli, "A closed-loop selective harmonic compensation for active filters," *IEEE Trans. Ind. Applicat.*, vol. 37, pp. 81–89, Jan./Feb. 2001.